

UNIVERSITÉ D'ORLÉANS

Energie, Matériaux, Sciences de la Terre et de l'Univers (EMSTU)

Centre National de la Recherche Scientifique (CNRS)

Institut de Combustion Aérodynamique Réactivité et Environnement (ICARE)

THÈSE présentée par :

Alfio Emanuele Vinci

soutenue le : **08 décembre 2022**

pour obtenir le grade de : **Docteur de l'Université d'Orléans**

Discipline/ Spécialité : **Energétique**

Physics of Magnetic Nozzles and Helicon Plasma Discharges

Physique des tuyères magnétiques et des décharges à plasma helicon

Thèse dirigée par :

M. Stéphane Mazouffre

Directeur de recherche, ICARE, CNRS Orléans

RAPPORTEURS :

M. Ivo Furno

Adjunct Professor, Swiss Plasma Center, EPFL

M. Georg Herdrich

Apl. Prof. Dr., Universität Stuttgart

JURY :

M. Ivo Furno

Adjunct Professor, Swiss Plasma Center, EPFL,
Président du jury

M. Fabrizio Paganucci

Associate Professor, Università di Pisa

M. Pablo Fajardo

Adjunct Professor, Universidad Carlos III de Madrid

M. Sylvain Iséni

Chargé de Recherche, GREMI - CNRS

M. Stéphane Mazouffre

Directeur de recherche, ICARE, CNRS Orléans

M. Georg Herdrich

Apl. Prof. Dr., Universität Stuttgart

Mme. Mercedes Ruiz

Project manager, SENER Aeroespacial (Invited guest)



DOCTOR OF PHILOSOPHY THESIS

UNIVERSITÉ D'ORLÉANS

Energie, Matériaux, Sciences de la Terre et de l'Univers (EMSTU)

CENTRE NATIONAL DE LA RECHERCHE SCIENTIFIQUE (CNRS)

Institut de Combustion Aérodynamique, Réactivité
et Environnement (ICARE)

Physics of Magnetic Nozzles and Helicon Plasma Discharges

ALFIO EMANUELE VINCI

Director: Stéphane MAZOUFFRE, Research director, ICARE - CNRS

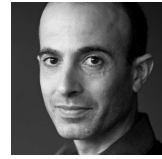
Rapporteurs: Ivo FURNO, Adjunct Professor, Swiss Plasma Center, EPFL
Georg HERDRICH, Apl. Prof. Dr., Universität Stuttgart

Jury members: Ivo FURNO, Adjunct Professor, Swiss Plasma Center, EPFL (President of jury)
Fabrizio PAGANUCCI, Associate Professor, Università di Pisa
Pablo FAJARDO, Adjunct Professor, Universidad Carlos III de Madrid
Sylvain ISÉNI, Chargé de Recherche, GREMI - CNRS
Stéphane MAZOUFFRE, Research director, ICARE - CNRS
Georg HERDRICH, Apl. Prof. Dr., Universität Stuttgart
Mercedes RUIZ, Project manager, SENER Aeroespacial (Invited guest)

December 8, 2022

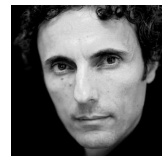
Questions you cannot answer
are far better than answers you cannot question.

YUVAL NOAH HARARI, 2018



Singuli singula novit et cetera taceat.

VALERIO APREA, 2021



Le nombre fait la loi,
mais le bien n'a rien à faire avec le chiffre.
Toute fiction s'expie [...].

HENRI-FRÉDÉRIC AMIEL, 1871



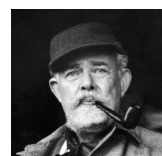
Se l'obiettivo della scienza fossero solo le predizioni,
Coperino non avrebbe scoperto nulla rispetto a Tolomeo.

CARLO ROVELLI, 2020



The best thing for disturbances of the spirit is to learn. [...]
That is the only thing which the poor mind can never exhaust,
never alienate, never be tortured by, never fear or distrust
and never dream of regretting.

TERENCE HANBURY WHITE, 1938



Abstract

Electrodeless plasma thrusters represent a new class of electric space propulsion possessing a number of interesting features. Their current-free nature and lack of plasma-exposed electrodes are valuable characteristics for meeting long lifetime requirements and operation with alternative propellants. However, given the complex physics involved in these devices, performance metrics are typically not competitive enough with other established technologies. Fundamental research is therefore needed to provide an insight on the relevant phenomena so as to suggest strategies for improvement.

In this framework, this thesis presents and discusses the results of several experimental campaigns specifically aimed at better understanding the physics underlying helicon plasma discharges and magnetic nozzles. Measurements have been performed on three different plasma devices using a multitude of diagnostic techniques. Parametric analyses have involved the use of different propellants, specific ranges of input power, diverse topologies of the applied magnetic field. As a function of these external parameters, ions and electrons properties have been extensively characterized to collect observations and findings that can support future designs of magnetic-nozzle-based thrusters.

Research activities have covered a number of relevant aspects such as: the effect of the magnetic throat location on the plasma plume; the impact of diverse magnetic field strengths on the plasma parameters; the electron thermodynamics along magnetic field lines as a function of the nozzle divergence degree; the impact of electron-cyclotron resonance on the electron flow throughout the magnetic nozzle; the atom and ion dynamics from inside the discharge chamber to the far-field plume of a helicon plasma thruster and of a waveguide electron-cyclotron resonance thruster; the use of iodine as propellant for electrodeless devices. All of these experiments have shown trends that lead toward some design strategies devoted to the enhancement of propulsive performance. These results can also be regarded as a repository of experimental evidence which can support validation and improvement of simulation tools.

Résumé

Les propulseurs à plasma sans électrodes représentent une nouvelle classe de propulseurs spatiaux électriques possédant un certain nombre de caractéristiques intéressantes. Leur absence de courant net et l'absence d'électrodes exposées au plasma sont des avantages précieux pour répondre aux exigences de longue durée de vie et de fonctionnement avec des propergols alternatifs. Cependant, étant donné la complexité de la physique de ces dispositifs, les indicateurs de performance ne sont généralement pas assez compétitives par rapport aux autres technologies établies. La recherche fondamentale est donc nécessaire pour fournir un aperçu des phénomènes pertinents afin de suggérer des stratégies d'amélioration.

Dans ce cadre, cette thèse présente et discute les résultats de plusieurs campagnes expérimentales visant spécifiquement à mieux comprendre la physique à la base des décharges plasma helicon et des tuyères magnétiques. Des mesures ont été effectuées sur trois dispositifs plasma différents en utilisant une multitude de techniques de diagnostic. Les analyses paramétriques ont impliqué l'utilisation de différents propergols, de gammes spécifiques de puissance, de diverses topologies du champ magnétique appliqué. En fonction de ces paramètres externes, les propriétés des ions et des électrons ont été caractérisées de manière approfondie afin de recueillir des observations et des résultats susceptibles d'étayer la conception de futurs propulseurs à tuyères magnétiques.

Les activités de recherche ont couvert un certain nombre d'aspects tels que : l'effet de l'emplacement de la gorge magnétique sur la plume de plasma ; l'impact de diverses intensités de champ magnétique sur les paramètres du plasma ; la thermodynamique des électrons le long des lignes de champ magnétique en fonction du degré de divergence de la tuyère ; l'impact de la résonance électron-cyclotron sur le flux d'électrons à travers la tuyère magnétique ; la dynamique des atomes et des ions depuis l'intérieur de la chambre de décharge jusqu'au champ lointain d'un propulseur à plasma helicon et d'un propulseur à résonance électron-cyclotron ; l'utilisation de l'iode comme propergol pour les propulseurs sans électrode. Toutes ces expériences ont montré des tendances qui mènent à des stratégies de conception visant à améliorer les performances de propulsion. Ces résultats peuvent également être considérés comme un référentiel de preuves expérimentales qui peuvent soutenir la validation et l'amélioration des outils de simulation.

Acknowledgments

History should teach us that every work, no matter how infinitely small or immensely large this may be, never deserves to bear a single signature. Every creation results from a community in the broadest possible sense of the term, from the influence of ideas to practical cooperation.

That said, I do not feel like filling this page with a variety of names that would remain anonymous to all those who were not part of the small group of people with whom I had the honor of sharing the years straddling which the efforts collected in these pages took place. What I want to thank with all sincerity are not the individuals, for they change, moving through time and space. Instead, what shall remain solid in my memory is the abstraction of this company, for better or worse. The set of behaviors, influences, values and everyday diversity that forms the background of the long days spent in the laboratory. Those who will read these lines and have spent time with me and/or for me during these years have every right to reflect themselves in the thanks that follow.

My attentions and gratitude go to persistence, resourcefulness, silence, complicity, independence, motivation, discouragement, sincerity, freedom, rigor, versatility, simplicity, quietude, empathy, awareness, doubt, curiosity. Thank you to those who have shown me owning at least one of these blessings.

Contents

Abstract	v
Résumé	vii
Acknowledgments	ix
List of Figures	xviii
List of Tables	xix
1 Introduction	1
1.1 Fundamentals of electrodeless plasma propulsion	1
1.1.1 Helicon plasma discharges	3
1.1.2 Magnetic nozzles	4
1.2 Research objective and outline	6
 I Research on a Helicon Source and Diagnostics Development	 9
2 Experimental Setup	11
2.1 Helicon plasma source	11
2.2 Diagnostics	13
2.2.1 B-dot probe	13
2.2.2 Capacitive probe	15
2.2.3 RF-compensated Langmuir probe	16
2.2.4 Planar probe with a guard ring	19
2.2.5 Retarding potential analyzer (model 1)	21
2.2.6 Retarding potential analyzer (model 2)	22
2.2.7 Laser-induced fluorescence spectroscopy	23
 3 Experimental Campaigns and Results	 27
3.1 Direct comparison of krypton and xenon discharge properties in the magnetic nozzle	27
3.1.1 RF propagating magnetic field	28
3.1.2 Floating potential fluctuations	30
3.1.3 Effect of different magnetic strengths	31
3.1.4 Summary and conclusion	39

3.2	Plasma properties conditioned by the magnetic throat location	39
3.2.1	Plasma plume visual inspection	41
3.2.2	Langmuir probe measurements	42
3.2.3	Plasma density profile model	46
3.2.4	Ion current density measurements	49
3.2.5	Atoms and ions velocity measurements	50
3.2.6	Summary and conclusion	55
3.3	Effect of magnetic nozzle divergence on ion and electron properties . .	55
3.3.1	Spatially resolved plasma properties	57
3.3.2	Ion energy influenced by the magnetic nozzle shape	58
3.3.3	Electron thermodynamics along magnetic nozzle lines	59
3.3.4	Summary and conclusion	64
3.4	Effect of electron-cyclotron resonance on the electron flow in the mag- netic nozzle	65
3.4.1	Electron properties in the magnetic nozzle	68
3.4.2	Summary and conclusion	71
3.5	Plasma oscillations and instabilities in the magnetic nozzle	71
3.5.1	Ion current fluctuations	71
3.5.2	Three-probe experiment	76
II	Research on Magnetic Nozzle Dynamics at UC3M	89
4	Atoms and ions dynamics in the magnetic nozzle of a HPT	91
4.1	Experimental arrangement	91
4.2	Considerations on experimental findings	93
4.3	Modeling of fluorescence lineshape	96
4.4	Atoms and ions velocity profiles	102
4.5	Comparison of RPA and LIF spectroscopy results	105
4.6	Summary and conclusion	107
5	Ion dynamics in the magnetic nozzle of a waveguide ECRT	109
5.1	Introduction to ECR thrusters	109
5.2	Experimental setup	110
5.3	Observed spectra	112
5.4	Modeling of fluorescence lineshape	114
5.5	Ion velocity profiles	118
5.6	Summary and conclusion	120
III	Research on Iodine Propellant for Helicon Plasmas	123
6	Preliminary Iodine Feeding System Development	125
6.1	Motivation behind the use of iodine as propellant	125
6.2	Architecture and design caveats	127
6.3	First prototype setup	131
6.4	Second prototype setup	134
6.5	Heuristic sublimation model	136

IV	Conclusion	145
7	Conclusion	147
7.1	Summary	147
7.2	Perspectives	149
V	Appendix	153
A	List of Publications and Conferences	155
A.1	Peer-reviewed journal papers	155
A.2	Conference contributions	156
B	Iodine Physical and Chemical Properties	159
B.1	Atomic iodine	159
B.2	Molecular iodine	162
B.2.1	Phase Diagram	162
B.2.2	Iodine Viscosity	162
B.2.3	Iodine thermal conductivity	165
B.2.4	Iodine Solubility	166
B.2.5	Iodine Immobilization	167
B.3	Iodine Plasma	167
B.3.1	Ionization Cross Section	167
B.3.2	Plasma Chemistry	168
C	Version française	171
C.0.1	Chapitre 1: Introduction	171
C.1	Partie I: Recherche sur une source de plasma hélicon et développement des diagnostics	173
C.1.1	Chapitre 2: Dispositifs expérimentaux	173
C.1.2	Chapitre 3: Campagnes expérimentales et résultats	173
C.2	Partie II: Recherche sur la dynamique des tuyères magnétiques à UC3M	174
C.2.1	Chapitre 4: Dynamique des atomes et des ions dans la tuyère magnétique d'un propulseur à plasma hélicon	174
C.2.2	Chapitre 5: Dynamique des ions dans la tuyère magnétique d'un propulseur ECR à guide d'ondes	175
C.3	Partie III: Recherche sur l'iode comme propergol pour les plasmas hélicon	176
C.3.1	Chapitre 6: Développement préliminaire d'un système de distri- bution de l'iode	176
C.4	Chapitre 7: Conclusion	176
	Bibliography	194

List of Figures

1.1	Conceptual schematics of a typical electrodeless thruster.	2
2.1	Helicon plasma reactor.	11
2.2	Helicon plasma reactor schematics.	12
2.3	Double-saddle antenna.	12
2.4	<i>B-dot</i> probe.	13
2.5	<i>B-dot</i> probe circuit schematics.	13
2.6	<i>B-dot</i> probe calibration setup schematics.	14
2.7	<i>B-dot</i> probe calibration results.	14
2.8	Capacitive probe.	15
2.9	Capacitive probe calibration schematics.	15
2.10	Capacitive probe characterization.	15
2.11	RF-compensated Langmuir probe.	16
2.12	Choke characterization circuit.	16
2.13	Voltage drops during choke characterization. Profiles refer to (left) the second harmonic choke and (right) the third harmonic choke.	17
2.14	Impedance of 1st, 2nd and 3rd harmonic chokes.	17
2.15	RF-compensated LP characterization.	18
2.16	Typical I-V curve.	18
2.17	Results of uncertainty analysis of inferred plasma properties.	19
2.18	Planar probe with a guard ring.	20
2.19	I-V curves from planar probe with guard ring.	20
2.20	Debye length, floating and high-voltage sheath thickness	21
2.21	Retarding potential analyzer model 1.	22
2.22	Typical RPA I-V characteristic.	22
2.23	Retarding potential analyzer model 2.	23
2.24	LIF optical bench.	24
2.25	Optics used for LIF spectroscopy measurements.	24
3.1	Externally applied magnetic field profile.	27
3.2	<i>B-dot</i> probe results related to the Kr discharge.	28
3.3	<i>B-dot</i> probe results related to the Xe discharge.	29
3.4	Capacitive probe results relative to the krypton discharge.	30
3.5	Capacitive probe results relative to the xenon discharge.	30
3.6	Evolution of krypton plasma properties along the reactor axis.	32
3.7	Evolution of xenon plasma properties along the reactor axis.	32

3.8	Radial profile of krypton plasma properties.	33
3.9	Radial profile of xenon plasma properties.	33
3.10	Computed profiles of electron azimuthal currents (krypton).	34
3.11	Computed profiles of electron azimuthal currents (xenon).	34
3.12	Contour plots of krypton plasma properties.	36
3.13	Contour plots of xenon plasma properties.	36
3.14	Volumetric forces acting on electrons.	37
3.15	Most probable krypton ion energy.	38
3.16	Most probable xenon ion energy.	38
3.17	2D profiles of the externally applied magnetic fields.	40
3.18	Externally applied magnetic field on-axis profiles	41
3.19	Photographs of the plasma plume.	42
3.20	Normalized plasma density for the five magnetic configurations.	43
3.21	Normalized electron temperature for the five magnetic configurations.	43
3.22	Normalized plasma potential for the five magnetic configurations.	44
3.23	On-axis profiles of plasma properties.	45
3.24	Ion density profile in the proximity of the back-plate for the five mag- netic configurations.	45
3.25	Plasma density profile from helicon dispersion relation.	48
3.26	Ion current density profiles.	50
3.27	Kr I velocity distribution functions.	51
3.28	Kr II velocity distribution function.	51
3.29	Kr II velocity distribution function.	52
3.30	Kr II velocity distribution function.	52
3.31	Kr II most probable axial velocity profiles.	53
3.32	Parametric Kr II axial VDFs.	54
3.33	Magnetic streamlines crossing the tube edge for different topologies.	56
3.34	Magnetic streamlines used to study electron cooling.	57
3.35	Contour plots of normalized plasma density for the three tested shapes of the MN.	58
3.36	Contour plots of normalized electron temperature for the three tested shapes of the MN.	59
3.37	On-axis evolution of the ion energy distribution function for the three tested shapes of the MN.	60
3.38	On-axis evolution of the electron energy probability function for the three tested shapes of the MN.	60
3.39	Electron cooling rate evaluated along the magnetic streamlines for three different magnetic nozzle shapes.	61
3.40	Value of γ_e as function of Θ and α	62
3.41	Plasma potential and polytropic index γ_e for three different magnetic nozzle shapes.	63
3.42	2-D maps of the external magnetic field.	66
3.43	On-axis z-component of the external magnetic field.	66
3.44	Photographs of the plasma plume as a function of P_{IN} and I_{PB3}	67
3.45	EEPFs measured at $z = 0$ as function of power.	69
3.46	EEPFs measured at $z = 0$ as function of mass flow rate.	69
3.47	Percentage change of n_e and T_e at $z = 0$	69
3.48	Percentage change of n_e and T_e at $z = 0$	70

3.49	Electron properties at $z = 0$ cm.	70
3.50	Electron properties at $z = 31.5$ cm.	70
3.51	Typical ion saturation current spectrum.	72
3.52	Radial evolution of krypton ion saturation current.	73
3.53	Radial gradient of krypton plasma density versus instability amplitude.	74
3.54	Instability amplitude along the azimuthal coordinate.	74
3.55	Drift instability geometry.	75
3.56	Radial evolution of xenon ion saturation current.	76
3.57	Radial gradient of xenon plasma density versus instability amplitude.	77
3.58	Instability amplitude along the azimuthal coordinate.	77
3.59	Three Langmuir probes mounted to measure the radial and axial wavenumber.	79
3.60	Axial propagation of drift wave (krypton).	81
3.61	Axial propagation of drift wave (krypton).	81
3.62	Axial propagation of drift wave (krypton).	82
3.63	Axial propagation of drift wave (krypton).	82
3.64	Radial propagation of drift wave (krypton).	83
3.65	Radial propagation of drift wave (krypton).	83
3.66	Radial propagation of drift wave (krypton).	84
3.67	Radial propagation of drift wave (krypton).	84
3.68	Azimuthal propagation of drift wave (krypton).	85
3.69	Azimuthal propagation of drift wave (krypton).	85
3.70	Azimuthal propagation of drift wave (krypton).	86
3.71	Azimuthal propagation of drift wave (krypton).	86
4.1	Axial profile of the HPT magnetic field strength.	92
4.2	Experimental setup schematics relative to LIF and RPA measurements.	93
4.3	On-axis LIF spectra of xenon atoms and ions resolved along z	94
4.4	On-axis LIF spectra of Xe II resolved along z	95
4.5	Examples of LIF spectra of Xe II from angular scans.	95
4.6	Instance of hyperfine and Zeeman components.	98
4.7	Experimental and modeled Xe I lineshape.	100
4.8	Experimental and modeled Xe II lineshape.	100
4.9	Experimental and modeled Xe II lineshape.	101
4.10	Axial velocity profile of Xe I for different propellant mass flow rates.	102
4.11	Axial velocity profile of Xe II for different propellant mass flow rates.	103
4.12	Axial velocity profile of Xe II for different levels of input power.	104
4.13	Contour maps of the most probable ion velocity perpendicular to the scanning arc.	104
4.14	Example of dataset acquired to compare LIF and RPA measurements.	106
4.15	Most probable axial velocity of Kr ions probed with RPA and LIF.	106
4.16	Most probable axial velocity of Xe ions probed with RPA and LIF.	106
5.1	Schematic top view of the experimental setup.	110
5.2	Axial profiles and maps of the ECRT magnetic field amplitude.	111
5.3	Photographs of the thruster in operation with two different magnetic nozzle shapes.	111
5.4	LIF spectra resolved along z	113

5.5	Comparison of experimental versus modeled lineshapes using arbitrary values for T_i	114
5.6	Instance of χ^2_{red} evolution with T_i	115
5.7	Experimental versus modeled lineshape of Xe II.	116
5.8	Experimental versus modeled lineshape of Xe II.	117
5.9	Experimental versus modeled lineshape of Xe II.	117
5.10	Experimental versus modeled lineshape of Xe II.	118
5.11	Most probable axial velocity profile of Xe II for different electromagnet currents.	119
5.12	Most probable axial velocity profile of Xe II for different propellant mass flow rates.	119
5.13	Most probable axial velocity of Xe II for different levels of input power.	119
6.1	Iodine feeding line schematics.	127
6.2	Iodine feeding system heaters.	128
6.3	Photograph of the temperature control system circuit.	129
6.4	Iodine feeding line temperature monitoring web app.	129
6.5	Instance of iodine feeding line thermal characterization.	130
6.6	Iodine immobilization strategies.	130
6.7	First prototype iodine tank.	131
6.8	Issues relative to the first iodine tank prototype.	132
6.9	Filter condition after system disassembly.	133
6.10	Sublimation cup with damaged nickel coating after disassembly.	133
6.11	Second prototype iodine tank schematics.	134
6.12	Photograph of the second prototype iodine tank.	135
6.13	Photograph of the filter relative to the second prototype iodine tank.	135
6.14	Photograph of iodine sublimation surface.	136
6.15	Results of steady thermal FEM simulation of the iodine tank.	137
6.16	Qualitative dynamics of local iodine sublimation.	138
6.17	Instance of sublimation temperature map obtained via FEM thermal simulation.	139
6.18	Definition of the sticking factor profile in space and time.	139
6.19	Instance of initial transient and steady state regime observed when computing \dot{m}	140
6.20	Sublimation model benchmark case.	141
6.21	Mass flow rate versus probed temperature.	141
B.1	Molecular iodine in solid and vapor phases.	159
B.2	Iodine phase diagram.	162
B.3	Intermolecular potential function.	163
B.4	Chung vs. Sutherland viscosity model.	165
B.5	Chung vs. Sutherland thermal conductivity model.	166
B.6	First ionization cross-section for different propellants.	168
B.7	Iodine plasma rates.	169

List of Tables

2.1	Uncertainty analysis of rf-compensated LP measurements: percentage error of plasma properties for four different magnetic field strengths. .	19
2.2	Xe I, Xe II, Kr I and Kr II probed optical transitions.	25
3.1	Matrix of electromagnets current for the tested magnetic topologies. .	40
3.2	Helicon wave parameters.	49
3.3	Plume divergence parameter.	49
3.4	Order of magnitude of relevant velocity quantities.	50
4.1	Order of magnitude of the reduced χ^2 to quantify the goodness of fit. .	99
6.1	Propellants comparison.	126
B.1	Atomic iodine properties	160
B.2	Molecular iodine solid phase properties.	160
B.3	Molecular iodine liquid phase properties	161
B.4	Molecular iodine gaseous phase properties	161
B.5	Antoine parameters for I ₂	161
B.6	Conditions at triple, boiling and critical Point for I ₂	161
B.7	Iodine Solubility	167
B.8	Chemical reactions in iodine plasma.	169

Chapter 1

Introduction

The objective of this Chapter is to introduce to the concepts of electrodeless discharges and magnetic nozzle acceleration as applied to space electric propulsion, paying special attention to helicon plasma sources. Section 1.1 addresses the current state-of-the-art on the physical knowledge that underlies these technologies. The scope and content of this thesis are discussed in Section 1.2.

1.1 Fundamentals of electrodeless plasma propulsion

Electric propulsion (EP) is currently employed in space platforms for orbit-raising, station keeping, de-orbiting and eventually deep-space exploration [1–5]. Nowadays, mission objectives span from building near-Earth satellite networks to lunar space stations and Mars colonization [2, 6–8]. The need of reducing propellant consumption in parallel with the increased availability of power have made electric propulsion systems in general an attractive option. In the last few years, intense research activities have been focusing on electrodeless discharges to extend the mission range typically covered by mature technologies, e.g. Gridded Ion thrusters and Hall thrusters. The latter are still the most successful and long-standing concepts since they effectively provide good performance metrics both in terms of thrust level and specific impulse at low, moderate and high power ranges [5]. Another technology that merits attention is certainly that of Field Emission Electric Propulsion (FEEP) thrusters which possess a relatively high efficiency at the expense of a fairly modest thrust. To date, over 100 units have been deployed on-board of space platforms [9].

In general, each mission brings with it unique requirements in terms of specific impulse and service life. Current plasma thrusters often do not benefit from exceptional lifetimes, mainly due to strong erosion of exposed electrodes and discharge channel walls by ion and electron fluxes impinging on the surface. Furthermore, even the most advanced electron sources typically coupled with thruster heads, e.g. filament cathodes and hollow cathodes, still represent a critical component that hinders the reliability for extended operation. Another matter to consider is that the vast majority of EP systems currently proven in space operates on noble gases, primarily xenon though more recently also krypton [10]. The exclusivity of these propellants, albeit offering unparalleled practical advantages in certain respects especially during laboratory testing, is a huge limitation. Production of xenon remains limited and consequently its price

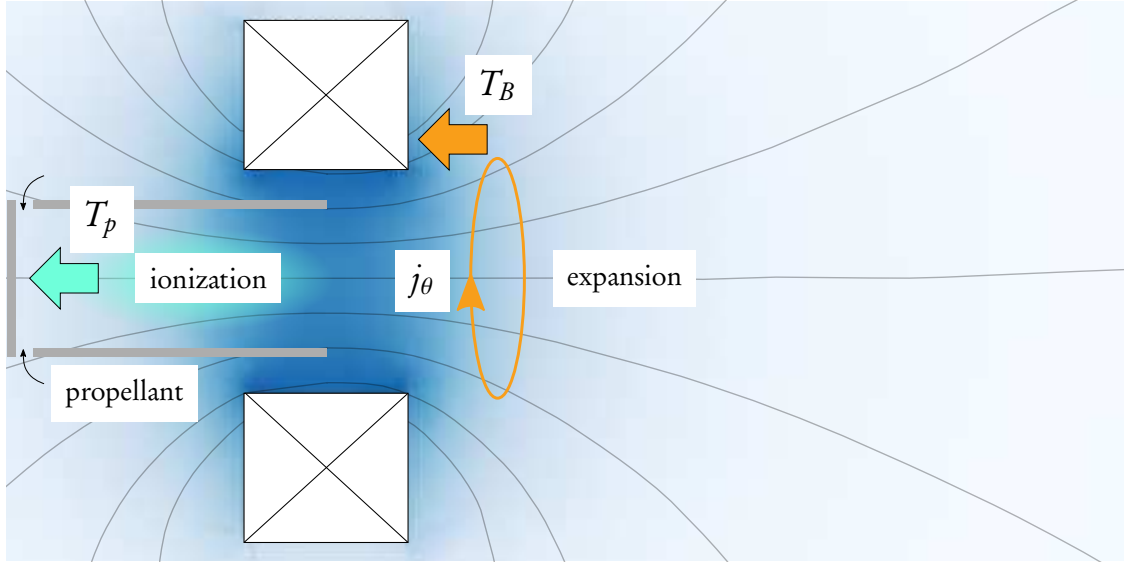


Figure 1.1: Conceptual schematics of a typical electrodeless thruster. Specific characteristics, such as magnetic field topology and propellant injection strategy, may vary depending on the nature of the discharge. T_p and T_B represent the electrothermal and electromagnetic thrust contribution, respectively.

tends to fluctuate considerably¹. Krypton on the other hand is more abundant, yet its adoption translates into lower propulsive performance and lower storage density with respect to xenon. A recently space-proven Gridded Ion thruster operating on iodine is to date nothing but a remarkable exception [13].

In short, longer lifetimes and compatibility with non-conventional propellants are deemed as valuable enabling characteristics for an EP system. These qualities extensively support the interest in electrodeless thrusters. Characteristics like a current-free nature, the elimination of plasma-electrodes interaction, the design simplicity, are the asset of these devices which can nominally operate without a dedicated neutralizer and on virtually any propellant [14–16]. Figure 1.1 illustrates a generalized and simplified representation of a conventional electrodeless thruster. The concepts that are currently studied by the research community and fall into the class of electrodeless devices essentially include Helicon Plasma Thrusters (HPT), Electron Cyclotron Resonance Thrusters (ECRT) and Variable Specific Impulse Magnetoplasma Rocket (VASIMR). All electrodeless systems operate on AC power but the way the electromagnetic radiation couples with the gas discharge strongly depends on the working frequency and field geometry [17, 18]. In the kHz and MHz range, gas ionization is achieved using alternating electric fields (named capacitive or E-coupling) or alternating magnetic fields (named inductive or H-coupling) by way of electrodes or coils that are not in contact with the plasma. In the presence of an external steady magnetic field, other types of energy deposition mechanisms are possible, such as propagation of helicon waves and electron-cyclotron resonance [17], the latter typically exploited in the GHz frequency range. Regardless of the specific working frequency and the nature of the alternating electromagnetic field, the input power couples to the electron population in the form of thermal energy which is

¹The global supply chain of noble gases has been experiencing substantial disruptions because of the invasion of Ukraine in the early 2022. Leading world news titles have discussed the situation in [11] and [12], among others.

in turn spent for ionization and acceleration². Transferring this energy to heavy particles via elastic collisions is an especially inefficient process in low-pressure plasmas [18], therefore virtually any electrodeless thruster embeds a magnetic nozzle (MN) as acceleration stage. The latter allows the ions to gain momentum through volumetric forces of electrostatic and electromagnetic nature.

This thesis specifically focuses on helicon plasma discharges and magnetic nozzles, which are the two fundamental constituents of an ordinary HPT. These two components are separately detailed in the following Sections 1.1.1 and 1.1.2.

1.1.1 Helicon plasma discharges

Helicon plasma devices are low-temperature plasma sources that rely on wave heating mechanisms to sustain a gas discharge. A conventional helicon source comprises three main components: *i*) a dielectric tube that physically delimits the plasma domain, *ii*) a radio-frequency (rf) powered antenna for gas ionization, and *iii*) an axial steady magnetic field for propagation of helicon waves and for reducing plasma-wall interactions. In any HPT, the external magnetic field also shapes a divergent geometry downstream the discharge tube to accelerate the plasma, as detailed in Section 1.1.2. Perhaps the most attractive aspect of these sources is the fact that they can operate over a quite broad range of input parameters while still providing remarkable ionization levels.

Studies on the propagation of helicon waves in a gas discharge have been relatively intense in the '70s and throughout the '90s mainly for applications in the semiconductor industry [19–24]. In the late '90s, the fundamental generalized theory of helicon waves has been reported in [25, 26]. Helicon modes are whistler waves that propagate in an axially magnetized plasma column with radially bounded cylindrical geometry [17]. The wave electric and magnetic fields feature radial, axial and often azimuthal modes which vary according to the boundary conditions. The operation regime is characterized by

$$\omega_{lh} \ll \omega \ll \omega_{ce}, \quad (1.1)$$

where ω_{lh} is the lower hybrid frequency and ω_{ce} is the electron-cyclotron frequency. In typical devices, the working frequency lies in the range 1 – 50 MHz. Sources are generally designed to operate at 13.56 MHz and/or its harmonics as they correspond to industrial standards. Modes excitation is achieved via an rf-powered antenna which essentially is a conductor placed outside the discharge tube having a specific shape. In the literature, the most common types include Nagoya III [27–29], double-saddle [19, 29–33], helical [27–29, 34–38], simple loop [38–40] and birdcage [41–45]. The major difference related to the antenna geometry lies in the azimuthal mode that it can excite, identified by the m number. It is still not fully understood if a specific azimuthal mode, either a right-hand polarized $m = +1$ or symmetric $m = 0$, represents a preferred choice. At laboratory level, the power system follows a conventional design with 50 Ω output that drives the antenna through a matching network to adapt the impedance.

Derivation of the dispersion relation [25] begins considering the wave fields vary as

$$\tilde{\mathbf{E}}, \tilde{\mathbf{B}} \sim \exp[i(m\theta + k_z z - \omega t)], \quad (1.2)$$

²This mechanism does not fully apply for the VASIMR. It in fact consists of two stages, the second of which does directly heat the ions by means of ion-cyclotron resonance.

1.1. FUNDAMENTALS OF ELECTRODELESS PLASMA PROPULSION

where θ is the azimuthal coordinate and k_z is the axial wavenumber. Maxwell equations are written in the form

$$\nabla \cdot \tilde{\mathbf{B}} = 0, \quad (1.3a)$$

$$\nabla \times \tilde{\mathbf{E}} = i\omega\tilde{\mathbf{B}}, \quad (1.3b)$$

$$\nabla \times \tilde{\mathbf{B}} = \mu_0 \mathbf{j}, \quad (1.3c)$$

and the electron momentum equation reads

$$-i\omega m_e \mathbf{v} = -e \left(\tilde{\mathbf{E}} + \mathbf{v} \times \mathbf{B} \right) - m_e \nu \mathbf{v}, \quad (1.4)$$

where m_e is the electron mass, \mathbf{v} is the velocity vector, \mathbf{B} is the external magnetic field and ν is a lumped collision rate. Combining the previous equations, one obtains

$$\left(\frac{\omega + i\nu}{\omega_{ce}} \right) \nabla \times (\nabla \times \tilde{\mathbf{B}}) - k_z \nabla \times \tilde{\mathbf{B}} + \frac{\mu_0 e \omega n_p}{B} \tilde{\mathbf{B}} = 0, \quad (1.5)$$

where n_p is the plasma density. Equation 1.5 can be factored as

$$(k_1 - \nabla \times) (k_2 - \nabla \times) \tilde{\mathbf{B}} = 0, \quad (1.6)$$

with k_1 and k_2 total wavenumbers that solve

$$\left(\frac{\omega + i\nu}{\omega_{ce}} \right) k^2 - k k_z + \frac{\mu_0 e \omega n_p}{B} = 0. \quad (1.7)$$

In the limit of negligible electron inertia, i.e. $m_e \rightarrow 0$, a simplified dispersion relation is immediately retrieved from Equation 1.7 as

$$k k_z = \frac{\mu_0 e \omega n_p}{B}, \quad (1.8)$$

The value of k_z is fixed by considerations on the antenna length d_A which show that efficient plasma coupling occurs only at $k_z = \pi/d_A, 3\pi/d_A$, etc. [17]. In general, two roots solve Equation 1.7. The first one (small wavenumber) corresponds to the usual helicon wave identified by Equation 1.8, whereas the second root (short wavelength) is an electron cyclotron wave first identified by Trivelpiece and Gould and therefore it is referred to as TG wave. It appears that at relatively intense external magnetic fields, the two waves are well separated. At weaker fields instead, the solutions tend to merge together and the helicon wave disappears when $\omega \geq \omega_{ce}/2$ [25].

The electromagnetic power associated with the excited modes is converted into electron thermal energy that rules a series of transport phenomena within the plasma domain. Inside the source tube, the conservation of axial momentum implies that the energy stored as static electron pressure is converted into ion acceleration [46]. This represents an electrothermal thrust component depicted in Figure 1.1 as T_p .

1.1.2 Magnetic nozzles

A conventional magnetic nozzle (MN) essentially is a steady magnetic field having a convergent-divergent geometry whose purpose is to accelerate and direct a plasma beam into vacuum [47, 48]. In the case of ECRTs, the magnetic throat is located upstream

the chamber backplate [49, 50], therefore plasma species only experience a divergent field. A set of electromagnets and/or permanent magnets are employed to shape the desired magnetic topology. Early experiments [51] have observed a close similarity between magnetic nozzles and classical gas-dynamics de Laval nozzles, with a plasma flux undergoing subsonic to supersonic transition in correspondence of the magnetic throat. However, MN physics retains a more complicated nature, where volumetric electromagnetic forces add to the classical pressure-driven expansion. In 1968, in his landmark book covering countless EP applications, Jahn [18] described the principle of magnetic nozzle acceleration using these words:

*"As in most glow discharges, the electrons acquire energies of a few electron volts from the electric field (an **electrothermal** process), but the ions remain relatively cold. Because of the magnetic field geometry, these energetic electrons are constrained to expand axially outward (an **electromagnetic** process), and in so doing they establish an electric field between themselves and the cold ions left behind, which in turn accelerates these ions to follow the electrons (an **electrostatic** interaction). The net effect is to convert electrical input energy from the glow discharge circuit into an axial streaming of cold plasma, but the detailed process clearly does not submit to any single electrical classification."*

In the simplest scenario where the dynamics of a single particle is analyzed, a magnetic nozzle acts as a force on the particle in the parallel direction [52]. Because of conservation of total energy and adiabatic invariance of the magnetic moment [52], the component of the particle kinetic energy aligned with the magnetic streamlines increases at the expense of the perpendicular one. In other words, the particle accelerates along the magnetic field lines by conversion of its thermal energy. When collective effects of multiple alike particles and also multiple species are considered, other phenomena need to be taken into account.

In the typical range of magnetic field intensities used in HPT and ECRT, only electrons are fully magnetized given their lower mass. Therefore they are forced to flow accordingly to the magnetic field topology. Ions are thereby axially accelerated by the ambipolar electric field that results from the higher electron mobility. Furthermore, magnetic confinement in the plasma source produces radially non-uniform profiles of pressure and plasma potential. Starting from the macroscopic transport equations for ions and electrons written in cylindrical coordinates (r, θ, z) , it can be derived [53] that the axial variation of the momentum flux τ throughout a magnetic nozzle reads

$$\frac{\partial \tau}{\partial z} = -en_p (u_\theta - v_\theta) B_r, \quad (1.9)$$

where n_p , u_θ , v_θ and B_r are the plasma density, ion and electron azimuthal velocity, and radial component of the magnetic field. This formulation assumes quasi-neutrality, negligible electron inertia, isotropic electron pressure and cold ions. Equation 1.9 shows that electromagnetic thrust is produced in the MN thanks to the Lorentz force that results from the net azimuthal current $j_\theta = en_p (u_\theta - v_\theta)$ and the radial component of the magnetic field B_r . The thrust term T_B shown in Figure 1.1 results from volume integration of Equation 1.9. From the momentum conservation equations in the radial direction, one can assess the ion and electron azimuthal velocities,

$$en_p u_\theta = -en_p \frac{E_r}{B_z}, \quad (1.10)$$

1.2. RESEARCH OBJECTIVE AND OUTLINE

$$en_p v_\theta = -en_p \frac{E_r}{B_z} - \frac{1}{B_z} \frac{\partial p_e}{\partial r}, \quad (1.11)$$

where $p_e = n_p k_B T_e$ is the electron pressure. Equations 1.10 and 1.11 illustrate that an azimuthal ion current, i.e. the swirl current, originates because of the $\mathbf{E} \times \mathbf{B}$ force only, whereas the electron counterpart, i.e. the Hall current, comprises also a diamagnetic component given by the pressure gradient along r . Experimental identification of the net j_θ and its correlation with the measured magnetic thrust have demonstrated this working principle in converting electron thermal energy into ion kinetic energy [54]. Numerical analyses have also highlighted this phenomenon [47, 55].

1.2 Research objective and outline

The former Sections provide sufficient details to picture that electrodeless propulsion systems involve relatively complex physical phenomena. Over the past few years, a significant progress has been made by investing a great deal of effort in experimental and numerical analyses. Nonetheless, the maturity of this technology is still relatively low and various aspects merit investigation. This thesis aims at further researching on the underlying physics. The main objective is to gather experimental findings that can serve as a starting point for improving the competitiveness of electrodeless thrusters. The availability of experimental data is also of particular interest for development and validation of predictive numerical models. The structure of this document is as follows.

Chapter 2 provides a comprehensive description of the most relevant components constituting the experimental apparatus. These include the helicon plasma source and all the diagnostics that have been used throughout this work.

Chapter 3 reports on the results obtained during several experimental campaigns. These primarily explore the effect on different plasma properties when varying a given external parameter, e.g. propellant, rf power, magnetic field intensity and topology. The last section of this chapter is dedicated to plasma oscillations observed in the magnetic nozzle.

Chapter 4 describes methods and findings of an experimental campaign aiming at characterizing the ions and atoms acceleration profiles in the magnetic nozzle of a HPT. These measurements have been performed in collaboration with the EP research team of Universidad Carlos III de Madrid.

Chapter 5 follows the same methodology applied in the previous one for analyzing the ion dynamics in the magnetic nozzle of a ECRT. These experiment likewise results from a collaboration Universidad Carlos III de Madrid.

Chapter 6 details a preliminary analysis on the use of iodine as propellant for electrodeless thrusters. The chapter addresses the development of a feeding system along with important caveats to be noted when dealing with such a propellant.

Chapter 7 summarizes the main conclusions of this work and suggests future lines of research.

PART I

RESEARCH ON A HELICON SOURCE
AND DIAGNOSTICS DEVELOPMENT

Chapter 2

Experimental Setup

The present chapter aims at providing a comprehensive description of the principal components of the experimental setup, which comprises of the plasma source and the suite of diagnostics. It is a reference portion of the entire manuscript since the experimental campaigns described thereafter substantially rely on these diagnostic tools.

2.1 Helicon plasma source

The helicon plasma (HP) source used at ICARE is depicted in Figure 2.1a and Figure 2.1b, while Figure 2.2 shows a detailed schematics. It comprises a vertically oriented quartz tube with $\phi = 9$ cm inner diameter and $L = 58$ cm length, whose open exit defines the origin of the system axial coordinate z . The top aperture is equipped with

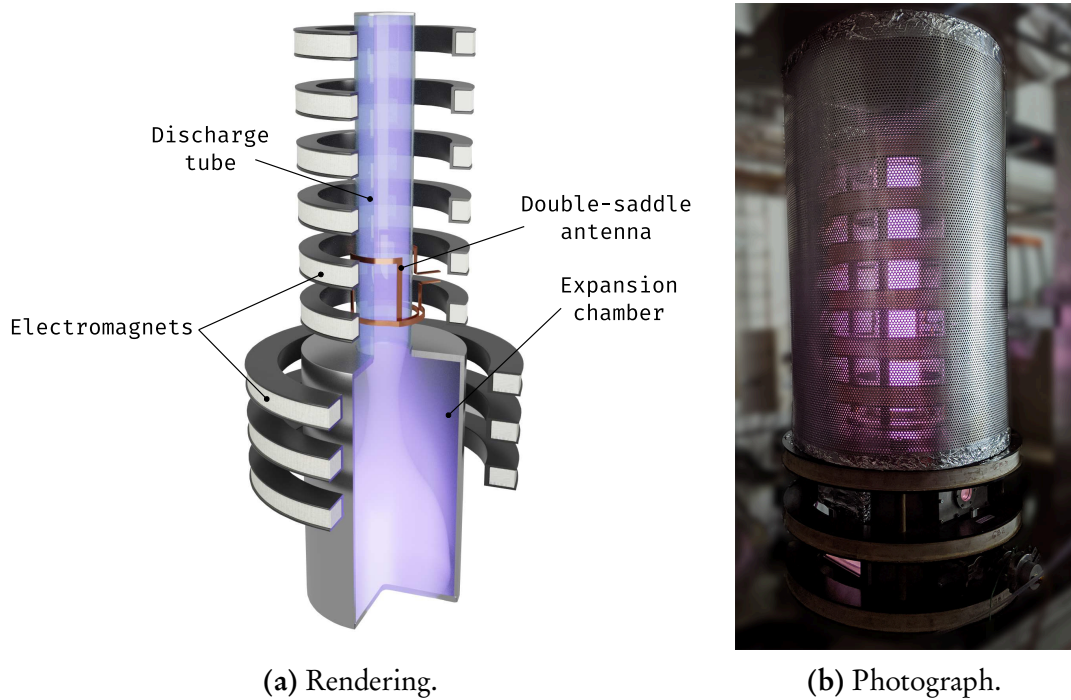


Figure 2.1: Helicon plasma reactor.

2.1. HELICON PLASMA SOURCE

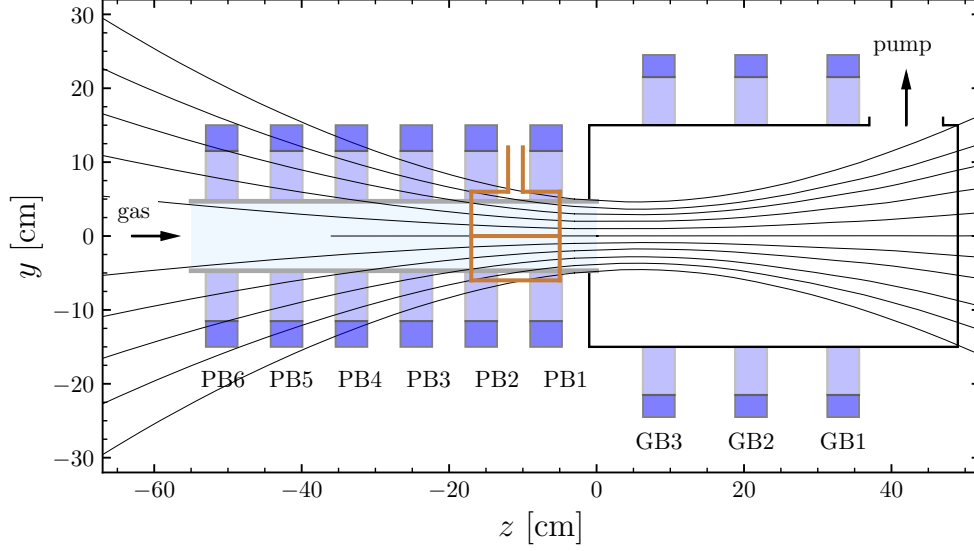


Figure 2.2: Helicon plasma reactor schematics. The $z = 0$ position refers to the tube outlet, $y = 0$ refers to the reactor axis.



Figure 2.3: Double-saddle antenna.

an off-axis gas injector, while the bottom part is connected to a 30 cm inner diameter and 50 cm length expansion chamber. One lateral side of the chamber is connected to a turbomolecular/primary pumping system providing an ultimate base pressure on the order of 10^{-5} mbar. Typical values of pressure during operation lay in the 10^{-3} mbar range.

RF power is generated by a 1 kW class power supply at 13.56 MHz and fed into a copper-made double-saddle antenna, see Figure 2.3, through a 2 kW custom π -type matching network. The antenna is 12 cm high and its centre is located at $z \simeq -11$ cm. It is designed such that it is directly connected to the matching network to reduce power transfer losses.

The HP source features nine electromagnets, also depicted in the previous figures. The electromagnets surrounding the expansion chamber are named GB and numbered from 1 to 3, moving upstream. The same progression is applied to those surrounding the quartz tube, named PB from 1 to 6. Each electromagnet is made up of a 2 mm diameter copper wire, constituting 510 loops for PB1 – 6 and 430 loops for GB1 – 3. As a result, the magnetic field produced by each coil has a peak value of $\sim 2 \text{ mT A}^{-1}$ and $\sim 1 \text{ mT A}^{-1}$ for PB and GB electromagnets, respectively. The presence of multiple electromagnets enables the investigation of profoundly different magnetic field topologies.



Figure 2.4: B-dot probe (without protective cover).

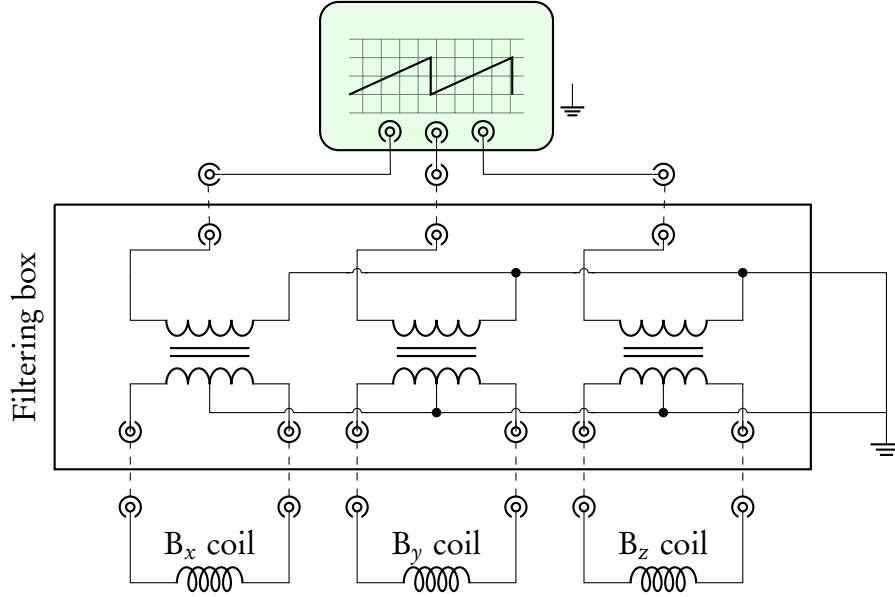


Figure 2.5: B-dot probe circuit schematics.

In this regard, most of the experimental campaigns performed in the framework of this work focus on a specific geometry of the magnetic field. For this reason, specifications on the magnetic field used for any particular experiment are provided hereafter within the respective sections.

2.2 Diagnostics

2.2.1 B-dot probe

The 3D B-dot probe developed for this work is inspired by the design reported in [43]. It consists of a main body, three orthogonal magnetic pick-up coils, a protective cover, and a non-inductive pick-up rejection filtering unit. Figure 2.4 depicts the probe without the protective cover.

The main body is a 4 mm outer diameter alumina tube, which has been manually shaped to allow winding of the coils. Each coil consists of three loops of 0.22 mm insulated copper wire. The coils assembly is shielded from direct exposure to plasma by using a PEEK cover with 8 mm outer diameter. Wire leads are first arranged in the twister pair configuration nearby the coils assembly, and finally, they are converted

2.2. DIAGNOSTICS

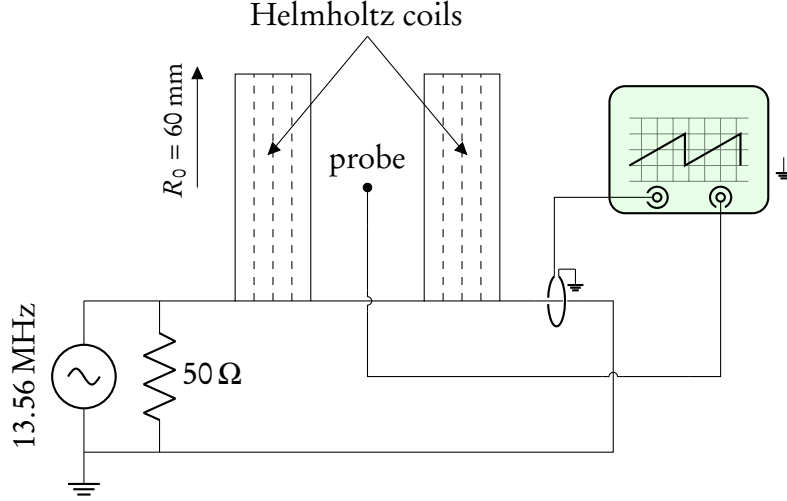


Figure 2.6: B-dot probe calibration setup schematics.

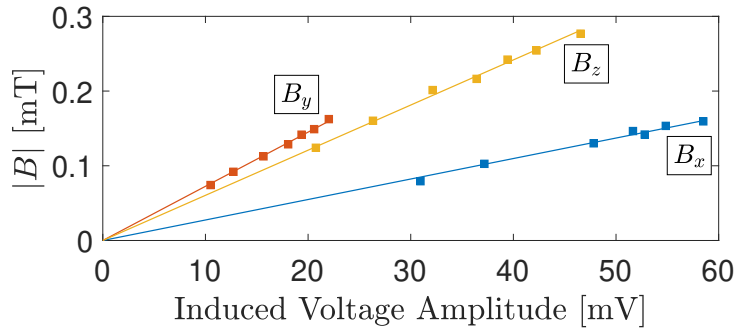


Figure 2.7: B-dot probe calibration results.

into six coaxial cables. These are eventually connected to a 2.5 GS/s digital oscilloscope through the non-inductive pick-up rejection filtering unit [56, 57]. It consists of one sub-unit per coil, each of which features a Coilcraft SWB2010-PCL 1:1 centre-tapped transformer and a Faraday shield. A schematics of the whole circuit is provided in Figure 2.5.

The magnetic sensitivity of the probe is absolutely calibrated using two magnetic coils in the Helmholtz configuration with a radius of 60 mm and 100 loops, as illustrated in Figure 2.6. Power at 13.56 MHz between 5 W and 20 W is fed into the coils connected in parallel to a 50 Ω resistor to the ground. Current flowing in the coils $I(t)$ is measured using a Pearson current monitor 2878,

$$I(t) = I_0 \sin(\omega t). \quad (2.1)$$

Then it is post-processed using a SavitzkyGolay filter and used to compute the rf magnetic field amplitude which reads

$$B_H(t) = \left(\frac{4}{5}\right)^{3/2} \frac{\mu_0 n I(t)}{R_0} = B_0 \sin(\omega t). \quad (2.2)$$

By knowing that the induced voltage $V_{ind}(t)$ is related to $B_H(t)$ by way of the Faraday-Lenz law

$$V_{ind}(t) = -\frac{d\Phi_B(t)}{dt} = -nA \frac{dB(t)}{dt} = -nA\omega B_0 \cos(\omega t), \quad (2.3)$$



Figure 2.8: Capacitive probe.

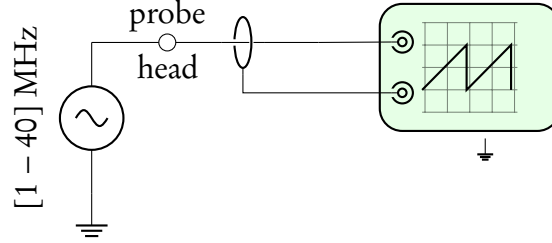


Figure 2.9: Capacitive probe calibration schematics.

B_0 is finally related to the measured induced voltage in the probe coil by a linear fit. The resulting calibration curves are reported in Figure 2.7.

2.2.2 Capacitive probe

The capacitive probe developed for this work is based on the design reported in [58] and is depicted in Figure 2.8. It comprises an exposed electrode made of stainless steel and an inner electrode connected to a coaxial cable. An exposed insulator layer made of PEEK is interposed between the two electrodes. The coaxial cable is carried into the plasma inside a 4 mm alumina tube, which also provides structural support to the electrode assembly. The probe has a cylindrical geometry with an outermost diameter of 10 mm.

For calibration, an aluminium foil envelopes the primary electrode and the PEEK layer. A 10 V amplitude sine wave is generated at 1 MHz to 40 MHz and applied to the aluminium foil. The probe is connected to a 2.5 GS/s digital oscilloscope to acquire the measured voltage and retrieve the calibration factor. A schematics of the calibration setup is provided in Figure 2.9. The calibration factor κ is reported in Figure 2.10(a)

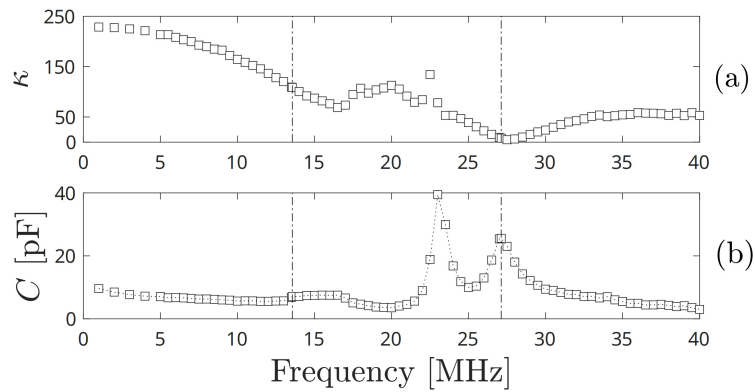


Figure 2.10: Capacitive probe (a) calibration coefficient and (b) capacitance versus frequency.

2.2. DIAGNOSTICS

as a function of the input frequency. Probe capacitance C is inferred by measuring the current flowing in the probe cable using a Pearson current monitor 2878. Results are reported in Figure 2.10(b). In both plots, dash-dotted lines indicate 13.56 MHz and its second harmonic. Values for κ and C at the third harmonic are approximated to those at 40 MHz due to setup limitations. Note that the probe exhibits a non-ideal behaviour in the $\sim 17 - 35$ MHz range.

2.2.3 RF-compensated Langmuir probe

The rf-compensated Langmuir probe (RFCLP) developed for this work is depicted in Figure 2.11. Its design is based on the results and guidelines reported in [59–61]. A tungsten wire of 0.38 mm in diameter and 5 mm in length constitutes the probe tip. An additional electrode made of stainless steel contributes to rf compensation and provides mechanical support to the assembly. The electrode is electrically insulated from the probe tip using a 1 mm in outer diameter alumina tube. A 1 nF axial capacitor is soldered to the compensation electrode and connected in parallel with the probe tip and a series of three axial chokes, each of which self-resonates at one of the first three harmonics. The employed chokes are Bourns 78F270J-RC for the fundamental harmonic, API Delevan 1025-60K for the second one, and Bourns 9230-52-RC for the third one. The whole assembly is encapsulated inside a borosilicate glass tube of 6 mm outer diameter, which also accommodates the coaxial cable for probe biasing and current measuring.

Characterization of the chokes is a crucial aspect of probe development as they are typically manufactured to satisfy a requirement on the inductance value but not on the self-resonating frequency. Therefore, an Agilent 4264A precision analyzer has been used to characterize the choke for the fundamental harmonic. It also allowed validation of a more easily accessible method hereafter described which has been used to characterize the other two chokes. A 10 V amplitude sine wave is fed to one lead of the testing choke. The other lead is connected to a resistor (46.52 k Ω is used in this setup) and the series circuit closes to the ground. The circuit schematics is reported in Figure 2.12. Input frequency is changed while the voltage drop across the resistor is measured and used to calculate the current flowing in the circuit. The frequency at which the current is mini-

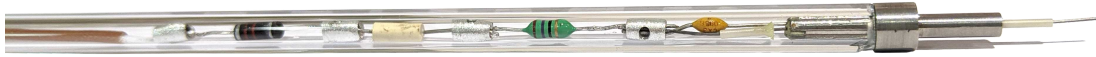


Figure 2.11: RF-compensated Langmuir probe.

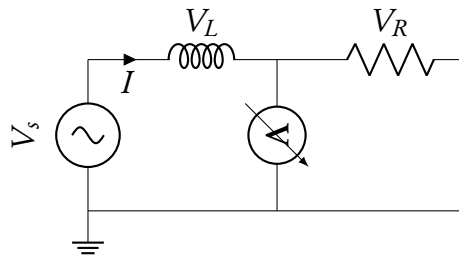


Figure 2.12: Choke characterization circuit.

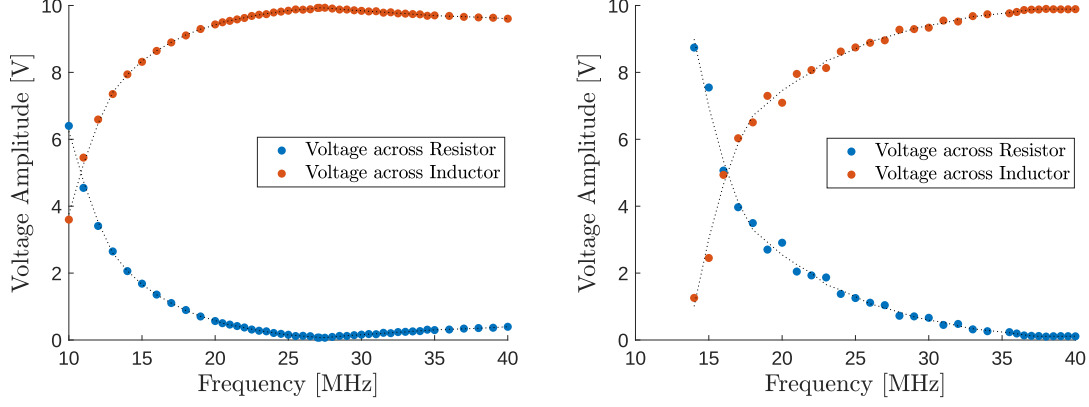


Figure 2.13: Voltage drops during choke characterization. Profiles refer to (left) the second harmonic choke and (right) the third harmonic choke.

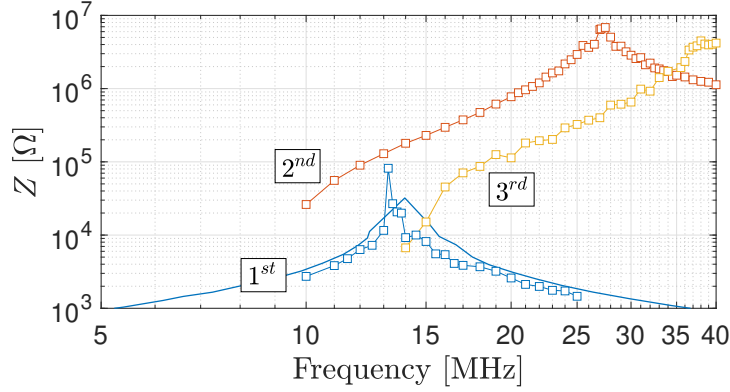


Figure 2.14: Impedance of 1st, 2nd and 3rd harmonic chokes.

mum is the self- resonating frequency of the choke. The voltage drop across the choke is maximum at resonance, as clearly shown in Figure 2.13. Impedance is then computed using Ohm's law. Chokes characterization results are reported in Figure 2.14. The blue solid line represents the impedance profile obtained using the Agilent 4264A precision analyzer and blue squares are obtained with the aforementioned method, showing good agreement. The theory illustrated in [59] allows stating that this configuration of chokes series and compensating electrode enables proper rf compensation for plasma potential fluctuations up to 99.5 V in krypton and 85.1 V in xenon. The whole probe is characterized by applying a 10 V amplitude sine wave to the tip at different frequencies. The probe output is illustrated in Figure 2.15 in dB, showing local minima for the desired harmonics (dash-dotted vertical lines indicate first and second harmonics).

Implementation, theory and measurements uncertainty

During experimental phases, the probe is typically displaced within the plasma region using a manual single-axis translation stage and I-V curves are recorded using an ALP control unit by Impedans Ltd. Thereafter, data is post-processed relying on OML theory [61,62]. Assuming local quasineutrality, plasma density n_p is inferred from the linear fit

2.2. DIAGNOSTICS

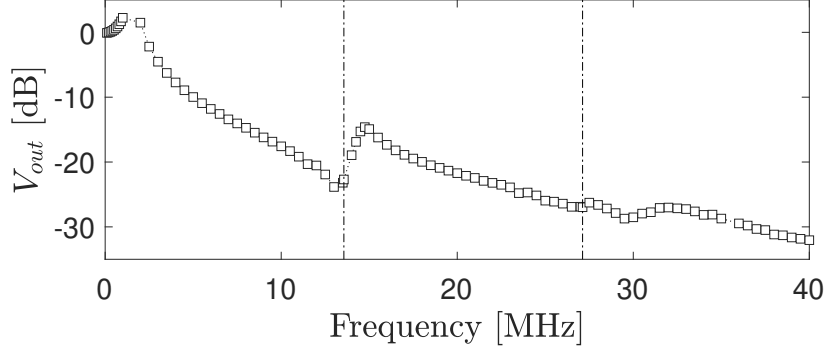


Figure 2.15: RF-compensated LP characterization.

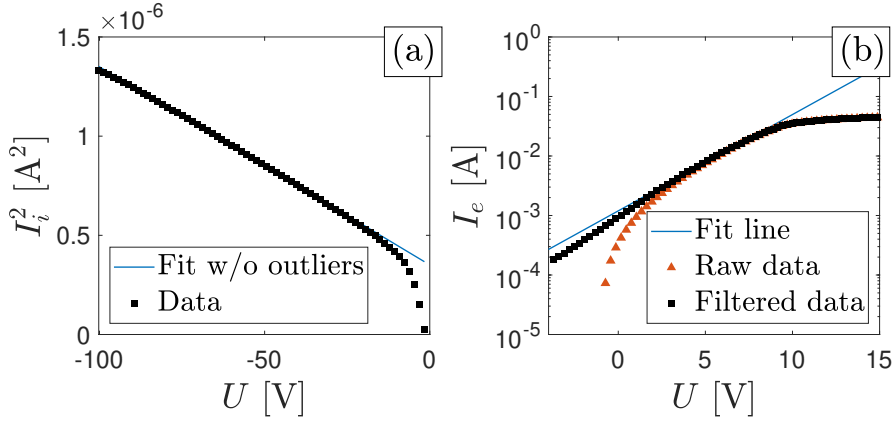


Figure 2.16: Typical (a) squared ion current and (b) electron current vs. probe potential. Curves obtained for $P_{IN} = 750$ W, $\dot{m} = 1$ mg s⁻¹ Kr, 10 mT peak value of the external B field.

of the ion current I_i squared versus the probe potential U , using the following equation

$$I_i = A_p n_p e \frac{\sqrt{2}}{\pi} \left[\frac{e(V_{s1} - U)}{m_i} \right]^{1/2}. \quad (2.4)$$

The ion current fit is then subtracted from the total current to obtain a better estimation of the electron current I_e . Pretending the electrons are described by a Maxwell-Boltzmann distribution function, the logarithmic profile of the electron current is linearly fitted, enabling the estimation of the electron temperature T_e . The plasma potential V_p is either computed as the probe bias voltage where the first derivative of the I-V curve features its peak value or as the value that satisfies the electron current equation, i.e.

$$I_e = A_p n_p e \left(\frac{k_B T_e}{2\pi m_e} \right)^{1/2} \exp \left[\frac{e(U - V_p)}{k_B T_e} \right]. \quad (2.5)$$

An example of experimental data and fitted curves is provided in Figure 2.16.

A statistical analysis is performed to evaluate the uncertainty associated with the assessment of plasma properties: *i)* the RFCLP is placed on-axis at $z = -5$ cm and $z = 10$ cm; *ii)* at each location twenty I-V characteristics are recorded in different moments of the day, randomly switching between the magnetic configurations detailed

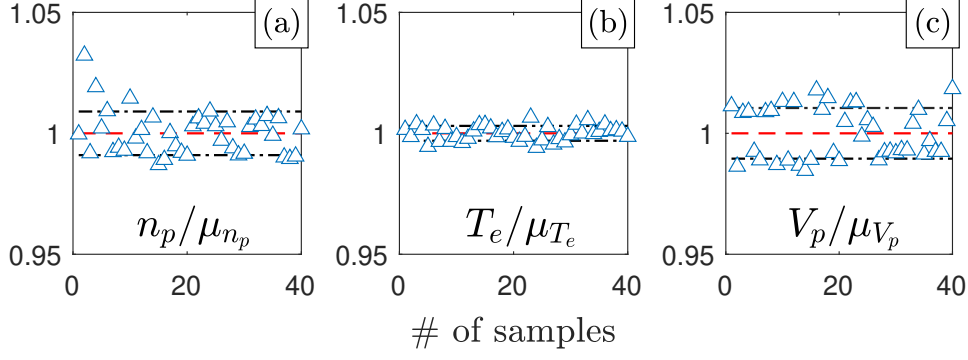


Figure 2.17: Uncertainty analysis of inferred plasma properties. Typical normalized *a*) plasma density, *b*) electron temperature and *c*) plasma potential with respect to μ . Red dashed lines represent unitary μ , black dash-dotted lines represent normalized $\pm\sigma$. Input parameters: $P_{IN} = 750$ W, $\dot{m} = 1$ mg s⁻¹ Kr, 4 mT peak value of the external B field.

Table 2.1: Uncertainty analysis of rf-compensated LP measurements: percentage error of plasma properties for four different magnetic field strengths.

	$\sigma_{n_p}/\mu_{n_p} \times 100$		$\sigma_{T_e}/\mu_{T_e} \times 100$		$\sigma_{V_p}/\mu_{V_p} \times 100$	
	Kr	Xe	Kr	Xe	Kr	Xe
4 mT	0.90 %	0.64 %	0.31 %	0.37 %	1.05 %	0.56 %
5 mT	1.07 %	0.85 %	0.59 %	0.34 %	1.99 %	1.17 %
7 mT	0.76 %	0.78 %	0.69 %	0.51 %	2.17 %	0.72 %
10 mT	1.22 %	0.49 %	0.84 %	0.43 %	1.41 %	0.75 %

later in Section 3.1; *iii*) values of n_p , T_e and V_p are computed as previously discussed, together with the associated mean value μ and standard deviation σ ; *iv*) the error is evaluated as the ratio σ/μ . An example of data dispersion is provided in Figure 2.17 and completed outcomes are reported in Table 2.1. It results that all plasma properties are inferred with a statistical deviation always below about 2 % for all operating conditions.

2.2.4 Planar probe with a guard ring

A planar probe with a guard ring (PPGR) shown in Figure 2.18 is used to measure the ion current density j_i . This probe has been designed by the author of [63]. It mainly comprises a disk-shaped collector and an outer ring, both made in stainless steel. The role of the guard ring is to concentrate sheath edge effects far from the collector, thus ensuring that the ion collection area exactly corresponds to the collector geometrical area [64]. For correct functioning of the probe, it is required that *i*) the width of the guard ring is much larger than the local plasma sheath thickness and *ii*) the gap between the two electrodes is smaller than the local sheath thickness (see Figure 2.20) to introduce negligible potential irregularities. Additional design requirements include: the collector thickness must be as small as possible to minimize ion collection on the

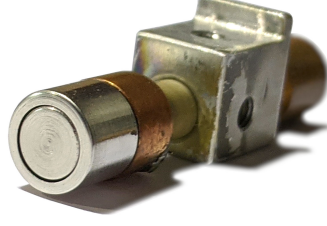


Figure 2.18: Planar probe with a guard ring.

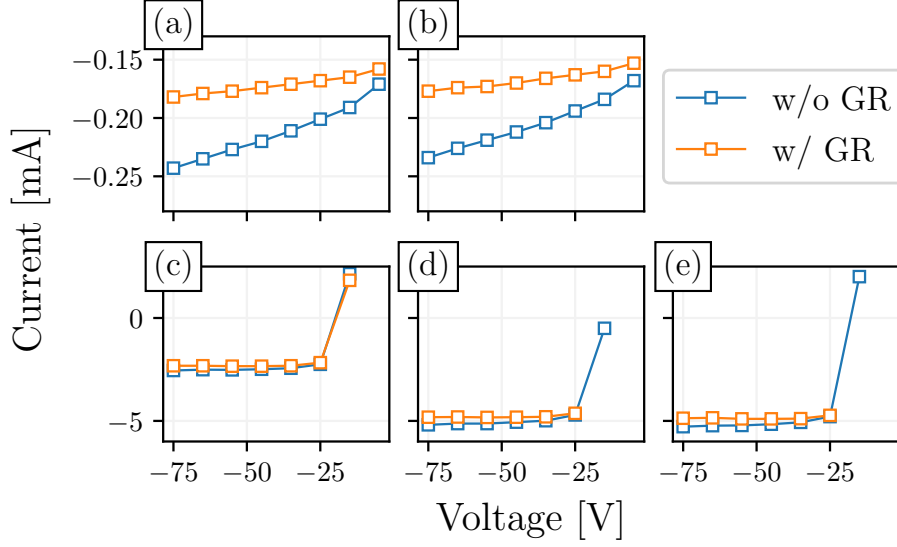


Figure 2.19: Ion current profiles at $(x, y = 0; z = 15)$ cm. Subplots denomination is linked to magnetic configurations Conf.s A-E (see Section 3.2).

sides; the collector surface roughness must be minimized in order to not overestimate the collected current density. The collector is 5.6 mm in diameter and 1 mm in thickness, whereas the ring width is 1 mm. A gap of 100 μm is maintained between the two electrodes to ensure electrical insulation. Each electrode features a separated electrical connection for polarization and current measurement. Voltage is applied to the collector by way of a Keithley 2410 SourceMeter, which is also used to measure the flowing current. The guard ring is biased using a TTIEX752M power supply.

Functional check of the probe is carried out by recording the I-V curves at $(x, y = 0; z = 15)$ cm for the five magnetic configurations denominated Conf.s A-E, cf. Section 3.2. The curves obtained with a biased and floating guard ring are compared in Figure 2.19.

Saturation of the ion current is achieved for Conf.s C-D-E at voltages lower than about -40 V, while no complete saturation is recorded for Conf.s A and B due to the fact that the guard ring width is not compatible with the local values of the sheath thickness. This can be confirmed by computing the local values of the characteristic lengths over the radial coordinate using the values of n_p and T_e . Floating and high voltage sheath thickness, s_f and s_{hv} respectively, are computed in accordance with [65] as

$$s_f = \frac{5}{\exp(-1/2)} \lambda_D \quad (2.6)$$

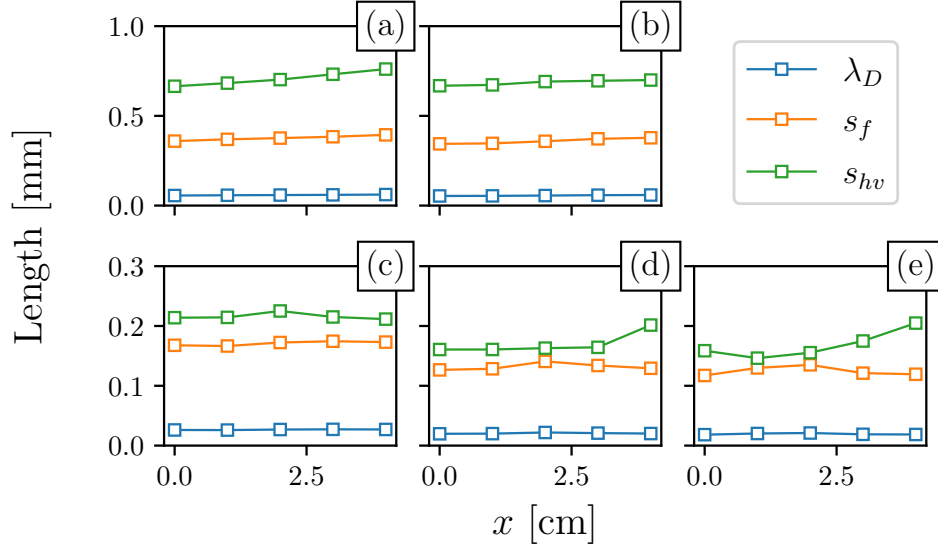


Figure 2.20: Debye length, floating and high-voltage sheath thickness at $z = 15$ cm. Subplots denomination is linked to magnetic configurations Conf.s A-E (see Section 3.2).

$$s_{hv} = \frac{1}{3} \sqrt{\frac{2}{\exp(-1/2)}} \lambda_D \left(\frac{2V}{T_e} \right)^{3/4} \quad (2.7)$$

using -75 V for Conf.s A-B and -50 V for Conf.s C-D-E. Outcomes are plotted in Figure 2.20. It results evident that values of s_{hv} for Conf.s C-D-E are much smaller than the guard ring width, whereas those for Conf.s A and B approach its size. It shall be noted that the attainment of a perfectly flat profile of the ion saturation current would require a guard ring width 5 – 10 times larger than the actual one. Thus, the overall probe size would probably lead to serious plasma perturbations. Furthermore, the scope of the measurements performed with this probe and reported in Section 3.2 is not to, e.g., focus on indirect propulsive performance estimation but rather to perform a more qualitative-like comparison of the magnetic configurations.

2.2.5 Retarding potential analyzer (model 1)

The first model of Retarding potential analyzer (RPA) used in this work is shown in Figure 2.21. It was designed and manufacture for previous experiments at ICARE and it has been adapted to operate under the plasma conditions of interest here. It consists of four mesh grids with 0.4 mm mesh size: the entrance grid (G1), the electron repeller grid (G2), the ion filtering grid (G3) and the secondary electron repeller grid (G4). A collector (C) is placed downstream the grids assembly to enable ion current measurement. The whole assembly is encapsulated in an aluminum body with 4.5 cm outer diameter and 1 cm entrance orifice. The gap between all the elements is kept constant at 1 mm. In principle, this is not compatible with the expected value of Debye length in the bulk of the plasma (in the order of 10^{-2} mm), implying a requirement on the grid spacing to be smaller than about 0.15 mm to avoid space charge limited flow [66]. Such a grid spacing is technologically difficult to achieve. Hence, to reduce the plasma flux entering the probe, i.e. the plasma density inside the probe itself, an additional grid (G0)

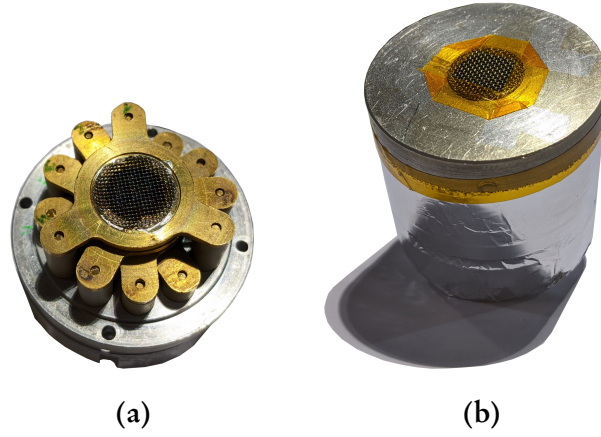


Figure 2.21: Retarding potential analyzer model 1.

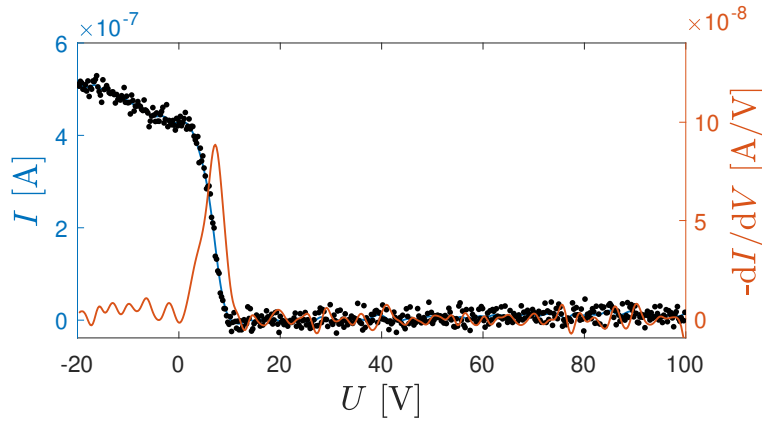


Figure 2.22: Typical RPA (blue-axis) ion current and (red-axis) its first derivative. $P_{IN} = 750 \text{ W}$, $\dot{m} = 0.2 \text{ mg s}^{-1}$ Xe, 7 mT peak value of the external B field.

is placed in contact with the outer body, as visible in Figure 2.21. This allowed to significantly increase the quality of the measured I-V signal. Typically, the grid polarization scheme with respect to ground is: G0 at 0 V; G1 at 0 V; G2 at -60 V; G3 swept from -20 V to 100 V with 0.2 V step size; G4 at -30 V; C at -3 V. A typical I-V characteristic is shown in Figure 2.22 together with its first derivative.

2.2.6 Retarding potential analyzer (model 2)

An improved model of the RPA has been designed and manufactured to better comply with the requirements set by the plasma under analysis. In the actual configuration, the RPA comprises a series of four stainless-steel grids with holes size of 0.15 mm and a thickness of 0.1 mm. The transparency of each grid is about 25 %. This relatively small mesh size has been achieved through chemical etching and it enables measuring the ion energy in regions where the local plasma density exceeds 10^{17} m^{-3} . The grids are labeled using the conventional notation: entrance grid (G1), electron repeller grid (G2), ion filtering grid (G3), and secondary electron repeller grid (G4). A collector (C) made of molybdenum is placed downstream the grids assembly to enable the ion current measurement. An alumina layer of 0.2 mm thickness is placed between two subsequent grids, functioning both as a spacer and as electrical insulator. The same



Figure 2.23: Retarding potential analyzer model 2.

strategy is employed to insulate G1 and C from the probe housing. By changing the thickness of the multiple alumina layers (while being compliant with the constraints set by the local Debye length), it is possible to add a secondary ion filtering grid with the aim of improving the energy resolution of the probe. The instrument port size is set by an extra metallic layer whose aperture is 5.4 mm in the present configuration. The whole assembly is encapsulated into a non-magnetic stainless-steel body resulting in a probe size of 26 mm in diameter and 11 mm in height. The assembled probe is shown in Figure 2.23. The rear side features the electrical connections required to bias the probe elements along with a K-type thermocouple to monitor the probe temperature during operation. The polarization scheme that is typically used (in particular for the experiment discussed in Section 4.5) is as follows: G1 at plasma floating potential; G2 at -20 V; G3 swept from -10 V to 65 V with 0.5 V step size; G4 at -70 V; C at -1 V. I-V characteristics are recorded using an automated control unit by Impedans, Ltd. and numerically derivated to retrieve the ion EDF.

2.2.7 Laser-induced fluorescence spectroscopy

Ions and atoms velocity distribution functions (VDFs) are measured by means of laser-induced fluorescence (LIF) spectroscopy. The technique and the optical bench in use shown Figure 2.24 have been extensively described in references [67,68]. With reference to Figure 2.24, the numbered components are:

1. Amplified laser diode;
2. High resolution wavelength meter;
3. Stabilized HeNe laser;
4. Fabry-Pérot interferometer;
5. Monochromator;
6. Photomultiplier tube (PMT);
7. Mechanical chopper;
8. Photodiode;
9. Optical fiber launcher;

2.2. DIAGNOSTICS

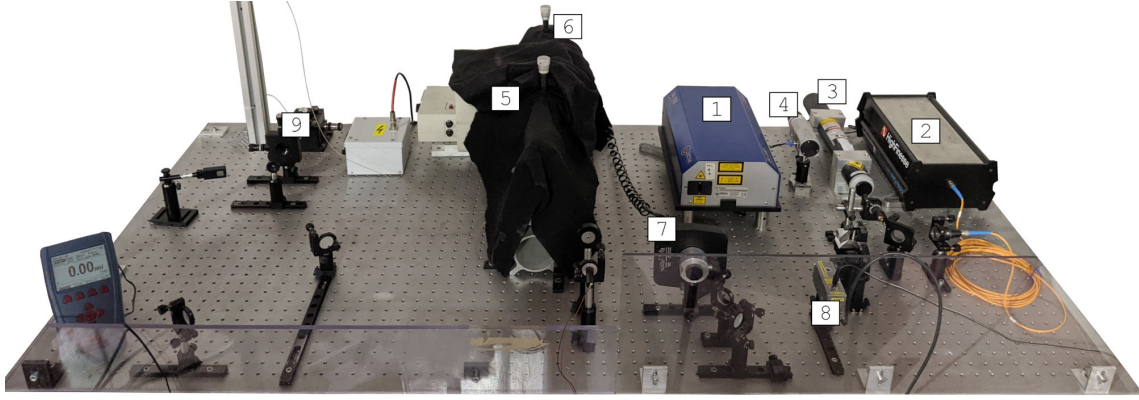
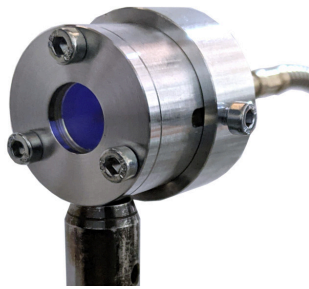
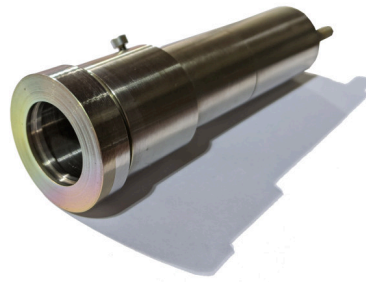


Figure 2.24: LIF optical bench.



(a) Laser collimator.



(b) Detection optics.

Figure 2.25: Optics used for LIF spectroscopy measurements.

Excitation of the probed species is achieved via injection of a laser beam produced by an amplified tunable single-mode laser diode by TOPTICA Photonics AG in the near-infrared spectral range. The laser diode can deliver up to 600 mW in the 810 – 840 nm wavelength range. In the experiments reported in Section 3.2 and Part II, the laser remains mod-hop free over a frequency tuning range larger than 5 GHz. The primary laser beam is split into multiple beams to: *i*) monitor continuously the laser mode and detect any mode hop by means of a Fabry-Pérot interferometer; *ii*) accurately measure the laser wavelength by way of a calibrated wavemeter whose absolute accuracy is 80 MHz ($\approx 60 \text{ m s}^{-1}$). Modulation of the laser beam is achieved using a mechanical chopper at about 1.9 kHz. The VDFs are inferred by scanning over the laser frequency (wavelength) ν (λ) and computing the particles velocity component v_k aligned with the laser wavenumber vector \mathbf{k} from the Doppler effect equation which reads

$$\Delta\nu = \nu - \nu_0 = \frac{1}{2\pi} \mathbf{k} \cdot \mathbf{v}, \quad (2.8)$$

where ν_0 is the unshifted transition frequency.

Further details about the experimental arrangement of optics are provided within each section dedicated to a particular experiment. For most of the experiments discussed in the following, the laser is coupled to a 50 μm multi-mode optical fiber which transports the beam from the optical bench to the inside of the vacuum facility. Here a custom collimator shown in Figure 2.25a is employed to shine the laser beam towards the plasma source in the direction of the thruster axis z . At the output of the collimator, the laser beam diameter is about 4 mm, whereas the power density is maintained

Table 2.2: Xe I, Xe II, Kr I and Kr II probed optical transitions.

	Excitation transition	λ_{exc} (air)	λ_{fluor} (air)
Xe I	$5p^5(^2P_{1/2}^\circ)6s^2[1/2]_1^\circ \rightarrow$ $\rightarrow 5p^5(^2P_{1/2}^\circ)6p^2[3/2]_2$	834.682 nm	473.41 nm
Xe II	$5p^4(^3P_2)5d^2[4]_{7/2} \rightarrow$ $\rightarrow 5p^4(^3P_2)6p^2[3]_{5/2}^\circ$	834.724 nm	541.91 nm
Kr I	$4s^24p^5(^2P_{3/2}^\circ)5s^2[3/2]_1^\circ \rightarrow$ $\rightarrow 4s^24p^5(^2P_{3/2}^\circ)5p^2[3/2]_2$	819.006 nm	760.154 nm
Kr II	$4s^24p^4(^3P)4d^4F_{7/2} \rightarrow$ $\rightarrow 4s^24p^4(^3P)5p^2D_{5/2}^\circ$	820.273 nm	461.92 nm

to $\sim 2 \text{ mW mm}^{-2}$, which ensures a weak saturation effect. Note that, in the described configuration, $\mathbf{k} \cdot \mathbf{v} < 0$. The collimator is kept at a safe distance from the thruster exit plane in order to minimize plume perturbations and avoid overheating and damage of optics. The fluorescence light is collected using a bi-convex lens with 60 mm focal length focusing on a 200 μm core diameter optical fiber, see Figure 2.25b. The latter transports the fluorescence light to a monochromator which isolates the selected line from the whole spectrum. Afterwards, a photomultiplier tube converts the light signal into voltage, which is fed into a lock-in amplifier operating at the laser modulation frequency to distinguish the signal from the natural plasma emission.

The optical transitions that have been probed throughout this work are reported in Table 2.2, together with the excitation and fluorescence wavelengths [67–71].

Chapter 3

Experimental Campaigns and Results

This chapter presents and discusses several experimental campaigns performed on the HP source detailed in the previous chapter. Each of the following sections is dedicated to a specific experimental campaign.

3.1 Direct comparison of krypton and xenon discharge properties in the magnetic nozzle

This section analyzes measurements of a variety of plasma properties performed for comparing krypton and xenon propellants in the MN region that extends upstream the exit plane. All the spatially-resolved measurements presented hereafter are obtained by feeding 750 W of rf power to the antenna. Reflected power is below 2.5 % for all operating conditions. Krypton and xenon are injected at 1 mg s^{-1} and 0.2 mg s^{-1} , respectively. Assuming the two gases have the same molar volume, the neutral density is about 8 times larger for krypton. These mass flow rate values are implicitly assumed in the following when not specified. The probes presented in Chapter 2 are manually actuated using a single-axis translation stage with a resolution of $10 \mu\text{m}$ and 150 mm stroke. They are individually employed and displaced with a step size of $5 \pm 0.05 \text{ mm}$. Probe alignment is ensured by use of a cross-line laser pendulum.

Figure 3.1 illustrates the measured and simulated intensity of B_z used for this experiment which is obtained by driving 7 A through GB3 and 1 A through PB1-6 and

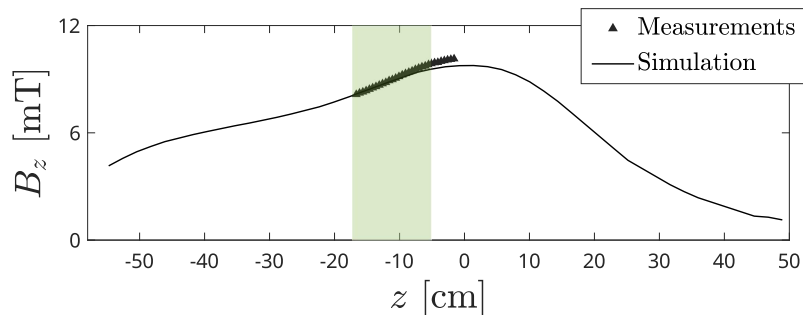


Figure 3.1: Externally applied magnetic field profile. The shaded area indicates the antenna location.

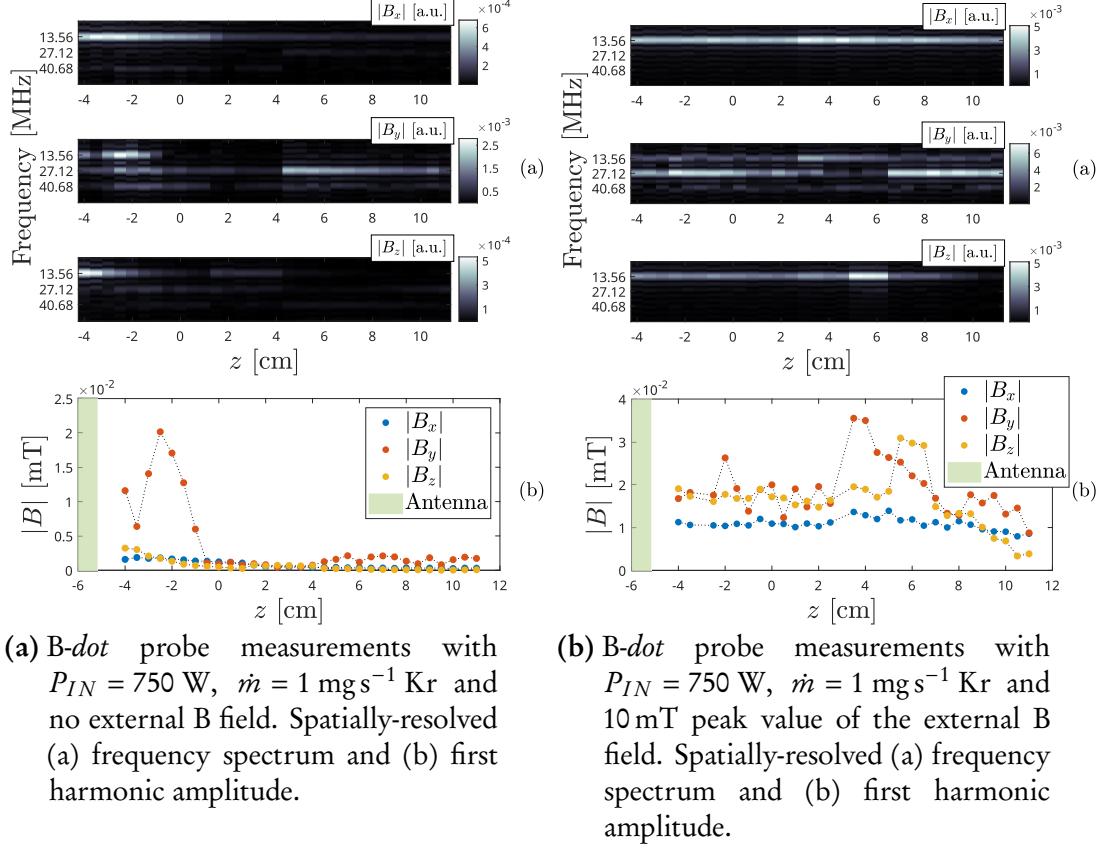


Figure 3.2: B-dot probe results related to the Kr discharge.

GB2. This arrangement allows obtaining a specific magnetic topology with the throat exactly at $z = 0$ and strength of about 10 mT. The same qualitative topology applies for three additional scaled-down magnetic profiles with peak values of about 7 mT, 5 mT and 4 mT, which are investigated to obtain the results shown in the following.

3.1.1 RF propagating magnetic field

The B-dot probe is located off axis at 30 mm and displaced axially. It is mounted in such a way that the vector defining its y -coil, i.e. the coil probing the B_y component of the propagating field, is aligned with the antenna feeding lines. The notation is consistent with the reference frame illustrated in Figure 2.2. It should be noted that there is an ambiguity of 180° in the phase of the recorded signals, yet it is of no relevance for this study.

At each axial location of the probe, the waveform of the induced voltage on the three coils is acquired using a 2.5 GS/s digital oscilloscope. Noise reduction on the signal is attained using a Savitzky-Golay filter. Fast Fourier Transform (FFT) is then performed to infer the spatially-resolved frequency spectrum for B_x , B_y and B_z . Since the probe is absolutely calibrated at 13.56 MHz only, the FFT component at this frequency is extracted to quantitatively evaluate the rf B field amplitude.

Results using krypton as propellant are reported in Figure 3.2a and Figure 3.2b. The measurements of Figure 3.2a are obtained without applying any external DC magnetic field, while those in Figure 3.2b result from the application of the magnetic profile de-

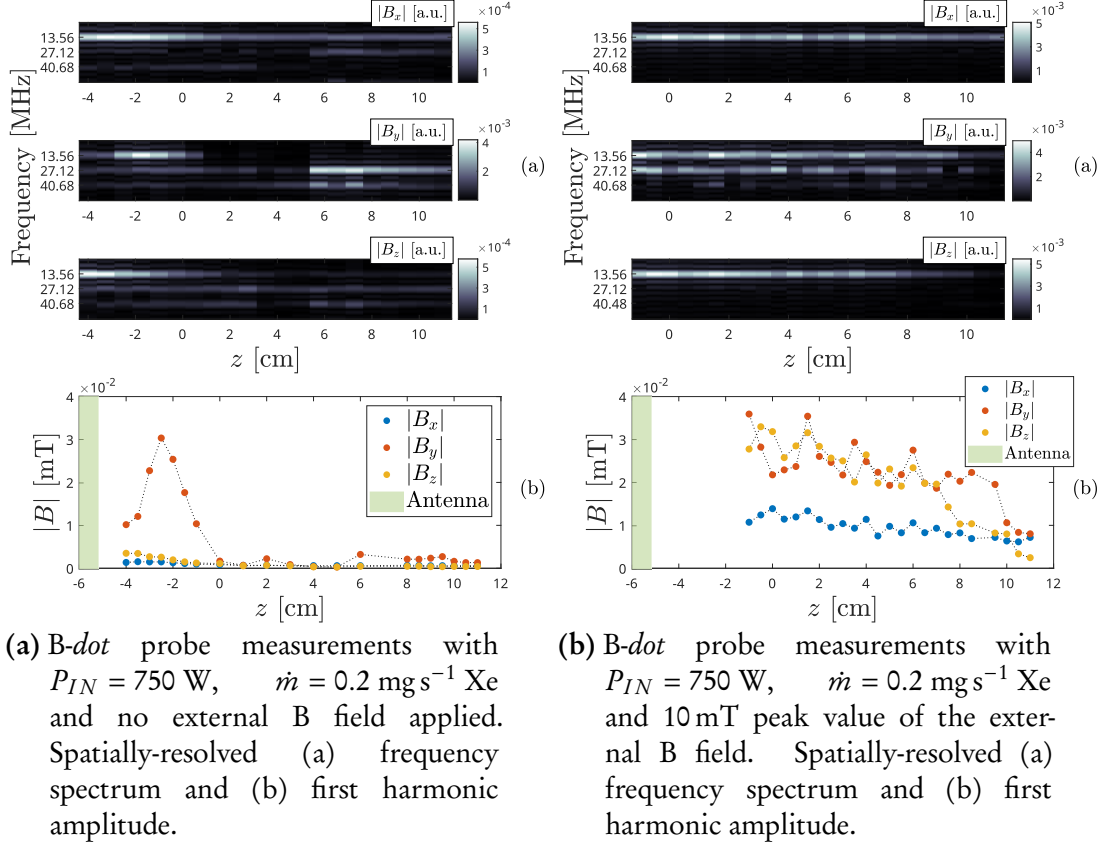


Figure 3.3: B-dot probe results related to the Xe discharge.

picted in Figure 3.1. Similar qualitative results are obtained using xenon as propellant and are reported in Figure 3.3a for the $B = 0$ case and in Figure 3.3b for the externally applied magnetic field case.

It is immediately evident from Figure 3.2a and Figure 3.3a that no electromagnetic wave propagates in the $B = 0$ case, as expected. Indeed, visual inspection of the reactor operating in this condition strongly suggests an inductively-coupled regime, with a very bright plasma just below the antenna and very low light emission elsewhere, either using krypton or xenon. Differently, when the external magnetic field is applied, the plasma column appears quite uniform over a length about ten times larger than the antenna length, suggesting higher power absorption and transport downstream, typical of helicon mode plasmas [24, 27]. In the $B = 0$ configuration, a larger amplitude of B_y is recorded in the upstream region of the axial scan, see Figure 3.2a(b) and Figure 3.3a(b), suggesting it is related to the field radiated by the antenna [72]. By comparing Figure 3.2a(a) and Figure 3.2b(a), as well as Figure 3.3a(a) and Figure 3.3b(a), it is noted that the presence of higher harmonics in B_x and B_z components is reduced when the external magnetic field is applied, while they are anyhow present in the B_y component. Higher order harmonics cannot be attributed to the rf power supply, which is certified to carry harmonics below -40 dBc. As their presence is susceptible to the external magnetic field, it is reasonable to consider they are related to some physical phenomenon. However, it is not possible to accurately quantify the influence of each harmonic due to the lack of calibration factors at frequencies different from the fundamental one. Furthermore, with reference to Figure 3.2b(b) and Figure 3.3b(b), an

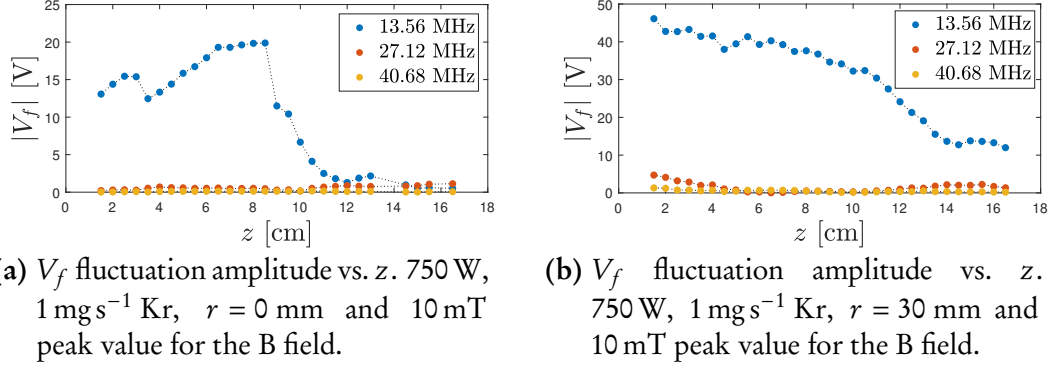


Figure 3.4: Capacitive probe results relative to the krypton discharge.

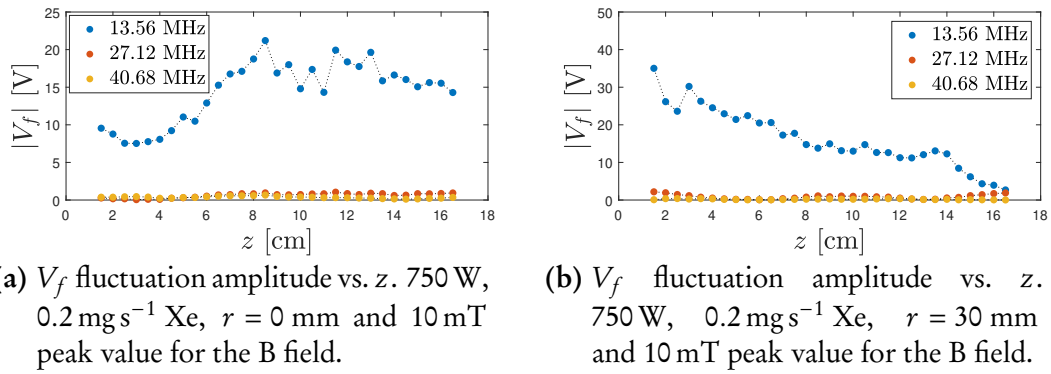


Figure 3.5: Capacitive probe results relative to the xenon discharge.

important amplitude decay can be observed for B_z approximately for $z > 7 \text{ cm}$. This could be explained by observing that the applied magnetic field starts weakening rapidly at $z \cong 7 \text{ cm}$, cf. Figure 3.1. Also, it shall be shown in Section 3.1.3 that the plasma density n_p monotonically increases for $z > 0$. Using the 0-D dispersion relation for helicon waves [17, 24, 73],

$$kk_z = e\mu_0\omega\frac{n_p}{B_0}, \quad (3.1)$$

where k and k_z are respectively the total and axial wavenumbers, n_p is the plasma density, B_0 is the assumed uniform external magnetic field and the rest is conventional, it can be qualitatively stated that as the ratio n_p/B_0 increases, the condition for wave propagation is met only for higher order axial wavenumbers. These are not necessarily efficiently coupled with the antenna, therefore helicon waves could not propagate further downstream. However, lack of data at larger axial locations prevents excluding that the amplitude decay of B_z is rather due to modulation, which has been previously observed and attributed to the presence of multiple axial wavenumbers [24, 74].

3.1.2 Floating potential fluctuations

It is well known that typical plasma potential fluctuations occurring in rf plasmas substantially alter the I-V characteristic of a LP, leading to a poor estimation of plasma properties [59–61]. In order to properly design a passively RFCLP, i.e. chokes selec-

tion and compensating electrode sizing [59], it is important to estimate the amplitude of these fluctuations within the operating condition of interest. To do so, the capacitive probe described in Section 2.2.2 is immersed in the plasma and displaced axially in a similar fashion to the *B-dot* probe. Axial scans have been performed at $r = 0$ and $r = 30$ mm radial locations. At each axial location, the measured voltage is recorded using a 2.5 GS/s digital oscilloscope. FFT allows isolating the first three harmonics out of the signal which are scaled according to the calibration outcomes. Results obtained using krypton are reported in 3.4a and Figure 3.4b, while those using xenon are in Figure 3.5a and Figure 3.5b. It is clearly evident that fluctuations at the second and third harmonic are weakly present in the spectrum. With reference to Figure 3.4b and Figure 3.5b, larger amplitudes of the oscillating floating potential are recorded off-axis, starting from few tens of volts close to the quartz tube exit and then smoothly decaying to zero downstream. Comparing on-axis profiles using krypton and xenon, cf. Figure 3.4a and Figure 3.5a, it is evident that substantially different results are obtained. After a shared increase of $|V_f|$, a very sharp edge is present in Figure 3.4a at $z = 8.5$ cm. The reason behind this remains unclear.

Ultimately, it is observed that V_f fluctuations amplitude can reach an upper value of about 50 V. This value is taken as requirement in designing the RFCLP described in Section 2.2.3.

3.1.3 Effect of different magnetic strengths

Characterization of plasma properties has been carried out as function of the external magnetic field strength by using the RFCLP and the RPA model 1. The tested magnetic field strengths have been previously reported in Figure 3.1.

Measurements involving the RFCLP are performed both axially and radially. On-axis scans of n_p , T_e and V_p are reported in Figure 3.6 and Figure 3.7 using krypton and xenon, respectively. Electron pressure p_e is computed using the measured density and temperature. Notably, substantial differences between the two propellants are drawn. In Figure 3.6(c), it is shown that the plasma potential changes from a rapidly dropping profile to an almost constant profile as the strength of the external magnetic field is increased. Furthermore, with reference to Figure 3.6(a), the plasma density peak moves downstream. Quantitative explanation of this phenomenon is later provided when discussing Figure 3.12 and Figure 3.13. Visual inspection of the plasma source in operation agrees with these results. Indeed, at 4 mT and 5 mT, it is observed that plasma concentrates just below the antenna region, with almost null light emission elsewhere. On the contrary, a visibly homogeneous plasma column appears at 10 mT extending over several antenna lengths. This strongly suggests that a magnetic field between 7 mT and 10 mT is somewhat a threshold external parameter characterizing the transition from inductively-coupled regime to a wave-mode regime. Differently, when the plasma source operates with xenon, no mode transitions have been recorded. Qualitatively speaking, this is clearly shown in Figure 3.7(a),(c) where the density and potential profiles shift up as the external magnetic field strength is increased. It has been previously reported the presence of density peaks at low externally applied magnetic fields [21]. In this particular experimental setup, either using krypton or xenon as working gas, no larger plasma density at lower magnetic fields has been recorded. Note that the density in Figure 3.6(a) is larger than that in Figure 3.7(a) because the reactor operates with a larger \dot{m} for krypton.

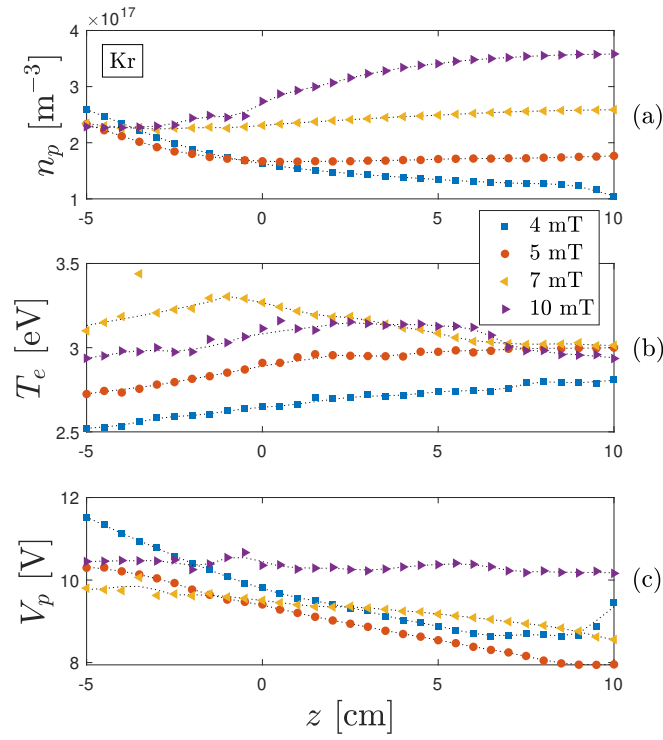


Figure 3.6: Evolution along the reactor axis of (a) n_p , (b) T_e and (c) V_p for different magnetic strengths. 750 W, 1 mg s^{-1} Kr, $r = 0 \text{ mm}$.

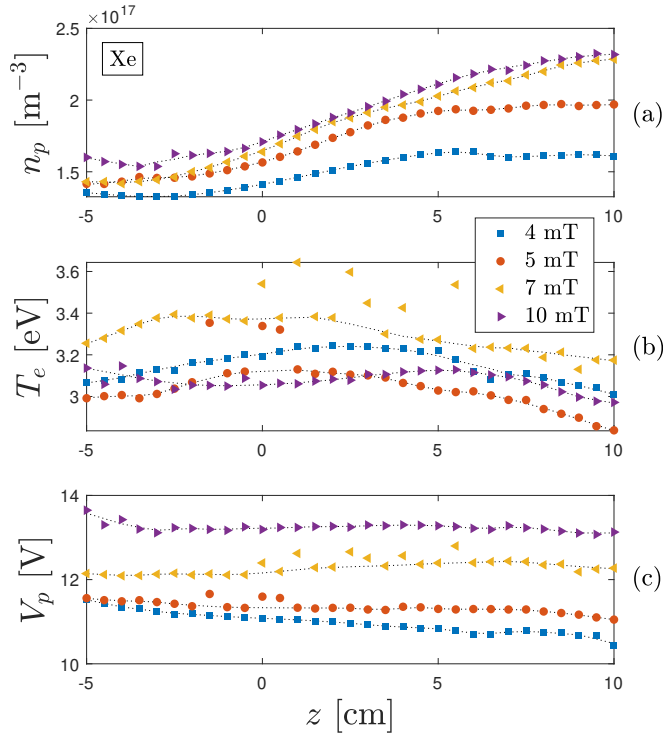


Figure 3.7: Evolution along the reactor axis of (a) n_p , (b) T_e and (c) V_p for different magnetic strengths. 750 W, 0.2 mg s^{-1} Xe, $r = 0 \text{ mm}$.

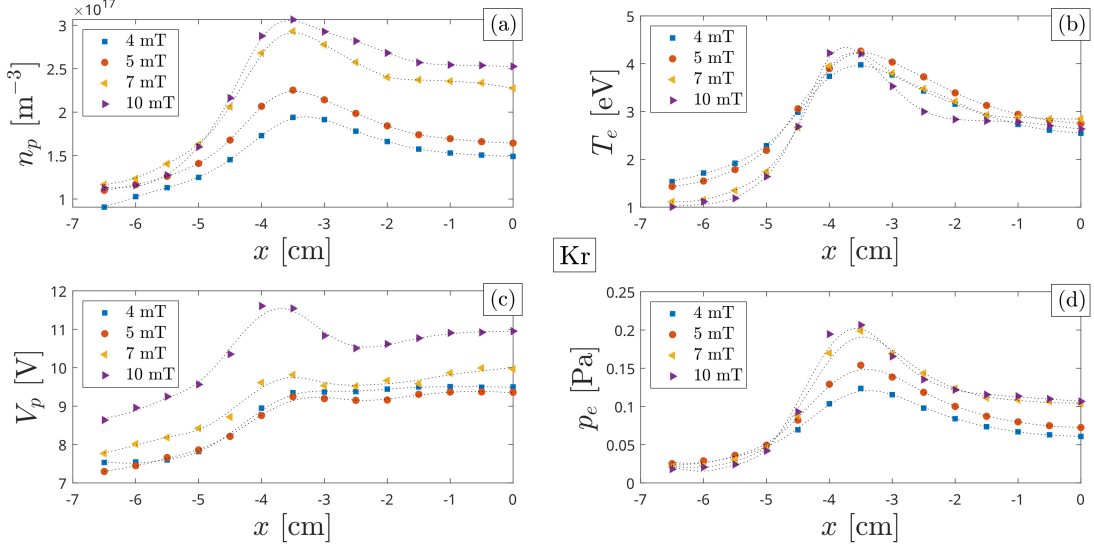


Figure 3.8: Radial profile of (a) n_p , (b) T_e , (c) V_p and (d) p_e for different magnetic strengths. $P_{IN} = 750 \text{ W}$, $\dot{m} = 1 \text{ mg s}^{-1}$ Kr, $z = 3 \text{ cm}$.

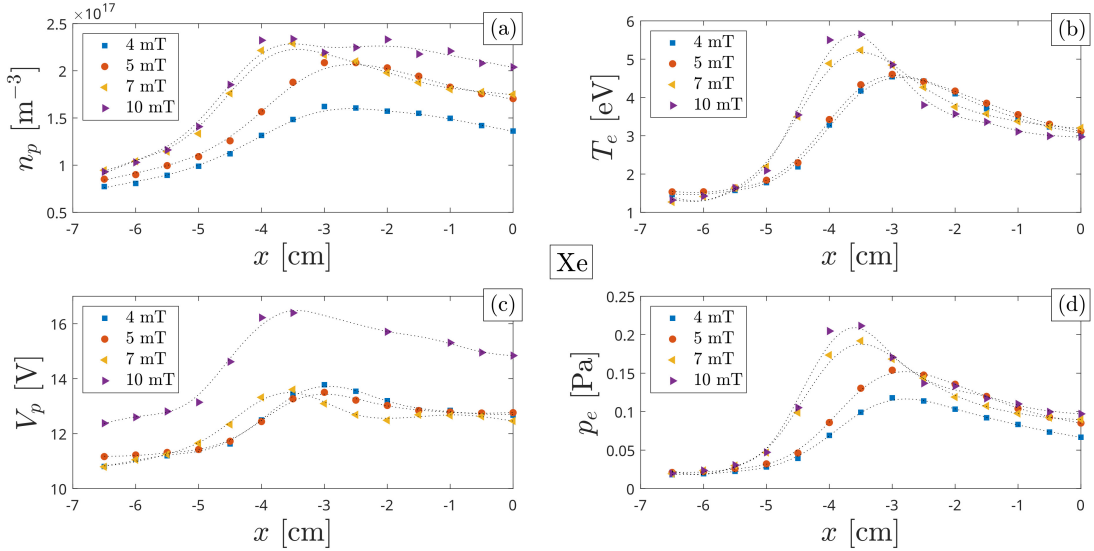


Figure 3.9: Radial profile of (a) n_p , (b) T_e , (c) V_p and (d) p_e for different magnetic strengths. $P_{IN} = 750 \text{ W}$, $\dot{m} = 0.2 \text{ mg s}^{-1}$ Xe, $z = 3 \text{ cm}$.

Detailed plasma properties measurements were also performed in the radial direction at $z = 3 \text{ cm}$ for the four different magnetic profiles. In accordance with the reference system in Figure 2.2, the measurements were performed along the x axis. The results are given in Figure 3.8(a)-(d) and Figure 3.9(a)-(d) for krypton and xenon respectively. Scatter points represent measurements data and dotted lines are smoothed profiles to enhance visualization. Density, temperature and potential peak values are localized off-axis. Similar outcomes have been previously reported for n_p and T_e [54, 75], but not for the plasma potential to the knowledge of the authors. It has been suggested that off-axis density peak is due to transport of high temperature electrons from the plasma discharge along the surface of the MN [76]. Figure 3.8(a) and Figure 3.9(a) show how ionization efficiency is enhanced at stronger magnetic fields. No relevant advantages in

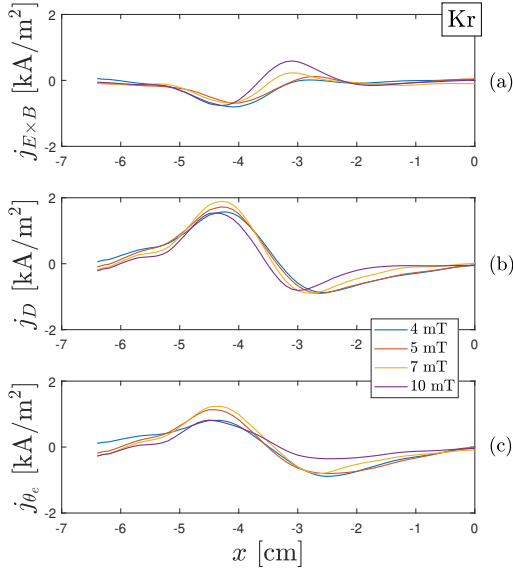


Figure 3.10: Computed profiles of (a) electron $E \times B$ current density, (b) electron diamagnetic current density and (c) Hall current $j_{E \times B} + j_D$ from plasma properties in Figure 3.8.

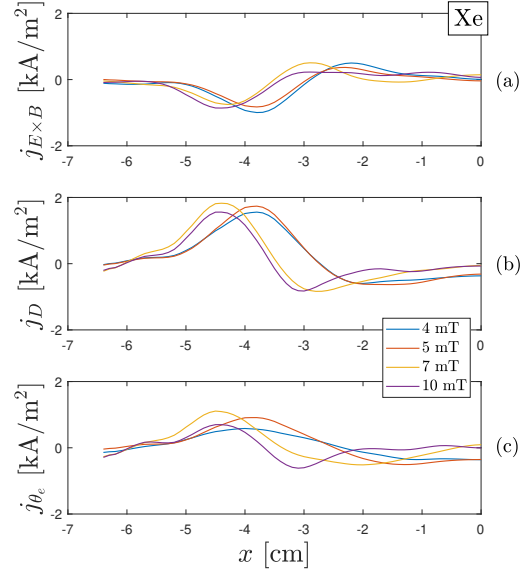


Figure 3.11: Computed profiles of (a) electron $E \times B$ current density, (b) electron diamagnetic current density and (c) Hall current $j_{E \times B} + j_D$ from plasma properties in Figure 3.9.

terms of electron temperature are obtained by increasing the applied field for krypton, as seen in Figure 3.8(b). Differently, peak value of T_e increases by more than 20 % (4 mT vs. 10 mT) when xenon is used, cf. Figure 3.9(b). Similarly, V_p profiles in Figure 3.8(c) and Figure 3.9(c) show that a more energetic plasma is obtained at larger B fields.

Radially non-uniform pressure and potential profiles shown in Figure 3.8 and Figure 3.9 inherently imply the presence of a Hall current j_{θ_e} in the expanding plasma, which has been analyzed theoretically/numerically [47] and experimentally [54]. When describing the evolution of axial momentum in a single conducting fluid description, i.e. combining electrons and ions momentum equations, it is deduced that thrust generation mechanisms in a HP thruster are due to an electrothermal acceleration and an electromagnetic Hall acceleration [47, 53]. The first contribution results from the plasma pressure acting inside the discharge chamber and on the "walls" of the diverging MN, while the second one results from a Lorentz force proportional to the net azimuthal current j_{θ} . However, it has been experimentally observed [77] that the swirl current j_{θ_i} , i.e. the ion contribution to j_{θ} , is fairly negligible for the values of applied magnetic field in analysis as the ions are unmagnetized. The profile of j_{θ_e} in this particular experiment can be inferred by using the radial component of the electron momentum equation in cylindrical coordinates, which reads

$$-n_p e E_r + j_{\theta_e} B_z - \frac{\partial p_e}{\partial r} = 0, \quad (3.2)$$

where E_r is the radial electric field, B_z is the axial magnetic strength and the rest has already been introduced. It is shown that the Hall current comprises an $E \times B$ drift

component $j_{E \times B}$ and a diamagnetic drift j_D component:

$$j_{\theta_e} = j_{E \times B} + j_D = n_p e \frac{E_r}{B_z} + \frac{1}{B_z} \frac{\partial p_e}{\partial r}. \quad (3.3)$$

The smoothed profiles of p_e and V_p in Figure 3.8 and Figure 3.9 have been used to calculate the current densities reported in Figure 3.10 and Figure 3.11, for krypton and xenon respectively. Taylor Series Method (TSM) is used to evaluate the uncertainty associated with the indirect estimation of j_{θ_e} through Equation 3.3. It has been assumed that propagation of the error is only due to n_p , T_e and V_p , whose error values are shown in Table 2.1. By expanding Equation 3.3 and substituting partial derivatives with finite differentiation terms, the expression for the uncertainty of j_{θ_e} truncated to the first order reads [78]

$$\left(\frac{U_{j_{\theta_e}}}{j_{\theta_e}} \right)^2 = 2 \left(\frac{U_{n_p}}{n_p} \right)^2 + \left(\frac{U_{T_e}}{T_e} \right)^2 + \left(\sqrt{2} \frac{U_{n_p}}{\Delta n_p} \right)^2 + \left(\sqrt{2} \frac{U_{T_e}}{\Delta T_e} \right)^2 + \left(\sqrt{2} \frac{U_{V_p}}{\Delta V_p} \right)^2. \quad (3.4)$$

Typical values of $U_{j_{\theta_e}}/j_{\theta_e}$ are in the order of 3 % for all operating conditions in terms of magnetic field strength and propellant. Note that $j_{\theta_e} > 0$ at $x < 0$ indicates that current flows in the diamagnetic direction (i.e. the magnetic field associated to the net j_{θ} is directed along $-z$), while $j_{\theta_e} < 0$ at $x < 0$ indicates it flows in the anti-diamagnetic direction. No profound differences are found when using krypton or xenon. With both propellants, $j_{E \times B}$ flows in the diamagnetic direction in the inner radial region and in the anti-diamagnetic direction in the outer radial region, cf. Figure 3.10(a) and Figure 3.11(a). The opposite behavior is recorded for j_D , cf. Figure 3.10(b) and Figure 3.11(b). Since the local thrust component due to the Lorentz force expressed in cylindrical coordinates is proportional to the product $r j_{\theta_e} B_r$, only values of j_{θ_e} flowing in the positive θ direction contribute to thrust generation. In the Cartesian reference system presented here, positive thrust contribution is given by $j_{\theta_e} > 0$ at $x < 0$ and vice versa. At the specific axial location where the radial scans are performed, integration over the radial direction outlines that a net thrust is produced for all the magnetic field magnitudes. Estimation of the total thrust would require a complete map of the plume and integration over the plasma volume.

Two-dimensional plasma properties are additionally provided for the 10 mT peak magnetic profile. Data are collected by displacing the probe radially between $r = 0$ mm and $r = 30$ mm and axially, both directions with a step size of 5 mm. Seven axial profiles for n_p , T_e and V_p are obtained. By interpolation, contour plots for krypton and xenon are derived and shown in Figure 3.12(a)-(d) and Figure 3.13(a)-(d), respectively. Electron pressure p_e is computed using the measured density and temperature. Peak values for T_e are about $4.5 \div 5$ eV both for krypton and xenon, occurring off-axis and few centimeters downstream the antenna. Then, from $z \cong 0$ on, the temperature decays monotonically. Counter-intuitively, n_p is peaked downstream where T_e is low. It is notable that the same qualitative results have been previously found in numerical [79] and experimental [27] studies using completely different setups in terms of scale and input parameters, such as antenna type and associated azimuthal mode numbers, input power frequency, magnetic field strengths and propellant. It shall be noted that likewise reported in [27], also in the present case this phenomenon is due to pressure balance. In a simplified 1-D two fluids description of the plasma, the axial component of the electron momentum equation in cylindrical coordinates reads

$$-n_p e E_z - j_{\theta_e} B_r - \frac{\partial p_e}{\partial z} = 0, \quad (3.5)$$

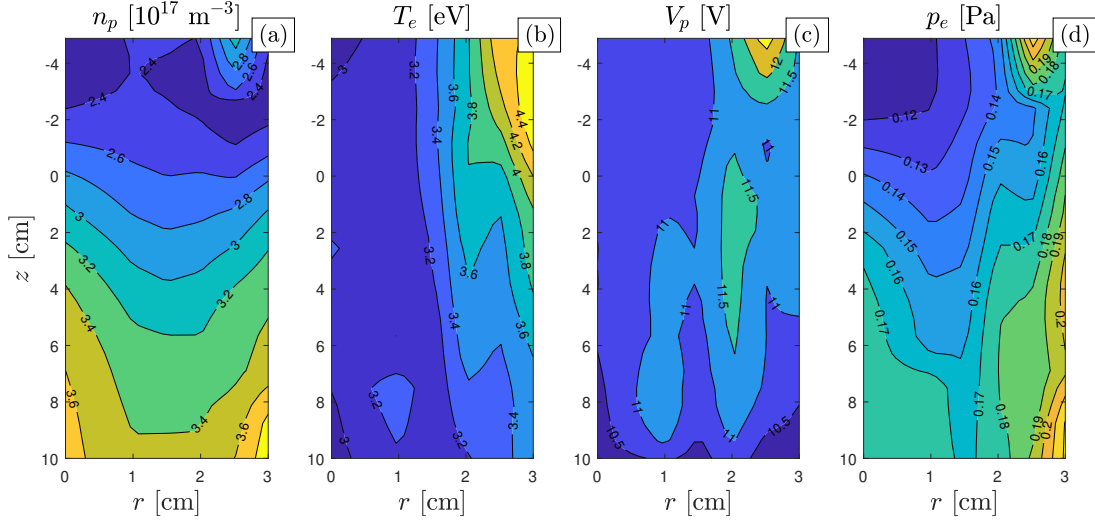


Figure 3.12: Contour plot of (a) plasma density, (b) electron temperature, (c) plasma potential, (d) electron pressure. Input parameters are: $P_{IN} = 750$ W, $\dot{m} = 1$ mg s⁻¹ Kr, 10 mT peak value of the external B field.

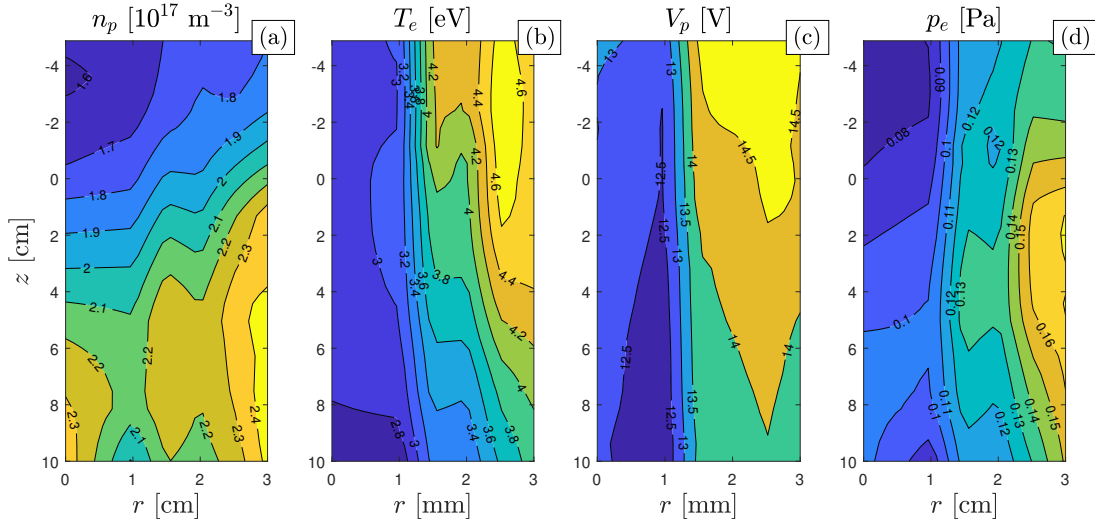


Figure 3.13: Contour plot of (a) plasma density, (b) electron temperature, (c) plasma potential, (d) electron pressure. Input parameters are: $P_{IN} = 750$ W, $\dot{m} = 0.2$ mg s⁻¹ Xe, 10 mT peak value of the external B field.

where p_e is the electron pressure, E_z is the axial electric field, j_{θ_e} is the electron azimuthal current density and B_r is the radial component of the applied magnetic field. For simplicity, the momentum transfer collisional term has been neglected. This is justified by observing that the mean free path λ is much larger than the source diameter. Values of λ are computed using average values for n_p and T_e from Figure 3.12 and Figure 3.13 together with the available dataset for the elastic momentum transfer cross section [80], yielding $\lambda \approx 25$ m for krypton and $\lambda \approx 15$ m for xenon. With reference to Figure 3.1, it can be observed that $B_r/B_z \ll 1$ in the region where the scan is performed, with typical values of $B_r \approx 10^{-6} \div 10^{-7}$ T. The electron current density shall be shown to be $j_{\theta_e} \lesssim 10^3$ A m⁻², cf. Figure 3.10 and Figure 3.11 later described. Hence, the electrons momentum equation reduces to a balance between the volumetric electric

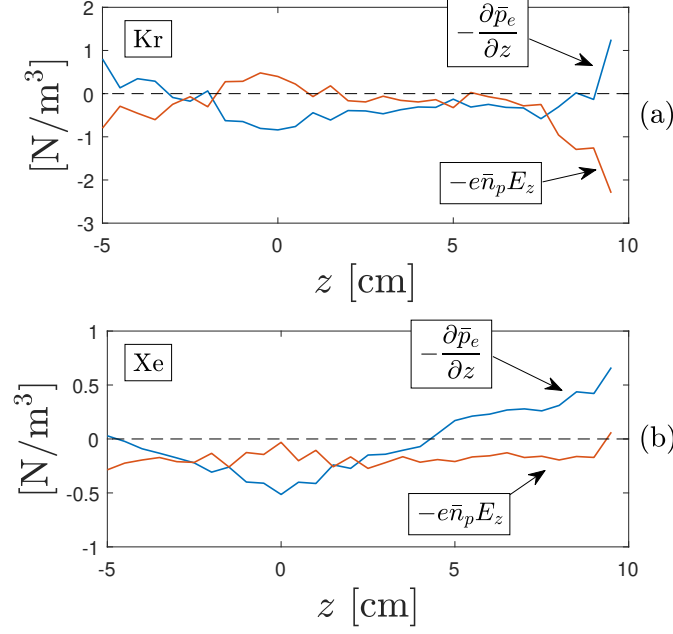


Figure 3.14: Volumetric forces acting on the electrons for (a) krypton and (b) xenon propellants. Variables \bar{p}_e and \bar{n}_p refer to radially averaged quantities.

forces term, i.e. $-n_p e E_z$, and the volumetric pressure forces term, i.e. $-\partial p_e / \partial z$. By averaging the measured $n_p(r, z)$, $V_p(r, z)$ and $p_e(r, z)$ over the radial direction, both terms of Equation 3.5 can be easily evaluated. Results are reported in Fig. 3.14(a) for krypton and Figure 3.14(b) for xenon. It is shown that pressure gradient and potential gradient are nearly equal and opposite through all the scanned region. Yet, this is more evident for krypton than for xenon, potentially due to the neglected collisional term in Equation 3.5. Hence, it is concluded that the density peak localized downstream is due to pressure balance. As the external magnetic field reduces the cross-field electron mobility, a relatively large axial conductivity ensues, which determines an almost constant plasma potential profile. This results in a small pressure gradient for equilibrium reasons, cf. Equation 3.5. The density peaks downstream because the temperature drops.

It is worth noting that, by knowing the number of neutrals injected in the system per unit time $\dot{N}_g = \dot{m} / M_i$, where M_i is the ion mass, and by taking a tentative value for the average plasma density \bar{n}_p accounting for all measured values in Figure 3.12(a) and Figure 3.13(a), it is possible to further compare the two working gases in terms of local propellant utilization efficiency η_p . It is implicitly assumed that the two gases share the same mean ion charge as T_e is relatively low to enable a significant amount of multiply charged particles. Since $\eta_p \propto \bar{n}_p / N_g$, it is computed that $\eta_p^{Xe} / \eta_p^{Kr} \approx 5$, suggesting that xenon is much more efficiently ionized, as expected.

Additional measurements include the investigation of ion energy as function of the externally applied magnetic field. In doing so, the RPA detailed in Section 2.2.5 has been employed. To increase data resolution, magnetic profiles with 6 mT and 8 mT peak values have been added to the four ones previously discussed. The probe has been placed downstream at $z = 33$ cm. While operating the HP source at one specific magnetic configuration, fifty I-V characteristics are acquired in groups of ten. Data is firstly smoothed and later numerically derived to obtain the ion energy distribution function (IEDF).

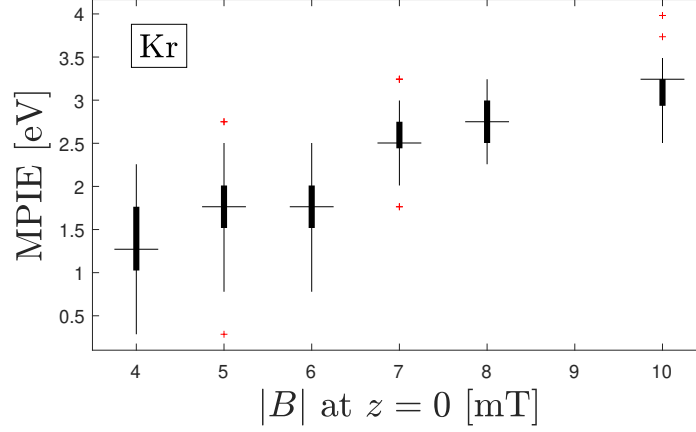


Figure 3.15: Most probable ion energy as function of the magnetic field. $P_{IN} = 750$ W, $\dot{m} = 1$ mg s⁻¹ Kr, $z = 33$ cm. Horizontal mark indicates median value, thick box delimits 25th and 75th percentiles, red marks represent outliers.

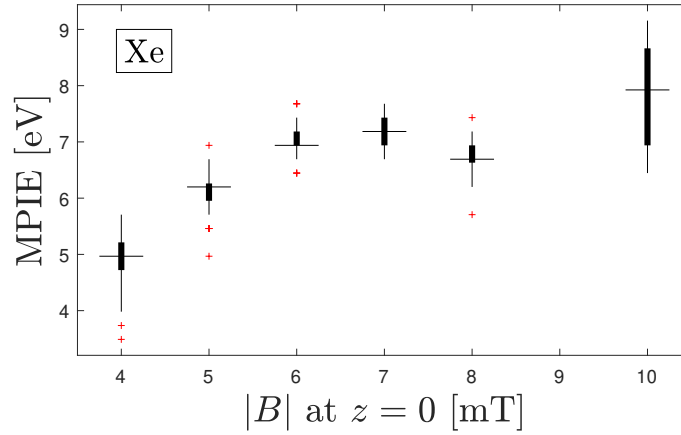


Figure 3.16: Most probable ion energy as function of the magnetic field. $P_{IN} = 750$ W, $\dot{m} = 0.2$ mg s⁻¹ Xe, $z = 33$ cm. Horizontal mark indicates median value, thick box delimits 25th and 75th percentiles, red marks represent outliers.

The most probable ion energy (MPIE) is then extracted as the IEDF peak value. Results in terms of MPIEs for krypton and xenon are reported in Figure 3.15 and Figure 3.16, respectively. As expected, higher ion energies are measured as the external magnetic field strength is increased, coherently with what reported in Figure 3.6(c) and Figure 3.7(c). Generally speaking, although consistent with the values of plasma potential, typical ion energies herein reported are very small, suggesting low propulsive performance of the HP source in analysis. The measured ion energies imply ultimate electrostatic ion speeds of about 2.7 km s⁻¹ for Kr⁺ and about 3.5 km s⁻¹ for Xe⁺, both estimated for the highest strength of the magnetic field. Higher beam energies in the range of few tens of eV have been reported in previous works [81–85]. It is reasonable to state that this large performance discrepancy with respect to other HP sources comes from a complete different set of input parameters. The source analyzed in this work features a relatively large geometry and operated at relatively weak magnetic fields and small mass flow rates.

3.1.4 Summary and conclusion

In conclusion, the two gases are compared as function of the externally applied magnetic strength. It is found that plasma potential axial profiles exhibit qualitative and quantitative differences when using krypton for distinct strengths of the magnetic field. This suggests that the plasma source operates in inductive mode below a threshold value of the applied field. In contrast, no qualitative differences have been recorded when using xenon. Measurements along the radial direction revealed that all plasma properties peak off-axis for all the tested magnetic strengths. Krypton and xenon plasma properties are 2D-mapped when the source operates with a magnetic field peak value of 10 mT at the exit cross section of the discharge chamber. It is found that the electron temperature peaks off-axis just before the exit cross section, while the peak in plasma density occurs similarly off-axis but downstream where the electrons are colder. This phenomenon is quantitatively attributed to pressure balance effects. Ion energy is measured as function of the applied magnetic field strengths, showing that xenon performs better. Nevertheless, low ion energies are recorded.

3.2 Plasma properties conditioned by the magnetic throat location

According to the operation principles discussed in Section 1.1.2, the shape of the magnetic nozzle and the location of the throat are presumably strongly linked to the amount of the input energy that can be usefully converted into axial thrust. Energetic electrons are mainly produced close to the region occupied by the antenna. Several phenomena occur in the nozzle, such as transport due to pressure gradient and electron cooling via convection and/or conduction, which determine the conversion efficiency of inlet thermal energy into ion acceleration. Furthermore, as the throat is shifted along the thruster axis with respect to the antenna location, the expansion ratio of the plasma beam changes, thus resulting in possibly different thrust levels.

In an effort to model HP discharges, previous analyses have considered different magnetic topologies inside the source tube, e.g. uniform [46, 86], Helmholtz and Maxwell configurations [87]. The magnetic field inside the source is then matched with a divergent geometry through a magnetic throat localized in the proximity of the tube exit. This firm condition is not necessarily the most convenient solution, as demonstrated in [88] where a stepped-diameter tube is employed and the magnetic throat is placed downstream the exit cross section of the small main tube. Besides, virtually every numerical and experimental work studying the influence of magnetic nozzle on the plasma properties, limited the analysis to the exploitation of different magnitudes at the throat. A fruitful investigation is reported in [89], where the location of the magnetic throat is indirectly shifted with respect to the antenna – which is constantly located at the back plate – by changing the discharge tube length. Another relevant analysis is reported in [90], where the authors characterized the plasma and the rf power circuit when the magnetic throat localized either within the source or at the exhaust. Bennet *et al.* [91] studied the generation of plasma as a function of the MN throat location. Yet, their setup did not include plasma expansion outside the discharge tube and many operating conditions relied on magnetized ions, which is not a typical scenario in propulsion.

For the purpose of this study, five magnetic configurations are studied by powering two electromagnets at once. In doing so, the location of the magnetic throat is inten-

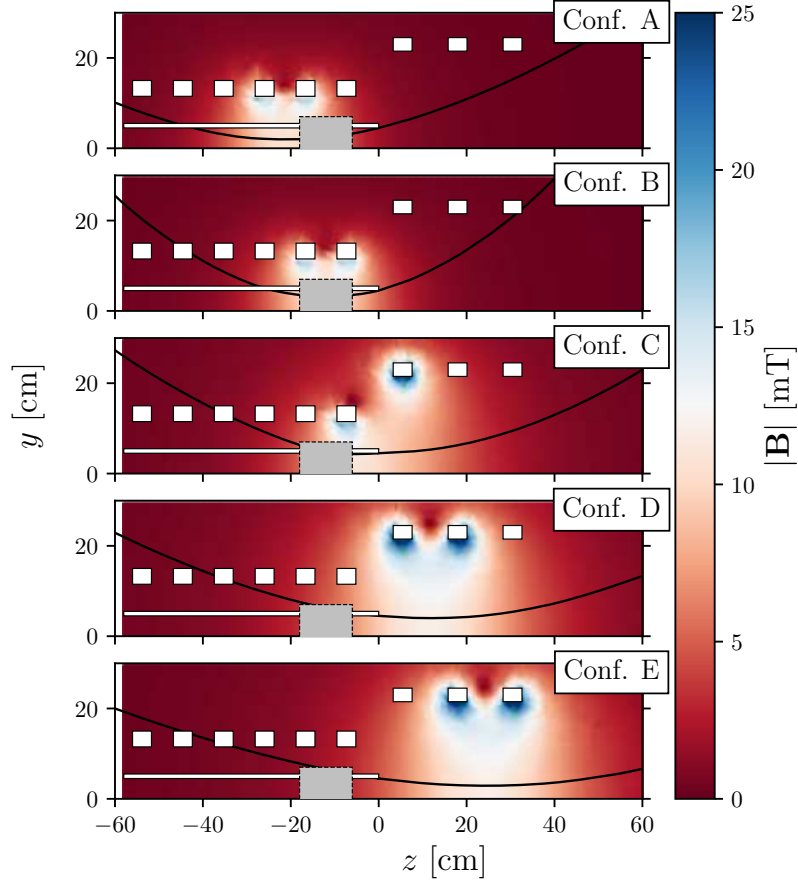


Figure 3.17: 2D profiles of the externally applied magnetic fields. White line indicates the discharge tube walls, white rectangles represent the magnetic coils, the gray rectangle indicates the antenna region and the black solid line exemplifies the magnetic streamline crossing the tube edge at $z = 0$.

Table 3.1: Matrix of electromagnets current for the tested magnetic topologies.

	Electromagnets current [A]								
	PB1	PB2	PB3	PB4	PB5	PB6	GB1	GB2	GB3
Conf. A	0	3	3	0	0	0	0	0	0
Conf. B	3	3	0	0	0	0	0	0	0
Conf. C	3	0	0	0	0	0	0	0	6
Conf. D	0	0	0	0	0	0	0	6	6
Conf. E	0	0	0	0	0	0	6	6	0

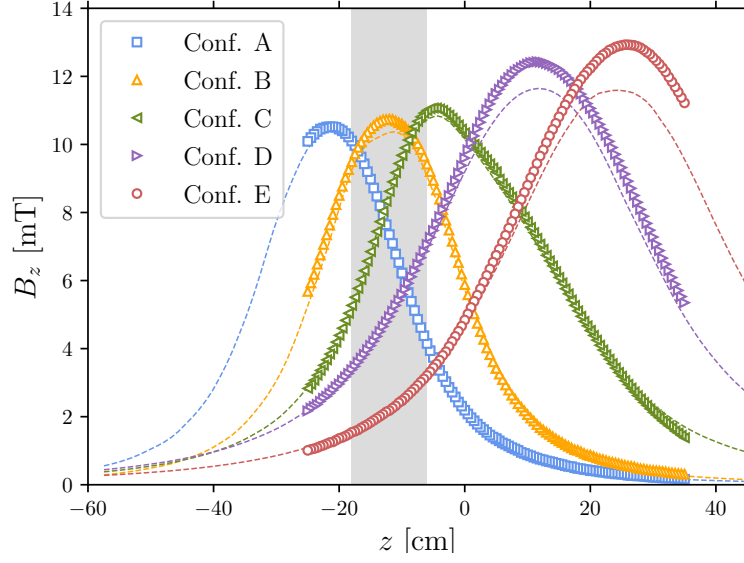


Figure 3.18: Externally applied magnetic field on-axis profiles. Shaded area indicates the antenna location. Dashed lines represent simulation profiles, scatter points indicate probe measurements.

tionally relocated along the z axis. The tested magnetic configurations are progressively labeled as Conf. A to Conf. E. When involved, PB coils are powered with 3 A and GB coils with 6 A of direct current. The detailed current schematics is provided in Table 3.1. Figure 3.17 shows the 2D magnetic field maps calculated via FEM simulation, highlighting the streamline that crosses the discharge tube edge at $z = 0$, thus defining the ideal shape of the plasma plume. With reference to Figure 3.17, it is noteworthy to emphasize on the magnetic throat location. It moves from upstream the antenna in Conf. A to far downstream the antenna in Conf. E. The first axial mode the antenna can generate translates in an axial wavelength as $\lambda_z = 24$ cm. Notice that the magnetic throat in Conf. D is approximately one wavelength downstream of the antenna center. The magnitude of the on-axis magnetic field is reported in Figure 3.18 by comparing computed values and measured values which are evaluated using a commercial Gaussmeter. All magnetic configurations feature a peak value of 10 – 13 mT with a similar qualitative profile but shifted along z .

3.2.1 Plasma plume visual inspection

The very first piece of information regarding the way the plasma responds to the applied magnetic field topology is provided by visual inspection. The photographs of the plasma plume reported in Figure 3.19 are taken using a common DSLR camera framing the region $8 < z < 28$ cm and set at $f/8$ and $1/40$ s exposure time. It results evident how significant differences characterize the extracted plasma plume when employing the different magnetic topologies. A faint plume is visible when the reactor operates in Conf. A and Conf. B. Instead, a well defined plasma beam is noticed when Conf.s C, D and E are chosen. In the latter cases, the plasma radius visibly delineates the local magnetic streamlines, cf. Figure 3.17 and Figure 3.19. It is interesting to notice that the local magnitude of the axial component B_z is nearly equal for Conf. C and Conf. E at

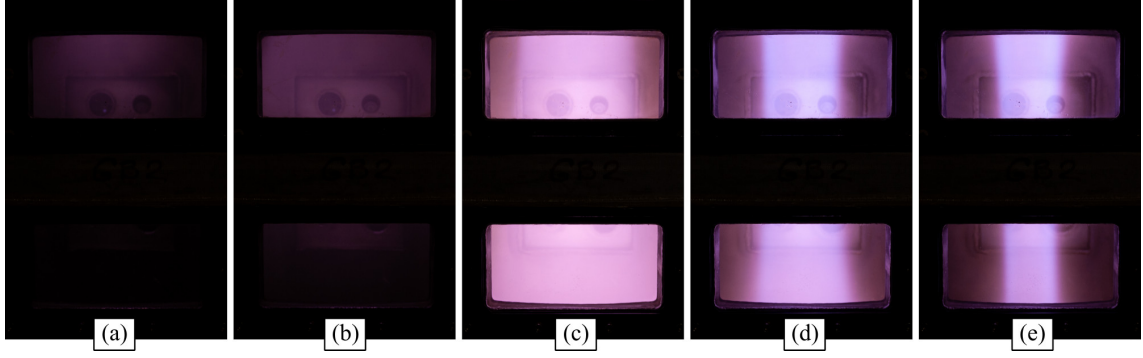


Figure 3.19: Photographs of the plasma plume in (a) Conf. A, (b) Conf. B, (c) Conf. C, (d) Conf. D and (e) Conf. E. Windows are centered at $z = 12$ and $z = 24$ cm.

$z = 12$ cm (see Figure 3.17), i.e. at the center of the top window in Figure 3.19. Yet, the two plasma beams show a very different structure. As a matter of fact, local values of the field radial component B_r and gradient $\partial B_z / \partial z$ significantly differ. This finding agrees with previous numerical models [46, 92] and intrinsically points out that both $|\mathbf{B}|$ and $\nabla \mathbf{B}$ have an impact on the plasma behavior.

3.2.2 Langmuir probe measurements

Plasma properties are characterized using the diagnostics described in Section 2.2. The region delimited by $0 < y < 4$ cm and $-4 < z < 21$ cm is probed by means of the RF-CLP. I-V characteristics are recorded with a spatial resolution of 5 mm. Data are post-processed as discussed in Section 2.2.3 and eventually interpolated to enhance visualization. Figures 3.20, 3.21 and 3.22 illustrate normalized 2D maps of n_p , T_e and V_p , respectively, for the five magnetic topologies. Normalization values are: $6 \times 10^{17} \text{ m}^{-3}$ as regards to n_p , 6 eV for T_e and 25 V for V_p . The solid black lines included in the figures represent the magnetic streamlines delimited by the discharge tube edge at $z = 0$. Furthermore, on-axis profiles of n_p , T_e and V_p are shown in Figure 3.23. These experimental measurements show that:

1. when the HP source operates in Conf. A, the extracted plasma plume is characterized by a low monotonically decreasing profile of n_p ranging between $\sim 1 \times 10^{17}$ and $\sim 9 \times 10^{15} \text{ m}^{-3}$ along the reactor axis. The profile of T_e features a monotonic behavior as well, with a peak value of ~ 3 eV. In a similar fashion, V_p drops from ~ 24 V to ~ 15 V. All plasma properties peak on-axis at $z < 0$. These quantitative observations agree with the faint light emitted in the nozzle region, as stated beforehand. Visual check of the plasma also reveals that light is instead concentrated within the discharge tube. It suggests that the radial and back boundaries represent a major loss term of plasma [40, 46].
2. when the HP source operates in Conf. B, analogous arguments can be put forward. The profile of n_p likewise peaks on-axis at $z < 0$ and decays monotonically downstream. Altogether, slightly larger values of n_p are measured with respect to Conf. A. In the bulk of the plasma, T_e remains in the order of ~ 3 eV with lower values downstream. However, a population of relatively more energetic electrons ($T_e \sim 3.5$ eV) appears off-axis, in correspondence of the magnetic nozzle edge,

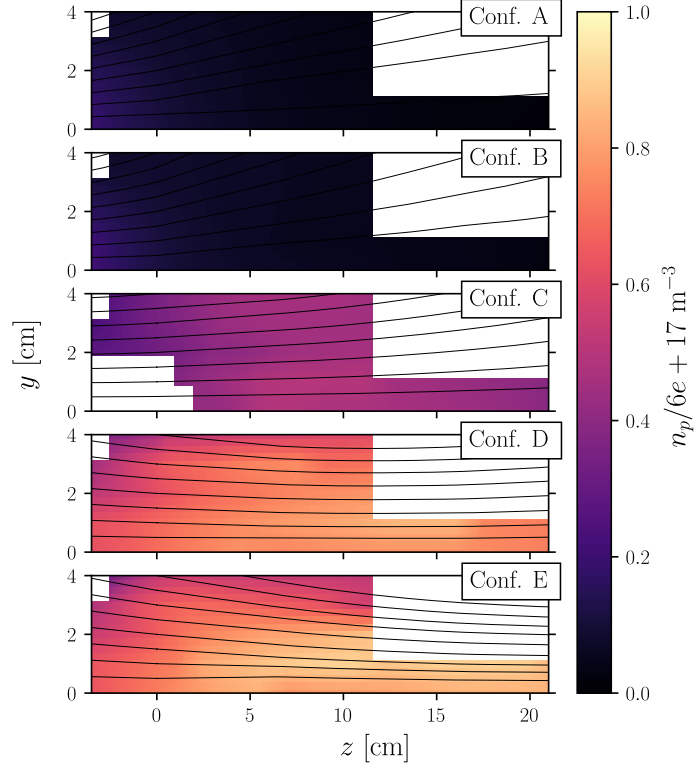


Figure 3.20: Normalized plasma density for the five magnetic configurations. Normalization factor is $6 \times 10^{17} \text{ m}^{-3}$. Solid black lines represent magnetic streamlines.

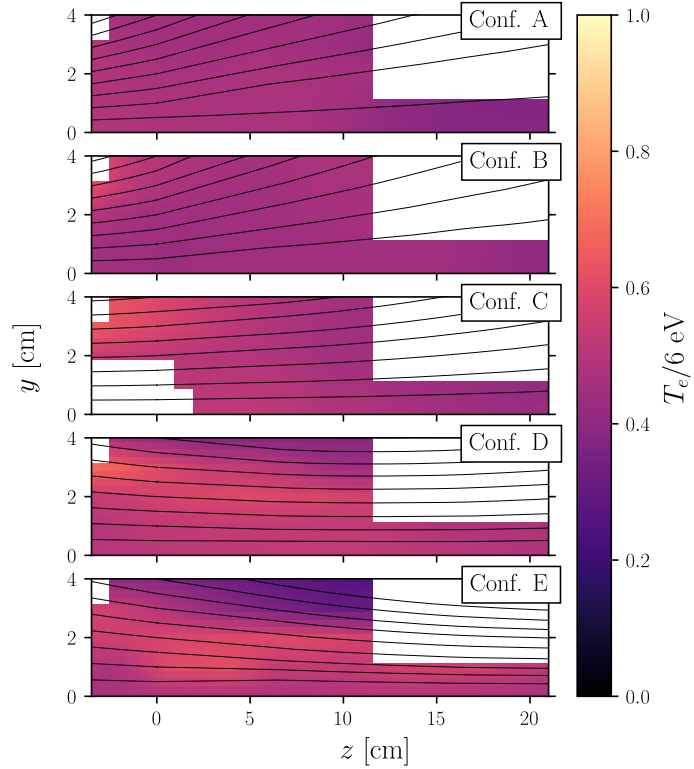


Figure 3.21: Normalized electron temperature for the five magnetic configurations. Normalization factor is 6 eV. Solid black lines represent magnetic streamlines.

3.2. PLASMA PROPERTIES CONDITIONED BY THE MAGNETIC THROAT LOCATION

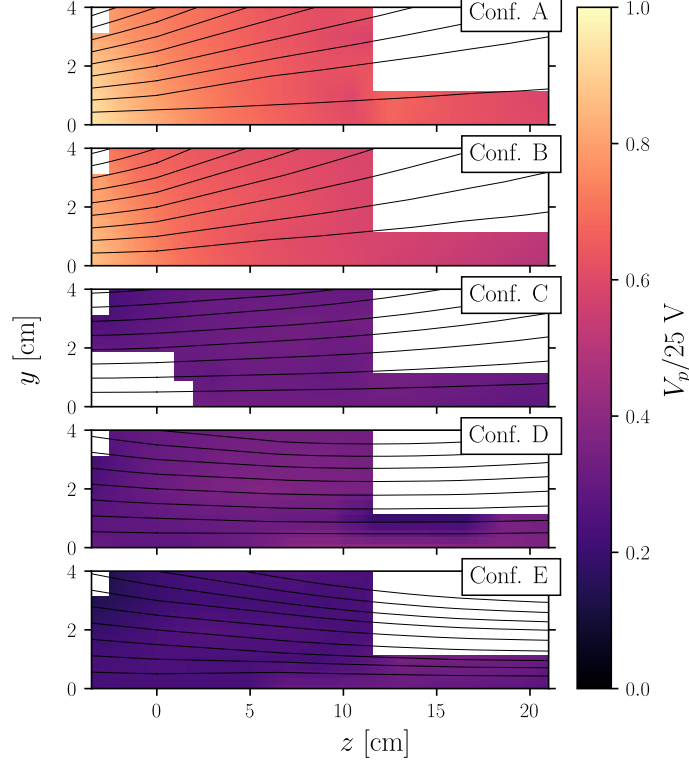


Figure 3.22: Normalized plasma potential for the five magnetic configurations. Normalization factor is 25 V. Solid black lines represent magnetic streamlines.

visible at $z < 0$ in Figure 3.21(b). Although qualitatively very similar, the distribution of V_p for Conf. B presents lower values with respect to Conf. A of a few volts.

3. when the HP source operates in Conf. C, results similar to those previously reported in [32] using the same HP source are obtained. As a matter of fact, in both the experiments the magnetic throat is located at $z = 0$. In contrast to what was discussed in points (1) and (2), all plasma properties peak off-axis. Data acquisition in the region ($0 < r < 2$, $z < 0$) was not possible due to discharge instability possibly induced by the probe presence. The largest value of n_p is recorded at $z > 0$ and it reads $\sim 3 \times 10^{17} \text{ m}^{-3}$, whereas T_e reaches a peak of 4 eV at $z < 0$. The distribution of V_p is relatively isotropic, ranging in the $8 \pm 0.5 \text{ V}$ interval. The reason why n_p and T_e present separated regions of the respective maximum values has been explained in [27, 32] in terms of pressure balance. When considering the z component of the electron momentum conservation equation in the limit of negligible contribution due to momentum transfer collisions and due to the Lorenz force, the potential gradient and the pressure gradient balance each other. In the region where $B_r/B_z \ll 1$, i.e. where the local magnetic field divergence angle is small, the reduced cross field electron mobility yields a relatively large axial conductivity, resulting in a nearly null potential gradient. Hence, for equilibrium reasons, the pressure gradient is required to be small, which results in a larger n_p where T_e is lower and vice versa. Similar results are numerically found and discussed in [79].

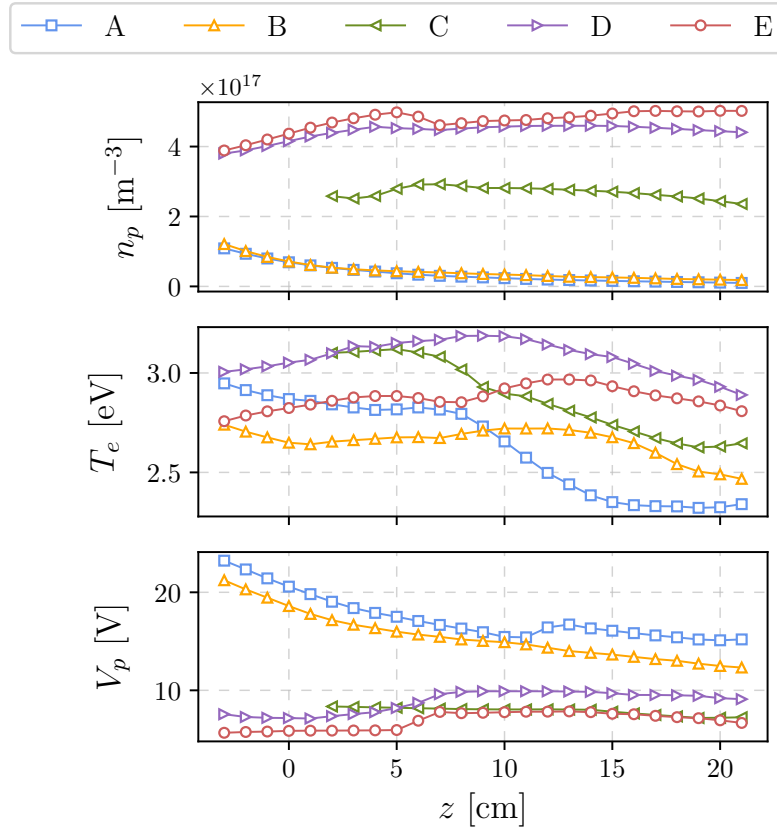


Figure 3.23: On-axis profiles of (top) plasma density, (middle) electron temperature and (bottom) plasma potential. Data is extracted from Figures 3.20-3.22 and down-sampled to enhance visualization.

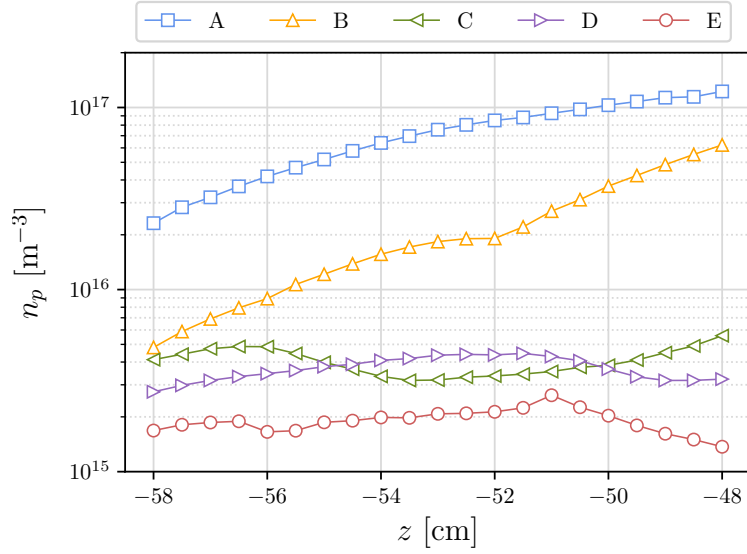


Figure 3.24: Ion density profile in the proximity of the back-plate for the five magnetic configurations.

4. when the HP source operates in Conf. D, light emission upstream the antenna is almost absent, hinting that plasma losses at the back and lateral walls are mitigated with respect to the previous cases. With reference to Figure 3.20(d), it is evident that n_p follows the axial gradient of B_z . The maximum value of $\sim 5 \times 10^{17} \text{ m}^{-3}$ is therefore located in correspondence of the magnetic throat. In Figure 3.21(d), it is relevant to notice the distinct transport pattern of a relatively more energetic electron population along the magnetic field lines at the edge of the nozzle, which exhibits $T_e \approx 3.5 \div 4.2 \text{ eV}$. A relatively small V_p is measured throughout the probed region, with a peak value in the order of 10 V in the area of maximum n_p .
5. when the HP source operates in Conf. E, similar observations to those stated in point (4) can be raised. Profiles of n_p and T_e have a strong dependence on the spatial distribution of B_r and B_z . The highest plasma density value among all the studied magnetic configurations is herein recorded to be $\sim 5.5 \times 10^{17} \text{ m}^{-3}$ nearby the magnetic throat. As highlighted in point (4), also in this case a more energetic population of electrons is transported along the external surface of the magnetic nozzle, cf. Figure 3.21(e). At $z \cong 10 \text{ cm}$, all the electrons with $T_e \gtrsim 3 \text{ eV}$ are concentrated in a radius of about 3 cm, as visually confirmed by Figure 3.19(e).

Eventually, it is worth observing that the different configurations of B possibly influence the power deposition map. This, in turn, very likely relates to the different spatial distributions of n_p and T_e as discussed in points (1)-(5).

In addition to the measurements performed using the RFCLP, a simple uncompensated LP is inserted on-axis at the back/injection plate of the HP source to measure n_p as an indicator of the plasma flux lost in this region. The probe is biased to scan over the ion saturation branch only. No significant distortions due to rf oscillations are expected in this part of the I-V curve [60]. For obtaining this particular set of data, the reactor injection plate has been modified in order to accommodate the probe and its related wiring. The propellant is still injected off-axis but it goes through a plenum first and eventually reaches the discharge tube via a multi-perforated surface, resulting in a axial gas flow. An uncompensated probe is chosen due to limitations on the available room. The measured profiles of n_p are shown in Figure 3.24 for Conf. A to E. Since the magnetic throat in Conf. A is located upstream the antenna, the ions are mostly transported towards the back plate by following the convergent-divergent shape of the magnetic field. As the magnetic throat moves farther downstream from the antenna center, lower densities are measured in the proximity of the injection plate, as expected.

3.2.3 Plasma density profile model

Using a simplified description of the plasma, the measured axial profiles of n_p can be compared with theoretical profiles retrieved from the helicon wave dispersion relation, which is thereafter derived accounting for the non-uniformity of the external magnetic field along z . This approach implicitly assumes that the plasma production entirely relies on the wave-mode power coupling. Although the helicon regime is not proven here by direct measurement of the excited wave, the experiments in Section 3.1.1 have shown the presence of the propagating wave for similar ranges of magnetic field strength and input power. Considering that the electric $\tilde{\mathbf{E}}$ and magnetic $\tilde{\mathbf{B}}$ components of the

exited wave are described [17, 25] as

$$\tilde{\mathbf{E}}, \tilde{\mathbf{B}} \sim \exp[i(m\theta + k_z z - \omega t)], \quad (3.6)$$

where m is the azimuthal mode number, θ is the azimuthal angle and k_z is the axial wavenumber, Maxwell equations assume the form

$$\nabla \cdot \tilde{\mathbf{B}} = 0, \quad (3.7a)$$

$$\nabla \times \tilde{\mathbf{E}} = i\omega\tilde{\mathbf{B}}, \quad (3.7b)$$

$$\nabla \times \tilde{\mathbf{B}} = \mu_0 \mathbf{j}. \quad (3.7c)$$

The electron momentum equation is written as

$$-en_p \tilde{\mathbf{E}} = i \frac{m_e}{e} \mathbf{j}_e (\omega + i\nu) - \mathbf{j}_e \times \mathbf{B}, \quad (3.8)$$

where \mathbf{j}_e is the electron current density, \mathbf{B} is the external magnetic field and ν is a collision rate accounting for all dissipation phenomena. Additional comments and derivation of Equation 3.8 are reported in [25]. The widespread ideal assumption of perfectly uniform magnetic field is not appropriate in the actual case. Therefore, although still simplistic, it is assumed that $\mathbf{B} = B(z)\hat{\mathbf{z}}$, i.e. only the variation of the magnetic field along z is accounted for. Combining Equation 3.7a-(3.7c) and Equation 3.8, one obtains

$$\left(\frac{\omega + i\nu}{\omega_{c_e}} \right) \nabla \times (\nabla \times \tilde{\mathbf{B}}) - k_z \nabla \times \tilde{\mathbf{B}} + \frac{\mu_0 e \omega n_p}{B} \tilde{\mathbf{B}} = 0, \quad (3.9)$$

where the explicit dependence on z has been omitted, ω_{c_e} is the electron cyclotron frequency and the rest is conventional. Detailed derivation of Equation 3.9 is likewise included in [25]. Eventually, in the limit of $m_e \rightarrow 0$, the local dispersion relation is retrieved in the same shape of the well known 0D dispersion relation, i.e.

$$k(z)k_z = \frac{\mu_0 \omega e n_p(z)}{B(z)}, \quad (3.10)$$

where $k(z)$ indicates the total wavenumber. The wave boundary conditions are fixed by [17]

$$mk(z)J_m[k_r(z)r_p(z)] + k_z J'_m[k_r(z)r_p(z)] = 0, \quad (3.11)$$

where J_m and J'_m are the Bessel function of the first kind of order m and its derivative, respectively, $k_r(z)$ is the local radial wavenumber and $r_p(z)$ is the local plasma radius. The value of k_z is fixed by the antenna length, i.e. $k_z = \pi/d_A$, $3\pi/d_A$, $5\pi/d_A$, etc. Pretending that only the first order axial mode is coupled with the antenna, the computation algorithm includes:

- the axial wavenumber is estimated as $k_z = \pi/d_A$, therefore the axial wavelength is $\lambda_z = 24$ cm;
- $r_p(z)$ is set equal to the radius of the magnetic streamline crossing the tube edge at $z = 0$, see Figure 3.17;
- considering the geometry of the antenna and the direction of the external magnetic field, it is imposed that $m = +1$;

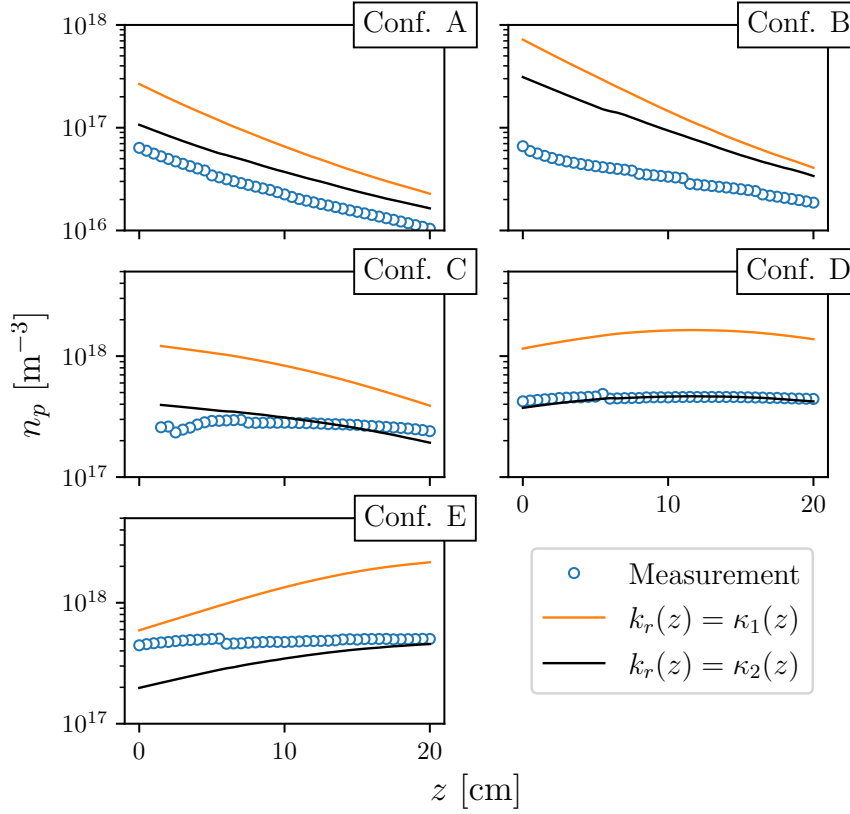


Figure 3.25: Plasma density at $r = 0$ computed using the helicon waves dispersion relation in the $k_r(z) = \kappa_1(z)$ and $k_r(z) = \kappa_2(z)$ cases compared to measurement data.

- two cases are distinguished:
 1. $k_r(z)$ is computed numerically from Equation 3.11 and it is named as $\kappa_1(z)$ for the sake of clarity in the following;
 2. $k_r(z)$ is evaluated as $\kappa_1(z) \sin[\alpha(z)]$ referred to as $\kappa_2(z)$ hereafter. Here $\alpha(z)$ is the local magnetic field divergence angle. The purpose of this heuristic strategy is to provide the model with the information that the applied magnetic field is not purely axial. In doing so, it is postulated that the helicon wave resonance cone reduces to a line at the magnetic throat, i.e. where $\alpha = 0$, thus k equals k_z .
- the profile $n_p(z)$ is consequently computed from Equation 3.10 for the aforementioned two cases.

Numerical values of the relevant parameters are reported in Table 3.2 for all magnetic configurations. In Figure 3.25, the obtained theoretical curves are compared with measurements of n_p extracted from Figure 3.20 at $x, y = 0$ for all the tested magnetic configurations. In general, it is found that the case $k_r(z) = \kappa_1(z)$ provides an overestimation of the plasma density. When dealing with Conf.s D and E, the $k_r(z) = \kappa_2(z)$ case is in very good agreement with the data in correspondence of the magnetic throat, that is where the strong assumption $\mathbf{B} = B(z)\hat{\mathbf{z}}$ is more representative. Ultimately, n_p

Table 3.2: Helicon wave parameters at $z = 10$ cm.

	Conf. A	Conf. B	Conf. C	Conf. D	Conf. E
r_p [cm]	7.3	8.1	5.1	4.0	3.5
k_z [cm ⁻¹]	0.26	0.26	0.26	0.26	0.26
λ_z [cm]	24	24	24	24	24
κ_1 [cm ⁻¹]	0.46	0.41	0.68	0.88	1.03
κ_2 [cm ⁻¹]	0.14	0.17	0.07	-0.01	-0.08

measured in Conf. C is in relatively good agreement with the latter case. It is noted that even the $k_r(z) = \kappa_2(z)$ case overestimates the measured values of n_p for Conf.s A and B, although matching the qualitative profile. This suggests that the helicon wave is evanescent in this region of the plasma since the measured n_p is lower than the one required by the dispersion relation. In conclusion, these profiles of n_p computed from the dispersion relation represent a first effective estimation of the actual spatial evolution of plasma density. Therefore, these quantitative information can be of some convenience for guessing the propagation region of helicon waves and for preliminary modeling of the plasma dynamics and/or design of the axial magnetic field profile.

3.2.4 Ion current density measurements

A further insight into the properties of the plasma when operating with the different magnetic topologies is rendered by the employment of the PPGR described in Section 2.2. The probe is displaced radially along the x axis at $z = 5$ cm and $z = 15$ cm in order to analyze the divergence of the extracted plasma plume. The measurements of j_i are shown in Figure 3.26(a-b). Table 3.3 gathers the values of the divergence parameter δ computed as the ratio $j_i(x = -11.5 \text{ cm})/j_i(x = 0 \text{ cm})$. Results confirm that a low-current high-divergence ion beam is extracted from the HP source when operating in Conf. A and B. Differently, the ion beams related to Conf.s C, D and E feature a similar low-divergence profile of j_i in the proximity of the tube exit, see Figure 3.26(a). Yet, the divergence angle of Conf. C rapidly grows as the plasma expands downstream, cf. Figure 3.26(b). The highest value of j_i is recorded in Conf.E at $z = 15$ cm, in agreement with the largest n_p probed in the same configuration. Larger values of j_i relate well with higher propellant utilization efficiency, which is a desirable working condition for space propulsion applications.

Table 3.3: Plume divergence parameter δ from data in Figure 3.26.

	Conf. A	Conf. B	Conf. C	Conf. D	Conf. E
δ at $z = 5$ cm	0.218	0.359	0.041	0.014	0.021
δ at $z = 15$ cm	0.523	0.567	0.224	0.028	0.035

3.2. PLASMA PROPERTIES CONDITIONED BY THE MAGNETIC THROAT LOCATION

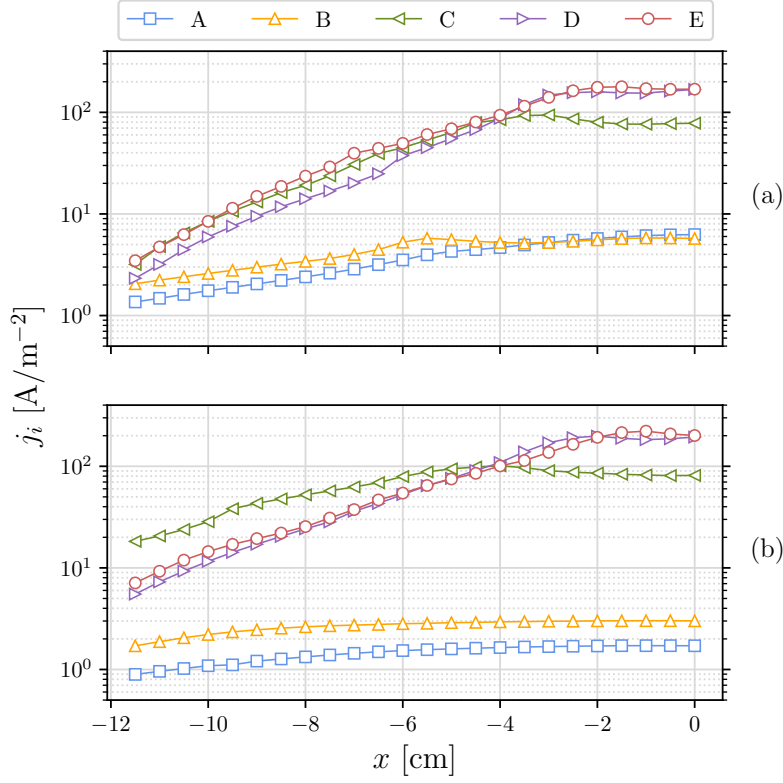


Figure 3.26: Ion current density at (a) $z = 5$ and (b) $z = 15$ cm for the five magnetic configurations.

Table 3.4: Order of magnitude of relevant velocity quantities.

	$O(v)$
Ion acoustic velocity	$v_B = \sqrt{kT_e/m_i} \approx 2000 \text{ m s}^{-1}$
Thermal velocity	$v_{th} = \sqrt{8kT_i/\pi m_i} \approx 275 \text{ m s}^{-1}$

3.2.5 Atoms and ions velocity measurements

Using LIF spectroscopy, the velocity distribution functions of krypton atoms Kr I and ions Kr II are inferred. Information about the velocity of the ions is of particular interest for driving conclusions about propulsive performance. On the other hand, knowledge of the atoms velocity is useful for modeling of the plasma flow. Table 3.4 exemplifies the order of magnitude of the relevant velocity terms in the HP source operating with Kr. Radial profiles of Kr I VDF are evaluated at $z = 12$ cm and shown in Figure 3.27 for all magnetic configurations. The spatial resolution is 10 mm. In this case, the reported data did not require any post-processing as a adequate signal-to-noise ratio was found. These measurements show that the most probable velocity of Kr I is nearly unchanged over the different magnetic topologies, reading $\sim 250 \div 300 \text{ m s}^{-1}$, therefore in the order of the thermal velocity assuming $T_i \approx 300 \text{ K}$, cf. Table 3.4. No dependence of the velocity on the radial location y is recorded. Dissimilar values of velocity spread are found between the magnetic configurations, with a broader VDF for Conf. C and Conf. D.

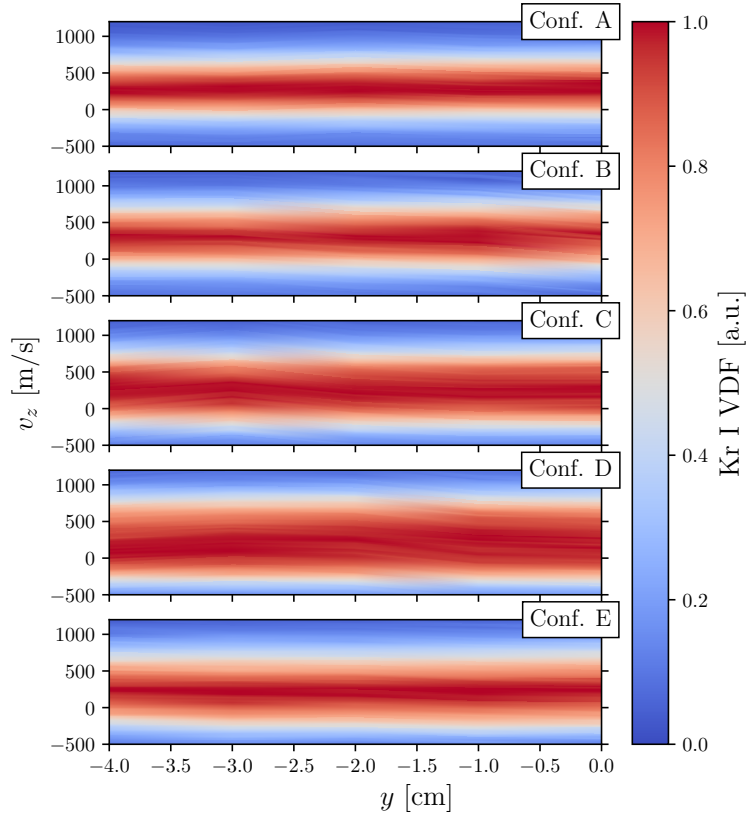


Figure 3.27: Kr I velocity distribution function for the five magnetic configurations measured along the y axis at $z = 12$ cm.

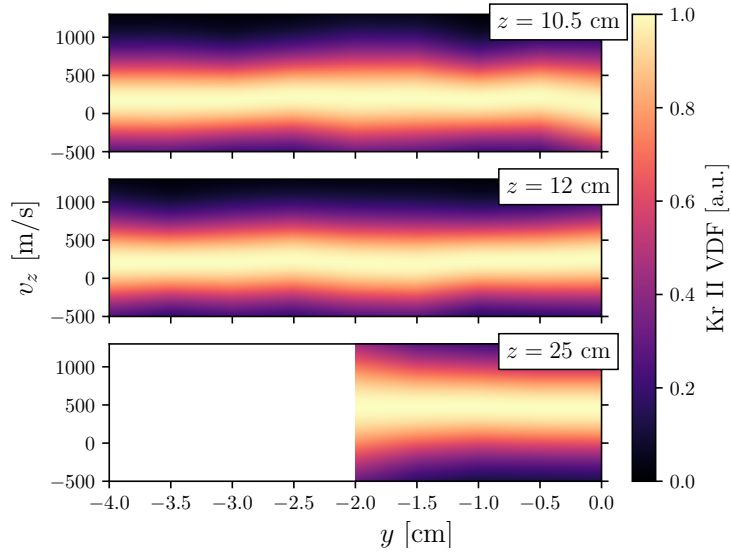


Figure 3.28: Kr II velocity distribution function for Conf. C measured along the y axis at $z = 10.5, 12$ and 25 cm.

3.2. PLASMA PROPERTIES CONDITIONED BY THE MAGNETIC THROAT LOCATION

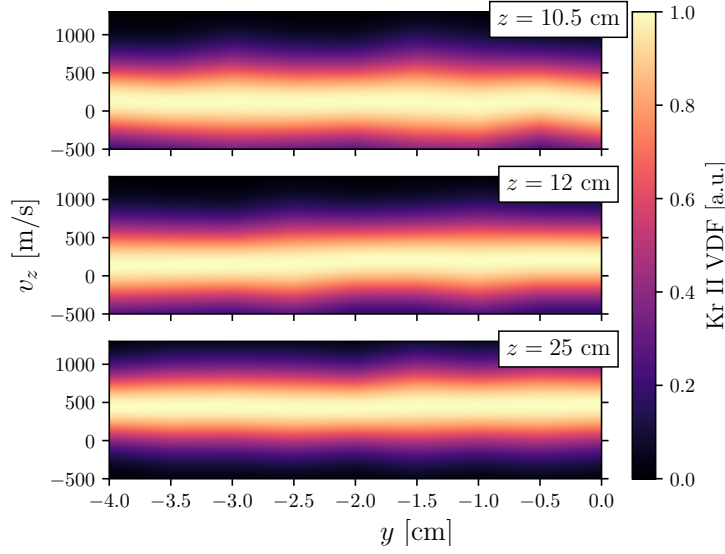


Figure 3.29: Kr II velocity distribution function for Conf. D measured along the y axis at $z = 10.5, 12$ and 25 cm.

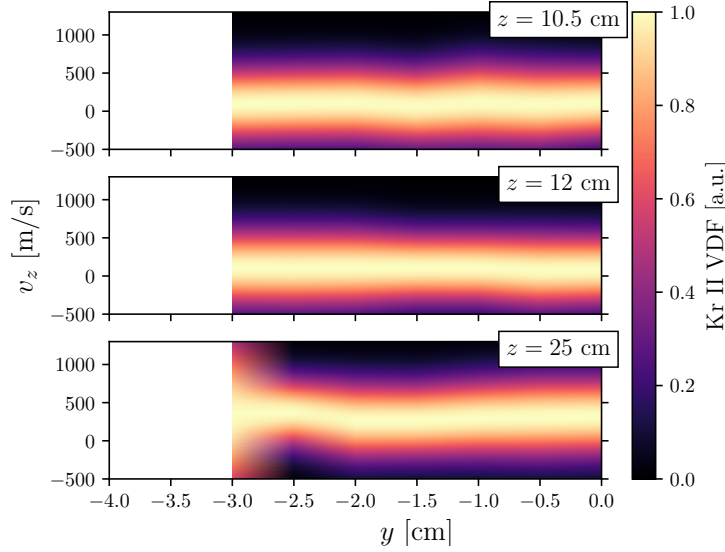


Figure 3.30: Kr II velocity distribution function for Conf. E measured along the y axis at $z = 10.5, 12$ and 25 cm.

Axial VDFs of Kr II are probed in the same radial region with a spatial resolution of 5 mm at three distinct axial positions, i.e. $z = 10.5$ cm, $z = 12$ cm and $z = 25$ cm. At some y locations, the LIF signal was not distinguishable from the background noise due to small local values of n_p , therefore mapping of the VDFs was not possible. For the very same reason, Conf.s A and B did not allow obtaining an appropriate signal-to-noise ratio in any of the probed locations. Raw VDFs are post-processed using a least squares Gaussian fit. The resulting profiles when the HP source operates in Conf.s C, D and E are reported in Figure 3.28, 3.29 and 3.30, respectively. In addition, the most probable velocity is extracted and plot in Figure 3.31 thus to facilitate compari-

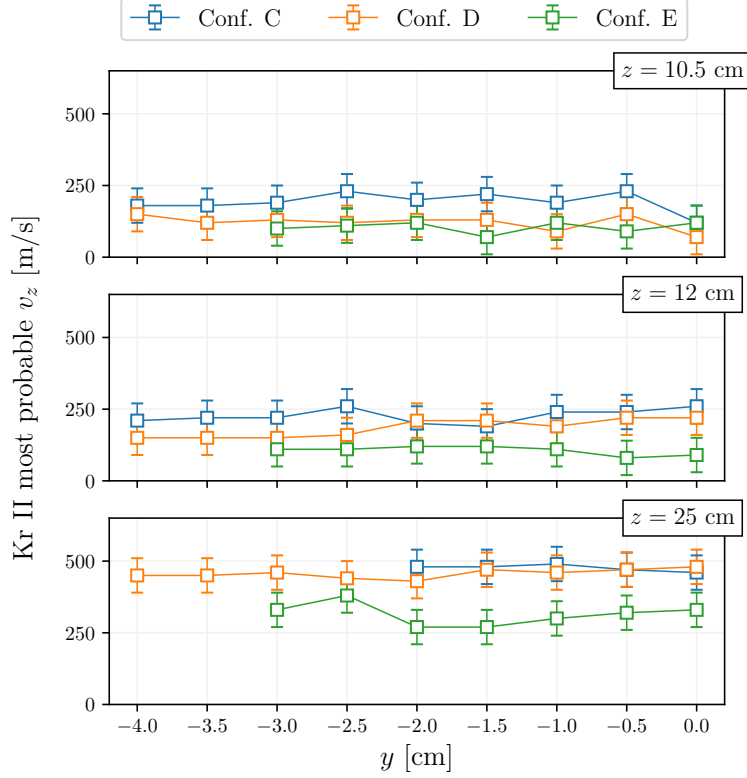


Figure 3.31: Kr II most probable axial velocity extracted from Figure 3.28-3.30. Error bar is 60 m s^{-1} (typical instrument absolute error).

son among the various magnetic configurations. It is noticed that the profiles related to Conf.s C and D feature a nearly identical trend, whereas the ion velocity in Conf. E generally retains lower readings. This is in agreement with the measured values of V_p which remain below those concerning Conf. C and D, cf. Figure 3.22. In the further upstream regions, namely $z = 10.5 \text{ cm}$ and $z = 12 \text{ cm}$, velocities smaller than $\sim 250 \text{ m s}^{-1}$ are measured, therefore in the order of the thermal velocity assuming $T_i \approx 300 \text{ K}$. Conversely, at $z = 25 \text{ cm}$, all the velocities increase by a factor of 2 to 3, reaching values as high as $\sim 500 \text{ m s}^{-1}$. These small velocities somewhat concur with the fact that the magnetic field is weakly divergent in the probed region for Conf.s C and D, while $z = 25 \text{ cm}$ represents the throat location for Conf. E. A weakly divergent magnetic field does not allow for a significant momentum gain imparted by the Lorentz force. Measurements farther downstream were prevented due to the limited size of the vacuum chamber. Similar small values of ion velocity are reported in [93] using LIF on a large scale HP source. In all of the magnetic configurations, the drop of V_p is fairly small (in the order of 1 V) within $z < 21 \text{ cm}$, cf. Figure 3.22. Considering Conf. E for instance, since at $z < 25 \text{ cm}$ the magnetic field is convergent, it is expected that the favored inward transport of electrons do not allow for a significant potential drop in this region. In the purely electrostatic case, a potential drop of $\sim 1 \text{ V}$ translates into an ion velocity increase of $\sim 1.5 \text{ km s}^{-1}$. Hence, the acceleration of the ions throughout the MN does not fully exploit the available energy. This phenomenon is related to some dissipation phenomenon, e.g. collisions, as later discussed. Moreover, although no sonic condition is achieved at the magnetic throat in Conf.s C and D, ions experience a further accel-

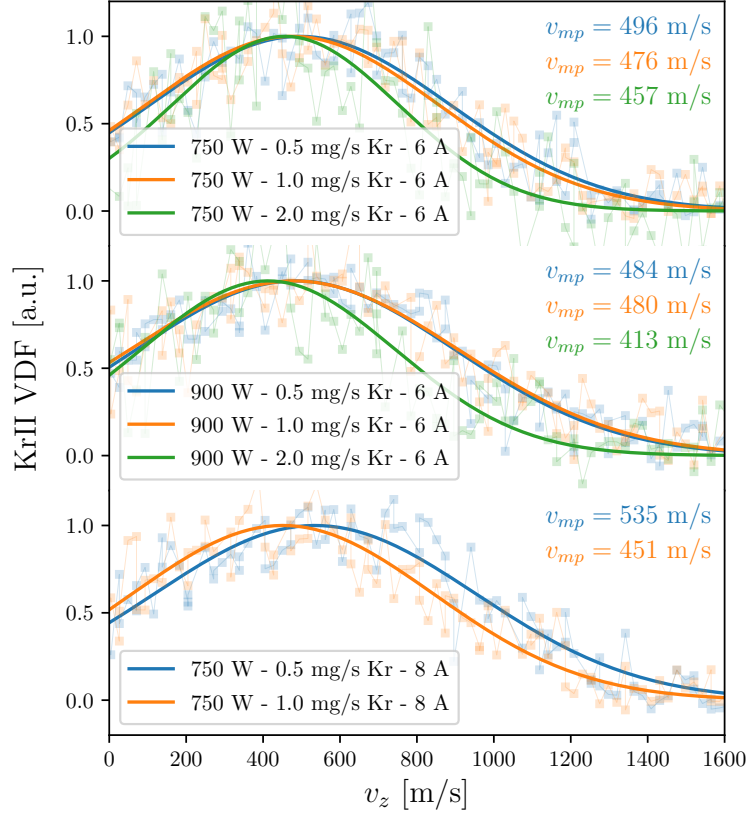


Figure 3.32: Kr II axial VDF for Conf. D at $z = 25$ cm as function of P_{IN} , \dot{m} and electromagnets current. Scatter points indicate raw data, solid lines exemplify least squares Gaussian fittings.

eration in the divergent part of the nozzle, see Figure 3.31. It suggests that the sonic point, if ever reached, is shifted downstream, in contrast with the ideal postulation of gas-dynamics-like plasma expansion [51]. In this experiment, the ions might reach the sonic speed only at the sheath edge that forms downstream between the chamber wall and the plasma plume. Numerous works focusing on modeling of magnetic nozzle dynamics have assumed that the ion Mach number equals unity at the throat [47, 94, 95]. Albeit this condition conveniently allows separating the processes of plasma generation and plasma acceleration, it is not representative in this case as well as in some other plasma beams [96, 97]. Collard *et al* [97] have examined a list of phenomena which are potentially responsible for separation of the magnetic throat and the sonic point, namely electron-neutral collisions, charge-exchange collisions and ionization within the plume. In the device herein analyzed, a combination of several dissipative phenomena is likely to contribute in introducing a drag force term that prevents the ions to reach the sonic speed. In Conf. C, for instance, a significant level of ionization is localized in the near-field plume downstream the magnetic throat, as previously noted when commenting on Figure 3.20. This suggests that the energy stored in the electrons is spent for ions generation rather than acceleration.

A parametric evaluation of the Kr II axial VDF is additionally performed at

$z = 25$ cm for the purpose of better grasping the mechanisms occurring within the nozzle. The exploited parameters are: input power (750 W and 900 W); mass flow rate (0.5 mg s^{-1} , 1 mg s^{-1} and 2 mg s^{-1}); current in the electromagnets (6 A and 8 A). The magnetic configuration is fixed to Conf. D for this experiment because of its divergent shape at $z = 25$ cm and larger signal-to-noise ratio with respect to Conf. C. The resulting VDFs are shown in Figure 3.32, which includes the raw data, the Gaussian fittings and the unfold most probable velocities obtained at each working condition. The overall tendency results clear. Indeed, higher ion velocities are attained as the mass flow rate decreases and the magnetic field is increased, whereas slower ions are recorded with larger mass flow rates. These outcomes suggest that collisions resulting from a larger pressure do play a role in the acceleration process. At lower pressures, a larger mean free path is expected, therefore allowing for greater values of T_e .

3.2.6 Summary and conclusion

In summary, several plasma properties are inferred via direct measurement. The magnetic throat is displaced along the reactor axis and the resultant plasma is studied in the near-field plume using electrostatic diagnostics and LIF spectroscopy. It is found that a low-current high-divergence plume is extracted from the plasma source when the magnetic throat is located upstream or in correspondence of the antenna center point. Plasma density measurements at the back plate emphasize that, in those cases, the generated plasma mainly remains within the discharge tube and is lost at the radial and back boundaries. Larger ion currents and higher confinement levels are attained when the magnetic throat is located downstream the antenna, namely at a distance at least equal to the wavelength corresponding to the first order axial mode of the helicon wave. The measured ion axial velocities exhibit small values of useful kinetic energy, being below the sonic condition at the magnetic throat. By measuring the most probable ion velocity obtained under different working parameters (input power, magnetic strength and mass flow rate), it is conjectured that ionization and collisions occurring in the near-field plume contribute to limiting the ion acceleration process.

3.3 Effect of magnetic nozzle divergence on ion and electron properties

As already stated in Section 3.2, the shape of the magnetic nozzle is presumably strongly linked to the amount of the input energy that can be usefully converted into axial thrust. Manipulation and integration of the axial momentum conservation equation leads to a quantitative expression of the magnetic thrust, i.e. the thrust obtained throughout the MN, which reads as [54]

$$T_B(z) = -2\pi \int \int r j_\theta B_r dr dz, \quad (3.12)$$

written for a cylindrical $r - z$ reference frame, where j_θ is the net azimuthal current density and B_r is the radial component of the magnetic field. It is evident that a larger divergence of the magnetic field, therefore a larger B_r , would enhance the axial momentum of the ions if j_θ remains unchanged. Yet, the azimuthal current, which is dominated

3.3. EFFECT OF MAGNETIC NOZZLE DIVERGENCE ON ION AND ELECTRON PROPERTIES

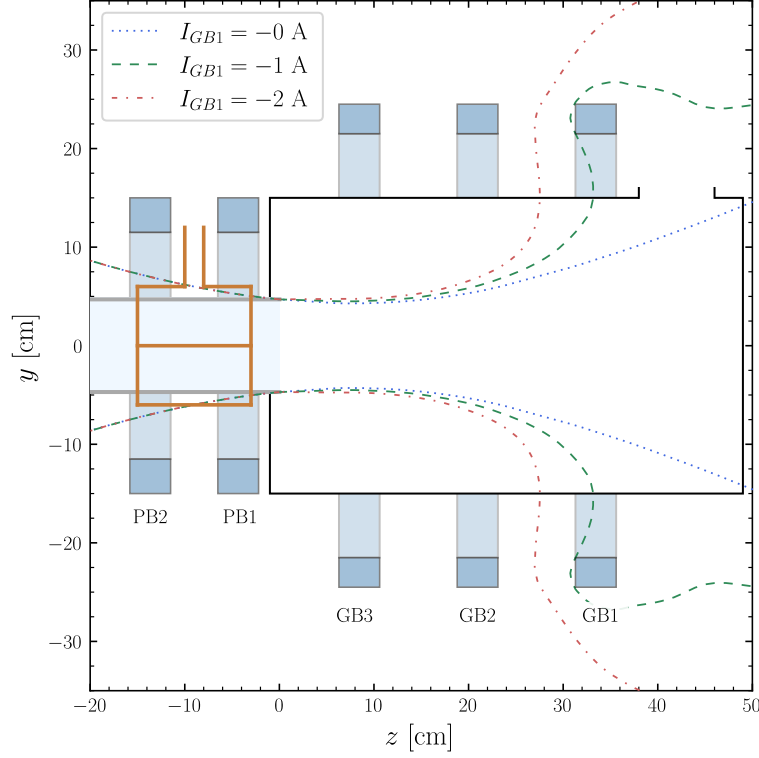


Figure 3.33: Magnetic field lines crossing the edge of the tube at $z = 0$. The different line styles refer to the different topologies in analysis.

by the electron contribution at these low values of the magnetic field [54], is influenced by the MN topology. A different radial gradient of B_z translates into a different radial gradient of electron pressure and plasma potential. This can be clearly seen through the radial component of the electron momentum equation in cylindrical coordinates:

$$j_{\theta_e} = j_{E \times B} + j_D = n_p e \frac{E_r}{B_z} + \frac{1}{B_z} \frac{\partial p_e}{\partial r}. \quad (3.13)$$

Hence, it is of interest to investigate the plasma properties conditioned by the divergence degree of the MN nozzle. A typical helicon device usually features a permanent magnets assembly or a simple coil. Both situations clearly do not allow for arbitrary selection of the nozzle divergence. On the contrary, the setup in use described in Section 2.1 comprises nine electromagnets which enable the selection of several desired topologies.

In general terms, the shape of the MN can be changed basically using two strategies: *i*) by physically moving the location of the electromagnets or *ii*) by playing with the current, in amplitude and sign, that flows in the coils. The second approach is employed here. Countless topologies can be obtained with the nine electromagnets available, yet it is chosen to limit the study to three relevant configurations. The electromagnet named GB3 is always powered with 9 A of DC current. It is responsible for the throat of the magnetic field. The current in the electromagnet named GB1, instead, is varied thus obtaining the three configurations: 0 A, -1 A and -2 A. A positive (negative) value of the current means that the generated B field points along the +z (-z) direction. Each set of currents generates a different shape of the MN whose divergence increases together with

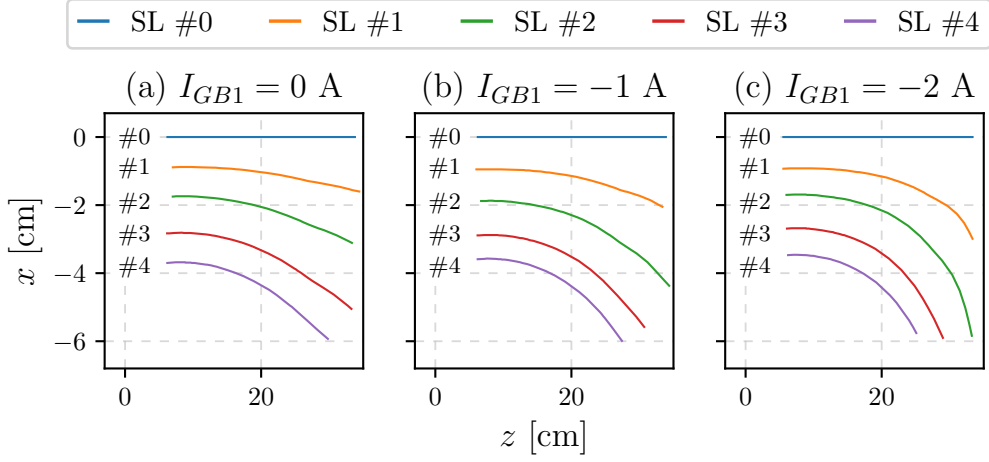


Figure 3.34: Magnetic nozzle streamlines for three different cases. The throat is fixed at $z = 8.5$ cm. The nozzle divergence is tuned using different values of I_{GB1} , whereas $I_{GB3} = 9$ A. The color code of the streamlines (SLs) is consistent with that of Figure 3.39

the absolute value of I_{GB1} . The peak strength of B is 8.6 ± 0.3 mT in correspondence of GB3. At $z \simeq 30$ cm, the on-axis value of B_z is about 2 mT, 1 mT and 0 mT for the three conditions $I_{GB1} = 0, -1, -2$ A, respectively. Figure 3.33 exemplifies the magnetic streamlines crossing the tube edge at $z = 0$ for the three magnetic configurations. In addition, selected streamlines are represented in Figure 3.34. Every streamline (SL) is numbered and associated with a color which is used afterward for the interpretation of measurement outcomes discussed in Section 3.3.3. The numbering is also included beside each SL within the plots for the sake of clarity. As an example, the on-axis SL is numbered #0 and associated with the blue color, cf. Figure 3.34.

During the whole experimental campaign, the helicon reactor operates with a mass flow rate of $\dot{m} = 0.2 \text{ mg s}^{-1}$ Xe and input power of $P_{IN} = 800$ W.

3.3.1 Spatially resolved plasma properties

For the purpose of studying the electron thermodynamics along the magnetic SLs, the RFCLP described in Section 2.2.3 is displaced in the region $-6 < x < 0$ cm and $0 < z < 30$ cm to resolve the electron properties. The I-V curves are recorded with a spatial resolution of 5 mm along z and 10 mm along x . Data post-processing involved the use of OML theory to retrieve n_p and T_e , along with a smoothing algorithm based on a dynamic Savitzky-Golay filter. The resulting normalized $(x - z)$ profiles of n_p and T_e are shown in Figure 3.35 and Figure 3.36, respectively. Normalization factors are $4 \times 10^{17} \text{ m}^{-3}$ for n_p and 5.5 eV for T_e . The dashed black lines included in each plot reproduce the magnetic SLs as previously displayed in Figure 3.34. Figure 3.35 shows that the expanding plasma features a high density region along the HP source axis along with high density conics, which are often observed in other experiments [33, 75, 98]. In the $z \lesssim 10$ cm domain, the density increases due to the increasing magnitude of the external magnetic field. Regardless of the MN shape, the highest value of n_p is located off-axis. Yet, the density peak moves upstream as the MN divergence is increased. As a matter of fact, with reference to Figure 3.35, the maximum of n_p is observed at (a) $z \simeq 17$ cm, (b) $z \simeq 13$ cm and (c) $z \simeq 10$ cm. A positive density gradient beyond the

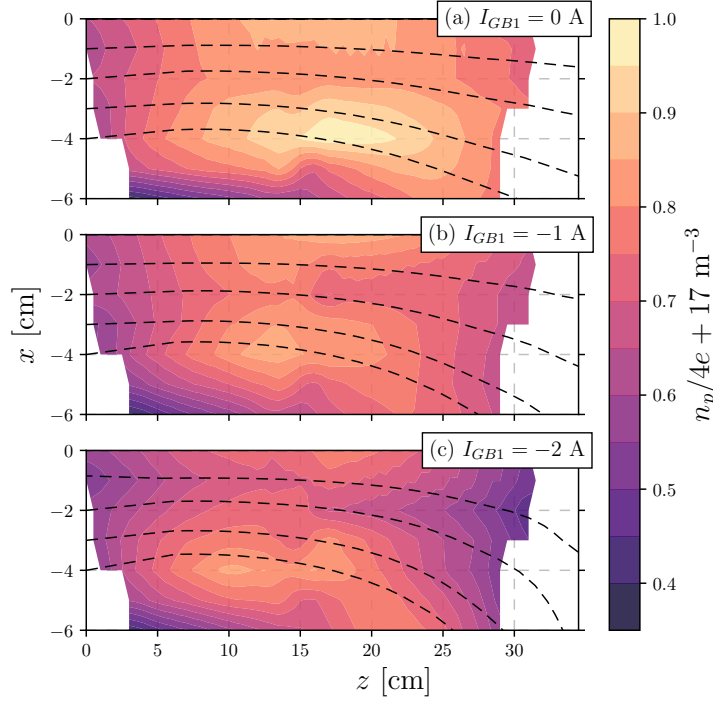


Figure 3.35: Contour plots of normalized plasma density for the three tested shapes of the MN. The normalization factor is $4 \times 10^{17} \text{ m}^{-3}$. Dashed black lines represent the magnetic SLs.

magnetic throat is likely linked to pressure balance effects as analyzed in [32] where the plasma source was operated under similar conditions. Furthermore, the spatial evolution of the high density conics largely resembles the shape of the MN, highlighting that the electrons are visibly magnetized in all of the studied configurations.

Similar comments can be drawn concerning the electron temperature profiles in Figure 3.36. Relatively higher temperature electrons are localized on-axis and at the external surface of the MN. T_e is larger in the latter region regardless of the MN shape. Some works associate the presence of higher energy electrons at the edge of the MN to heating phenomena near the rf antenna and transport along the SLs [99]. The region at $z \lesssim 10 \text{ cm}$ is visibly unchanged albeit the MN is differently shaped, cf. Figure 3.36(a-c). It suggests that the discharge process inside the source tube is not deeply influenced by the downstream conditions. At $z > 10 \text{ cm}$, in contrast, the maps of T_e exhibit important dissimilarities owing to the different shape of the MN. Consistently to what is observed in Figure 3.35, the spatial evolution of T_e similarly resembles the computed magnetic SLs, further hinting that the electrons are strongly magnetized.

3.3.2 Ion energy influenced by the magnetic nozzle shape

For analyzing the evolution of the ion energy along the nozzle axis as its divergence is varied, the RPA detailed in Section 2.2.6 is employed. The probe is displaced in the region $13 < z < 28 \text{ cm}$ so that the ion energy distribution function is spatially resolved with a resolution of 5 mm. It is assumed that derivation of the I-V characteristic images the local IEDF, i.e. $f(E_i) \propto dI_i/dV$, where E_i is the total ion energy (kinetic and potential). Results are shown in Figure 3.37. It is observed that, in all cases, the decay of

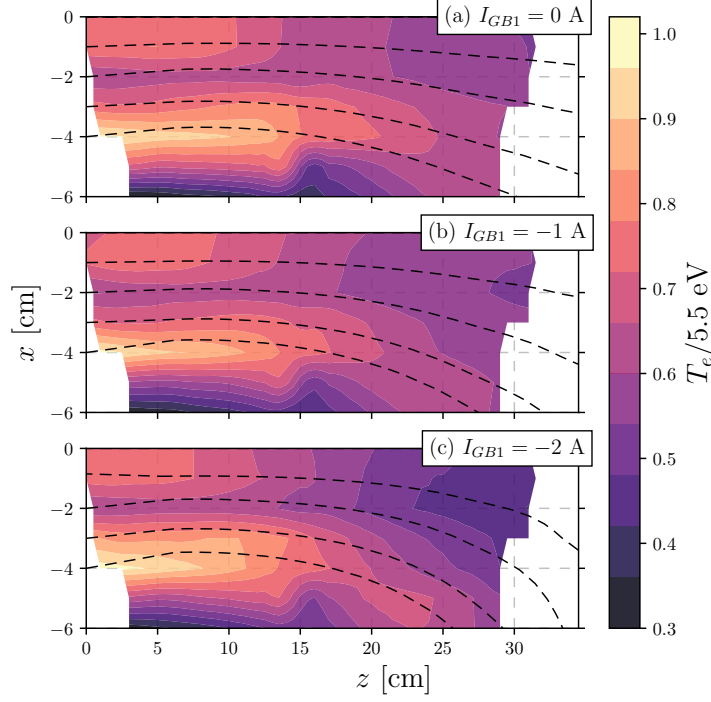


Figure 3.36: Contour plots of normalized electron temperature for the three tested shapes of the MN. The normalization factor is 5.5 eV. Dashed black lines represent the magnetic SLs.

E_i with z is nearly linear. Furthermore, E_i decreases as the magnetic nozzle divergence increases. It therefore appears that the ultimate ion energy is not improved as the magnetic nozzle is enhanced. It shall be highlighted that in the present plasma source, and especially at these relatively small axial distances, the typical plasma potential is in the order of 10 V whereas the order of magnitude of the ion kinetic energy reads 0.1 V, see Section 3.2.

3.3.3 Electron thermodynamics along magnetic nozzle lines

The data mapped in the MN as shown in Figure 3.35 and Figure 3.36 is used for a more detailed analysis of the electron flow properties. The evolution of the electrons is often modeled with a polytropic state equation,

$$T_e / n_p^{\gamma_e - 1} = C(\psi), \quad (3.14)$$

where γ_e is the polytropic index and C is constant along a characteristic magnetic surface ψ . Note that T_e is in general an effective value of the electron energy. In the present case, T_e can be computed as discussed in Section 2.2.3 since the EEPF remains nearly Maxwellian as exemplified in Figure 3.38. Assuming that the electron inertia is negligible and the electrons are fully magnetized, the magnetic SLs coincide with the electron flow SLs [101]. Hence, the polytropic law is evaluated along the (x, z) coordinates that define the computed magnetic SLs. In order to evaluate (n_p, T_e) at the exact same point $[x, z]$ belonging to the magnetic SL, the experimental maps are numerically interpolated by means of a linear method. Given that n_p increases in the upstream portion of the probed domain, cf. Figure 3.35, the data of this region is disregarded. In other terms,

3.3. EFFECT OF MAGNETIC NOZZLE DIVERGENCE ON ION AND ELECTRON PROPERTIES

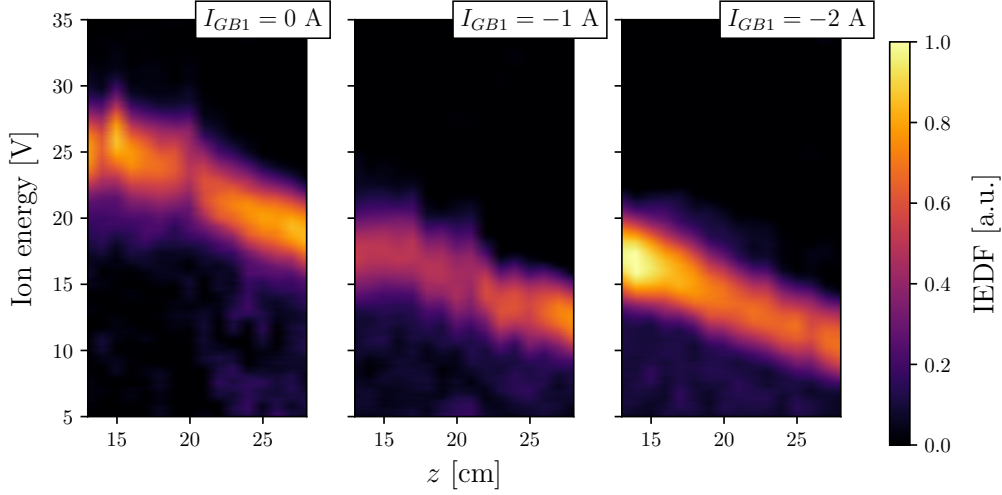


Figure 3.37: On-axis evolution of the ion energy distribution function for the three tested shapes of the MN.

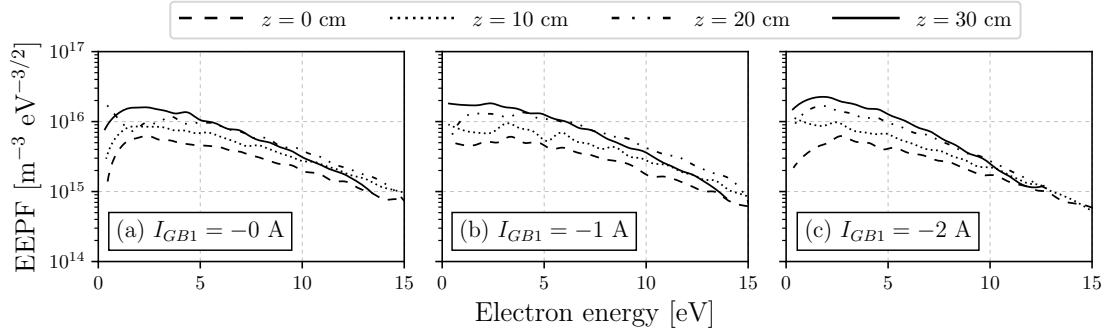


Figure 3.38: On-axis evolution of the electron energy probability function for the three tested shapes of the MN. Curves are computed using the Druyvesteyn method as reported in [100]. The slope of the EEPF steepens at larger values of z implying cooling of the electrons.

only the region where $\nabla n_p < 0$ is considered as the focus here is to analyze the expansion process. Eventually, the polytropic index γ_e is inferred using a linear regression of the $\log_{10}(T_e)$ vs. $\log_{10}(n_p)$ datasets. Figure 3.39 gathers the results obtained evaluating γ_e along the magnetic SLs previously shown in Figure 3.34 for each of the studied MN shapes. The colors in Figure 3.39 are consistent with those in Figure 3.34, thus allowing to identify the magnetic SL that corresponds to each set of scatter points and fitting lines.

Interestingly, γ_e has dissimilar values along distinct SLs. Furthermore, in some cases it reads $\gamma_e > 5/3$ (adiabatic value with $N = 3$ degrees of freedom) and each of the magnetic nozzles being tested features a unique structure of γ_e . Indeed, as evident from Figure 3.39(a), the polytropic index in the first MN ranges from $\gamma_e \simeq 1.3$ along SL#2 to $\gamma_e \simeq 1.8$ along SL#0 and SL#4. In Figure 3.39(b), instead, the smallest value $\gamma_e \simeq 1.4$ is found along SL#0 and SL#1 whereas the maximum $\gamma_e \simeq 1.8$ occurs along SL#3 and SL#4. Figure 3.39(c) manifests a further different case in which $\gamma_e \simeq 1.4 - 1.5$ regardless of the SL. The cases $\gamma_e \simeq 2$ imply that the degrees of freedom of electrons can be

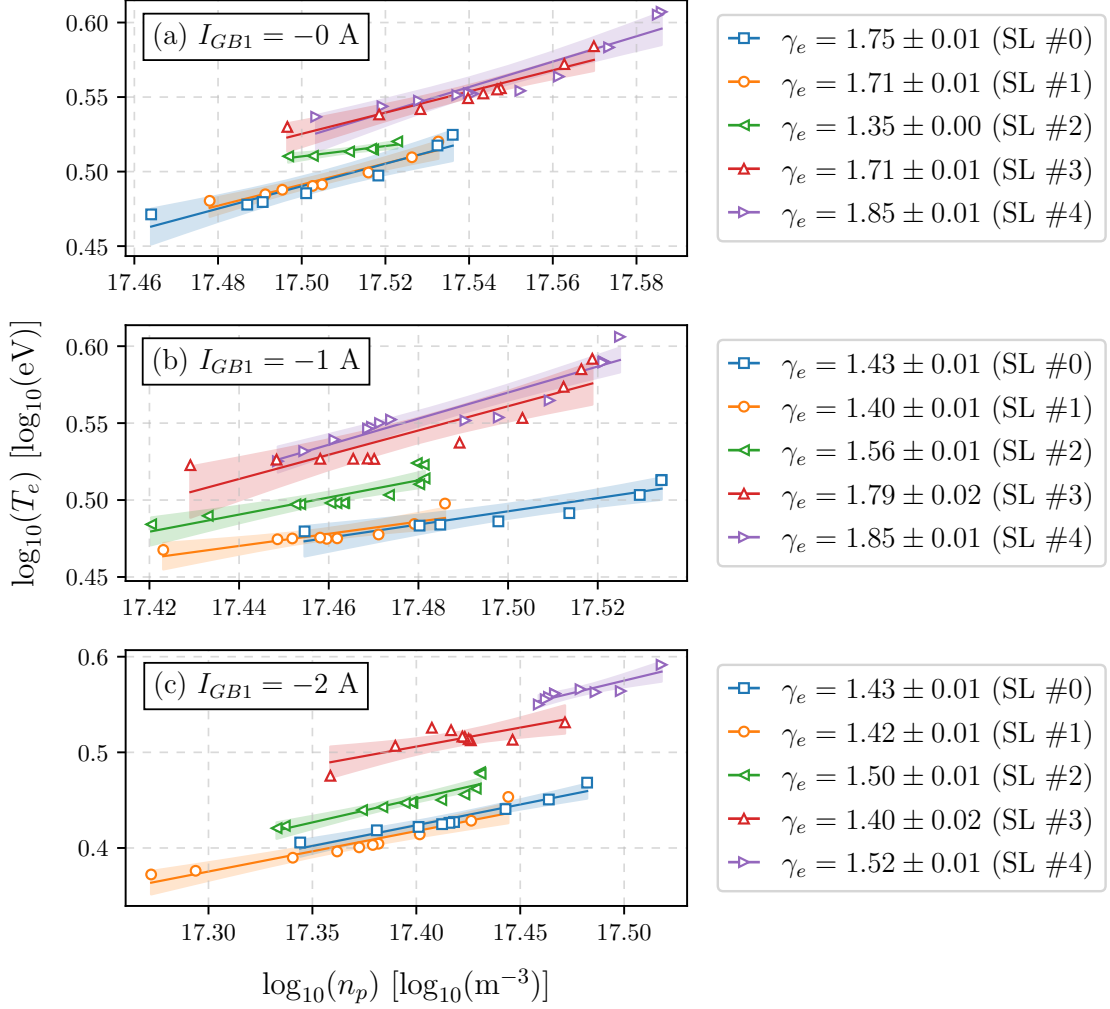


Figure 3.39: Electron cooling rate evaluated along the magnetic streamlines for three different magnetic nozzle shapes (a)-(c). The color code relates to Figure 3.34 to identify the SL corresponding to each dataset. Scatter points represent the interpolated experimental data. Solid lines are the least square linear regressions used to compute γ_e . Colored areas render the 95 % confidence interval of the Students t-distribution.

reduced to 2, while $\gamma_e < 5/3$ would suggest the presence of heat flux within the MN under the hypothesis of local thermodynamic equilibrium (LTE). The study reported in [102] shows that strongly non-Maxwellian EEPF yields an adiabatic expansion with $\gamma_e \approx 1.17$ in a collisionless regime. However, nearly Maxwellian electrons are found in the present experiment thereby collisionless phenomena are not of primary relevance here. Moreover, the theory developed in [89] fails to predict the values of γ_e observed in this experiment. By using the Spitzer resistivity [103] for the thermal conductivity, the estimation of the Nussel number based on the experimental data yields $Nu \sim 10^{-3}$. This would translate into $\gamma_e \approx 1.2$ according to [89] which does not agree with the actual observations. Burm *et al.* [104] suggest that the ionization process serves as an additional degree of freedom in plasma adiabatic expansions. Using the formulation provided in [104] for a monoatomic plasma in non-LTE, i.e. $T_i \neq T_e$ and different

3.3. EFFECT OF MAGNETIC NOZZLE DIVERGENCE ON ION AND ELECTRON PROPERTIES

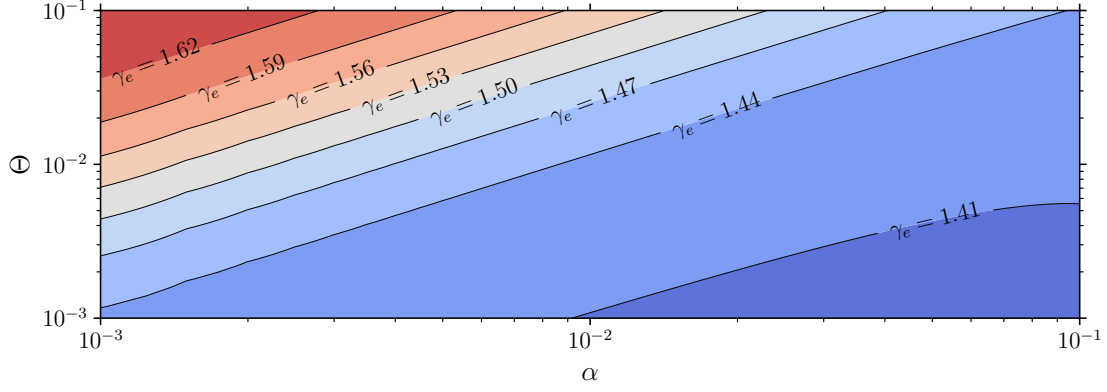


Figure 3.40: Value of γ_e computed from Equation 3.15 as function of Θ and α for $T_e = 4$ eV.

ionization degree with respect to Saha equilibrium, the value of γ_e is computed as

$$\gamma_e = \frac{c_p}{c_V} \frac{2\Theta + (1 - \Theta)\alpha}{2\Theta + (1 - \Theta)\alpha + (1 - \alpha)\alpha} \quad (3.15)$$

where $\Theta = T_i/T_e$ is the ions to electrons temperatures ratio and $\alpha = n_p/n_n$ is the plasma to neutrals density ratio. The expressions for the heat capacity at constant pressure c_p and constant volume c_V read [104]

$$c_p = \frac{5}{2} \frac{R}{\Theta} (\Theta + \alpha) + \frac{\alpha R}{\Theta} \frac{(1 - \alpha)(\Theta + \alpha)}{2\Theta + (1 - \Theta)\alpha} \left(\frac{5}{2} + \frac{\varepsilon_{ion}}{k_B T_e} \right)^2 \quad (3.16)$$

$$c_V = \frac{3}{2} \frac{R}{\Theta} (\Theta + \alpha) + \frac{\alpha R}{\Theta} \frac{(1 - \alpha)(\Theta + \alpha)}{2\Theta + (1 - \Theta)\alpha + (1 - \alpha)\alpha} \left(\frac{3}{2} + \frac{\varepsilon_{ion}}{k_B T_e} \right)^2 \quad (3.17)$$

where R is the universal gas constant and ε_{ion} is the first ionization energy of the propellant. The implementation of this theory yields $\gamma_e \simeq 1.3 - 1.5$ for $T_e = 3 - 6$ eV on the basis that $\Theta \sim 10^{-2}$ and $\alpha \sim 10^{-2}$ in the present experiment. However, the result of Equation 3.15 is not dramatically affected by small variations in Θ and α compared to the fitting confidence intervals in Figure 3.39, as exemplified in Figure 3.40. This means that very dissimilar values of γ_e in this experiment cannot be attributed to small local variations in Θ or α . The value of the polytropic index computed with Equation 3.15 agrees well with most of the findings shown beforehand in Figure 3.39. This effectively suggests that ionization within the plume does occur, as previously pointed out in other experiments using a MN [33, 97] and Hall thrusters [105]. Nonetheless, this scenario might not be representative in the far-field region. As collision frequencies drop and α approaches unity, other phenomena besides ionization such as collisionless cooling [55] likely become predominant.

Although the ionization process can clarify the occurrence of $\gamma_e < 5/3$, the physical phenomenon that makes $\gamma_e > 5/3$ has to be investigated. In a simplified picture, the dynamics of electrons in the MN primarily results from the forces associated with the external magnetic field and the spontaneous electric field. As hinted in [106, 107], the radial electric field in the plasma can profoundly affect the transport across the magnetic lines. In [107], relatively high potential regions concentrated off-axis identify a radial electric field which effectively withdraw the degree of freedom related to the motion

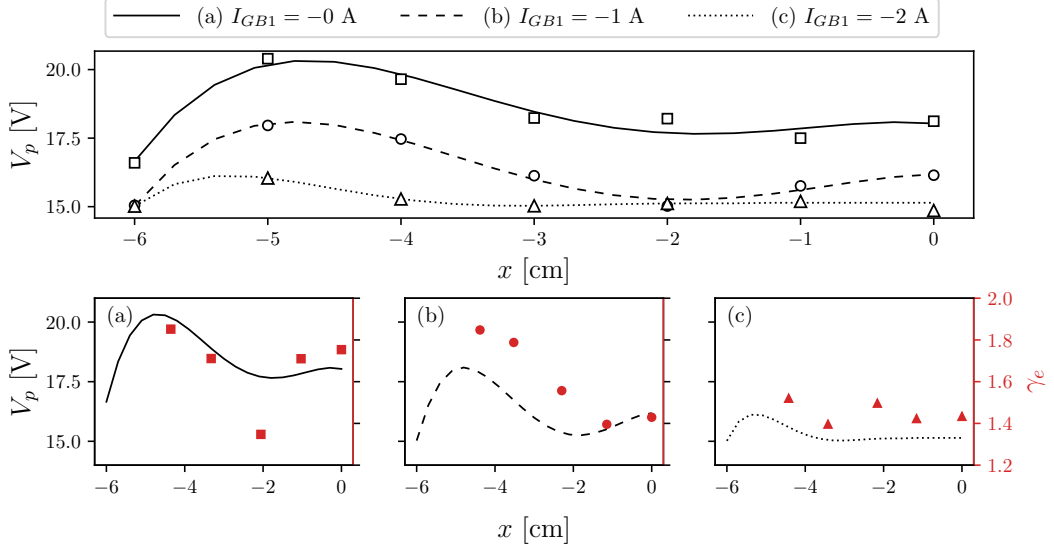


Figure 3.41: Radial distribution of plasma potential V_p and polytropic index γ_e at $z = 20$ cm for three different magnetic nozzle shapes (a)-(c). Upper graph: scatter points represent experimental data; lines are computed polynomial fitting curves. Bottom graphs: lines reproduce V_p from the upper plot to enhance visualization (left/black axis); scatter points represent the value of γ_e for each magnetic SL crossing $z = 20$ cm (right/red axis). The bottom graphs share the same scale on the vertical axes for better comparison.

perpendicular to \mathbf{B} . A correlation between the radial V_p and γ_e is therefore requested in the present experiments. The profile of V_p at $z = 20$ cm is retrieved from the measured I-V curves and smoothed as shown in Figure 3.41(top) for the three shapes of the MN. By determining the radial coordinate where each magnetic SL crosses the section at $z = 20$ cm, the resulting V_p and γ_e radial profiles are compared in Figure 3.41(bottom). It is found that the two quantities follow a similar qualitative trend along the x axis. As V_p experiences a relatively large variation in the radial direction, so does γ_e , cf. Figure 3.41(a)-(b). Likewise, a nearly flat profile of V_p produces a small variation in γ_e , as shown in Figure 3.41(c). At this stage, two points shall be addressed when comparing the studied MNs: (i) the different behavior of γ_e in the proximity of the MN axis; (ii) the relatively large γ_e close to the plasma potential peak. The formulation of a comprehensive theory is beyond the purpose of this paper, hence only a few possible explanations are provided in the following.

A value of $\gamma_e > 5/3$ close to $x = 0$ is found only for the first MN, cf. Figure 3.41(a). This is possibly linked to a more intense magnetic field considering that $\|\mathbf{B}\| \approx B_z$ spans from about 6 mT in case (a) down to 4 mT in case (c). Differently, an increase in γ_e along with V_p is observed in all cases of Figure 3.41(bottom), reaching $\gamma_e \approx 1.7 - 1.9$ in Figure 3.41(a-b). A larger γ_e where V_p is higher seems at odds with the claims in [106, 107]. In the region where the plasma potential is large, rather than owing to the radial electric field, the cross-field electron transport is more likely reduced because a large conductivity ensues in the direction parallel to \mathbf{B} which strongly promotes the longitudinal transport. This is supported by considering that T_e is higher where V_p is larger and that the cross-field diffusion coefficient $D_\perp \sim (k_B T_e)^{-1/2}$ [103], therefore D_\perp decreases in the high temperature region. It is worth stressing that $\gamma_e \approx 2$ implies a 2-D

electron motion, which is therefore reduced to transport along the \mathbf{B} lines and rotation around them. In extension to the results reported in [106, 107], the present findings suggest that the analysis of the electron cooling dynamics in a MN cannot be addressed regardless of the plasma properties radial profiles throughout the nozzle inlet which are in turn linked to the discharge process.

Nevertheless, it must be emphasized that under the hypothesis of a single isotropic electron fluid, the magnetic field cannot directly modify the number of degrees of freedom [52, 108]. The latter are instead determined by the kinetic nature of the dynamics. The presence of the external magnetic field would contribute to the complexity of the species dynamics, i.e. multiple populations, instabilities and anisotropies might arise thus turning the original assumption behind the concept of γ_e unrealistic. These phenomena and their occurrence are still not fully understood, therefore new and more detailed experimental evidence shall be sought.

Ultimately, a comment is due with regards to the boundary conditions of the plasma studied in this experiment. The interaction between the plasma plume and the vacuum chamber is typically unimportant. However, the diameter of the expansion chamber is about twice that of the plasma column in this case. The metallic walls of the chamber represent both a constant zero-potential boundary and a conductive medium within which closure of internal plasma currents can in principle occur. The latter effect might affect the internal plume structure. Furthermore, the plasma may be thermally connected to the relatively cold walls, thus implying the presence of a heat flux towards the system boundaries. In this experiment, plasma properties are intentionally inferred within a relatively small domain away from the chamber walls in order to downplay all of the aforementioned effects. Yet, their quantitative assessment represents a further challenge in the experimental process which definitely deserves future investigation.

3.3.4 Summary and conclusion

This experimental campaign shows that a MN with smaller divergence produces ions with higher energy and higher density. Lower ion energy qualitatively means lower ion velocity. Yet, a quantitative evaluation using LIF spectroscopy would provide a clearer insight. For the purpose of this particular experiment, access to a 2D LIF is even more attractive although being more complex. Measurements of the azimuthal current density, e.g. using a Hall probe, would further clarify the whole picture.

Moreover, the electron cooling rate is experimentally analyzed along the magnetic streamlines while the shape of the magnetic nozzle is varied. The simplest scenario describing an electron flow with 3 degrees of freedom does not provide an accurate picture of the plasma expansion in the present experiment. The introduction of the ionization as an additional degree of freedom allows to better predict the value of the polytropic index for some plasma conditions. In general, the electron polytropic index is observed to be inhomogeneous in space, which emphasizes the prevailing complexities of the MN expansion mechanisms. It is observed that a reduced cross-field transport possibly due to a large longitudinal conductivity can effectively reduce the electrons degrees of freedom (from 3 to 2).

This study represents a first effort in investigating the electron cooling process in a 2-D domain, therefore going beyond the routine analysis performed along the MN axis. The results herein reported are deemed of relevant interest for the purpose of predictive modeling. Nevertheless, additional experimental studies shall be addressed on different

kind of devices, e.g. electron cyclotron resonance thrusters, as well as on different scales in order to better identify the phenomena driving the electron cooling dynamics in a magnetic nozzle.

3.4 Effect of electron-cyclotron resonance on the electron flow in the magnetic nozzle

In order to maximize the momentum gained by the ions throughout the MN, efforts should focus on: *i*) reducing the fraction of neutrals in the plume which represent a drag contribution via collisions [97, 109]; *ii*) maximizing the thermal energy at the MN inlet available for conversion into ion kinetic energy. Accordingly, the key parameter that inherently rules the MN phenomena is the electron temperature T_e . Values of T_e up to tens of eV have been recorded in ECRTs [49, 110] at very low input power, whereas in rf discharges it seldom exceeds 10 eV. As a matter of fact, microwave devices can provide larger thrust efficiency at much lower power levels with respect to rf-based thrusters, whose competitiveness instead manifests in the kW range [38]. However, implementation of electrodeless ECR systems on-board of small spacecrafts might not be trivial, given the state-of-the-art of microwave power units [111–117]. This could be particularly true whenever the required input power exceeds tens of W and the system size is reduced, which translates into operating frequencies above 5 GHz [50]. Theoretically, though, it is possible to combine rf power and electron-cyclotron resonance in one single device without resorting to microwave sources, provided that the external magnetic field meets the ECR condition while the discharge stability is not compromised. At the typical rf operating frequency, i.e. 13.56 MHz, a magnetic field intensity equal to $B_{res} = \omega_{ce} m_e / e \simeq 0.484$ mT satisfies the resonance condition. This approach has been previously studied for plasma processing applications in an inductive discharge [118, 119] reporting effective heating of low energy electrons due to anomalous skin effect. Thus far, a similar approach applied to MN for propulsion purposes remains completely unexplored.

This study investigates how electrons in a MN are influenced when the ECR condition is met near the rf antenna. Measurements are performed in the helicon plasma source detailed in Section 2.1. Only two among the nine coils are powered in this experiment. Following the nomenclature of Figure 2.2, the first one, named GB2, is located at $z = 19$ cm and serves to generate the MN downstream the tube exit. The second one, named PB3, is located at $z = -25$ cm and it allows shaping the field topology inside the source. For the purpose of this analysis, two types of topologies are tested, as exemplified in Figure 3.42:

1. a simple magnetic nozzle as reference case, depicted in Figure 3.42(top). It is obtained setting $I_{GB2} = 9$ A and $I_{PB3} = 0$ A;
2. a specific configuration featuring a separatrix inside the source, see Figure 3.42(bottom). The same MN shape is preserved downstream the tube exit while the ECR condition is met near the antenna center. The coils currents are $I_{GB2} = 9$ A and $-5 < I_{PB3} < -1$ A.

A positive (negative) value of the coils current indicates that the relative B field points along the $+z$ ($-z$) direction. As the value of I_{PB3} is varied, the resonance region shifts

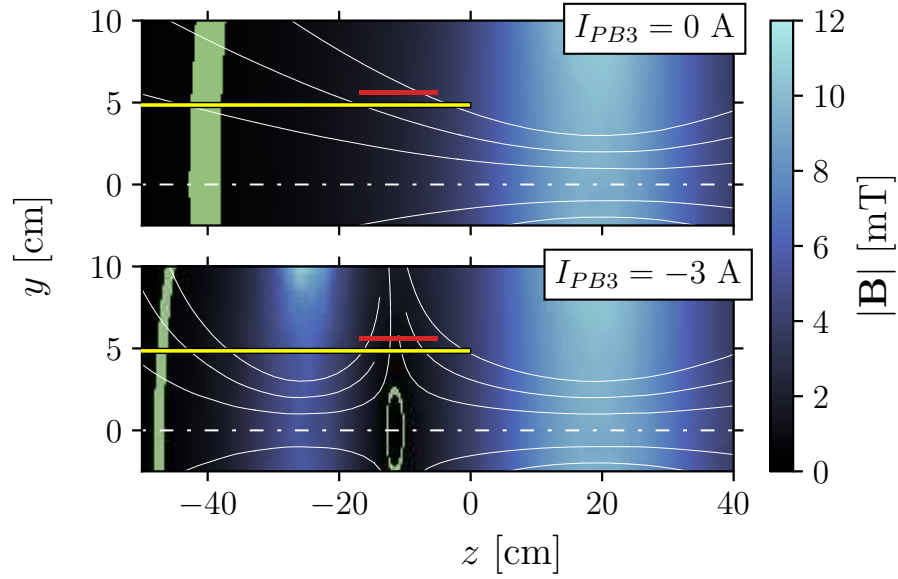


Figure 3.42: 2-D maps of the external magnetic field. The yellow rectangle depicts the source tube, whereas the red line identifies the antenna location. Magnetic streamlines are shown as white solid lines. The green pixels highlight the location where $|B|$ equals the resonance value ($\pm 10\%$).

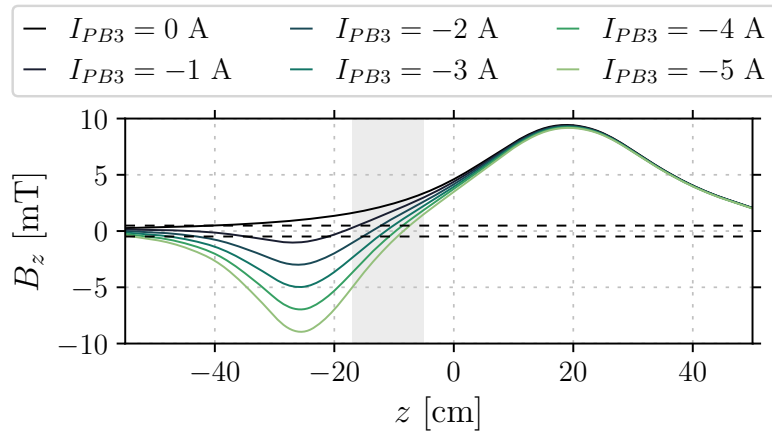


Figure 3.43: On-axis z -component of the external magnetic field for different values of I_{PB3} . The current flowing in GB2 is fixed to 9 A. The gray shaded area indicates the antenna region, while the black dashed lines identify the resonance value of the magnetic field strength.

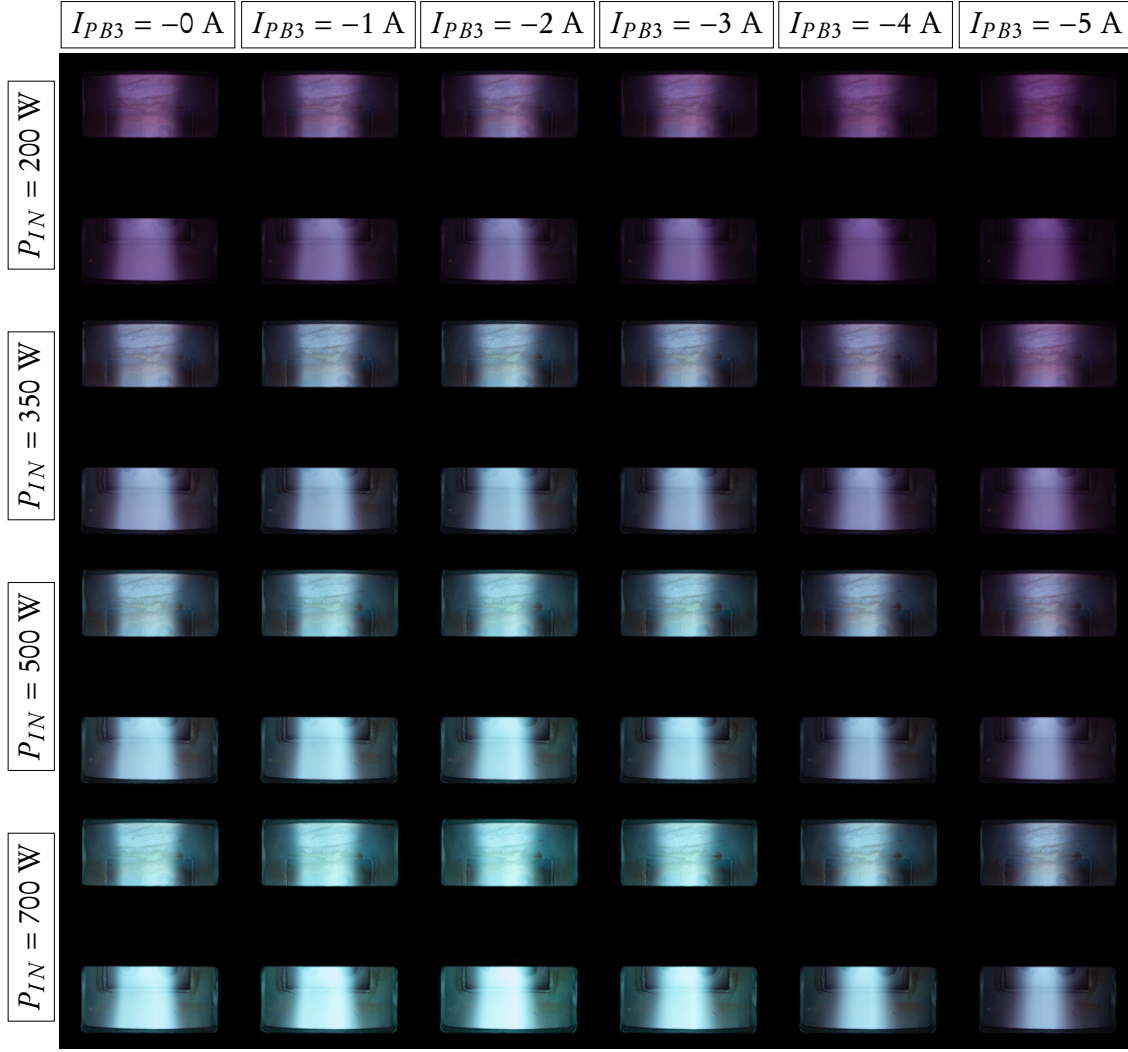


Figure 3.44: Photographs (f/8, 1/30 s) of the plasma plume in the region $8 < z < 28$ cm. Rows and columns of the matrix are associated with a specific value of P_{IN} and I_{PB3} , respectively.

along the tube axis. This is directly visible in Figure 3.43 which reports the axial profile of the magnetic field. In the general case of rf discharges when no resonance is required, an ECR region is present far upstream and far downstream, where a negligible amount of energy is deposited [120]. When PB3 is powered with a negative current, an additional resonance surface appears within the volume defined by the antenna, as desired. This simple reshaping of the field topology can conceivably underlie an enhancement of the electron properties.

It shall be remarked that, according to the generalized theory, typical helicon plasmas allow two wave modes to couple the antenna electromagnetic field, namely the helicon (H) and Trivelpiece–Gould (TG) modes [25]. However, when the external magnetic field is relatively weak, which is the case in this experiment to achieve ECR condition, only TG modes solve the dispersion relation. Hence, the discharge in analysis is most likely sustained in inductive mode with propagating TG waves, although H waves could in principle propagate downstream the antenna where magnetic field intensity and plasma density increase.

3.4.1 Electron properties in the magnetic nozzle

The experiment primarily consists in careful measurements of the electron energy probability function (EEPF) $f(\varepsilon)$ as the main external parameters are varied, namely input power P_{IN} , mass flow rate \dot{m} and I_{PB3} . The RFCLP detailed in Section 2.2.3 is used. In this experiment, the probe is oriented parallel to the magnetic field. I-V characteristics are recorded on-axis at $z = 0$ and $z = 31.5$ cm. Voltage sweep and current measuring are performed using a calibrated Keithley 2450 SourceMeter with about 15 Hz in step frequency. The EEPF is computed using the Druyvesteyn method [100, 121] and, accordingly, the electron density n_e and effective electron temperature T_{eff} are derived from the distribution function moments. The full probe characteristic, that is without subtraction of the ion current, is used for differentiation and inference of the EEPF because of the issues discussed in [122]. Note that the magnetic field at the two probed locations is weak enough to guarantee an electron Larmor radius larger than the probe length, so that the classical Druyvesteyn theory applies [121].

Figure 3.44 is an array of photographs showing how the plasma beam appears when P_{IN} and I_{PB3} are varied. Regardless of the input power, the plasma plume becomes brighter around $I_{PB3} \simeq -2$ A. The color is also more greenish that certainly indicates a larger ionization degree and excitation of high-energy atomic optical transitions. This observation qualitatively indicates enhanced plasma properties when the ECR condition is met near the antenna.

Parametric EEPFs measured at $z = 0$ are shown in Figure 3.45 and Figure 3.46 as a function of input power and mass flow rate, respectively. To a large extent, electrons exhibit a clear Maxwellian behavior in all cases. One can observe that, as I_{PB3} is decreased in magnitude, electrons experience an effective heating. Indeed, the EEPF changes slope, favoring higher electron energies. This phenomenon is more pronounced at larger input powers and lower mass flow rates because the fraction of neutrals decreases and the collision frequency drops. By integrating the distribution function, n_e and T_{eff} are derived and shown in Figure 3.47 and Figure 3.48 in terms of percentage change with respect to the simple nozzle configuration. Absolute values, instead, are reported in Figure 3.49 for $I_{PB3} = 0, -3$ A, where the plasma potential V_p results from the first derivative of the electron current. The most significant result concerns the gain in T_{eff} . Values between 20 % up to nearly 40 % are measured as soon as $I_{PB3} < -2$ A. The gain in T_{eff} flattens around $I_{PB3} = -3$ A, thus making a further reduction of I_{PB3} unnecessary. In addition, it is found that n_e grows by 20 % at $I_{PB3} \simeq -2$ A. When I_{PB3} is further decreased, the gain in n_e instead reduces, even reaching negative values in most cases. This phenomenon is linked to the axial location of the separatrix. At large negative currents driven in PB3, the magnetic separatrix moves downstream the antenna center. As a consequence, charged species are more likely transported towards $-z$, i.e. along the nozzle that forms upstream the antenna. This is qualitatively confirmed by a brighter plasma easily visible during experiments in the upstream part of the discharge tube. It becomes clear that a compromise between improved T_{eff} and greater plasma flux at the back plate shall be found to effectively enhance the overall performance. In this experimental configuration, a satisfactory gain in both n_e and T_{eff} is obtained at $I_{PB3} = -3$ A, regardless of the other external parameters.

Consequently, additional measurements are performed at $z = 31.5$ cm, that is in the divergent segment of the MN, at $I_{PB3} = 0$ A and $I_{PB3} = -3$ A. The probed plasma parameters are shown in Figure 3.50 as a function of P_{IN} . A remarkable gain in n_e and T_{eff} is also found downstream the MN throat. V_p raises as well, albeit less significantly

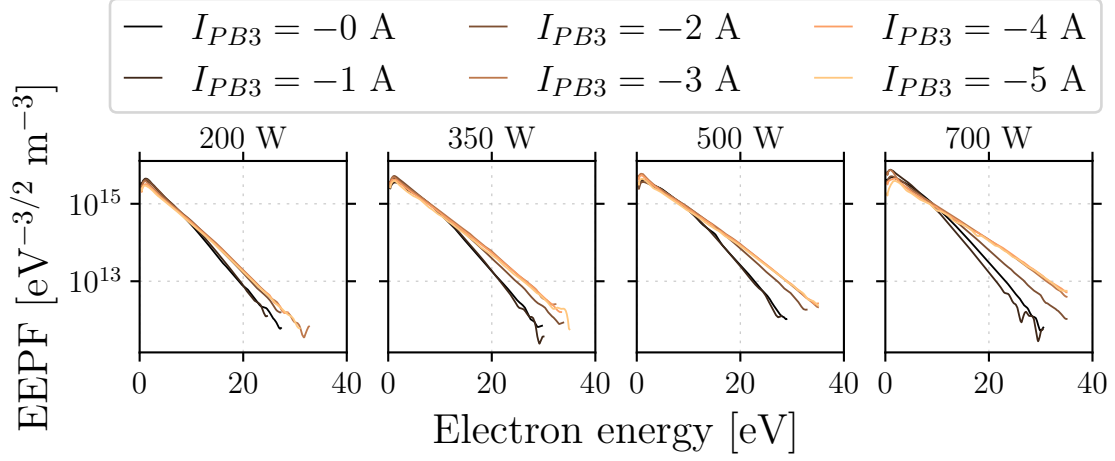


Figure 3.45: EEPFs measured at $z = 0$ as function of P_{IN} and I_{PB3} with $\dot{m} = 0.2 \text{ mg s}^{-1}$ Xe.

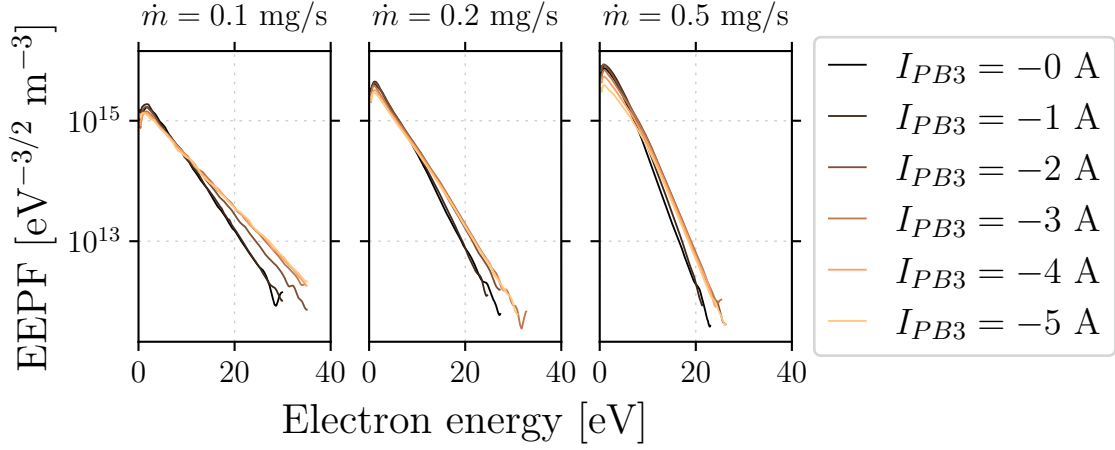


Figure 3.46: EEPFs measured at $z = 0$ as function of \dot{m} and I_{PB3} with $P_{IN} = 200 \text{ W}$.

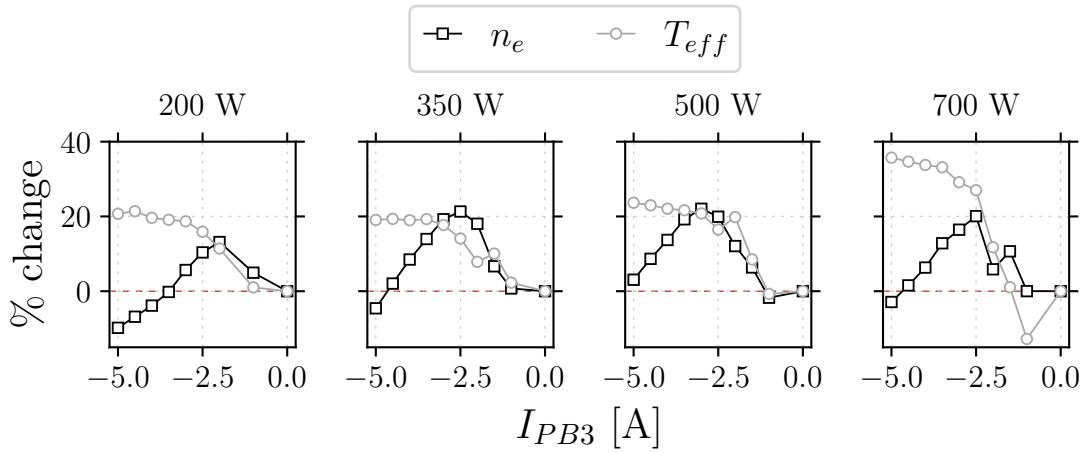


Figure 3.47: Percentage change of n_e and T_e at $z = 0$ for different values of P_{IN} with $\dot{m} = 0.2 \text{ mg s}^{-1}$ Xe. Reference case: $I_{GB2} = 9 \text{ A}$ and $I_{PB3} = 0 \text{ A}$.

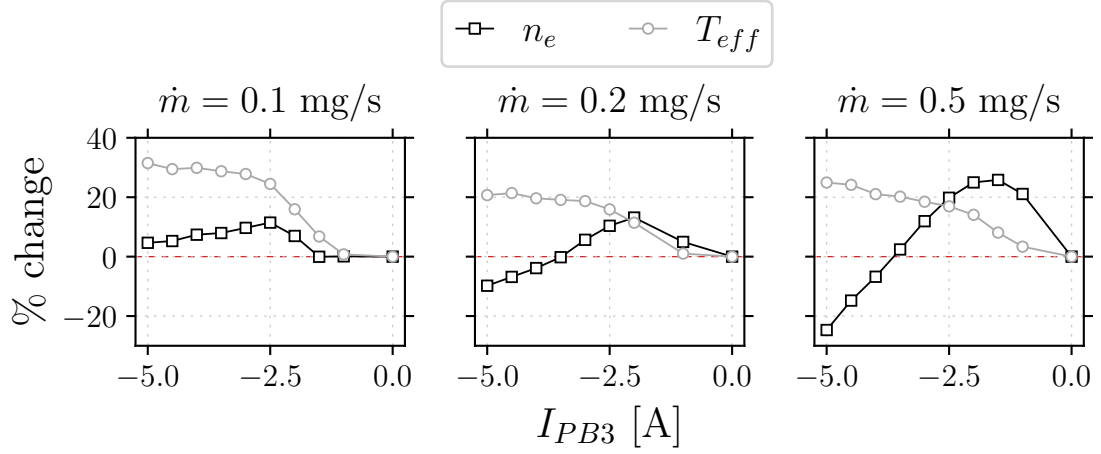


Figure 3.48: Percentage change of n_e and T_e at $z = 0$ for different values of \dot{m} with $P_{IN} = 200$ W. Reference case: $I_{GB2} = 9$ A and $I_{PB3} = 0$ A.

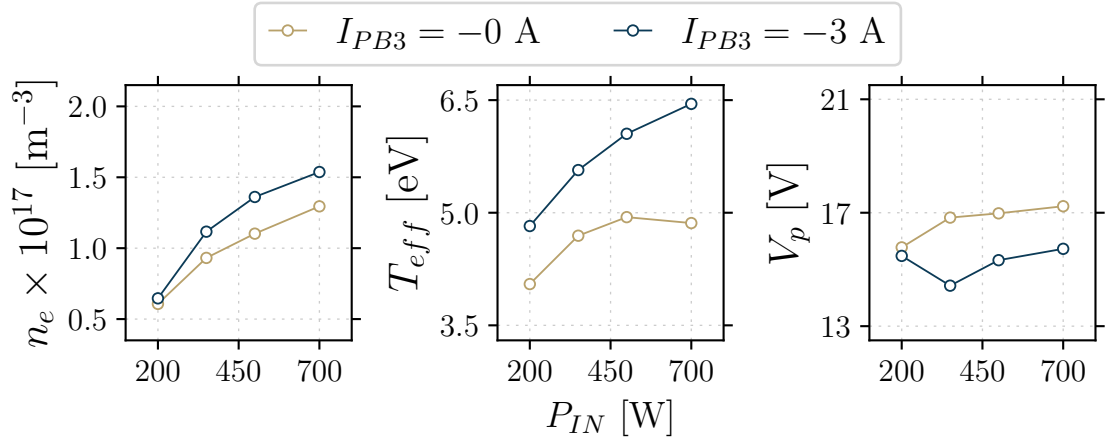


Figure 3.49: Electron properties at $z = 0$ cm as a function of P_{IN} with $\dot{m} = 0.2$ mg s⁻¹ Xe.

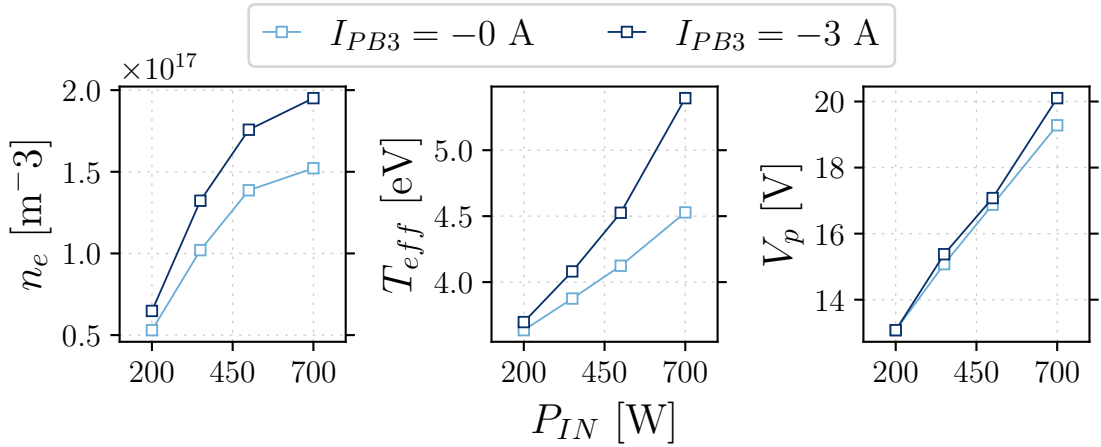


Figure 3.50: Electron properties at $z = 31.5$ cm as a function of P_{IN} with $\dot{m} = 0.2$ mg s⁻¹ Xe.

with respect to the other quantities. As mentioned beforehand, the improvement is more significant at larger P_{IN} .

3.4.2 Summary and conclusion

In summary, effective electron heating is observed in the MN of a rf discharge at 13.56 MHz when the ECR condition is met near the antenna center by tuning the magnetic field topology. In such cases, measurements show that the electron temperature easily increases by 20 %, hitting 40 % at high power. This strategy could significantly contribute to improving the efficiency of rf propulsion systems which rely on MN acceleration especially at low and moderate power levels.

3.5 Plasma oscillations and instabilities in the magnetic nozzle

It is well known that oscillations and instabilities of plasma properties impact the ideal dynamics in many plasma physics domains, such as fusion applications, astronomical phenomena and low-temperature plasmas. In magnetically confined and expanding plasmas, oscillations and instabilities result in non-classical transport of charged particles. The onset of these phenomena is often triggered by strong gradients in magnetic field strength and cross field gradients of density and plasma potential. The presence of these conditions in magnetic nozzles has been extensively documented in the literature and discussed in the previous sections of this manuscript. In MN applications, the investigation of cross-field transport of particles is of extreme interest because it is linked to the process of plasma detachment, i.e. the thrust generation mechanism. Furthermore, cross-field transport inside the source tube impacts plasma confinement and enhances wall losses. Research on helicon laboratory devices has confirmed the presence of plasma instabilities such as drift waves, Kelvin-Helmholtz and Rayleigh-Taylor instabilities [123–129]. Instabilities have recently been studied also in a smaller scale device [130] finding that non-classical transport of electrons is substantially enhanced by the presence of a low hybrid drift instability.

Different measurements about oscillations and instabilities are reported in this section. This experimental work has been conducted on the helicon plasma source described in Section 2.1. The purpose of these measurements and outcomes is mainly to illustrate the experimental methods. For the purpose of analyzing the impact of plasma instabilities on propulsion applications, it is believed that an exhaustive characterization of this non-ideal plasma behavior would be more physically representative if performed on a thruster-like device, therefore featuring a smaller size and a stronger magnetic field.

3.5.1 Ion current fluctuations

A simple uncompensated probe ($\phi = 0.68$ mm diameter, $L = 10$ mm length) is biased in the ion saturation region at -75 V using a TTiEX752M power supply. The AC component of current flowing in the probe is measured using a CP031A Hall sensor connected to a GS/s digital oscilloscope. The probe is actuated along the x axis and along the azimuthal direction while the time series of its current is recorded in the $\sim 0 - 120$ kHz window (where the drift instability is expected to be observed).

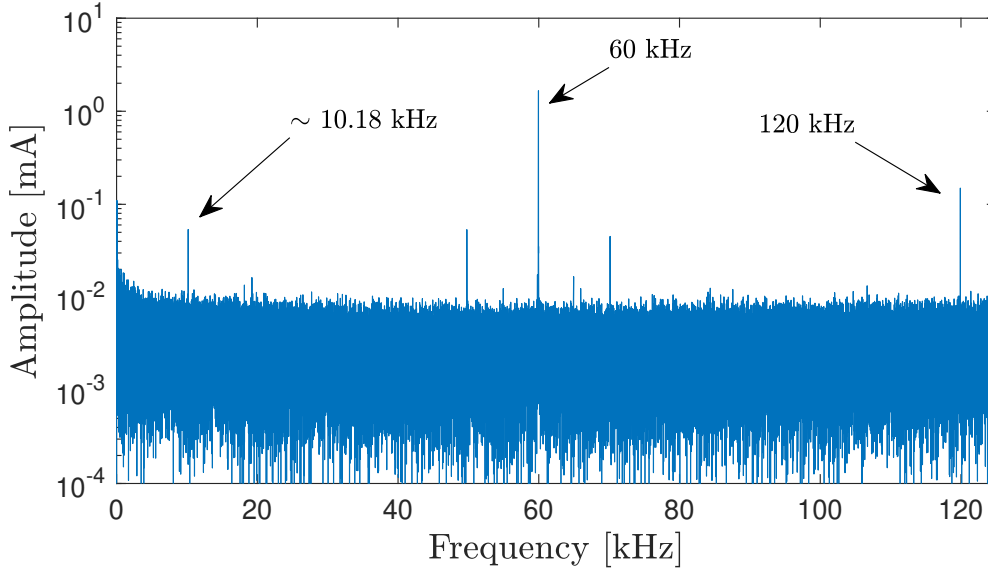


Figure 3.51: Typical ion saturation current spectrum. Simple uncompensated probe biased at -75 V.

A typical spectrum of the ion saturation current I_{sat} is shown in Figure 3.51, wherein a few peaks are distinct. The larger peaks at 60 kHz and its harmonic 120 kHz did not manifest any substantial dependence on the spatial location of the probe. In other words, their amplitude remains virtually unchanged as the probe is moved along the radial and/or azimuthal direction for a given working condition of the reactor. It is interesting to notice that these frequencies are exact divisors of the fundamental 13.56 MHz input frequency (e.g. $13.56 \times 10^6 / 60 \times 10^3 = 226$). As a result, it is interpreted that these peaks do not indicate an instability in the plasma, whereas they might directly be the result of the input rf electromagnetic field from the antenna. Differently, the peak shown in Figure 3.51 at ~ 10.18 kHz experiences substantial amplitude changes as the probe is actuated in space. Note that a similar value has been observed recently in a different device [128]. The two peaks at 50 kHz and 70 kHz were always present in the spectrum but no clear correlation with any physical phenomenon could be found. It is therefore decided to investigate the amplitude of the ~ 10.18 kHz frequency, which is referred to as ζ in the following. It is worth noting that the same frequency peaks are found with both krypton and xenon plasmas.

The helicon reactor is operated at different working conditions, i.e. some of the external parameters are changed in order to obtain different spatial distribution of the plasma parameters. For the sake of simplicity, only mass flow rate and magnetic strength are varied. Krypton propellant is injected at 1 mg s^{-1} and 2 mg s^{-1} , whereas xenon at 0.5 mg s^{-1} and 1 mg s^{-1} . The magnetic geometry is fixed to Conf. D, see Figure 3.17 and Figure 3.18, because it provides a good confinement degree (therefore relatively large radial gradients). The magnetic field amplitude is halved when required by halving the coils current. In the figures below, Conf. D relates to the nominal configuration employing 6 A through GB2 and GB3, cf. Table 3.1, whereas Conf. D/2 means that 3 A are used. The input power is fixed to 750 W.

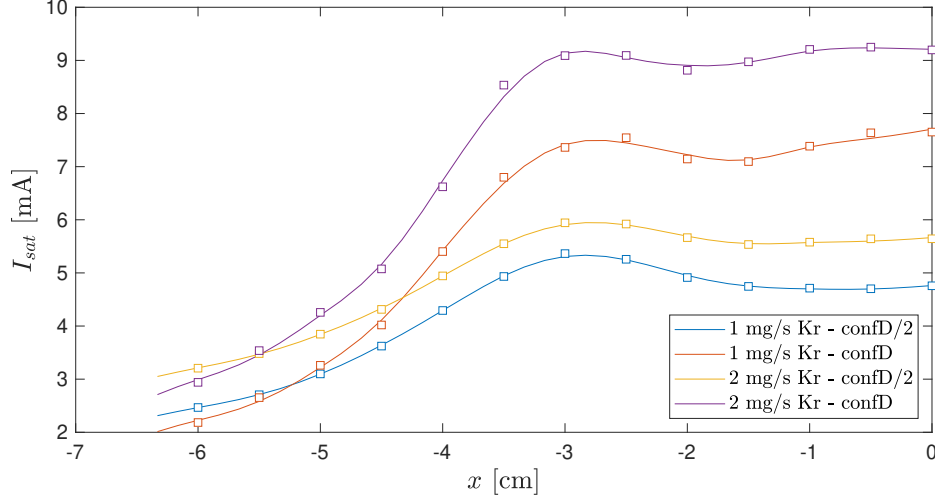


Figure 3.52: Radial evolution of the ion saturation current at $z = 12$ cm, 750 W, Kr propellant.

Krypton Discharge

In order to clarify the distribution of the ion saturation current instability, it is of convenience to first analyse the time-averaged quantities. Figure 3.52 shows the radial profile of the ion saturation current measured with the helicon reactor operating on krypton at $z = 12$ cm. Scatter points represent measurement data and solid lines are smoothed interpolated profiles. Since the ion current is directly proportional to the ion density, it is assumed that these curves qualitatively describe the radial evolution of the plasma density. As expected, the radial gradient is larger as the amplitude of the magnetic field is increased and larger currents are recorded when using larger mass flow rates. Each smoothed profile in Figure 3.52 is numerically derived and normalized, so as to obtain a radial profile of dn/dr which is compared to the radial evolution of ζ , i.e. the amplitude of the 10.18 kHz component of the spectrum. The frequency spectrum is recorded as explained in Section 3.5.1. Results are shown in Figure 3.53. It can be observed that, when the magnetic strength is at its maximum (graphs on the right-hand side), a clear correlation between dn/dr and ζ is found. In the configuration 1 mg s^{-1} Kr - Conf. D/2 (top left graph), the correlation is still visible yet less evident. This profile of ζ strongly suggests the presence of a drift wave, as previously observed in other helicon sources [124, 128].

The same uncompensated LP is mounted at $r = 2$ cm (where ζ is larger) on an azimuthal translation stage and actuated with a spatial resolution of 30° . The axial location is fixed to $z = 12$ cm. The azimuthal coordinate is defined conventionally considering that the z axis points downstream and the y axis points towards the antenna feeding lines. Non-trivial profiles are recorded for all the tested combinations of \dot{m} and magnetic field strength, as shown in Figure 3.54. The profile related to:

- 1 mg s^{-1} Kr - Conf. D/2 suggests the propagation of the azimuthal mode $m = 1$;
- 2 mg s^{-1} Kr - Conf. D/2 suggests the propagation of the azimuthal mode $m = 2$;
- 1 mg s^{-1} Kr - Conf. D suggests the propagation of the azimuthal mode $m = 4$;
- 2 mg s^{-1} Kr - Conf. D suggests the propagation of either $m = 1$ or $m = 2$.

3.5. PLASMA OSCILLATIONS AND INSTABILITIES IN THE MAGNETIC NOZZLE

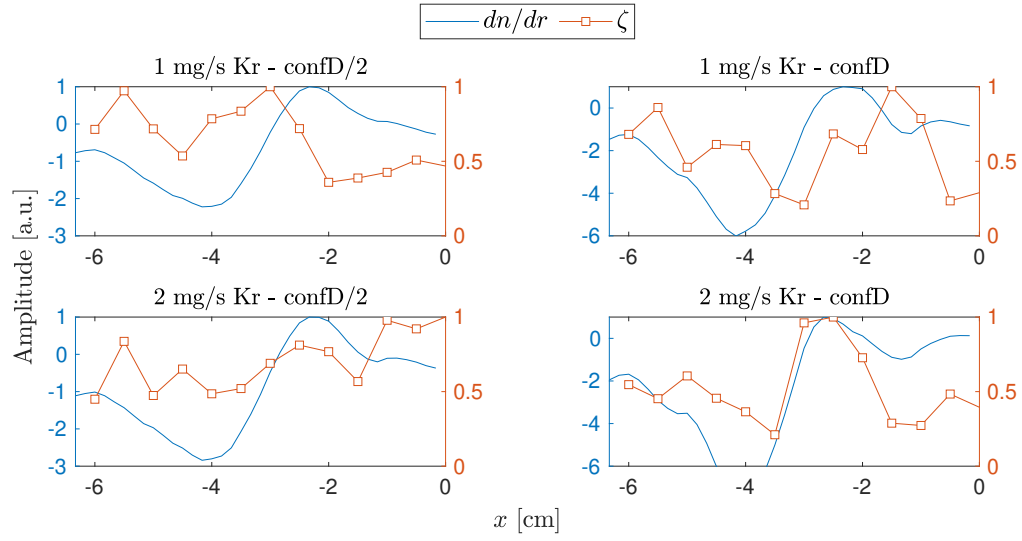


Figure 3.53: Normalized radial gradient of plasma density versus normalized amplitude of the 10.18 kHz instability. $z = 12$ cm, $P_{IN} = 750$ W, Kr propellant.

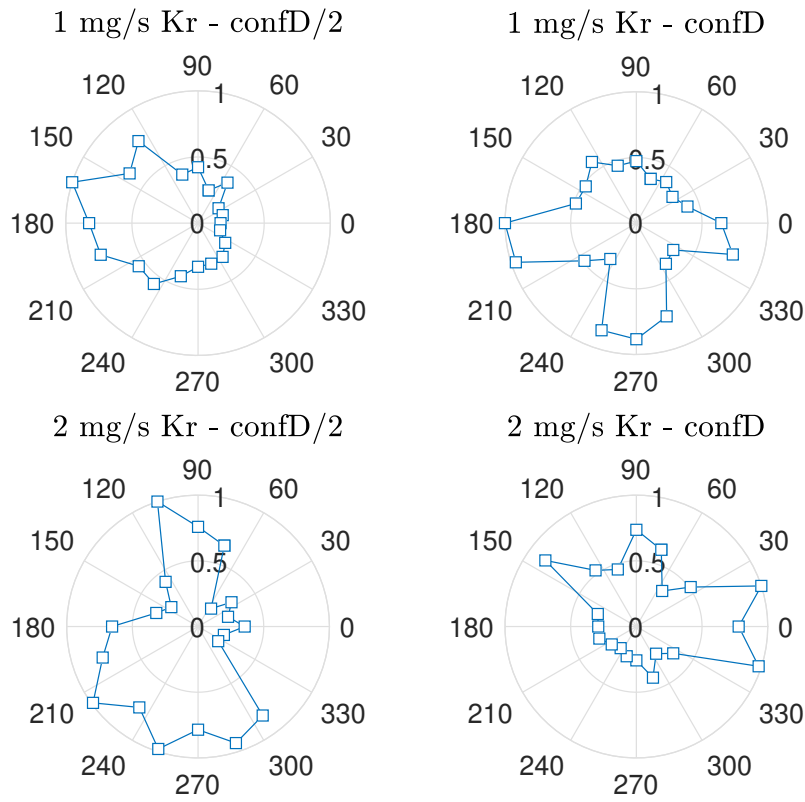


Figure 3.54: Normalized amplitude of the 10.18 kHz instability along the azimuthal coordinate. $z = 12$ cm, $P_{IN} = 750$ W, Kr propellant.

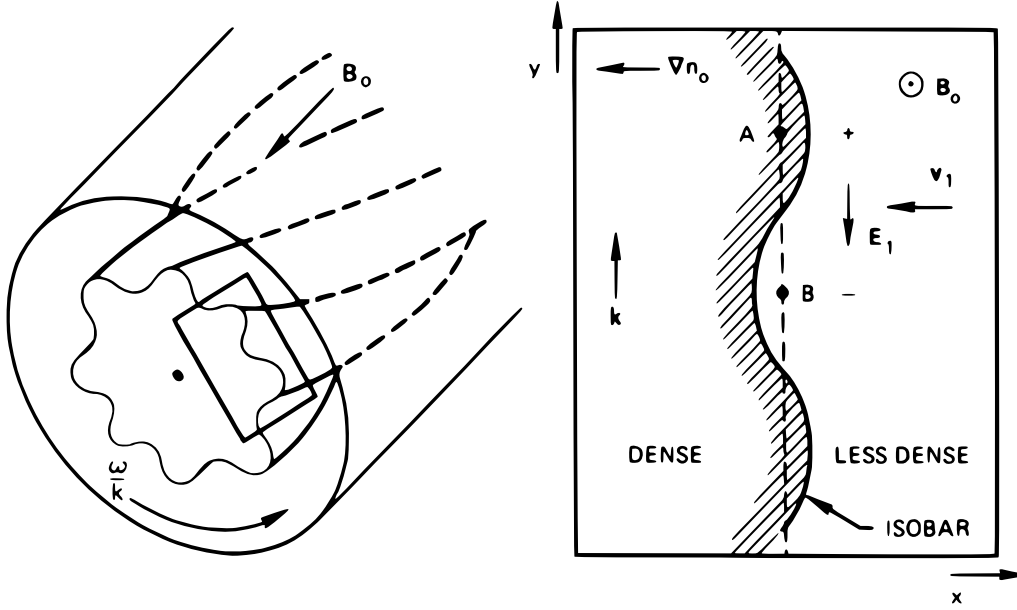


Figure 3.55: Drift instability geometry [103].

Making further deductions and conclusions is a rather complex task. Limitations in the experimental setup did not allow to readily and accurately access a full radial-azimuthal mapping, which would provide a more insightful set of data. Indeed, drift waves appear to have a highly three-dimensional structure [126]. It is worth noting that previous studies show similar structures of the drift wave amplitude along the radial and azimuthal directions with azimuthal mode $m = 9$ [126], $m = 5$ [123, 124] and $m < 5$ [129].

The azimuthal structure of ζ does not remain constant along z but instead rotates, as shown in Figure 3.55 [103]. Therefore, large fluctuations of the ion density on the azimuthal plane can lead to fluctuating axial currents localized within the azimuthal structure of the drift wave, as experimentally observed in [126] by reconstructing the fluctuating magnetic field in the azimuthal plane. The presence of fluctuating axial currents in a propulsion device is definitely not desired as it translates into an alternative push and pull axial force that increases the residence time of the ions in a given volume, thus increasing the likelihood of collisions that further limit the acceleration process. Quantifying this effect in a real thruster can be an extremely useful insight into the plasma dynamics and the related propulsive performance.

Xenon Discharge

The measurements presented and discussed in Section 3.5.1 are equally performed when the Helicon source operates using xenon as propellant. As previously pointed out, it is convenient analyze first the time-averaged radial profile of the ion saturation current. It is shown in Figure 3.56, obtained at $z = 12$ cm with the helicon reactor operating on Xe. Scatter points represent measurement data and solid lines are smoothed interpolated profiles. Since the ion current is directly proportional to the ion density, it is assumed that these curves qualitatively describe the radial evolution of the plasma density. It shall be noted that the difference in terms of radial gradient among these profiles is slightly less pronounced with respect to the case of krypton.

As described previously, the radial profile of dn/dr is compared to the radial evo-

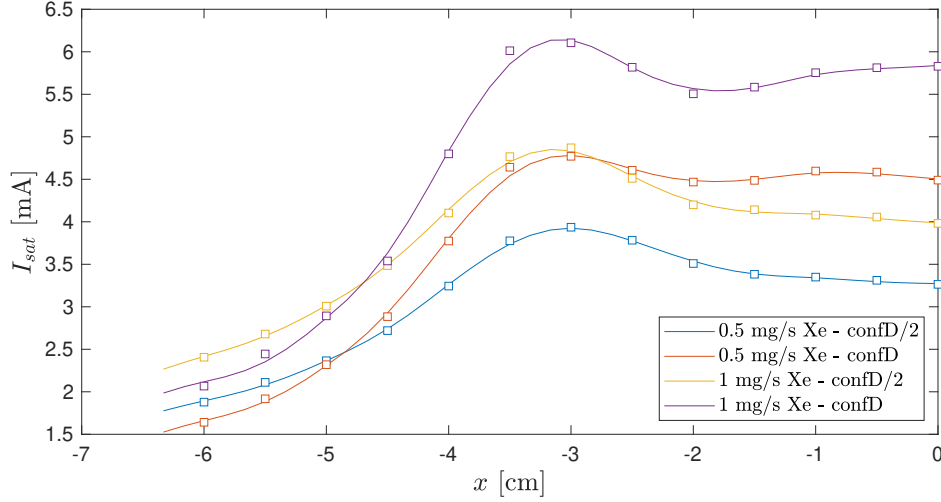


Figure 3.56: Radial evolution of the ion saturation current at $z = 12$ cm, 750 W, Xe propellant.

lution of ζ , i.e. the amplitude of the 10.18 kHz component of the spectrum. Similar results are found to those obtained using krypton. Indeed, the drift wave is not influenced by the nature of the propellant but instead is ruled by the radial density/pressure gradient, as previously stated. Figure 3.57 shows the obtained results. A very clear correlation between dn/dr and ζ is noticed for all the combinations of \dot{m} and magnetic field strength but at 0.5 mg s^{-1} Xe - Conf. D/2, for which the two profiles seem shifted along x with respect to each other. These results obtained at different values of plasma density further suggest the presence of a drift wave.

As previously described in Section 3.5.1, the same LP is mounted at $r = 2$ cm (where ζ is larger) and actuated azimuthally with a spatial resolution of 30° . The axial location is fixed to $z = 12$ cm. The measured profiles are shown in Figure 3.58 suggesting that the propagating azimuthal modes are:

- $m = 0$ at 0.5 mg s^{-1} Xe - Conf. D/2;
- either $m = 1$ or $m = 4$ at 0.5 mg s^{-1} Xe - Conf. D;
- $m = 3$ at 1 mg s^{-1} Xe - Conf. D/2;
- $m = 3$ at 1 mg s^{-1} Xe - Conf. D.

This set of measurements further shows the complex three-dimensional structure of the drift wave which is possibly hard to predict. Different radial gradients, in this case due to a different propellant, result in different azimuthal structures.

3.5.2 Three-probe experiment

The only information about the spatial distribution of the plasma fluctuations amplitude is not particularly disclosing from the engineering point of view. For propulsion applications, the interest is to control and minimize the undesired effects linked to the presence of instabilities, as described in [128]. For this reason, a larger picture including the propagation pattern in terms of wavenumber could in principle suggest mitigation strategies. In this study, the wavenumber spectra are estimated in a few points of the

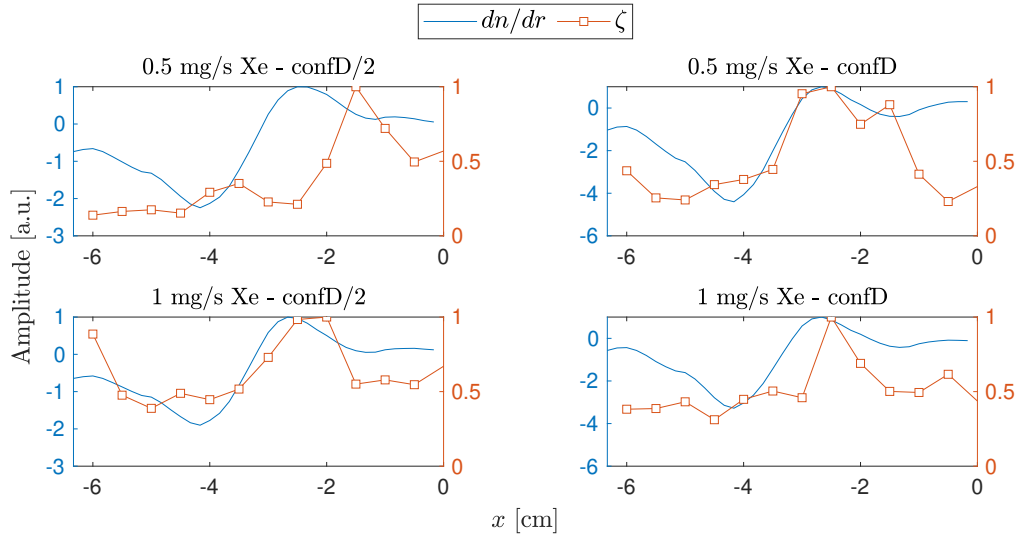


Figure 3.57: Normalized radial gradient of plasma density versus normalized amplitude of the 10.18 kHz instability. $z = 12$ cm, $P_{IN} = 750$ W, Xe propellant.

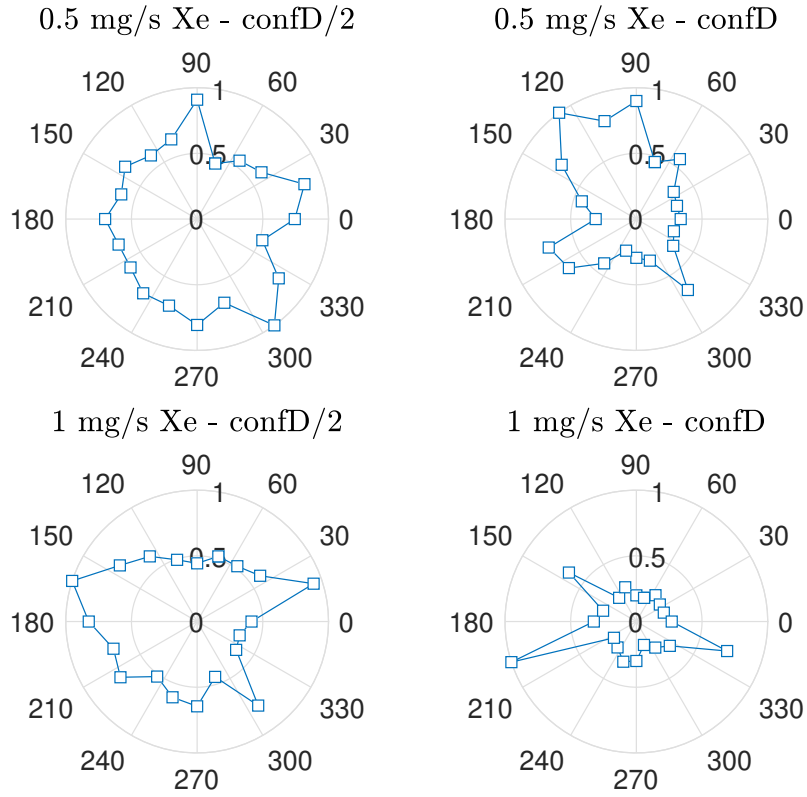


Figure 3.58: Normalized amplitude of the 10.18 kHz instability along the azimuthal coordinate. $z = 12$ cm, $P_{IN} = 750$ W, Xe propellant.

plasma domain by using three fixed probes. The technique reported in [131] is discussed in the following and is applied to the recorded spectra.

Spectral analysis and local wavenumber

Each fixed pair of probes allows inferring the local wavenumber k . The two probes are respectively located at x_1 and x_2 , being x a generic coordinate. The distance between the tips of the probes is defined as

$$\chi_p = x_2 - x_1. \quad (3.18)$$

As a result, the local value of k is unambiguously determined as a function of the frequency in the interval

$$k(\omega) \in \pm\pi/\chi_p. \quad (3.19)$$

Therefore, the probes are required to be spaced such that the quantity π/χ_p is larger than any significant spectral component in the system. Similarly, the frequency window is limited by the sampling frequency F_s and the time length of the recorded signal T :

$$f \propto F_s, T. \quad (3.20)$$

The latter parameters need to be tuned to avoid aliasing of frequencies higher than the Nyquist frequency. The fast Fourier-transform algorithm is applied to the time series of each probe thus obtaining the spectrum $\Phi(x, \omega)$. The two spectra are used to compute the cross spectrum H as:

$$H(\chi_p, \omega) = \Phi^*(x_1, \omega)\Phi(x_2, \omega), \quad (3.21)$$

where the superscript $*$ denotes complex conjugate. Finally, the local wavenumber k is estimated by accounting for the time delay of each frequency component, i.e. the phase angle θ . It is given by:

$$k(\omega) = \frac{\theta(x_2, \omega) - \theta(x_1, \omega)}{x_2 - x_1} = \frac{\arctan [\Phi^*(x_1, \omega)\Phi(x_2, \omega)]}{x_2 - x_1}. \quad (3.22)$$

The theory illustrated in [131] allows to further progress in the analysis by computing the local spectrum as a function of both frequency and wavenumber. This information can be useful in the case of plasma instabilities that manifest a complex structure in time and space, therefore f and k . By introducing the following subscripts as

$$i \rightarrow [..., k_i, ...] \quad \text{and} \quad j \rightarrow [..., f_j, ...], \quad (3.23)$$

the local wavenumber and frequency spectrum $\hat{S}_l(k_i, \omega_j)$ is computed by summing the power spectra $S(\omega_j)$ of each probe at a fixed frequency from those records which have a sample local wavenumber in the range $(k, k + \Delta k)$, and dividing by M

$$\hat{S}_l(k_i, \omega_j) = \frac{1}{M} \sum_{\gamma=1}^M I_{[0, \Delta k]} [k_i - k^{(\gamma)}(\omega_j)] \cdot \frac{1}{2} [S_1^{(\gamma)}(\omega_j) + S_2^{(\gamma)}(\omega_j)], \quad (3.24)$$

where the indicator function $I_{[0, \Delta k]} [...]$ is defined as

$$I_{[0, \Delta k]} [k_i - k^{(\gamma)}(\omega_j)] = \begin{cases} 1 & \text{if } [k_i - k^{(\gamma)}(\omega_j)] \cdot \Delta k \geq 0 \\ 0 & \text{in all other cases} \end{cases} \quad (3.25)$$

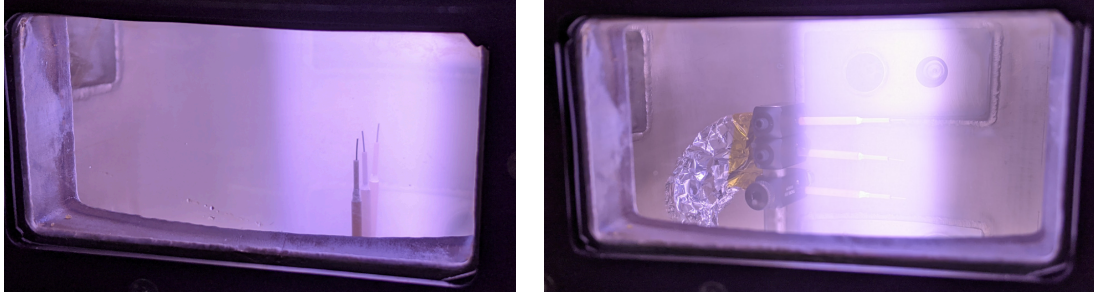


Figure 3.59: Three Langmuir probes mounted to measure the radial (left) and axial (right) wavenumber.

Experimental results

In this study, three fixed probes are used to investigate the instability propagation in space. Each probe consists in a simple uncompensated probe ($\phi = 0.6$ mm diameter, $L = 8$ mm length) biased in the ion saturation region at -75 V. The AC component of current flowing in each probe is measured using a dedicated current sensor. Due to unavailability of three identical current sensors, two CP031A Hall sensors and a Rogowski coil (Stangenes 0.5-1.0 W Wide Band Current Transformers) are used. The current sensors are connected to a GS/s digital oscilloscope. The time series recorded using the different sensors probing the same wire are preliminary compared to verify they output the same result. Good agreement in terms of frequency values and relative amplitude is found. The spectra of each probe are averaged over a few records (in the order of 10 to 15). Later, the theory illustrated in Section 3.5.2 is employed to obtain the local wavenumber k as a function of frequency. Following the considerations reported Section 3.5.1, the frequency window of interest here is around 10.18 kHz.

Similarly to what is discussed in Section 3.5.1, the Helicon reactor is operated at different working conditions. For simplicity, only mass flow rate and magnetic strength are varied. Krypton propellant is injected at 1 mg s^{-1} and 2 mg s^{-1} . The magnetic geometry is fixed to Conf. D, see Figure 3.17 and Figure 3.18, and its amplitude is halved when required by halving the coils current. The input power is fixed to 750 W.

The three probes are mounted in different configurations in order to exploit the cylindrical symmetry of the system and infer the local value of k along the r , ϕ and z directions. The configurations probing the radial and axial wavenumbers are shown in Figure 3.59. With reference to the coordinate system reported in Figure 2.2, the probes location in the three configurations is:

- $z = 12$ cm, $(x_1, x_2, x_3) = (0, -2.5, -4)$ cm when probing along r ;
- $x = 2.5$ cm, $(z_1, z_2, z_3) = (11, 13, 15)$ cm when probing along z ;
- $z = 12$ cm, $r = 2.5$ cm, $(\phi_1, \phi_2, \phi_3) = (0, 45, 90)$ deg when probing along ϕ ,

where subscripts 1, 2, and 3 refer to the probe number. These values of x , ϕ and z are selected by accounting for: *i*) the magnetic field strength since $z = 12$ cm represents the throat of the magnetic field; *ii*) the radial distribution of the instability amplitude, as shown in Figure 3.53; *iii*) limitations in the experimental setup related to assembly feasibility.

All the following results are reported in terms of cross spectrum $H(\chi_p, \omega)$, phase angle θ and wavenumber k . In each of the figures, the left column refers to the local

properties obtained using the first pair of probes (probe 1 and probe 2), whereas the right column refers to the local properties obtained analyzing the data related to the second pair (probe 2 and probe 3).

The results related to the axial propagation of the 10.18 kHz instability are illustrated in Figure 3.60 to Figure 3.63. By analyzing these figures, it is possible to outline a few considerations:

- in the 1 mg s^{-1} Kr - Conf. D/2 condition, the first pair of probes (left column) reveals a clear wavenumber of $k \simeq 0.5 \text{ cm}^{-1}$, suggesting a downstream propagation of the drift wave. The second pair of probes (right column), instead, does not show any clear pattern. This, in combination with a much noisier profile of H , suggests a weaker propagation in the region downstream the magnetic throat.
- in the 1 mg s^{-1} Kr - Conf. D condition, the first pair of probes reveals that $k \simeq 0.5 \text{ cm}^{-1}$, while the second pair shows that $k \simeq -1.2 \text{ cm}^{-1}$. It means that the drift wave propagates downstream at $z = 12 \text{ cm}$ while it propagates upstream in the region downstream the magnetic throat.
- in the 2 mg s^{-1} Kr - Conf. D/2 condition, the first pair of probes reveals that $k \simeq 0.5 \text{ cm}^{-1}$, while the second pair shows that $k \simeq -0.5 \text{ cm}^{-1}$.
- in the 2 mg s^{-1} Kr - Conf. D condition, the first pair of probes reveals that $k \simeq 0.5 \text{ cm}^{-1}$, while the second pair shows that $k \simeq 1.2 \text{ cm}^{-1}$. It suggests that the drift wave propagates downstream and that, as the magnetic field strength decreases downstream, the propagation occurs via shorter wavelength.

The results related to the radial propagation of the 10.18 kHz instability are illustrated in Figure 3.64 to Figure 3.67. The profiles of k obtained probing the radial direction do not reveal any clear pattern. Therefore, it is concluded that there is no propagation along r , as expected in the case of a drift wave instability.

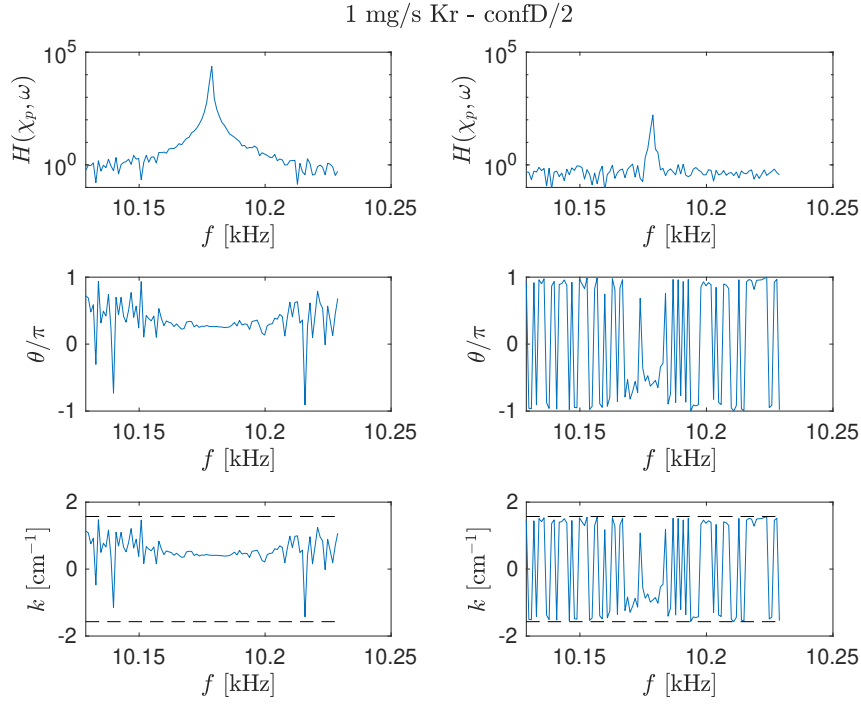


Figure 3.60: Axial propagation of drift wave in the case of 1 mg s^{-1} Kr and Conf. D/2. Cross spectrum (top), phase angle (middle) and wavenumber (bottom). Probes pair 1-2 (left column) and probes pair 2-3 (right column).

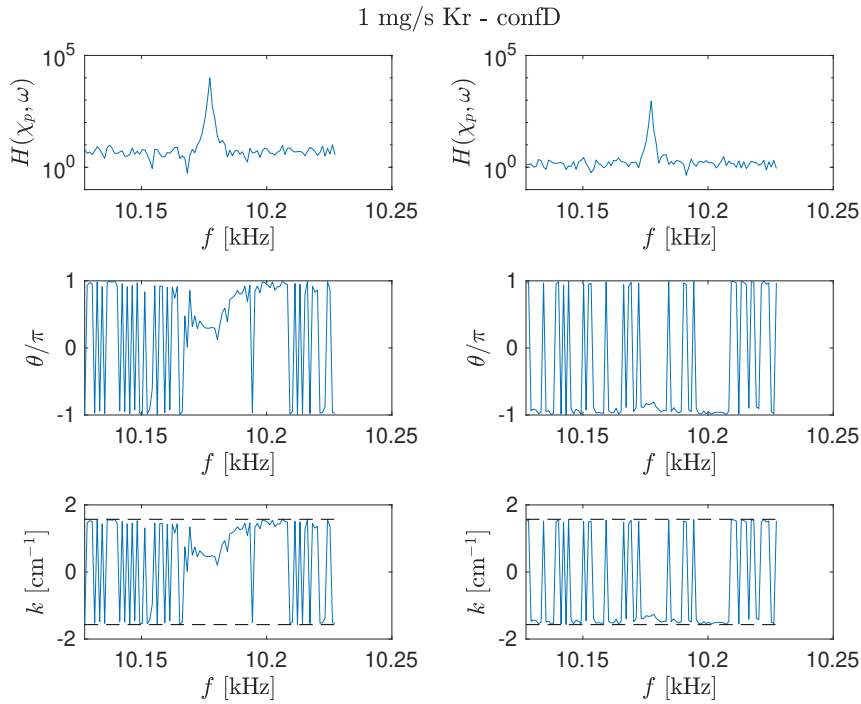


Figure 3.61: Axial propagation of drift wave in the case of 1 mg s^{-1} Kr and Conf. D. Cross spectrum (top), phase angle (middle) and wavenumber (bottom). Probes pair 1-2 (left column) and probes pair 2-3 (right column).

3.5. PLASMA OSCILLATIONS AND INSTABILITIES IN THE MAGNETIC NOZZLE

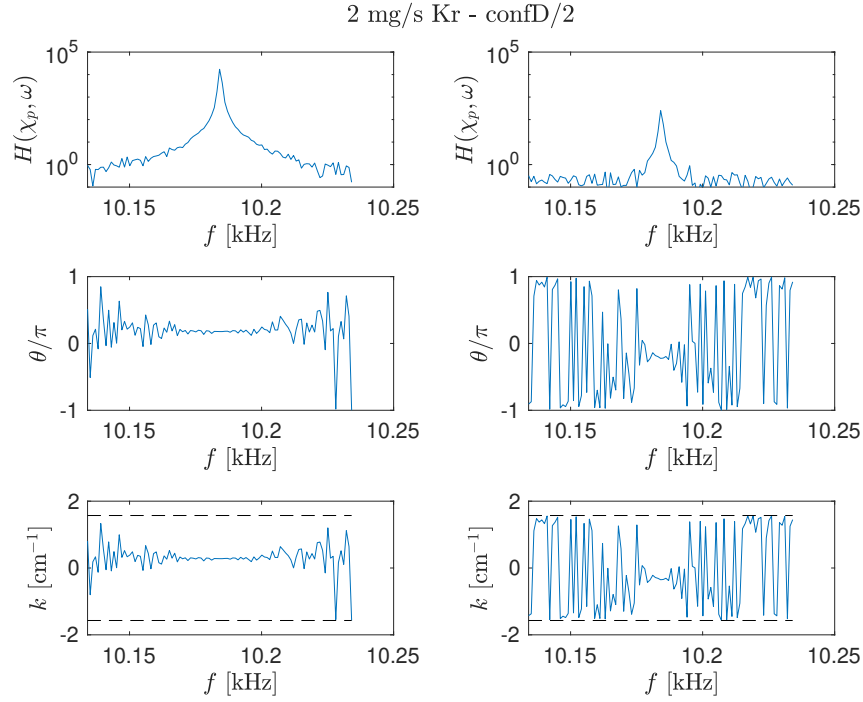


Figure 3.62: Axial propagation of drift wave in the case of 2 mg s^{-1} Kr and Conf. D/2. Cross spectrum (top), phase angle (middle) and wavenumber (bottom). Probes pair 1-2 (left column) and probes pair 2-3 (right column).

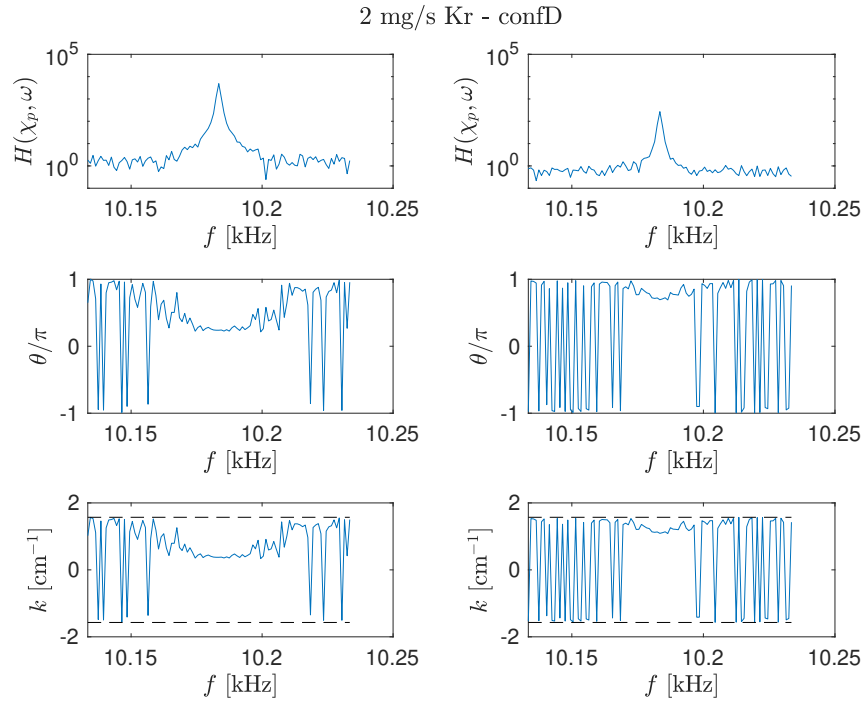


Figure 3.63: Axial propagation of drift wave in the case of 2 mg s^{-1} Kr and Conf. D. Cross spectrum (top), phase angle (middle) and wavenumber (bottom). Probes pair 1-2 (left column) and probes pair 2-3 (right column).

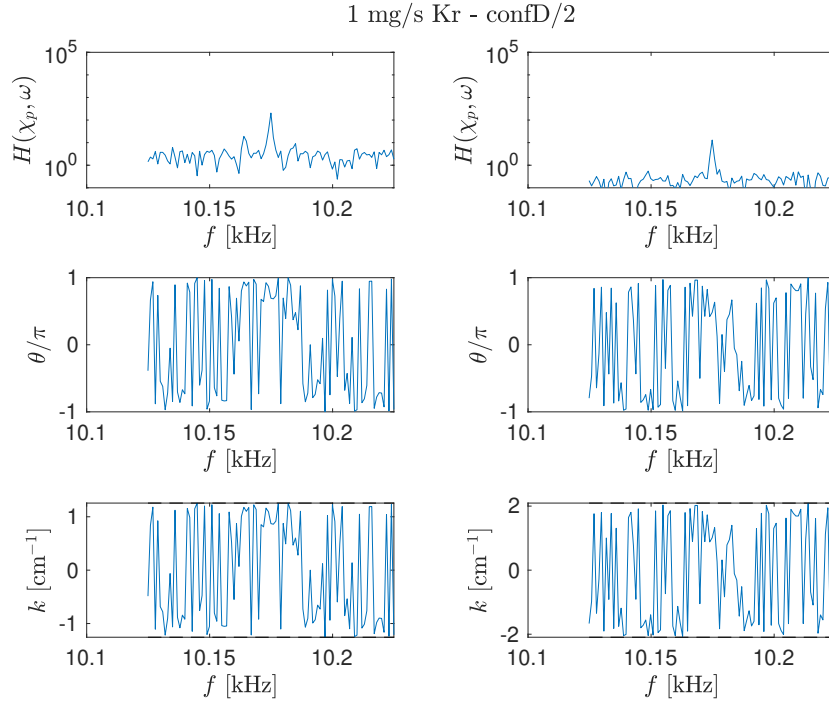


Figure 3.64: Radial propagation of drift wave in the case of 1 mg s^{-1} Kr and Conf. D/2. Cross spectrum (top), phase angle (middle) and wavenumber (bottom). Probes pair 1-2 (left column) and probes pair 2-3 (right column).

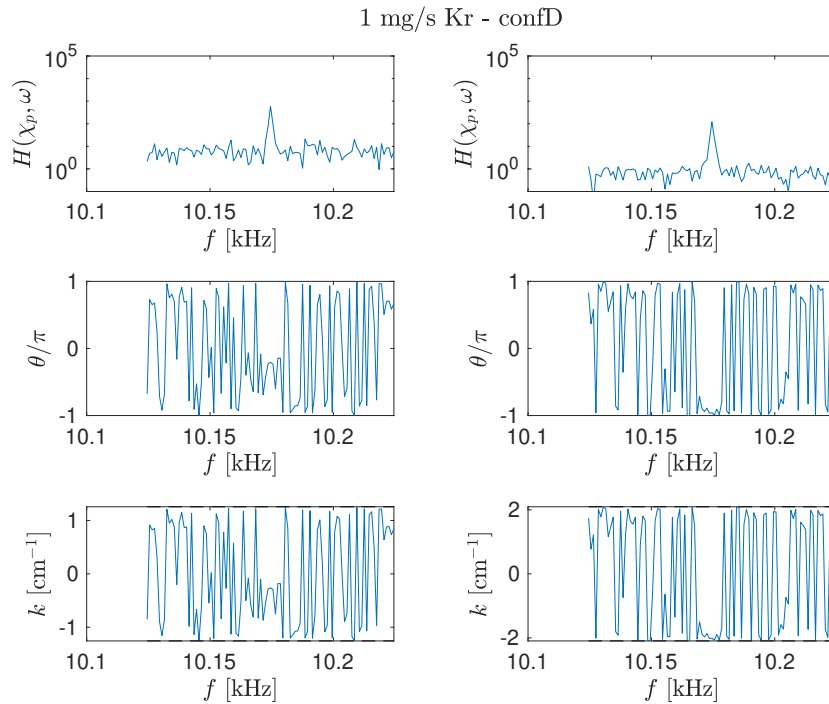


Figure 3.65: Radial propagation of drift wave in the case of 1 mg s^{-1} Kr and Conf. D. Cross spectrum (top), phase angle (middle) and wavenumber (bottom). Probes pair 1-2 (left column) and probes pair 2-3 (right column).

3.5. PLASMA OSCILLATIONS AND INSTABILITIES IN THE MAGNETIC NOZZLE

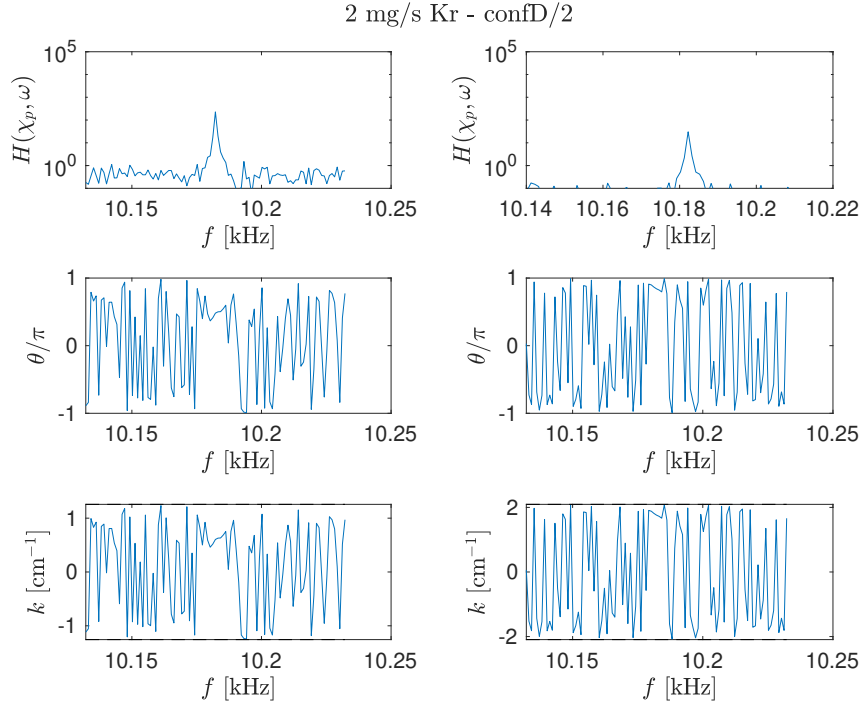


Figure 3.66: Radial propagation of drift wave in the case of 2 mg s^{-1} Kr and Conf. D/2. Cross spectrum (top), phase angle (middle) and wavenumber (bottom). Probes pair 1-2 (left column) and probes pair 2-3 (right column).

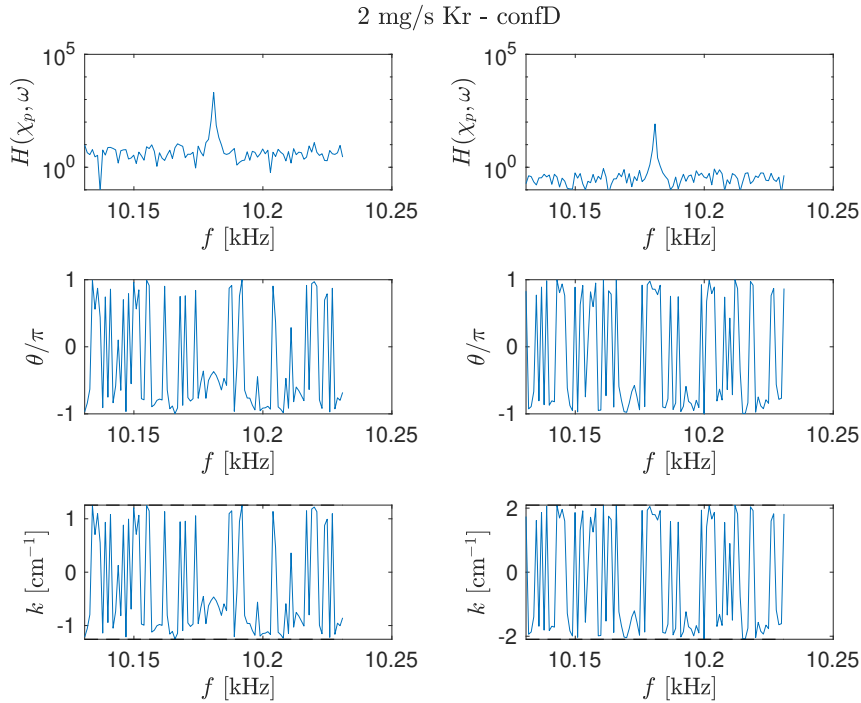


Figure 3.67: Radial propagation of drift wave in the case of 2 mg s^{-1} Kr and Conf. D. Cross spectrum (top), phase angle (middle) and wavenumber (bottom). Probes pair 1-2 (left column) and probes pair 2-3 (right column).

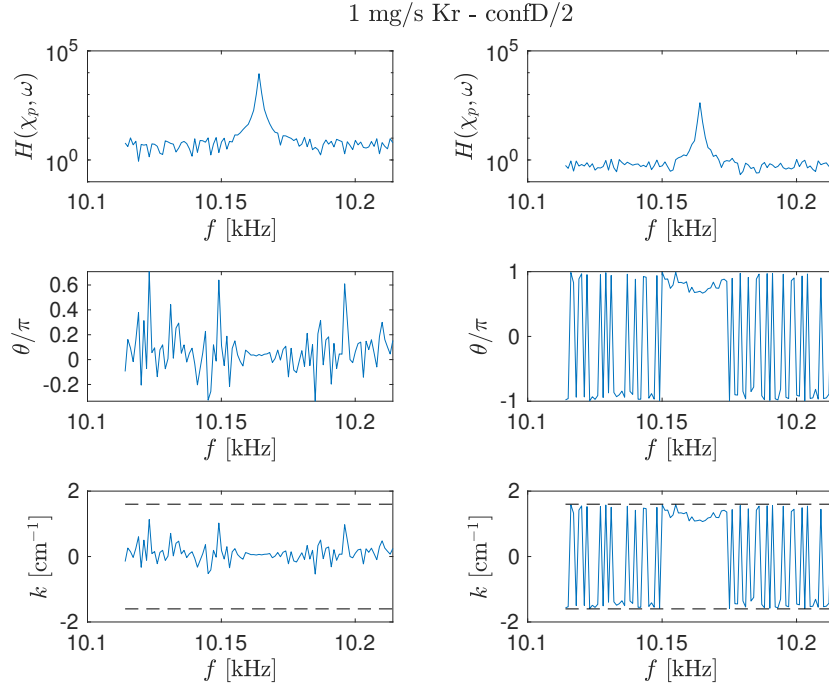


Figure 3.68: Azimuthal propagation of drift wave in the case of 1 mg s^{-1} Kr and Conf. D/2. Cross spectrum (top), phase angle (middle) and wavenumber (bottom). Probes pair 1-2 (left column) and probes pair 2-3 (right column).

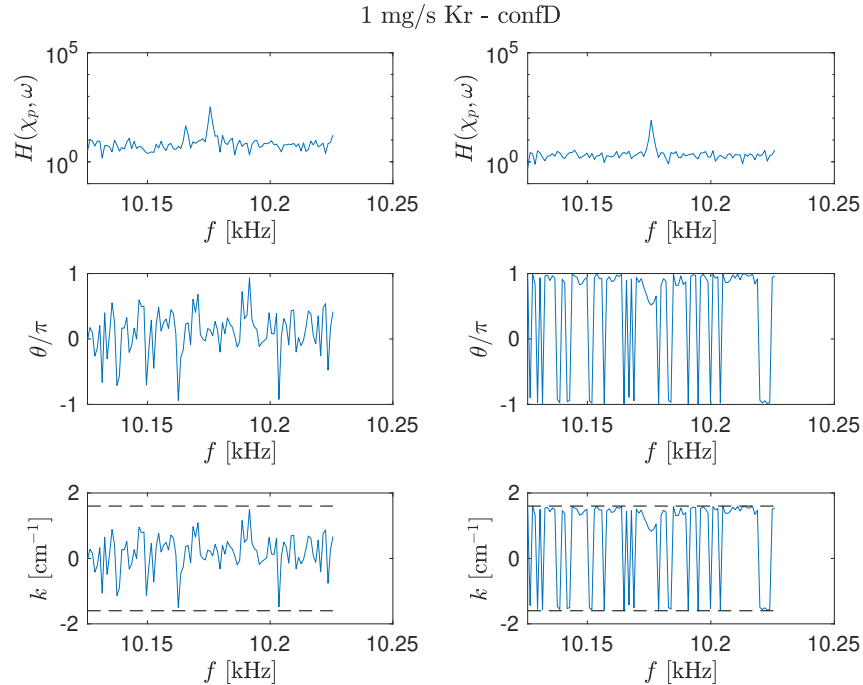


Figure 3.69: Azimuthal propagation of drift wave in the case of 1 mg s^{-1} Kr and Conf. D. Cross spectrum (top), phase angle (middle) and wavenumber (bottom). Probes pair 1-2 (left column) and probes pair 2-3 (right column).

3.5. PLASMA OSCILLATIONS AND INSTABILITIES IN THE MAGNETIC NOZZLE

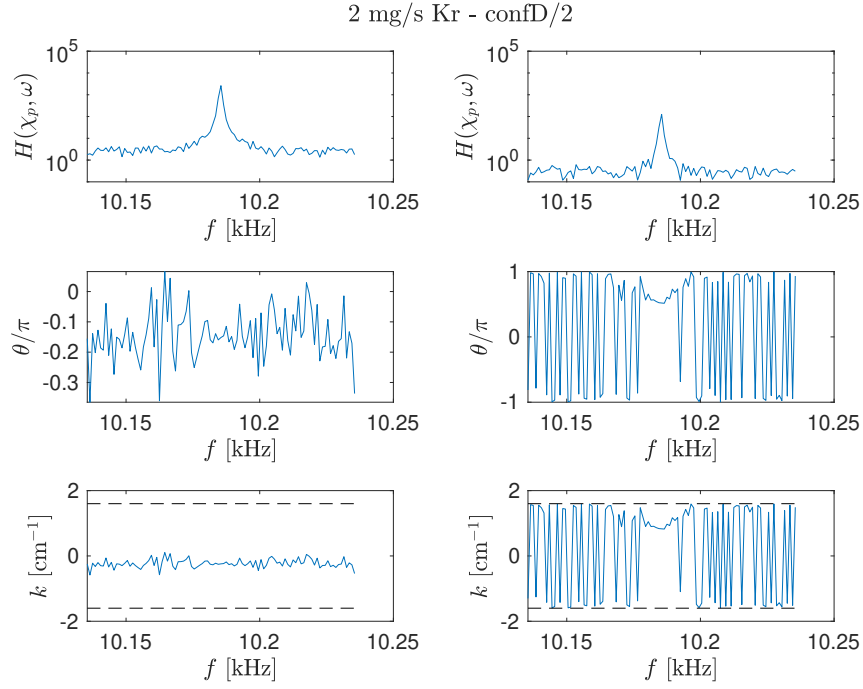


Figure 3.70: Azimuthal propagation of drift wave in the case of 2 mg s^{-1} Kr and Conf. D/2. Cross spectrum (top), phase angle (middle) and wavenumber (bottom). Probes pair 1-2 (left column) and probes pair 2-3 (right column).

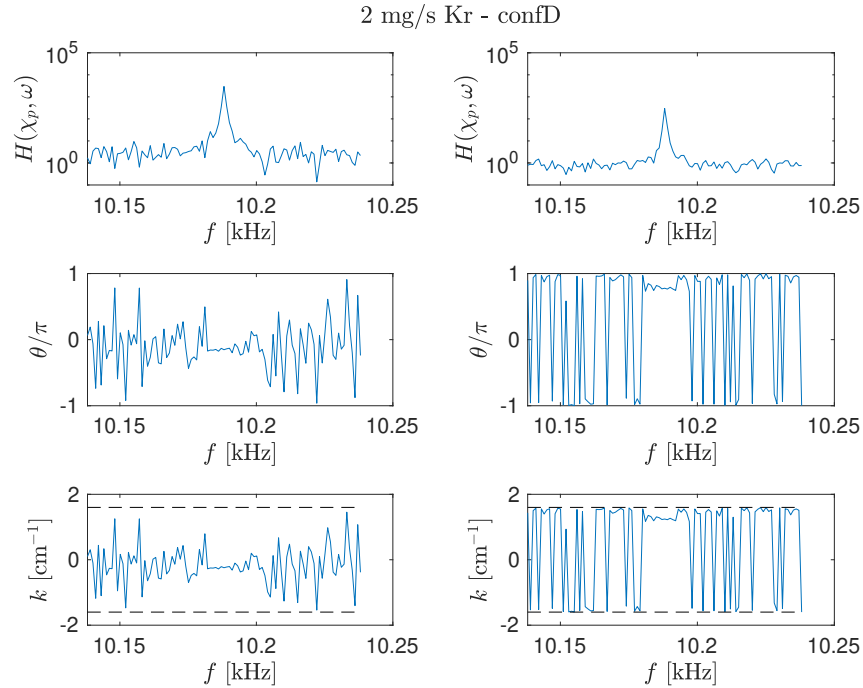


Figure 3.71: Azimuthal propagation of drift wave in the case of 2 mg s^{-1} Kr and Conf. D. Cross spectrum (top), phase angle (middle) and wavenumber (bottom). Probes pair 1-2 (left column) and probes pair 2-3 (right column).

The results related to the azimuthal propagation of the 10.18 kHz instability are illustrated in Figure 3.68 to Figure 3.71. By analyzing these figures, it is possible to outline a few considerations:

- in the 1 mg s^{-1} Kr - Conf. D/2 condition, the first pair of probes reveals that $k \simeq 0 \text{ cm}^{-1}$, while the second pair shows that $k \simeq 1 \text{ cm}^{-1}$. It suggests that the drift wave propagates in the region defined by $45 < \phi < 90 \text{ deg}$, in the counter-clockwise direction.
- in the 1 mg s^{-1} Kr - Conf. D condition, no clear profile is recorded for both of the probes pairs.
- in the 2 mg s^{-1} Kr - Conf. D/2 condition, similarly to the first condition, the first pair of probes reveals that $k \simeq 0 \text{ cm}^{-1}$, while the second pair shows that $k \simeq 1 \text{ cm}^{-1}$. It suggests that the drift wave propagates in the region defined by $45 < \phi < 90 \text{ deg}$, in the counterclockwise direction.
- in the 2 mg s^{-1} Kr - Conf. D condition, similarly to the first condition, the first pair of probes reveals that $k \simeq 0 \text{ cm}^{-1}$, while the second pair shows that $k \simeq 1.2 \text{ cm}^{-1}$. It suggests that the drift wave propagates in the region defined by $45 < \phi < 90 \text{ deg}$, in the counterclockwise direction.

In conclusion, the simple multi-probes experiment described in this section represents a powerful tool to grasp the spatial distribution of the instability propagation. A more sophisticated setup, e.g. involving fast automatic translation stages and a smaller Helicon device in a larger expansion chamber, could allow to resolve in space the whole drift wave. Knowing the 2D (or even 3D) structure of the wave vector would allow understanding the external parameters which influence the instability onset and its resulting effects on the propulsive performance thus suggesting mitigation strategies.

PART II

RESEARCH ON

MAGNETIC NOZZLE DYNAMICS AT UC3M

Chapter 4

Atoms and ions dynamics in the magnetic nozzle of a HPT

This chapter reports on results obtained through extensive experimental campaigns carried out in collaboration with the EP team at Universidad Carlos III in Madrid. The relevance of this analysis is to assess how ions and atoms behave in the magnetic nozzle of helicon plasma thruster. The availability of such accurate experimental data is critical for the advance in modeling of magnetic nozzle plasma dynamics and thruster design iteration. The measurements reported in this chapter have been performed via laser-induced fluorescence spectroscopy and an RPA, both diagnostics are presented in Section 2.2. A detailed description of the experimental arrangement is provided in Section 4.1, which includes the HPT, the vacuum facility and the optical setup. Fluorescence spectra are introduced first in Section 4.2, showing the need of lineshape modeling. Details of the model are then addressed in Section 4.3 and eventually theoretical and experimental lineshapes are compared to retrieve the Doppler shift. The resulting velocity profiles of ions and atoms are reported in Section 4.4 for a set of operating conditions. A comparison between LIF and RPA measurements is discussed in Section 4.5.

4.1 Experimental arrangement

The thruster unit (TU) tested in this work derives from a previous prototype developed by UC3M, whose main features were described in [35]. In the current version, the magnetic field generator has been upgraded from a solenoid-based solution to an assembly of radially polarized Neodymium permanent magnets (PM). These are allocated in an auxiliary annular aluminum structure, which allows for a wide flexibility on the PMs configuration, thus enabling the generation of different magnetic field topologies/strengths. In this work, the PMs are assembled to form an annular ring. Since the PMs are radially polarized, they generate a symmetric magnetic field with respect to the mid-plane of the assembly, perpendicular to the z axis in Figure 4.2. As a consequence, the PMs mid-plane represents a magnetic separatrix surface. A null field point appears at the center of the assembly. Downstream the separatrix plane, the shape of the magnetic field is convergent-divergent, thus forming the so called MN. Upstream the separatrix plane, the field resembles the same topology because of the mentioned symmetry. The width of the PM annular assembly is 40 mm and the internal radius is

4.1. EXPERIMENTAL ARRANGEMENT

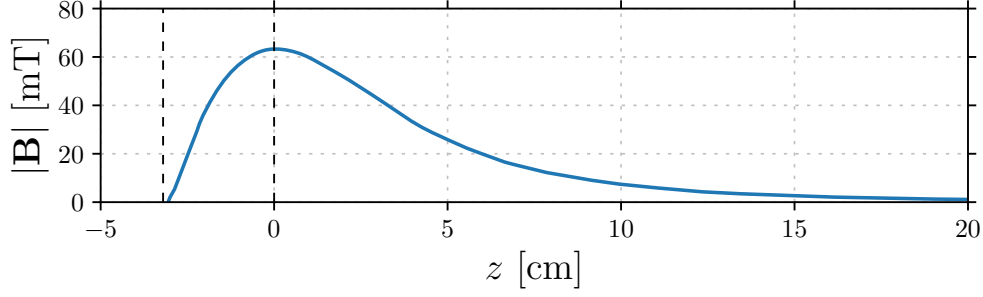


Figure 4.1: Axial profile of the HPT magnetic field strength. $z = 0$ refers to the exit plane of the discharge tube. The dashed vertical lines indicate the axial location of the null field and the maximum intensity which occurs at $z = 0$.

50 mm. Figure 4.1 shows the magnetic field strength at the centerline of the thruster in the region of interest for the LIF analysis, i.e. the exhausted plasma plume region. The peak of the magnetic field reads ≈ 65 mT and coincides with the outlet section of the plasma discharge chamber, also referred to as discharge tube within this paper. The latter is made of boron nitride, it is 60 mm long (outlet to injector plate distance), 25 mm in inner diameter and its wall thickness is 1.5 mm. The exit plane of the discharge tube is set as the reference $z = 0$ hereafter. The magnetic separatrix mentioned beforehand is placed at 40 mm upstream the tube outlet. A schematics of the thruster unit is reported in Figure 4.2. Radio-frequency power at 13.56 MHz is fed to the TU through a half-helical silver coated antenna, wrapped around the ceramic tube without entering in physical contact. The antenna is 45 mm long and it has a mid diameter of 30 mm. The RF power (P_{rf}) is generated with an industrial power amplifier Seren HR2100 and it is conditioned to the antenna with a Sener Aeroespacial S.A. customized L-type matching network and control system [132]. The system can be operated up to 600 W but in this work it has been limited to lower levels. Xenon gas is injected from the back side of the tube through an embedded multi-hole injector, also made in boron nitride, which allows a uniform distribution of the propellant. The mass flow rate is set/measured by a Bronkhorst EL-FLOW Select Xenon calibrated mass flow controller, with an accuracy of 0.1 sccm and 100 sccm full range.

The thruster unit has been tested inside the main vacuum chamber of the UC3M laboratory. It consists of a non-magnetic stainless-steel vessel of 1.5 m inner diameter and 3.5 m long. The facility background pressure is about 10^{-7} mbar, while the operating pressure is kept within the range 5.9×10^{-6} – 4.6×10^{-5} mbar for a Xe flow of 5 to 50 sccm. The vacuum technology implemented in the chamber consists of three cryopanel (COOLPOWER 140 T-V cryoheads by Leybold) and a couple of turbomolecular pumps, MAG2.200iP by Leybold. The thruster axis is aligned with the vacuum chamber axis, and the thruster outlet section is about 2.5 m away from the chamber downstream wall to minimize plume-chamber wall interactions.

As anticipated in Section 2.2.7, the near-infrared laser beam that starts from the optical bench is coupled to a 50 μ m multi-mode optical fiber which transports it to the inside of the vacuum facility. Here the beam is shone in the direction of the thruster axis, see Figure 4.2. The fluorescence light is collected using a bi-convex lens with 60 mm focal length focusing on a 200 μ m core diameter optical fiber that transports the light back to the optical bench. Due to line-of-sight constraints, the detection branch is placed

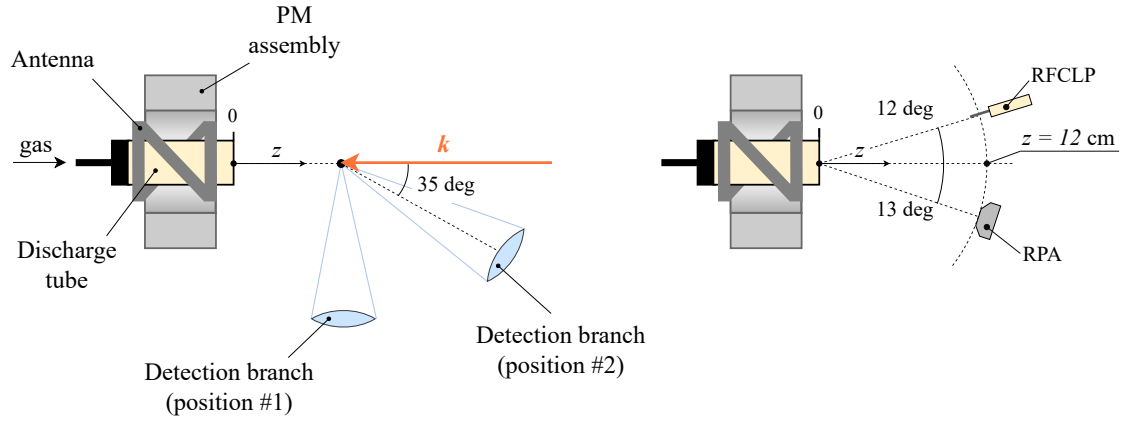


Figure 4.2: Experimental setup schematics relative to (left) LIF and (right) RPA measurements. The exit plane of the discharge tube is set as the reference $z = 0$.

perpendicularly to the laser beam when the measurements are resolved along $z > 0$, whereas it is tilted by 35 deg when scanning at $z < 0$. Both the excitation and detection branches are mechanically linked to a two-axes polar translation stage, whose radial and angular resolutions are 1 mm and 1 deg, respectively. Any relative displacement between the two optical branches is inhibited. Figure 4.2 also depicts the setup relative to the LIF-RPA comparison that is discussed in Section 4.5. These measurements involved the use of the RPA detailed in Section 2.2.6 and a RFCLP developed by UC3M whose description can be found in [133].

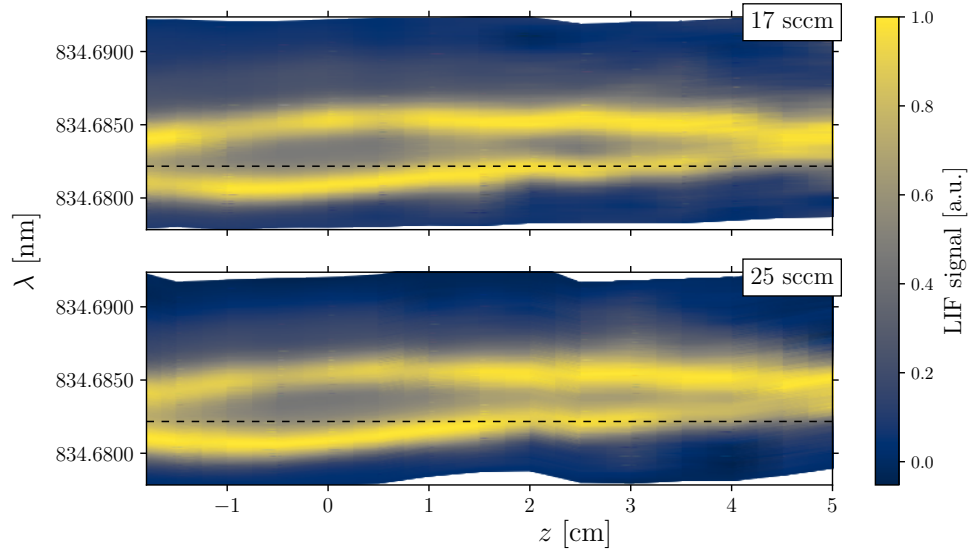
4.2 Considerations on experimental findings

In this section, the recorded LIF spectra are shown as a function of the laser wavelength λ . The density of Xe atoms in the probed resonant state is low due to its short lifetime [134]. As a consequence, the fluorescence signal is rapidly lost downstream the thruster exit plane, therefore the atoms profiles could only be resolved inside the discharge tube and in the near-field region of the plasma plume. Differently, the behavior of Xe ions could be investigated up to 15 cm downstream the exit plane, at the expense of longer integration times to increase the signal-to-noise ratio. The longest time required to scan over one entire profile is in the order of 8 min. The fluorescence profiles measured at large axial locations have been smoothed using a Savitzky-Golay filter.

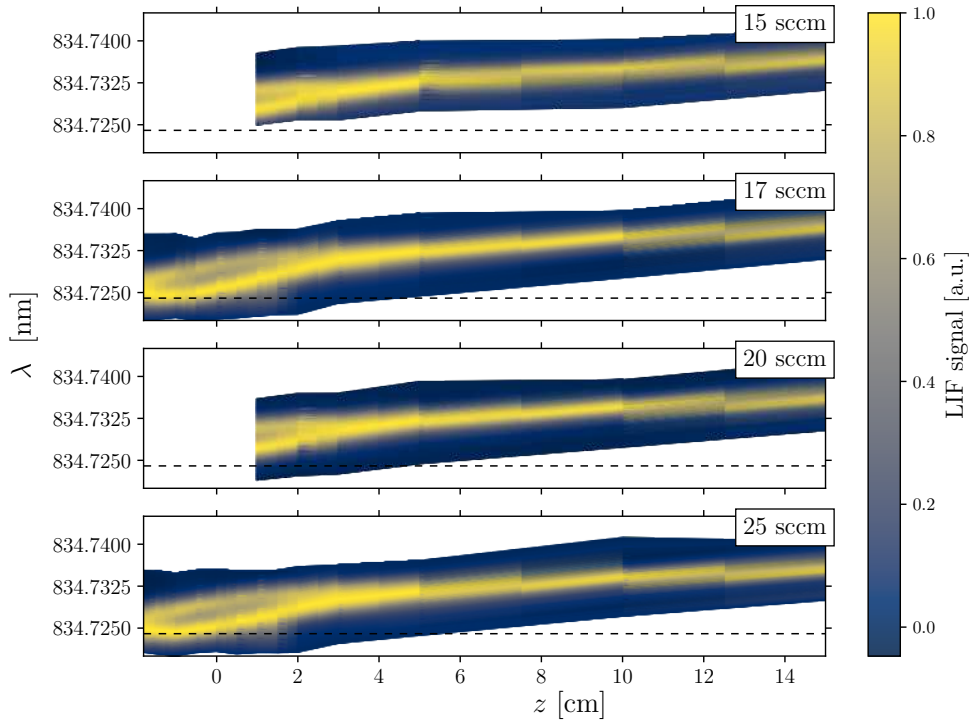
The LIF spectra recorded for the Xe atom are shown in Figure 4.3a for two values of the propellant mass flow rate. It is found that the profiles exhibit a double-peak shape in the region $-2 \lesssim z \lesssim 4.5$ cm. The gap between the two peaks is maximum at $z = 0$, it decreases with z and eventually the peaks merge completely behind the thruster exit plane at $z \simeq 5$ cm.

Figure 4.3b and Figure 4.4 report the Xe^+ LIF spectra recorded for several values of propellant mass flow rate and rf power, respectively. As discussed for the atoms, a double-peak lineshape is likewise observed also in this case in the region close to $z = 0$, i.e. where the magnetic field strength is maximum. In the Xe^+ profiles, the two peaks merge at $z \simeq 3$ cm and farther downstream the lineshape becomes almost

4.2. CONSIDERATIONS ON EXPERIMENTAL FINDINGS



(a) LIF spectra of Xe I resolved along z .



(b) LIF spectra of Xe II resolved along z .

Figure 4.3: On-axis LIF spectra of xenon atoms and ions resolved along z . The horizontal dashed line indicates the zero-velocity wavelength, cf. Table 2.2. Thruster input power is $P_{rf} = 350$ W.

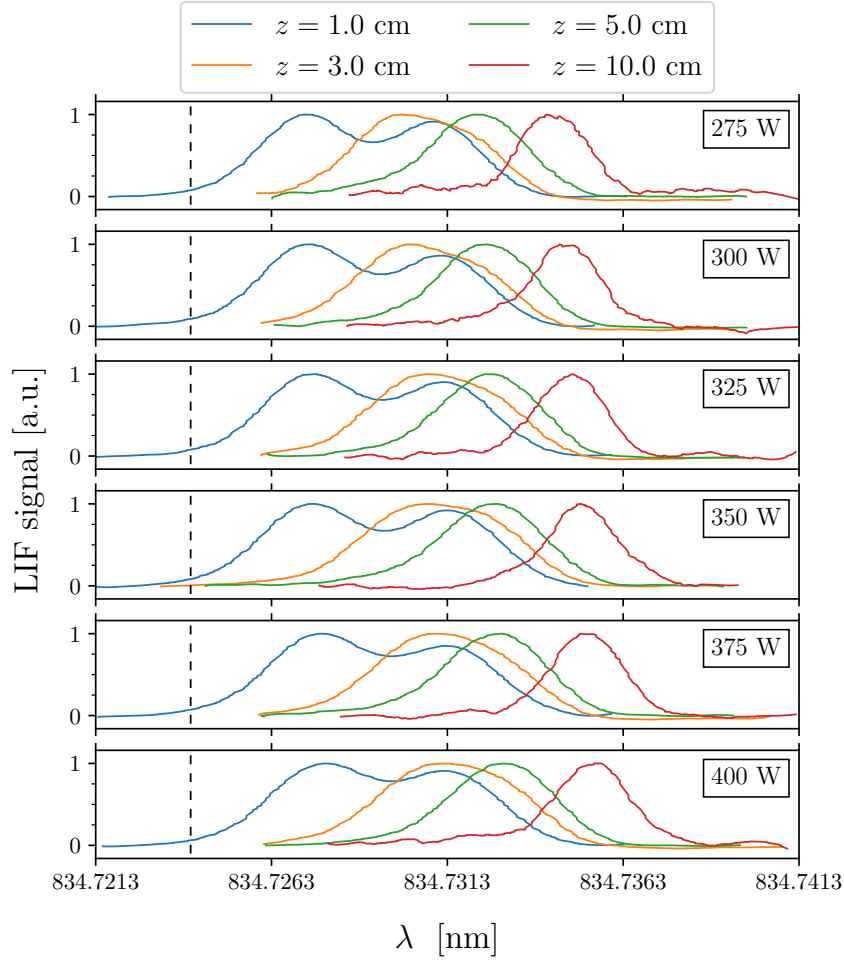


Figure 4.4: On-axis LIF spectra of Xe II resolved along z . The vertical dashed line indicates the zero-velocity wavelength, cf. Table 2.2. Thruster operation parameters are: $P_{rf} = 275$ W up to 400 W (from top to bottom), $\dot{m} = 17$ sccm.

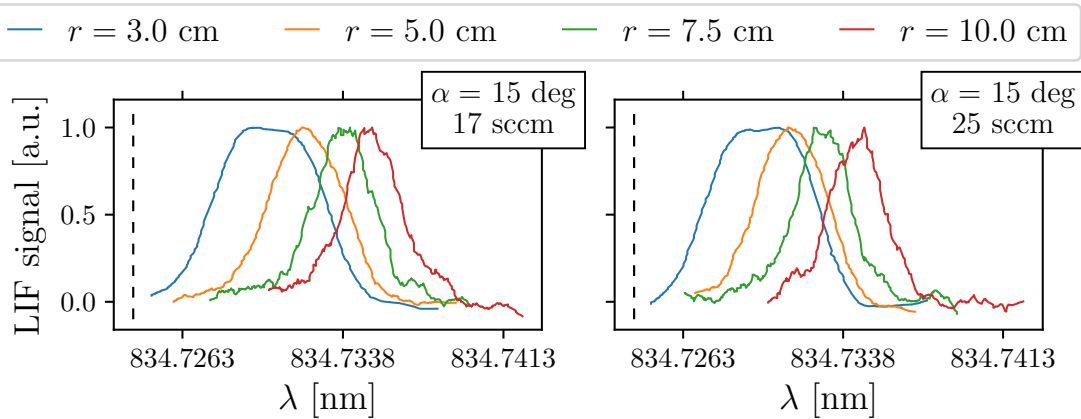


Figure 4.5: Examples of LIF spectra of Xe II from angular scan at $\alpha = 15^\circ$ for different radial distances. The vertical dashed line indicates the zero-velocity wavelength. Coordinates r and α are defined in Figure 4.2. Thruster operation parameters are: 350 W, (left) 17 sccm, (right) 25 sccm.

Gaussian, cf. Figure 4.4. With reference to the profiles measured far downstream, it follows that either a lower propellant mass flow rate or a higher input power increases the shift of the Gaussian centerline with respect to the zero-velocity wavelength. This allows anticipating that a larger axial ion velocity is expected when the HPT is operated at lower mass flow rates and higher levels of rf power.

LIF spectra on Xe^+ are also resolved along the angular direction α , which is defined in Figure 4.2. The probed region is delimited by $3 \leq r \leq 10$ cm and $0 \leq \alpha \leq 20^\circ$, where r is the distance from the center of thruster exit plane. Figure 4.5 shows examples of fluorescence lineshapes obtained at $\alpha = 15^\circ$ and different radii. At $r = 3$ cm, it is observed that the two peaks almost merge resulting in a spectrum that features a plateau at its center. A larger wavelength shift occurs at larger radii, in agreement with the previous spectra related to the axial velocity. This indicates that the velocity component orthogonal to the arc along which the measurements are taken is expected to increase downstream, picturing that the ions follow trajectories divergent from the thruster center line.

Since the spectra related to both Xe and Xe^+ exhibit relatively complex lineshapes nearby the thruster exit plane, the routine assumption that they image the local velocity distribution function (VDF) cannot be applied in this case. The most probable velocity of the probed species is given by the Doppler shift of the line center. However, when the fluorescence light profile does not feature a quasi-Gaussian shape, it is not possible to identify which peak of the profile corresponds to the shifted line center, making it impossible to accurately retrieve the most probable velocity. For this reason, it is necessary to model the expected lineshape by accounting for all the possible broadening mechanisms and fit the experimental profile thus to determine the accurate Doppler shift. Previous experiments relying on LIF have likewise observed a broadening of the recorded spectra, suggesting it was linked either to the Zeeman effect or to charge-exchange (CEX) collisions [49]. The occurrence of a population of slow ions resulting from CEX collisions cannot clarify the profiles recorded in this experiment. In fact, this hypothesis would not provide an explanation for the two peaks in the neutrals spectra as well as for the absence of slow ions farther downstream the exit plane. In Section 4.3, modeling of the atomic line profiles is addressed, proving that the form of measured lineshapes results from the Zeeman effect.

4.3 Modeling of fluorescence lineshape

Xenon has seven stable isotopes with abundance above 1 % [135]. Each isotope leads to the so called isotopic shift due to mass and volume differences in the nucleus. Isotopes with odd atomic number (^{129}Xe and ^{131}Xe) possess a non-zero nuclear spin I and therefore lead to the hyperfine structure (HFS). On top of that, the Zeeman effect further splits each spectral line into several components due to the presence of a relatively strong magnetic field. As a result, the absorption line comprises several optical transitions. The spectrum is modeled either in the weak or strong field approximation. The latter corresponds to the occurrence of the Paschen-Back effect. The choice of relying either on the weak or strong field approximation depends on the local strength of the external magnetic field in the context of the hyperfine interaction [136]. It is quantitatively assessed as customary by comparing the interaction energies associated with the

HFS and the magnetic field at each scanning location, i.e.

$$g_J \mu_B |\mathbf{B}| / A \ll 1 \quad \text{weak field} \quad (4.1)$$

$$g_J \mu_B |\mathbf{B}| / A \gg 1 \quad \text{strong field} \quad (4.2)$$

where g_J is the Landé g -factor, μ_B is the Bohr magneton, A is the magnetic dipole constant and $|\mathbf{B}|$ is the local magnetic field intensity. For what concerns the modeling of Xe I profiles, the weak field approximation is valid as long as the magnetic field intensity remains below ≈ 0.1 T, therefore it represents a justified assumption in the present experiment. Regarding the Xe II lines instead, distinction has to be done in function of the z -coordinate. Indeed, in the proximity of the thruster exit plane, the strong field approximation provides a more realistic picture for the ^{131}Xe lines as long as the magnetic field intensity exceeds ≈ 20 mT.

In practice, the whole modeling procedure consists in:

1. finding all the allowed optical transitions;
2. quantifying the associated detuning frequency;
3. determining the relative intensity of each line;
4. include Doppler broadening and Doppler shift to finally retrieve the lineshape.

This algorithm clearly needs to be implemented for the atoms and the ions separately.

In the weak field regime, the upper and lower energy levels of the probed transition are solved by determination of the total angular momentum F and the magnetic M_F quantum numbers for the hyperfine sub-levels, whereas the electronic angular momentum J and the magnetic M_J quantum numbers are required for the even isotopes [134, 137]. The hyperfine components are beforehand identified by the dipole-dipole selection rule $\Delta F = F - F' = [0, \pm 1]$, with $F = 0 \rightarrow F' = 0$ [136]. In the strong field case, F and M_F are undefined quantum numbers therefore the set (I, J, M_I, M_J) needs to be used instead. The allowed transitions are set by the values of $\Delta M_{F,J}$. The latter are selected by accounting for the laser polarization with respect to the magnetic field vector. As the light at the output of the optical fiber is unpolarized, when the measurement consists in performing an axial scan, the laser is shone in the direction of the magnetic field, therefore the polarization leads to the σ components ($\Delta M_{F,J} = \pm 1$) only. Though, when the angular scans are performed, a non-null angle does exist between the laser wavenumber vector and the local magnetic field vector. In the latter case, both σ and π components ($\Delta M_{F,J} = 0$) need to be accounted for. The selection rule $\Delta M_I = 0$ is additionally considered whenever the strong field condition is met. In the simplest case when only the σ components are allowed and the weak field approximation holds, the selection rules lead to 6 lines for each even isotope, 18 for ^{129}Xe and 54 for ^{131}Xe in the $6s^2 [1/2]_1^\circ \rightarrow 6p^2 [3/2]_2$ transition of Xe I. Regarding the $5d^2 [4]_{7/2} \rightarrow 6p^2 [3]_{5/2}^\circ$ transition of Xe II instead, the spectrum comprises 12 lines for the each even isotope, 36 for ^{129}Xe and 108 for ^{131}Xe . An instance of the allowed σ transitions due to hyperfine structure and Zeeman effect is shown in Figure 4.6 for ^{129}Xe isotope relative to the Xe I line at 834.682 17 nm. Several additional lines appear when the π components are included.

The energy shift of each transition is computed as the sum of three terms: the isotopic shift ΔE_{IS} , the contribution of the hyperfine structure ΔE_{hfs} , the contribution

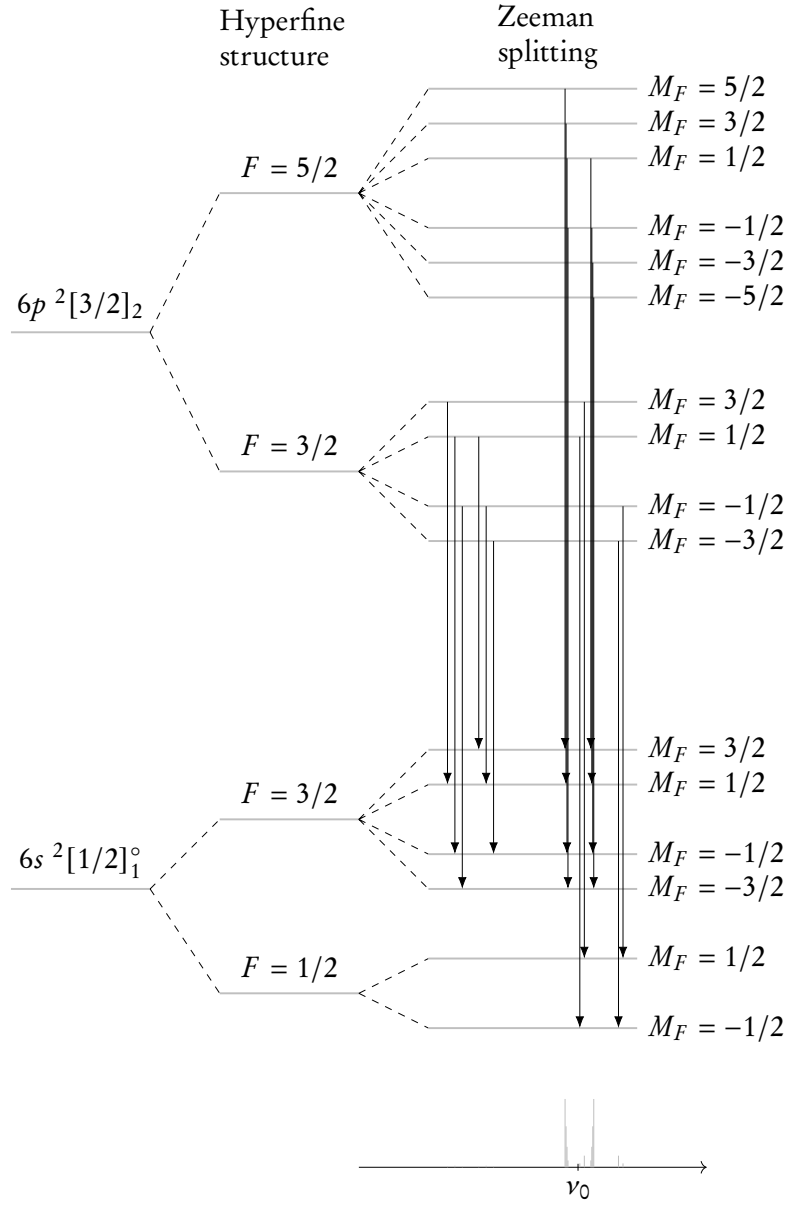


Figure 4.6: Instance of hyperfine and Zeeman components. Diagram relative to ^{129}Xe σ -transitions of the Xe I line at 834.682 17 nm. The lines are spaced in accordance with the computed detuning from the zero-velocity frequency ν_0 at $z = 0$. The relative intensity of each line is shown in the small graph at the base of the diagram.

Table 4.1: Order of magnitude of the reduced χ^2 to quantify the goodness of fit. A value $\chi^2 = 1$ indicates a good match between the model and the experimental profiles. The computed χ^2 for Xe I and Xe II accounts for all the experimental points related to Xe I and Xe II separately.

	χ_{red}^2		
	$z < 0$ mm	$0 < z < 20$ mm	$z > 20$ mm
Xe I	$\sim 10^1$	$\sim 10^0 - 10^1$	$\sim 10^0$
Xe II	$\sim 10^2$	$\sim 10^1 - 10^2$	$\sim 10^0 - 10^1$

of the Zeeman effect ΔE_Z . The values of ΔE_{IS} for the Xe I and Xe II lines here investigated are tabulated in [138] and [139], respectively. It is chosen to refer these shifts to ^{132}Xe since it is the most abundant isotope. The hyperfine structure term ΔE_{hfs} is nonzero for the odd isotopes only and it is the sum of magnetic dipole and electric quadrupole contributions [136, 137, 140]. The latter are function of the hyperfine constants A and B which can be found in [137, 141] for the two transitions used in this work. The last contribution to the total energy shift, i.e. ΔE_Z , is a function of the magnetic quantum number $M_{F,J,I}$, the strength of the magnetic field and the Landé g -factor g_F or g_J , depending on the isotope atomic number and weak/strong field regime. Complete expressions for ΔE_{hfs} , ΔE_Z and g_F can be found in [136]. The values of g_J and the nuclear magnetic dipole moments μ_I necessary to compute g_F are provided in [69, 142].

After the energy shift of each transition is known, the complete spectrum is built by determining the relative intensity. The equations of interest are reported in [136] for each of the π and σ components¹. They are function of F and M_F (J and M_J) for the odd (even) isotopes. The so computed intensities require to be weighted accounting for natural abundance of each isotope [135] and hyperfine components tabulated in [143] as a function of I , ΔJ and ΔF . Furthermore, in order to account for the laser polarization direction, the intensity of each π transition is scaled by $\sin(\theta)$, where θ is the local relative angle between \mathbf{k} and \mathbf{B} . The local vector \mathbf{B} is obtained from a 2-D numerical simulation which has been validated by measurements using a 3-axis gaussmeter.

At last, Doppler broadening of each transition is addressed. At this stage, two reasonable approximations are made: the laser beam profile is considered as a Dirac delta function due to its bandwidth (< 1 MHz), and the natural width (5 MHz) is neglected in comparison to the Doppler broadening full width at half maximum ($\simeq 0.65$ GHz at $T = 800$ K) [134]. It is assumed that ions and atoms share the same temperature. A Gaussian profile is applied to each component, exhibiting identical width and frequency shift. Eventually, the theoretical lineshape stems from the sum of all individual Gaussian profiles.

Figure 4.7 and Figure 4.8 illustrate two sets of the model outcomes compared to the experimental LIF spectra recorded in different locations of the plasma beam for atoms and ions, respectively. An additional comparison is provided in Figure 4.9 which refers to a scan performed at $\alpha = 15^\circ$. The spectra in Figure 4.7 and Figure 4.8 comprise the σ transitions only as \mathbf{k} and \mathbf{B} are parallel, whereas the π components had to be taken into account in modeling the spectrum shown in Figure 4.9. A kinetic temperature of 800 K

¹The results are obtained by direct substitution of $|JM_J\rangle$ and $|FM_F\rangle$ in the equations reported in [136]. The extent to which these intensities are approximations was not explored here.

4.3. MODELING OF FLUORESCENCE LINESHAPE

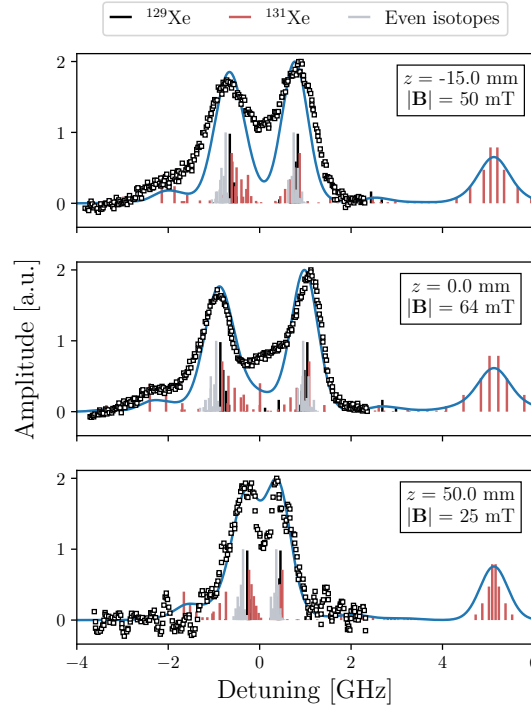


Figure 4.7: Experimental (squares) and modeled (line) lineshape for the $6s\ 2[1/2]_1^o \rightarrow 6p\ 2[3/2]_2$ transition of Xe I. The experimental data points are Doppler shifted to fit the model profile. Thruster operation parameters are: 350 W, 25 sccm.

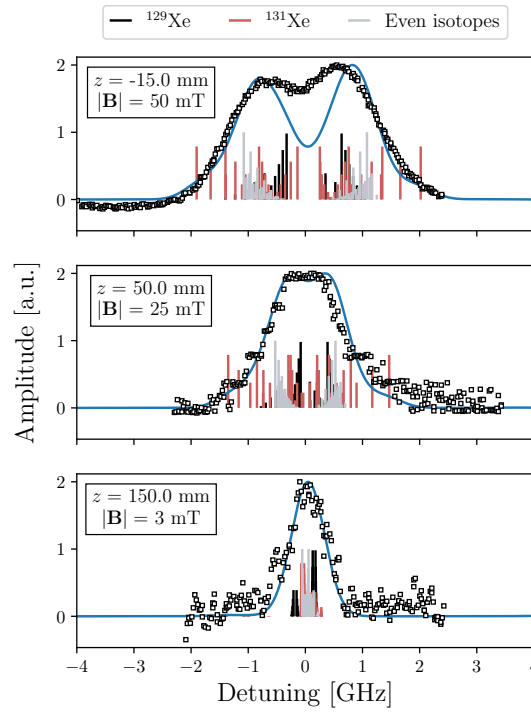


Figure 4.8: Experimental (squares) and modeled (line) lineshape for the $5d\ 2[4]_{7/2} \rightarrow 6p\ 2[3]_{5/2}$ transition of Xe II. The experimental data points are Doppler shifted to fit the model profile. Thruster operation parameters are: 350 W, 25 sccm.

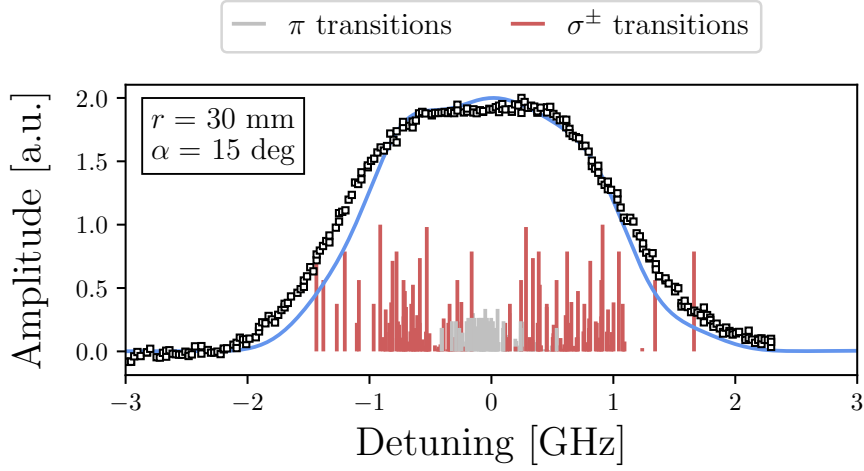


Figure 4.9: Experimental (squares) and modeled (line) lineshape for the $5d^2[4]_{7/2} \rightarrow 6p^2[3]_{5/2}^\circ$ transition of Xe II. The experimental data points are Doppler shifted to fit the model profile. The scan is performed at $r = 3$ cm and $\alpha = 15^\circ$. Thruster operation parameters are: 350 W, 17 sccm.

is used to fit the experimental profiles, which are Doppler shifted to overlap the model lineshape. It is observed that a portion of the Xe I spectrum has not been included in the experimental scan, cf. Figure 4.7. However, this fact is irrelevant considering that the focus here is on the Doppler shift. A poorly satisfactory match in the 0 GHz region is found for those profiles that exhibit a double-peak shape, for both Xe I and Xe II. In relation to this matter, the size of the laser beam and its alignment are possibly involved. For the spectra shown in Figure 4.7 and Figure 4.8, the model reasonably assumes that the excitation light is perpendicularly polarized with respect to the magnetic field. Yet, a slight misalignment and/or a relatively large probed volume would enable the occurrence of π transitions. The intensity of these transitions would be related to the angle between \mathbf{k} and \mathbf{B} . Nevertheless, it is virtually impossible to quantify this contribution. By manually implementing a non-zero angle between \mathbf{k} and \mathbf{B} in the simulation code, it is found that a misalignment in the order of $2-3^\circ$ is sufficient to visibly alter the 0 GHz region. These values are perfectly compatible with the uncertainty associated with the experimental setup and the magnetic field simulation accuracy. Besides, it shall be mentioned that the laser is vertically polarized at the output of the diode on the optical bench. Although the multi-mode $50\ \mu\text{m}$ fiber should not maintain any polarization, it may occur that a larger vertical component is preserved over the horizontal one. Given these experimental uncertainties, the goodness of fit requires a quantitative assessment. The reduced χ^2 , i.e. χ_{red}^2 , is herein used to estimate how well the model replicates the measured LIF profiles. Table 4.1 provides an overlook of the typical χ_{red}^2 computed for Xe I and Xe II in three different regions of the plasma plume. These values derive from gathering all the χ_{red}^2 's associated to each measurement position for each set of thruster operating parameters (input power and mass flow rate). It is observed that a large χ_{red}^2 characterizes the near-field region, whereas χ_{red}^2 of order unity is retrieved in the far-field. Given the important effects of the magnetic field on the fluorescence lineshape near the thruster exit plane, the aforementioned experimental uncertainties lead to a poorer agreement between model and measurements. This is however of little

4.4. ATOMS AND IONS VELOCITY PROFILES

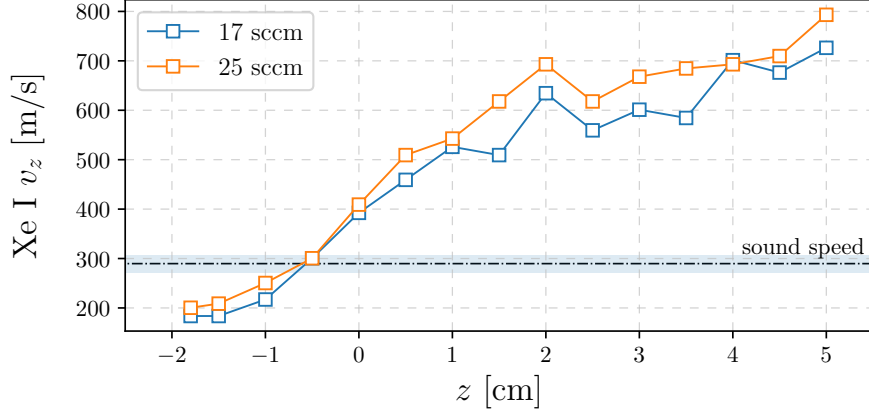


Figure 4.10: Axial velocity profile of Xe I for different propellant mass flow rates. Dash-dotted line indicates the sonic speed at $T = 800$ K, shaded area delimits the ± 100 K uncertainty interval. Thruster operating parameters are: 350 W, (blue) 17 sccm, (orange) 25 sccm.

relevance here since the main interest is to infer the most probable velocity.

In this regard, the most probable velocity is ultimately estimated from direct implementation of the Doppler shift equation [67]. This shift is equal to the off-set in the frequency axis that gives the best match between the experimental and modeled line-shapes with a precision of 10 MHz ($\approx 8 \text{ m s}^{-1}$). This procedure is clearly embedded in the simulation algorithm. The reference zero-velocity frequency ν_0 comes from previous experiments reported in [137] relying on two-beam saturated spectroscopy in a drift-free RF plasma. Altogether, this technique allows deducing the kinetic temperature and the most probable velocity with a reasonable accuracy. The error bar results from several contributing factor, such as the uncertainty on hyperfine constants and isotopic shifts in input, the quality of the raw data, the robustness of the fitting algorithm. Although the signal-to-noise ratio decreases downstream, the single-peak shape of the recorded profiles simplifies the fitting procedure. By exploring the full range of uncertainties of the input constants to the model (i.e. isotopic shifts and hyperfine constants) and different filtering parameters on the noisy signals, it is estimated that the typical uncertainty is in the order of $\pm 10 \text{ m s}^{-1}$ and $\pm 100 \text{ K}$ for the velocity and temperature, respectively.

4.4 Atoms and ions velocity profiles

The velocity profiles of Xe and Xe⁺ herein reported are extracted by means of the model illustrated in Section 4.3. The value of the kinetic temperature is fixed to 800 K for both species since it fits well the experimental data.

Figure 4.10 displays the evolution of the atoms axial velocity along the thruster center line. This data is deduced from the LIF spectra in Figure 4.3a. It is found that the neutrals drift towards the exit plane with a velocity smaller than the thermal speed ($v_{th} = \sqrt{8k_B T_i / \pi m_i} \approx 365 \text{ m s}^{-1}$ at 800 K). Then, the atom velocity increases within a few centimeters over the thruster exit plane up to 700 – 800 m s^{-1} . Note that at 800 K

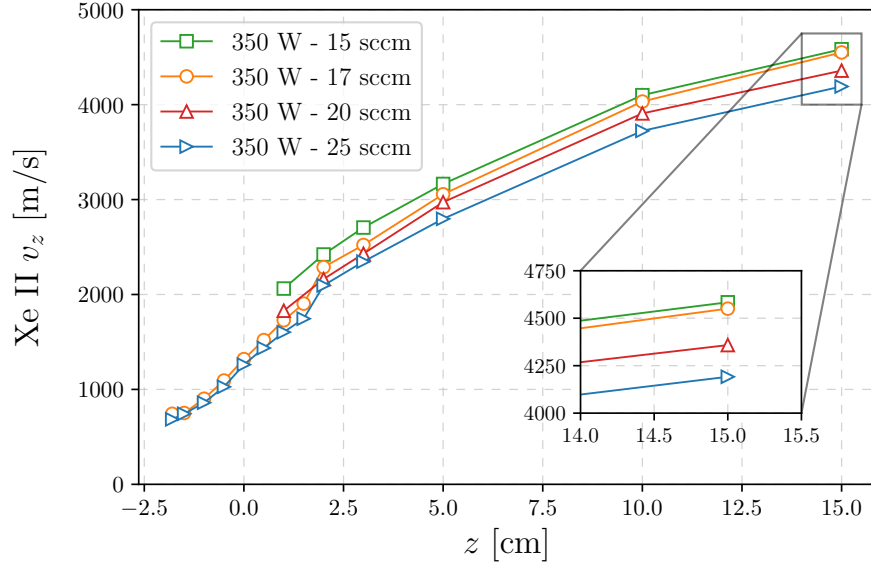


Figure 4.11: Axial velocity profile of Xe II for different propellant mass flow rates.

and with $\gamma = 5/3$, the sound speed reads $v_s = \sqrt{\gamma k_B T_i / m_i} \approx 295 \text{ m s}^{-1}$. Thus, the neutrals reach the sonic point in the proximity of the thruster outlet and expand supersonically within the plume. This behavior is not visibly influenced by a different value of the propellant mass flow rate. Similar upper values of the neutrals axial velocity have been found also in Hall thrusters [134]. This relatively high speed of the atoms is likely to result from various contributing phenomena. Inside the discharge chamber, the ions naturally recombine at the walls. They are reflected back with a fraction of the momentum carried before the recombination and therefore populate the high energy wing of the atoms distribution function. Ion-neutral elastic collisions may likewise contribute to increase the most probable atom velocity. The neutrals largely dominate the discharge chamber with a particle density of $\sim 10^{20} \text{ m}^{-3}$, derived from mass flow conservation and assumed uniform everywhere. As a result, the mean free path for ion-neutral momentum transfer collisions reads $\lambda \approx 3.5 \text{ mm}$ using an equivalent cross section $\sigma_{el} = 2 \times 10^{-18} \text{ m}^2$ at about 1 eV of ion energy [144]. For comparison, the cross section associated with CEX collisions reads $\sigma_{CEX} \approx 0.8 \times 10^{-18} \text{ m}^2$ [145], thus showing that elastic collisions are about 2.5 times more likely than CEX collisions. Furthermore, the slow wing of the atoms distribution function is selectively depopulated in the high electron density region, i.e. close to the magnetic nozzle throat, due to the relatively longer residence time that leads to higher ionization probability.

The profiles of the ions axial velocity are reported in Figure 4.11 and Figure 4.12 for several values of the propellant mass flow rate and input power, respectively. These profiles derive from the data shown beforehand in Figure 4.3b and Figure 4.4. For all the tested working points, it can be noticed that the ions still experience a non-negligible momentum gain several centimeters downstream the thruster exit plane. The evolution of the ion velocity at $z \lesssim 2 \text{ cm}$ is not visibly influenced by the thruster working condition. Indeed, all the profiles tend to merge close to the thruster exit plane. The ions leave the discharge chamber with a drift velocity of about 1.4 km s^{-1} . Assuming a conservative value of the local electron temperature of 4 – 5 eV at $z = 0$ according to previous measurements taken in a similar device [35], the Bohm speed equals $1.7 - 1.9 \text{ km s}^{-1}$. It

4.4. ATOMS AND IONS VELOCITY PROFILES

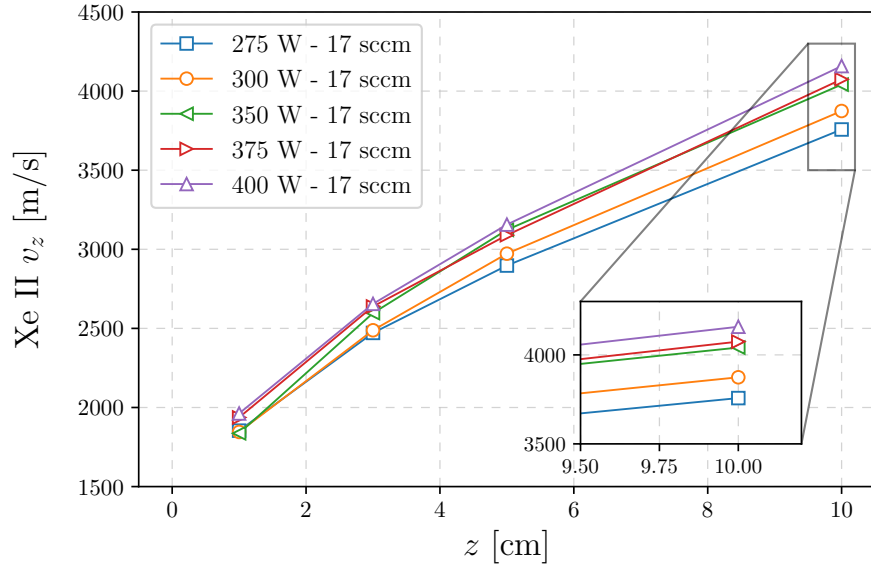


Figure 4.12: Axial velocity profile of Xe II for different levels of input power.

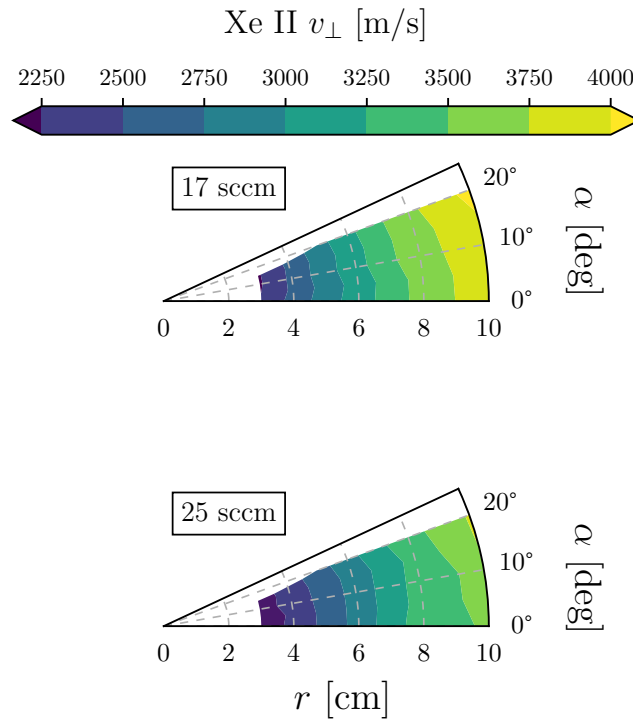


Figure 4.13: Contour maps of the most probable ion velocity perpendicular to the scanning arc.

clearly means that the sonic condition is reached downstream the throat of the magnetic field, in contrast with the ideal gas-dynamics analogy of the plasma expansion as routinely postulated in fluid models [46, 47]. Previous experiments in inductive and ECR thrusters [49, 96, 97, 109] have similarly observed a subsonic ion flow in correspondence of the magnetic nozzle throat. In this experiment, by accounting for positioning uncertainties in the experimental setup, the axial shift of the sonic transition is in the order of several millimeters, which is consistent with the findings reported in [49, 96]. Given that a single population of ions dominates the LIF spectra in this experiment, CEX collisions cannot explain the shifting of the sonic point. On the other hand, ion-neutral elastic collisions, electron-neutral collisions and ionization within the plume may represent a pivotal explanation to the axial shift of the sonic transition [97, 109]. The occurrence of ion-neutral collisions is compatible with the observed atom velocity profiles shown in Figure 4.10, as previously discussed.

The effect of a different working point of the thruster becomes more evident far downstream, cf. Figure 4.11 and Figure 4.12. A larger ultimate velocity is recorded at lower mass flow rates and higher input powers, as anticipated in Section 4.2. Altogether, the highest value of the ion axial velocity reads about 4600 m s^{-1} at $z = 15 \text{ cm}$, obtained for 350 W and 15 sccm.

The contour plots in Figure 4.13 show the most probable ion velocity related to the angular scans when the thruster operated at 17 sccm and 25 sccm. It is worth noting that the velocity in Figure 4.13 corresponds to the component that points in the direction identified by the angle α , see Figure 4.2. At small radial distances, the velocity remains nearly constant along the scanning arc. This suggests that the expanding plasma identifies a spherical surface centered at the thruster exit. Farther downstream, instead, measurements reveal that v_{\perp} is larger at larger angles, outlining that the spherical symmetry is broken. This is also confirmed by visual inspection of the thruster during operation. Consistently with the trend of the axial velocity profiles shown in Figure 4.11, a lower propellant mass flow rate implies faster ions.

4.5 Comparison of RPA and LIF spectroscopy results

The ion beam energy is additionally probed using the RPA described in Section 2.2.6 for the purpose of comparing the two measurement techniques. A consequence of the discussion reported in Section 4.2 and 4.3 is that the intense magnetic field in the close-field region prevents a direct comparison of the ion VDF retrieved with the two diagnostics simply because the LIF profile does not picture the true ion VDF. For this reason, measurements are performed and compared at a single point far downstream where the RPA does not substantially interfere with the plasma beam and the fluorescence signal still manifests a good signal-to-noise ratio while being negligibly altered by the magnetic field. The choice of a single point also stems from the fact that an extended scan, either along the axial or angular direction, is prohibited by alignment limitations due the nature of the radial-polar translation system whenever multiple probes are employed (RPA and RFCLP in this particular case).

In short, the experimental setup related to the RPA measurements is schematically depicted in Figure 4.2. The RPA and the RFCLP are mounted on the translation stage in such a way that they are both aligned with the thruster axis at $z = 12 \text{ cm}$. Data from the two probes are acquired nearly simultaneously after prior rotation of the arm system to

4.5. COMPARISON OF RPA AND LIF SPECTROSCOPY RESULTS

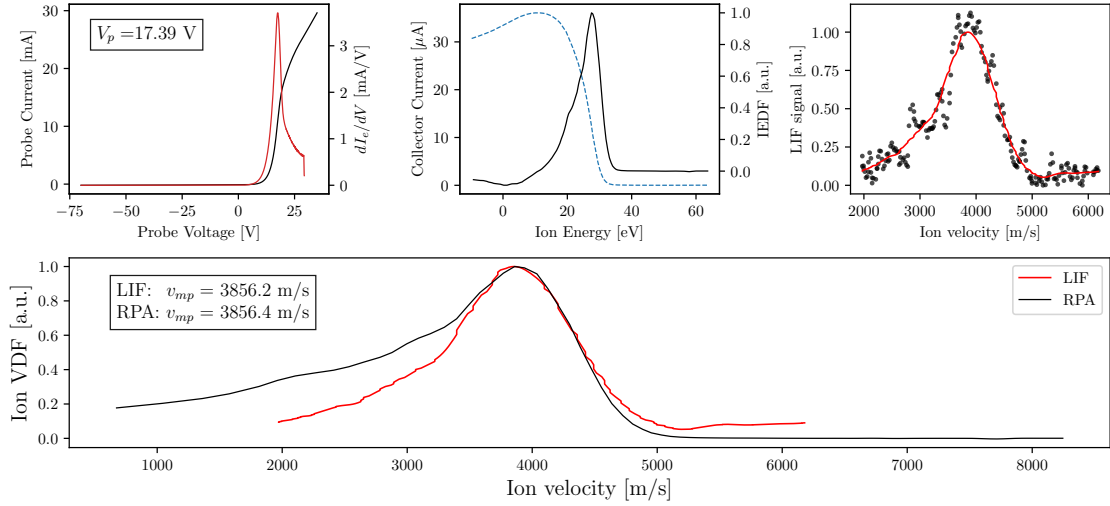


Figure 4.14: Example of dataset acquired to compare LIF and RPA measurements. (top-left) Langmuir probe I-V curve and I_e derivative, (top-center) RPA I-V curve and its derivative, (top-right) LIF spectrum, (bottom) ion VDF comparison. Thruster operation parameters are: $P_{rf} = 350$ W, $\dot{m} = 20$ sccm Xe.

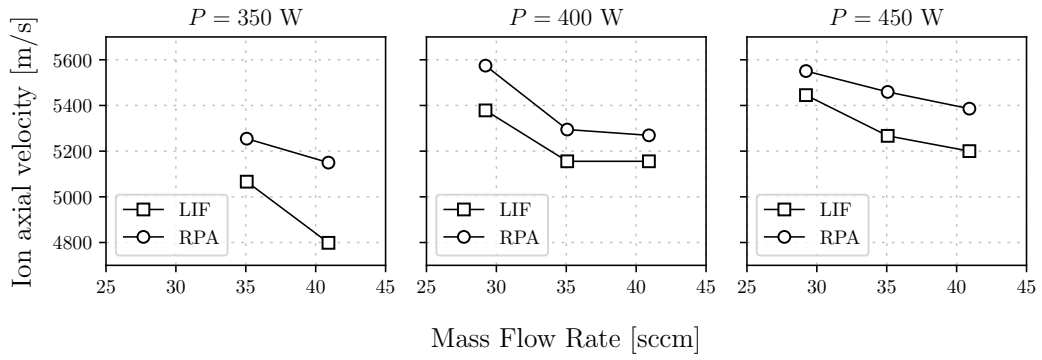


Figure 4.15: Most probable axial velocity of Kr ions probed with RPA and LIF at different levels of P_{rf} and \dot{m} .

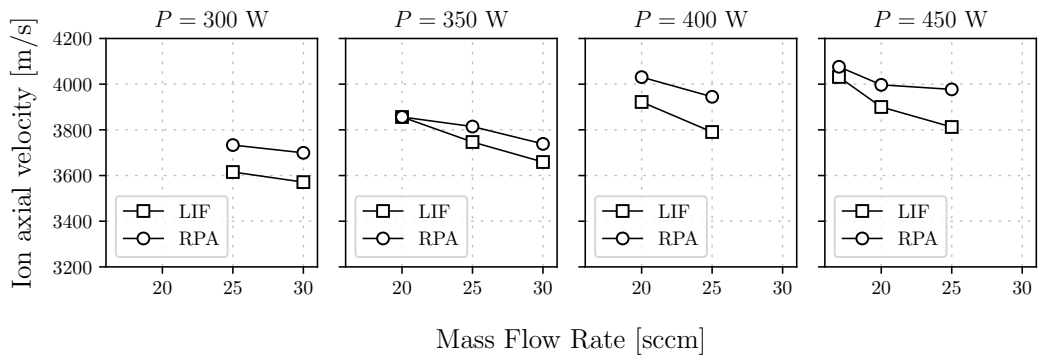


Figure 4.16: Most probable axial velocity of Xe ions probed with RPA and LIF at different levels of P_{rf} and \dot{m} .

ensure proper alignment of each probe. It shall be remarked that LIF and RPA measurements are performed over different days. The TU is operated with both krypton and xenon propellants under different values of input power and mass flow rate. For each operational point, the associated dataset comprises of an I-V curve from the RFCLP, an I-V curve from the RPA and a fluorescence profile from LIF, as exemplified in Figure 4.14. The resulting axial ion velocity probed with the two instruments is plotted in Figure 4.15 and 4.16 for krypton and xenon, respectively. These values are extracted from the LIF and RPA velocity profiles in correspondence of the peak, therefore they represent the most probable axial velocity. It is observed that the two measurement techniques are in reasonably good agreement. In general, the ion velocity determined with the RPA always results larger than that measured with LIF spectroscopy. The mean difference between the two measurements is 184.0 m s^{-1} with a standard deviation of 71.9 m s^{-1} when operating the thruster with krypton, whereas a mean difference of 96.3 m s^{-1} with a standard deviation of 47.7 m s^{-1} are observed in the case of xenon. These discrepancies are close to the accuracy of the LIF setup set by the wavemeter resolution. From Figure 4.14, it can be deduced that the ion VDF from both LIF and RPA is slightly asymmetric, which is possibly due to the presence of slow ions. These can result from ion-neutral and charge-exchange collisions, as previously discussed in Section 4.4. However, a detailed comparison of the VDF resulting from the two techniques is out of the scope of this study because several phenomena contribute altering its shape. Indeed, hyperfine structure and magnetic field do not allow measuring the unperturbed ion VDF using LIF, whereas the I-V curve from the RPA is sensitive to the specific device, the presence of secondary electrons, ionization and charge-exchange collisions occurring inside the probe.

4.6 Summary and conclusion

Plasma flow velocity has been spatially resolved using laser-induced fluorescence spectroscopy and a retarding potential analyzer in the magnetic nozzle of a Helicon plasma thruster operating under several conditions. The most probable ion axial velocity obtained with two instruments is compared in a single point of the far-field plume when the thruster operates with Xe and Kr propellants. It is found that the two diagnostics are in good agreement. In all tested conditions, the ion velocity measured with the RPA is larger than that resulting from LIF. The mean relative difference between the two techniques is in the order of 2–3 % accounting for all explored operating conditions.

Xenon atoms and ion dynamics is studied inside and outside the discharge chamber via LIF. In the near-field plume, the intense magnetic field induces the Zeeman effect, leading to a relatively complex shape of the fluorescence spectra. Consequently, it results impossible to accurately deduce the atoms and ions velocity in the strong magnetic field region without prior modeling of the atomic lineshape. Hence, this task is addressed by accounting for broadening mechanisms, namely isotopic shift, hyperfine structure and Zeeman effect. Fitting of the modeled and measured profiles allowed inferring the evolution of the most probable velocity both for the Xe atoms and ions. It is found that the neutrals axial velocity increases up to supersonic values downstream the thruster exit plane. This phenomenon is associated with parallel occurrence of several processes. The fast atoms wing of the distribution function is populated because of flow expansion, ions recombination at the walls and ion-neutral momentum transfer collisions, whereas the

4.6. SUMMARY AND CONCLUSION

slow atoms wing is selectively depopulated because of ionization. The axial evolution of the ions velocity uncovers the effect of the thruster working parameters. Faster ions are obtained at lower mass flow rates and higher levels of input power. The velocity profiles also show that the acceleration region extends several centimeters downstream the exit plane. The largest Xe ion velocity recorded in the probed region is about 4600 m s^{-1} at $z = 15 \text{ cm}$ for 350 W of input power and 15 sccm of mass flow rate.

The experimental findings reported in this chapter contribute to advance in understanding the ions and atoms dynamics in a magnetic nozzle. Development and validation of numerical models can largely benefit from the data herein presented. A parallel numerical and experimental investigation of the near-field atom and ion dynamics under different working conditions would further assist in clarifying the current picture. Implementation of collisions and wall recombination phenomena in particle-in-cell models is particularly advised. It is clearly of interest to conduct a system parametric analysis targeting a larger ultimate ion velocity in view of developing an efficient electric propulsion system.

Chapter 5

Ion dynamics in the magnetic nozzle of a waveguide ECRT

This chapter reports on results derived from an experimental campaign carried out in collaboration with the EP team at Universidad Carlos III in Madrid. The relevance of this analysis is to assess the ion dynamics in the plume and in the discharge chamber of a waveguide ECRT via near-infrared laser-induced fluorescence spectroscopy. Although the MN physics is common to other devices, these measurements represent the first ever reported for a waveguide thruster, therefore being of key importance for validating future MN models and plasma simulations. At first, an introduction about ECRTs is provided in Section 5.1. The experimental arrangement is detailed in Section 5.2; after commenting on the recorded spectra in Section 5.3 and discussing the procedure to infer the velocity profiles through lineshape modeling in Section 5.4, the results are presented in Section 5.5.

5.1 Introduction to ECR thrusters

The Electron Cyclotron Resonance Thruster (ECRT) is of central interest in the electrodeless thrusters class, as it exhibits interesting performance metrics [110]. The working principle of an ECRT relies on the electron cyclotron resonance to efficiently transfer power from an electromagnetic wave (typically in the microwave range) to the electrons, rising their perpendicular temperature. This phenomenon occurs locally at the resonance layer, where the condition $\omega_{ce} = \omega$ is met, being $\omega_{ce} = eB/m_e$, the electron cyclotron angular frequency and ω the frequency of the externally supplied electromagnetic wave [52, 146]. The conversion of electron thermal energy into ion kinetic energy is then conveyed by the plasma expansion in the magnetic nozzle [47]. The discharge and acceleration mechanisms thus require the existence of an externally applied magnetic field.

Two different microwave injection designs have been reported in literature for ECRTs, the coaxial [49, 110, 147, 148] and the truly electrodeless circular waveguide design [18, 149–152]. In the first case, a central conductor is present in the plasma chamber which can be seen as an extension of the coaxial cable delivering the microwaves from the source to the thruster. This component is subject to strong erosion and heat loads and it is absent in the waveguide version. The way microwave power is coupled to the plasma

5.2. EXPERIMENTAL SETUP

appears to be a relevant factor for electron heating and consequently ion acceleration. Lower performance levels have been reported for the waveguide configuration [148] for similar operating conditions (input microwave power of 25 W at 2.45 GHz, 1 sccm of Xenon) and thruster dimensions.

5.2 Experimental setup

Figure 5.1 shows a schematic view of the experimental arrangement in the vacuum chamber facility at the University of Carlos III de Madrid (UC3M). The thruster unit is shown at the top and a detailed description is available in [50]. It mainly comprises a circular waveguide constituting the plasma chamber (PC) and a magnetic field generator. The latter, is made up by two separate components: a permanent magnet (PM) and an electromagnet. The PM consists of a radially magnetized ring, which is made of twelve Sm-Co YXG-32 magnets glued together and enclosed in an aluminium box. The brown solid line in Figure 4.1(a) depicts the magnetic field strength produced by the PM along the thruster axis. On the other hand, the electromagnet can be used to alter the shape of the MN and displace the resonance position. The effects of the electromagnet on the magnetic field strength and divergence are shown in figures 5.2(a)-(b) and 5.3.

The microwave frequency used is 5.8 GHz, allowing for smaller waveguide dimensions than the usual 2.45 GHz frequency, and consequently lowering the size of the device, its mass flow rate and power requirements. A higher frequency comes with the need of a stronger field for reaching the resonance condition ($B_{res} = 0.207$ T at 5.8 GHz). The field generated by the PM alone suffices the ECR condition inside the PC.

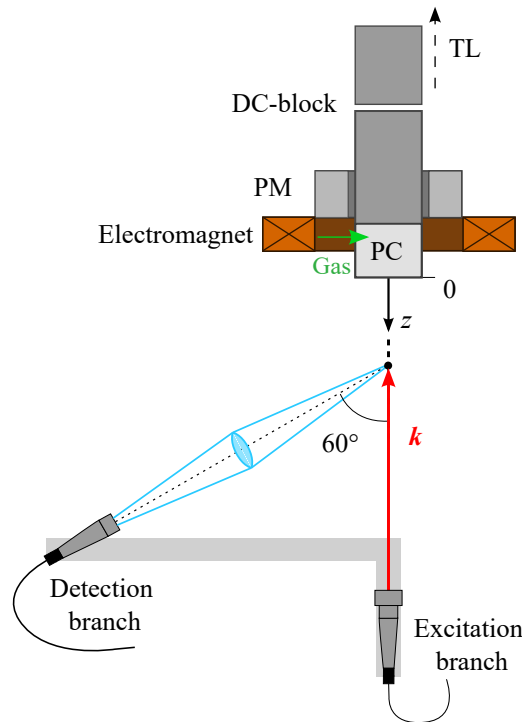


Figure 5.1: Schematic top view of the experimental setup. The thruster unit (top) and optical arrangement (bottom) are shown. Drawing not in scale.

5. ION DYNAMICS IN THE MAGNETIC NOZZLE OF A WAVEGUIDE ECRT

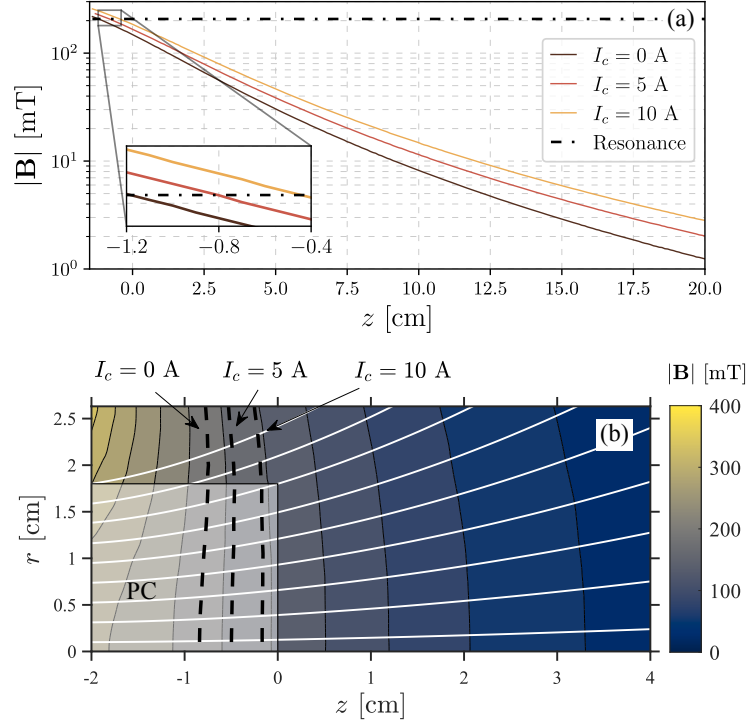


Figure 5.2: (a) Measured axial profiles of the ECRT magnetic field amplitude. The dash-dotted line indicates the resonance at 5.8 GHz. (b) Simulated 2-D maps of the MN highlighting the ECR surface as a function of I_c . $z = 0$ refers to the exit plane of the discharge tube.

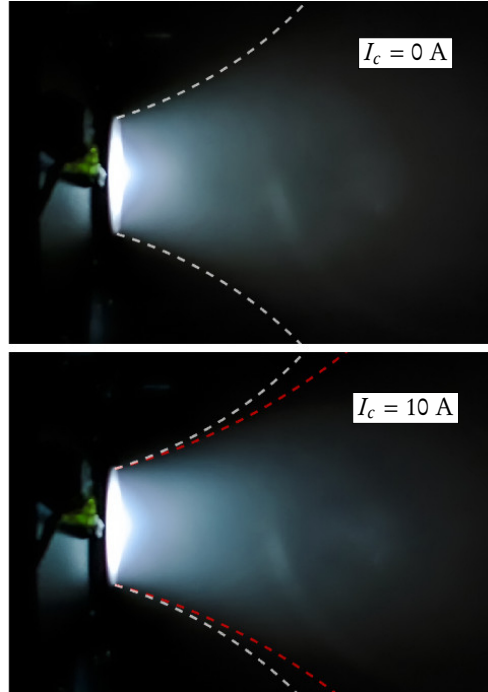


Figure 5.3: Photographs of the thruster in operation with two different magnetic nozzle shapes. The magnetic streamlines passing from the walls at the exit plane are shown with dashed lines, white for $I_c = 0$ A, red for $I_c = 10$ A.

The PC is made of stainless steel. Its diameter and length are $D_T = 36$ mm and $L_T = 20$ mm. The PC is separated from the aluminium circular waveguide at the back by a quartz window sealed with a FFKM o-ring. Xenon gas is injected radially in the PC from twelve, 1 mm diameter holes located at $z = -18$ mm on the lateral PC walls.

Microwave power is delivered from the source to the thruster through a waveguide transmission line (TL). More information on the TL used for this work can be found in reference [50] and [153]. The thruster waveguide and consequently the PC is electrically floating with respect to the rest of the TL. This is made possible by a vacuum-gap DC-block consisting of two waveguides aligned and separated by a distance of 2 mm. Negligible power ($< 2\%$) is lost if the gap is smaller than 3 mm. The thruster floating potential V_T was measured during the overall test campaign. Using the same nomenclature as in [50] the power associated to each of the spectra shown in the following sections is the forward power P_F measured with a directional coupler. P_F differs from the actual power delivered to the thruster, since some power is reflected back to the generator and some is absorbed in the transmission line. As well as P_F , the reflected power is measured with a directional coupler, whereas the transmission line power absorption has been characterized with a Vector Network Analyzer. In general, the power coupled to the plasma is estimated to be between 15 – 20 % lower of P_F for the tested operating point. A change in the operating conditions i.e. input power, mass flow rate or electromagnet current, can affect the amount of reflected power. A waveguide stub tuner has been used to keep its value always below 5 % of P_F .

Experiments are performed in the vacuum facility previously detailed in Section 4.1. Referring to Figure 5.1, LIF optics are positioned in front of the thruster and mounted on a linear translation stage. The description provided in Section 4.1 applies also for this experiment. The complete description of the optical diagnostics is available in Section 2.2.7.

5.3 Observed spectra

Fluorescence spectra are resolved along the thruster axis in a region that extends from $z < 0$ up to several centimeters downstream the exit plane. The farthest distance being probed is limited by the signal-to-noise ratio of the recorded spectra and it depends on the thruster operating conditions. Signal acquisition has been possible up to $z = 20$ cm at low mass flow rate. Close to the exit plane, the entire fluorescence profile covers a range of about 15 GHz, therefore three separated frequency scans needed to be recorded and merged during post-processing.

A typical series of axial scans is shown in Figure 5.4. It is observed that the fluorescence profiles feature a double-peak shape in the proximity of $z = 0$. At larger axial distances, the two peaks merge resulting in a broad profile (e.g. at $z = 5$ cm in Figure 5.4) that eventually reduces to a narrow Gaussian-like spectrum farther downstream. Qualitatively similar results have been observed in a recent experiment performed on a helicon plasma thruster [154]. Starting from the raw lineshapes, the most probable velocity of the probed species is given by the Doppler shift of the line center. However, when the fluorescence light profile does not feature a quasi-Gaussian shape, the shifted line center cannot be easily identified, making it impossible to accurately retrieve the most probable velocity. Following the discussion reported in [154], the raw spectra recorded near $z = 0$ do not image the local ion velocity distribution function (IVDF). The rel-

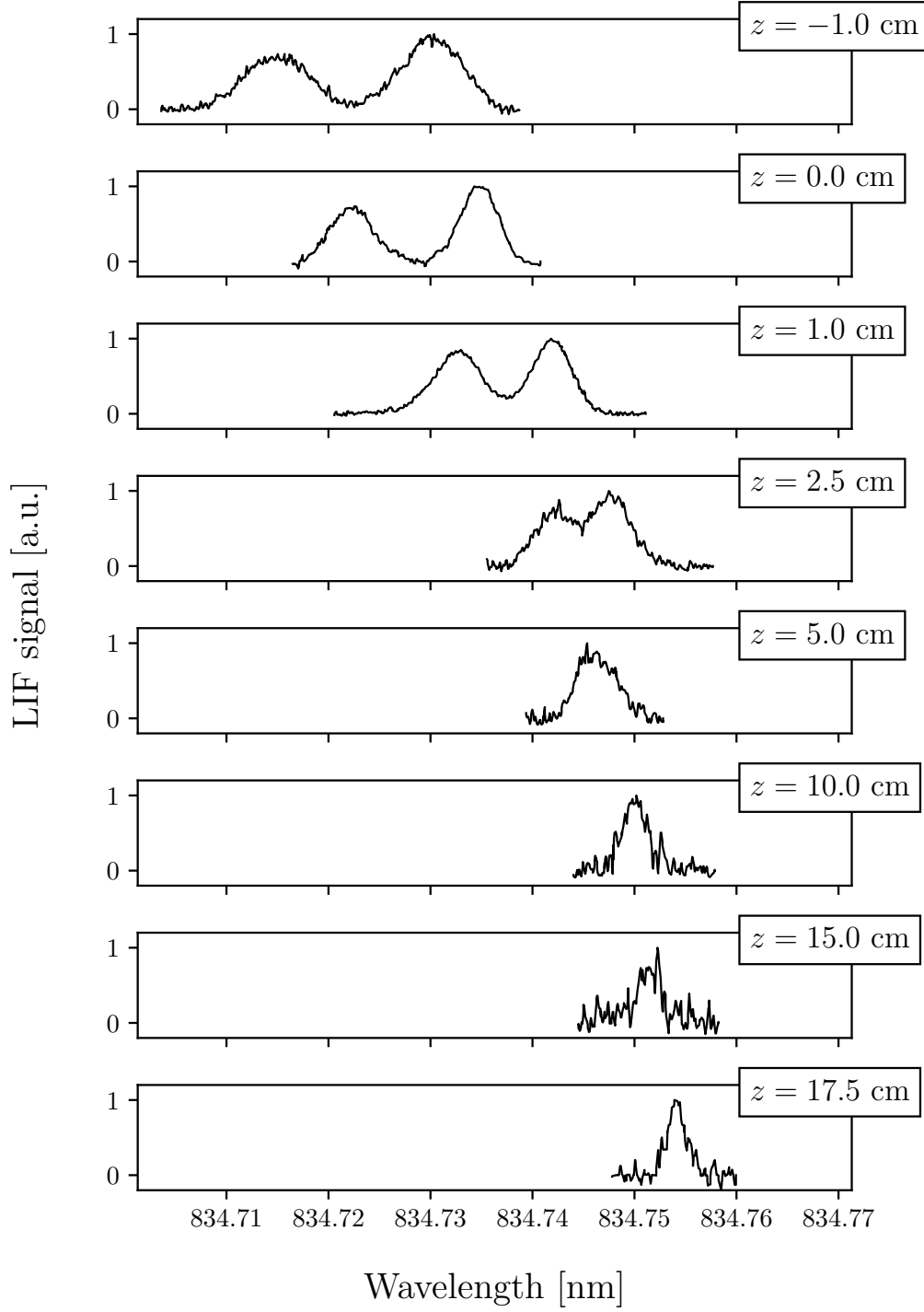


Figure 5.4: LIF spectra resolved along z . Wavelength values are expressed for air. Thruster operation parameters are: $P_F = 200$ W, $\dot{m} = 2$ sccm, $I_c = 0$ A.

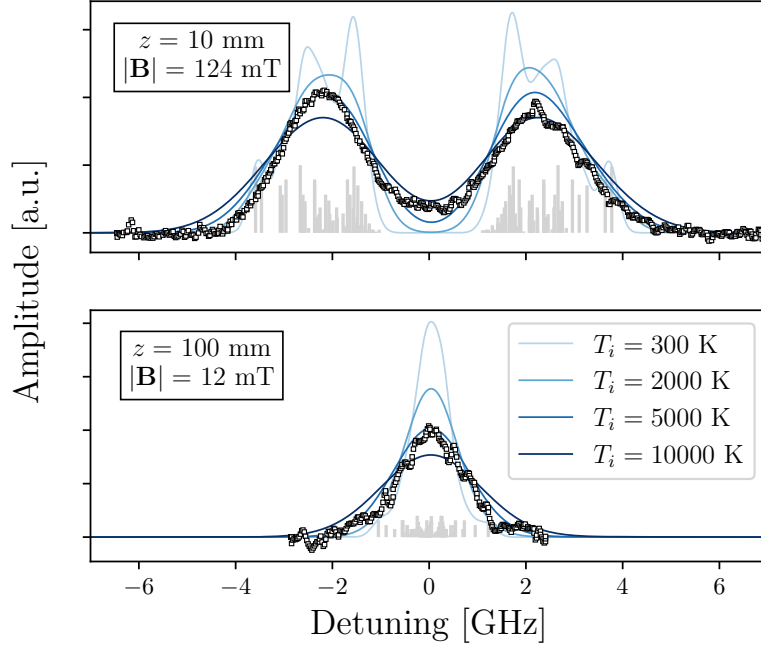


Figure 5.5: Comparison of experimental (squares) versus modeled (solid lines) lineshapes using arbitrary values for T_i . The experimental data points are Doppler shifted to fit the model profiles. The bar plot images the allowed optical transitions. Thruster operation parameters are: $P_F = 200$ W, $\dot{m} = 2$ sccm, $I_c = 5$ A.

actively strong magnetic field inside the source and in the near-field plume determines the splitting of the energy levels. This phenomenon leads to a complex lineshape as exemplified in Figure 5.4. Other LIF studies on ECR thrusters [49, 109] did not observe such a prominent effect on the experimental profiles. This fact has been attributed to the weaker magnetic field within the probed domain [109]. In the current experiment, it is found that departure from a quasi-Gaussian profile occurs at field strengths greater than ~ 30 mT. As a result, modeling of the fluorescence profiles needs to be addressed for the accurate determination of the ion velocity.

It is worth mentioning that the presence of multiple populations ions, e.g. resulting from charge-exchange (CEX) collisions, cannot justify the profiles recorded in this experiment. In fact, this hypothesis would not provide an explanation for the absence of slow ions farther downstream the exit plane.

5.4 Modeling of fluorescence lineshape

In this experiment, the fluorescence profiles are reconstructed using the same model detailed in Section 4.3. The only difference in this case relates to the way the ion kinetic temperature T_i is estimated, since it is a free parameter in the analysis. The value of T_i is linked to the width of which Gaussian component constituting the spectrum therefore it indicates the spread in the axial ion velocity. As an example, Figure 5.5 shows two experimental profiles along with a few theoretical lineshapes computed using arbitrary values of T_i for the sake of comparison. In this case, one can observe a good agreement with the

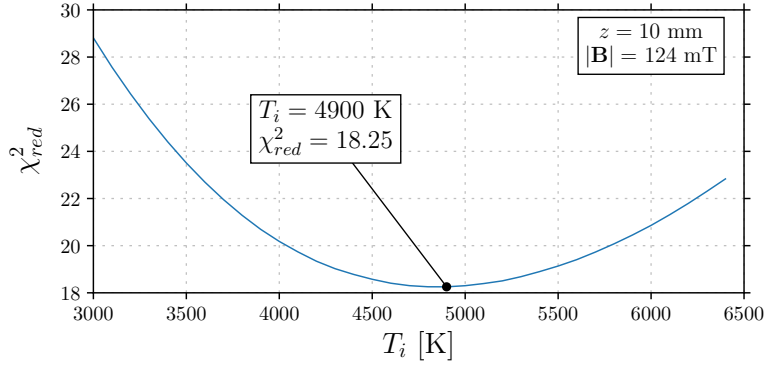


Figure 5.6: Instance of χ_{red}^2 evolution with T_i . The highlighted point at $T_i = 4900$ K identifies the value that best fits the spectrum recorded at $z = 10$ mm, whereas T_i that minimizes $\bar{\chi}_{red}^2$ of the whole series equals 4700 K. These data are relative to the set of profiles recorded at: $P_F = 200$ W, $\dot{m} = 2$ sccm, $I_c = 5$ A.

experimental data when $T_i \approx 5000$ K. For a more consistent determination of T_i , the algorithm relies on the computation of the reduced- χ^2 metric (χ_{red}^2), which quantifies the goodness of fit given the experimental and theoretical lineshapes. For a fixed set of thruster operating parameters, χ_{red}^2 is computed for each spectrum and then averaged over all spectra giving $\bar{\chi}_{red}^2$. By that means, T_i is chosen with a resolution of 100 K as the value that outputs a value of $\bar{\chi}_{red}^2$ closer to 1. An example of how χ_{red}^2 evolves as a function of T_i is provided in Figure 5.6. In doing so, it is intrinsically assumed that T_i does not change throughout the plasma expansion. However simplistic, this procedure did not show the need to consider different values of T_i as the axial position z varies. In fact, it shall be shown later that the theoretical and experimental profiles are generally found to be in good agreement. A different approach would consist in computing the ion kinetic temperature that provides the best fit for each individual measured lineshape, so as to yield a function in the form of $T_i(z)$ for a fixed set of thruster operation parameters. For further completeness, an implementation of this kind has been performed within the fitting algorithm. However, as a general remark, no clear trend of T_i associated with the axial coordinate is found. Thus, a relatively small ($\leq 10\%$) difference in T_i along z is most probably related to concurrent uncertainties, e.g. noise level, quantum constants, robustness of the fitting algorithm, thruster stability at fixed operation parameters, departure from equilibrium. Therefore, this more general analysis suggests that the proposed use of $T_i(z) = T_i$ can be regarded as a valid approach.

Figure 5.7 to Figure 5.10 provide different instances of model outcomes compared to experimental spectra. Figure 5.7 reports a series of axial scans which cover a broad region spanning from the thruster exit plane up to 20 cm downstream. The model adequately predicts the fluorescence lineshape for all of these very different conditions, i.e. from strong magnetic field at $z = 0$ up to fairly negligible magnetic field at $z = 200$ mm. For this series of spectra, a kinetic temperature of 3900 K represents the best fitting value, yielding $\bar{\chi}_{red}^2 \approx 2$. Figure 5.8, 5.9 and 5.10 show the theoretical and experimental LIF profiles at $z = 10$ mm and $z = 100$ mm when the additional coil of the thruster is powered with 0 A, 5 A and 10 A, respectively. Also in these cases, the modeled lineshape is in close agreement with the measurements. A kinetic temperature between 4700 K and 6400 K is found to fit these data, leading to $\bar{\chi}_{red}^2 \approx 5 - 20$, see Figure 5.6.

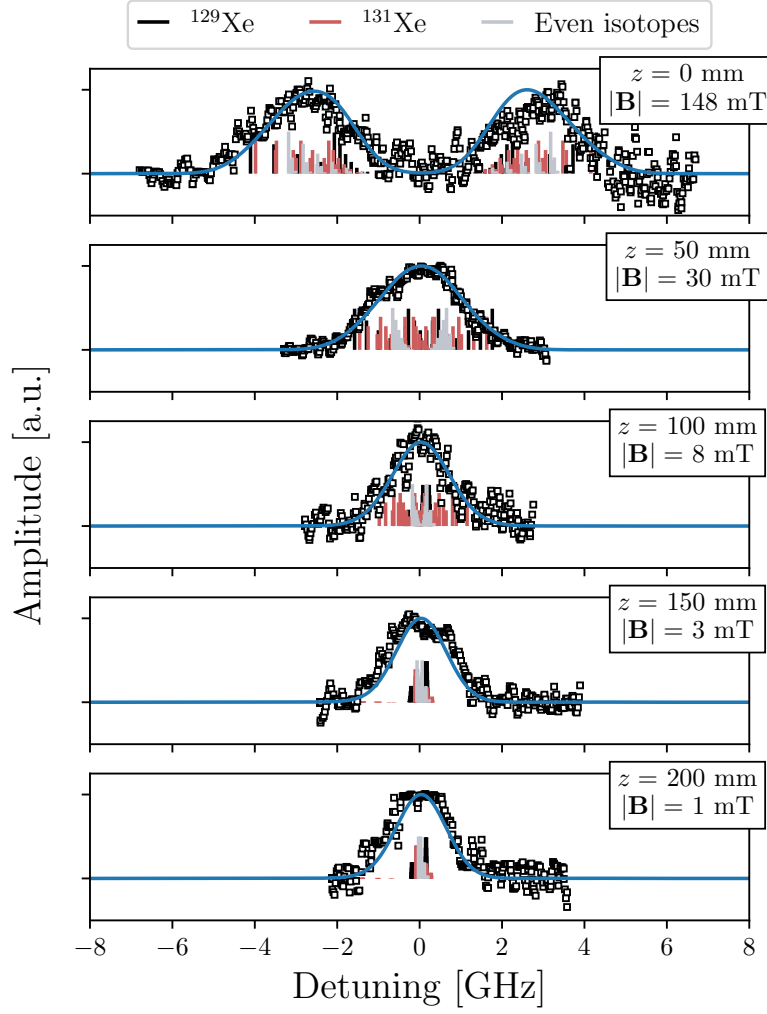


Figure 5.7: Experimental (squares) versus modeled (line) lineshape of Xe II. The experimental data points are Doppler shifted to fit the model profile. Thruster operation parameters are: $P_F = 200$ W, $\dot{m} = 1$ sccm, $I_c = 0$ A.

It shall be pointed out that the typical T_i observed in this experiment is notably larger than what reported in previous studies concerning magnetic nozzle dynamics [154], where $T_i < 1000$ K were found. At such low plasma pressures typical of the source in analysis here, ion heating due to electron impact collisions cannot explain such high temperatures. Thermalization is rather a relevant phenomenon for other operating regimes related to VASIMR and MPD thrusters. Conversely, in this case, a large value of T_i in the axial direction, i.e. a dispersion in the axial velocity, is rationally attributed to an extended ionization region that overlaps with the acceleration region. This process then would lead to an anisotropy in the ion kinetic temperature between parallel and perpendicular directions. The same phenomenon has been often observed in Hall thrusters, where the spread in axial velocity essentially matches the spread in potential across which ions are produced and it reads up to a few tens of eV [67, 155, 156]. However, the dispersion here is noticeably lower than what is typically found in Hall thrusters due to the presence of the magnetic nozzle which enhances the axial electron

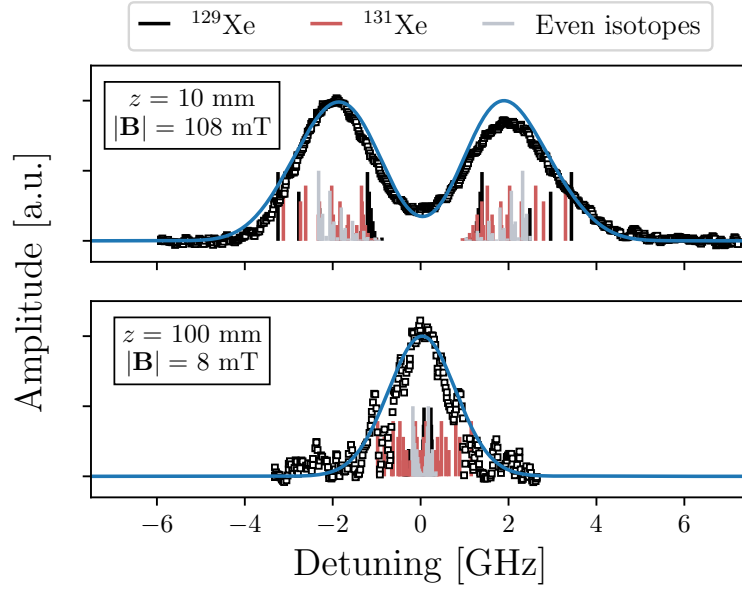


Figure 5.8: Experimental (squares) versus modeled (line) lineshape of Xe II. The experimental data points are Doppler shifted to fit the model profile. Thruster operation parameters are: $P_F = 200$ W, $\dot{m} = 2$ sccm, $I_c = 0$ A.

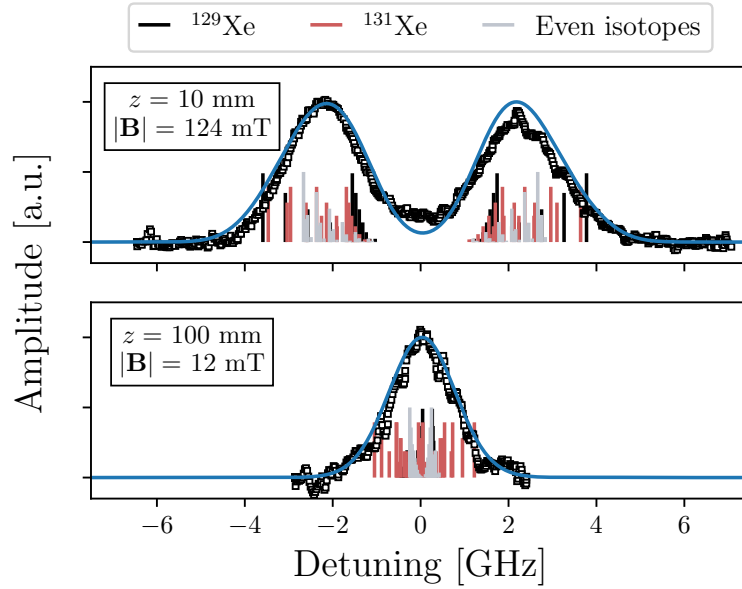


Figure 5.9: Experimental (squares) versus modeled (line) lineshape of Xe II. The experimental data points are Doppler shifted to fit the model profile. Thruster operation parameters are: $P_F = 200$ W, $\dot{m} = 2$ sccm, $I_c = 5$ A.

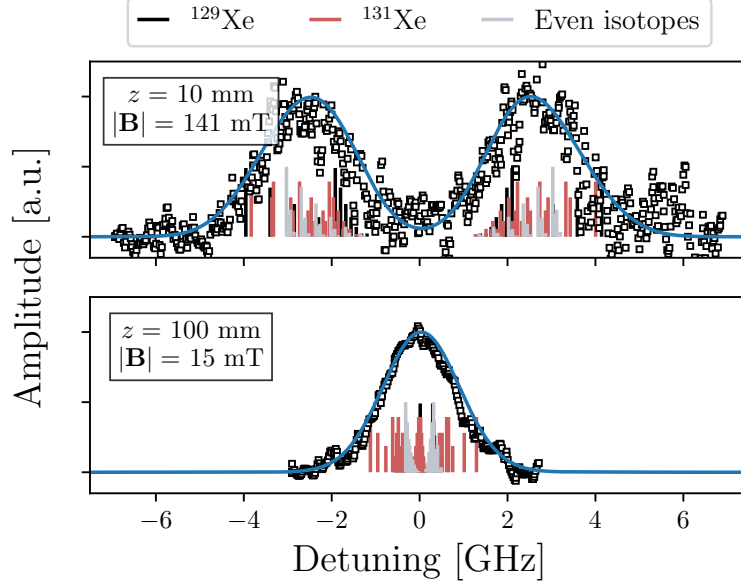


Figure 5.10: Experimental (squares) versus modeled (line) lineshape of Xe II. The experimental data points are Doppler shifted to fit the model profile. Thruster operation parameters are: $P_F = 200$ W, $\dot{m} = 2$ sccm, $I_c = 10$ A.

conductivity, whereby significant potential drops within short distances are unrealistic. In principle, dispersion in ion velocity could also originate from thruster unstable and/or oscillatory behaviors during a laser frequency tuning scan. The occurrence of these transients was continuously monitored by measuring the microwave reflected power and V_T and data were acquired only during steady state operation.

5.5 Ion velocity profiles

A parametric approach is followed in performing the present experiment. Measurements are clustered into three main blocks, each of which analyzes the effect due to the variation of a single external parameter: *i*) an electromagnet current series; *ii*) a mass flow rate series; *iii*) an input power series. Results in terms of most probable axial velocity of the ions are respectively reported in Figure 5.11, 5.12 and 5.13. These values are computed from the Doppler shift of the fluorescence spectra as discussed in Section 4.3 and 5.4.

The electromagnet current series, see Figure 5.11, is recorded using constant values of $P_F = 200$ W and $\dot{m} = 2$ sccm, whereas the current driven in the external electromagnet is varied between $I_c = 0, 5, 10$ A. Increasing the electromagnet current has three main effects: *i*) the magnetic field strength in the PC increases; *ii*) the ECR layer shifts downstream; *iii*) the expansion rate of the MN decreases or, in other terms, the nozzle becomes longer. It is observed that, at $z = -10$ mm, the ions are mostly directed towards the thruster backplate ($v_z \approx -500$ m s⁻¹), where they will recombine. This suggests that the peak in plasma potential is positioned between $-10 < z < 0$ mm. This result holds regardless of I_c . Most of the momentum gain occurs within 5 cm downstream the exit plane, yet at different rates depending on I_c . A higher I_c is associated with a lower acceleration, which is compatible with a lower axial variation rate of the

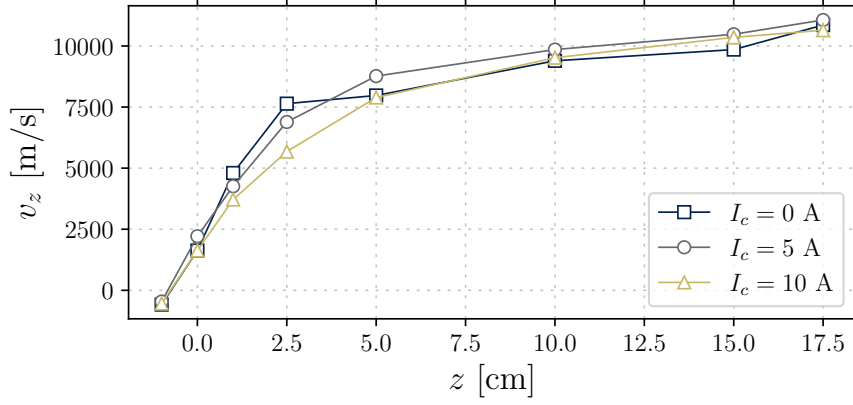


Figure 5.11: Most probable axial velocity profile of Xe II for different electromagnet currents. Constant thruster operation parameters are: $P_F = 200$ W, $\dot{m} = 2$ sccm.

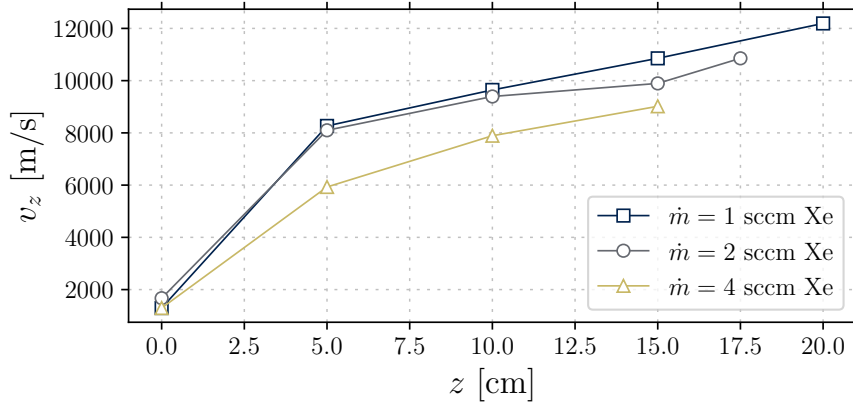


Figure 5.12: Most probable axial velocity profile of Xe II for different propellant mass flow rates. Constant thruster operation parameters are: $P_F = 200$ W, $I_c = 0$ A.

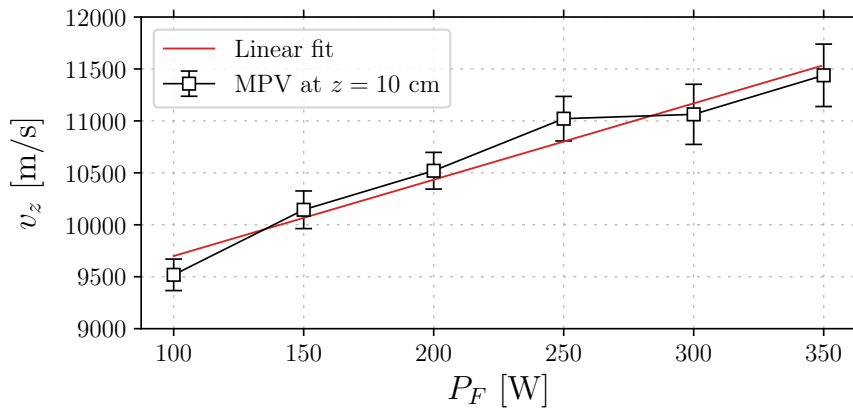


Figure 5.13: Most probable axial velocity of Xe II at $z = 10$ cm for different levels of input power. The error bar identifies the standard deviation given by T_i . Constant thruster operation parameters are: $\dot{m} = 2$ sccm, $I_c = 0$ A.

magnetic field intensity. Farther downstream instead, any difference linked to the shape of the MN is smoothed out and every configuration leads to a nearly identical axial velocity profile. This suggests that varying I_c does not significantly affect the total plasma potential drop in this experiment. A rather constant V_T has been observed between the three working points ($\approx 70 - 80$ V), qualitatively confirming that the condition in the source were similar. However, it is expected that a non-negligible difference among the various MN shapes might be preserved in terms of plume divergence, as visually noticed in Figure 5.3. This aspect, though analyzed in [153], requires further investigation and experimental data.

The mass flow rate series, cf. Figure 5.12, is recorded using constant values of $P_F = 200$ W and $I_c = 0$ A. The farthest distance at which the ion velocity could be resolved is limited by the LIF signal-to-noise ratio. The latter is deteriorated at larger mass flow rates due to larger collision rates giving a less populated group of ions in the metastable state. In accordance with previous observations reported in the literature in terms of specific impulse [50] and ion axial velocity [49, 154], ions gain a larger momentum as the pressure of neutrals drops. This phenomenon is attributed to two effects as the mass flow rate increases: a reduced amount of deposited energy per electron and a reduced mean free path for electron-neutral and ion-neutral collisions. The first effect leads to a reduced electron temperature, hence a smaller potential drop along the expansion. On the other hand, the electron-neutral collisions contribute to electron cooling inside the source therefore lowering the internal energy available for ion acceleration through the MN, whereas ion-neutral collisions represent a drag force component which further reduces the ion kinetic energy [97].

The input power series, whose results are reported in Figure 5.13, is recorded at $z = 10$ cm at constant value of $\dot{m} = 2$ sccm and $I_c = 0$ A. Within the explored range of P_F , the ion axial velocity along the MN axis shows an approximately linear growth with the microwave input power, although it is expected to saturate as the thrust efficiency decays for higher powers, as shown by direct thrust measurements performed on this device [50]. As opposed to the case shown in Figure 5.12, increasing the power at constant \dot{m} rises the available energy per electron, therefore T_e increases along with the plasma potential drop. It is noted that the value of v_z for $P_F = 200$ W measured in the power series differs by roughly 10 % from the same point shown in Figure 5.11 and Figure 5.12. This discrepancy is attributed to a slightly different condition of the thruster operation, since the two measurements are performed over different time frames. As a matter of fact, the reading of the floating potential at the source walls differs by about 15 V from one day to the next. This qualitatively indicates that the conditions in the source were slightly different and most probably a lower plasma potential drop was achieved, giving rise to a difference in the measured ion velocity.

5.6 Summary and conclusion

The dynamics of xenon ions has been spatially resolved by way of laser-induced fluorescence spectroscopy along the axis of a circular waveguide electron cyclotron resonance thruster. In the near-field plume and inside the source chamber, inference of ion velocity and parallel ion temperature requires intensive lineshape modeling efforts. One must account for several broadening mechanisms, namely isotopic shift, hyperfine structure and Paschen-Back/Zeeaman effect. This is especially true for ECRTs operating at rela-

tively high frequencies which imply the need for more intense magnetic fields to meet the resonance condition.

Findings show that ions are considerably accelerated within a few centimeters downstream the exit plane, although a non-negligible amount of kinetic energy is gained in the far-field region. When the divergence of the magnetic nozzle is reduced, the acceleration profile stretches out along the axis but altogether the ultimate ion velocity on-axis does not exhibit a visible dependence on the nozzle shape, in accordance with the simplest MN theories. As a general rule already observed elsewhere, a faster ion beam is attained at lower mass flow rates and higher levels of input power. Pertaining to the range explored in this experiment, it is observed that the ion velocity increases linearly with input power. Overall, the largest ion velocity recorded here reads about 12 km s^{-1} at $z = 20 \text{ cm}$ for 200 W of input power and 1 sccm of mass flow rate. Furthermore, negative ion velocities were found in the middle of the plasma chamber at $z = -10 \text{ mm}$, indicating non-negligible ion flux lost at the thruster backplate, which emphasizes that this is an important loss term in the overall thruster efficiency.

By modeling the fluorescence lineshape, it was possible to deduce the Doppler broadening width which reads about 1.5 GHz (full width at half maximum), yielding a parallel ion kinetic temperature in the order of a few thousands of K. This relative high dispersion in ion axial velocity likely results from a broad ionization region which overlaps with the acceleration region. Measurements show no evidence of ion temperature evolution along the plume expansion axis, in agreement with collisionless MN theories.

Further work must include measurements of complementary quantities of the expanding flow. Among others, it is of major relevance to investigate the neutrals velocity, the neutrals temperature and the perpendicular ion temperature. The latter two are expected to be close to the chamber walls temperature, i.e. in the order of a few hundreds of K. Ultimately, iterations on the thruster design could target the propellant injector position to reduce the amount of back-streaming ions as well as altering the overlapping acceleration-ionization regions.

PART III

RESEARCH ON IODINE PROPELLANT
FOR HELICON PLASMAS

Chapter 6

Preliminary Iodine Feeding System Development

This chapter deals with the use of iodine as propellant for electric space propulsion. At first, the needs behind this topic are addressed, showing the reasons why a valid alternative to xenon is desired and why iodine is possibly the best candidate. Afterwards, the chapter covers all the research activities performed in the framework of this thesis to evaluate the use of iodine in electrodeless thrusters. A feeding system prototype is presented along with its modeling and preliminary tests.

6.1 Motivation behind the use of iodine as propellant

In electric space propulsion, an external power source is required to provide the input power P_{IN} thus to generate and accelerate ions. The energy carried by the ejected ions is referred to as kinetic energy. This energy per unit time is the kinetic power P_{kin} , which is given by

$$P_{kin} = \frac{1}{2} \dot{m} v_e^2 = \frac{1}{2} T v_e = \frac{T^2}{2\dot{m}}, \quad (6.1)$$

where v_e is the effective exhaust velocity [18] which can be assumed equal to the ion velocity v_i as a first approximation. P_{kin} is more precisely defined as the minimum power strictly required, in principle, to obtain a given thrust T with a given mass flow rate \dot{m} . The ratio between the useful power P_{kin} and the available power P_{IN} defines the thrust efficiency η_T ,

$$\eta_T = \frac{P_{kin}}{P_{in}} = \frac{T^2}{2\dot{m}P_{in}}. \quad (6.2)$$

Combination of Equations 6.1 and 6.2 yields

$$\frac{P_{in}}{T} = \frac{v_e}{2\eta_T} \simeq \frac{v_i}{2\eta_T}. \quad (6.3)$$

Assuming a simplified scenario where the acceleration process entirely exploits the plasma potential V_p inside the source, the speed gained by a single ion results to be

$$v_i \simeq \sqrt{\frac{2qV_p}{M_i}}, \quad (6.4)$$

Table 6.1: Propellants comparison.

Element	I ₂	I	Xe	Kr
Mass [Da]	253.809	126.904	131.293	83.798
First Ionization Energy [eV]	9.3	10.5	12.1	14.0
Density [g cm ⁻³] @15°C, 1.013 bar	4.93	N/A	5.584·10 ⁻³	3.749·10 ⁻³
Storage density [g cm ⁻³]	4.93	N/A	1.79*	0.42*
Price [€/kg]	~350 ¹	N/A	~10000 ²	~1500 ²

*Data from nist.gov at 10 MPa and 25 °C.

where q is the ion charge and M_i is the ion mass. Equation 6.3 implies that there exists an optimal value of the exhaust velocity. If this condition is violated, the process would be characterized by a very low propellant consumption but a very high power to be supplied. To satisfy the need of a small enough effective exhaust velocity, from Equation 6.4, it is convenient to employ ions with large mass-to-charge ratio. Furthermore, a low ionization potential allows minimizing the ionization losses [18].

As a result, xenon is the principal propellant currently employed in this type of technology. It is inert, heavy and has a large ionization cross section, cf. Figure B.6. Either way, xenon requires supercritical storage conditions in large, high pressure tanks (up to about 150 – 200 bar). Moreover, it is expensive and, given its increasing application in several high technology industries, its availability and price fluctuate substantially thus to burden the development of a space project. Consequently, metallic and non-metallic condensable propellants have been proposed as substitutes, both to reduce costs and to enlarge the application envelope of this technology. Among all the options, iodine possesses particular features, reported in Table 6.1 and comprehensively gathered in Appendix B, that favor its employment as an alternative propellant for electric propulsion. Its atomic mass is slightly lower than the xenon one, it has lower first ionization energy and larger ionization cross section, which directly means a more efficient generation of the plasma with respect to other options. A low dissociation energy of 1.567 eV [157] leads to a mainly atomic I⁺ plasma [158]. It is stored as a solid at low pressure, it costs almost a tenth as much as xenon and it features virtually unlimited availability. These characteristics agree with the growing interest towards small spacecrafts rolling out for which dense and low-power propulsion systems are required. Iodine chemical reactivity can represent a drawback of this technology. Indeed, it is a halogen and, although it is the least reactive of its group, it still has an important effect on numerous materials of interest for space applications. This feature imposes new constraints on the selection of materials used in the propulsion system and poses significant qualification issues for iodine adoption in space applications. Novel challenges appear since the early experimentation phases. Tests require to be conducted with careful handling of propellant loading, thermal control and delivery to the discharge chamber at issue.

In 2021, the first iodine-fed plasma-based thruster has been successfully deployed and operated by the French startup ThrustMe [13]. In the same year, a cathode-less thruster produced by the Italian startup T4i has been deployed as well [14]. The propulsion

¹Purity ≥99.8 %, estimation from sigmaaldrich.com (2022).

²Purity ≥99.999 %, estimation valid for typical laboratory amount (2022).

system by ThrustMe was a miniaturized iodine-fed gridded ion thruster with nominal power of 55 W [13]. Ion beam neutralization is achieved via thermionic emission of a carburized thoriated tungsten filament cathode. However, when the beam current exceeds a few hundreds of mA (e.g. in low-power Hall thrusters), other neutralization strategy such as hollow cathodes become necessary. Yet, the reliable functioning of these systems is strongly limited by their lifetime when operating on iodine [159, 160]. As a consequence, it is more likely that electrodeless thrusters, such as helicon plasma thrusters, will represent a favored solution in the mid-high power range. As a direct consequence, the experimental investigation of iodine in electrodeless devices becomes of interest. Thus far, only a few studies have been addressed to the use of iodine in Helicon devices. The purpose of this work is both to acquire a deeper knowledge of propellant management strategies and to characterize the plasma generated with such a propellant in a Helicon discharge.

6.2 Architecture and design caveats

Iodine is stored as a low-pressure solid at room temperature and pressure. Below the triple point, i.e. at pressures lower than 12 kPa to avoid the formation of a liquid phase, equilibrium conditions hold between solid and vapor phases inside the iodine tank. Indeed, the vapor generated by way of a sublimation process is characterized by pressure and temperature conditions constituting the solid-gas phase equilibrium line. This implies that a high pressure stage is not required and that the pressure at which the propellant leaves the tank can be controlled through thermal control of the storage assembly.

The architecture investigated in this study is largely inspired by the design proposed in [161, 162]. Figure 6.1 shows a conceptual schematics of the feeding line. This system is meant to operate outside the vacuum chamber and to be linked to the plasma source through appropriate piping. The assembly comprises of a cylindrical reservoir where solid iodine is stored. The bottom interface of the iodine block undergoes sublimation due to thermal contact with a hot perforated surface named filter. Heat power is supplied by electric resistors in contact with a cup-shaped metallic body. Past the filter, iodine vapor enters the sublimation cup cavity which acts as a plenum and pro-

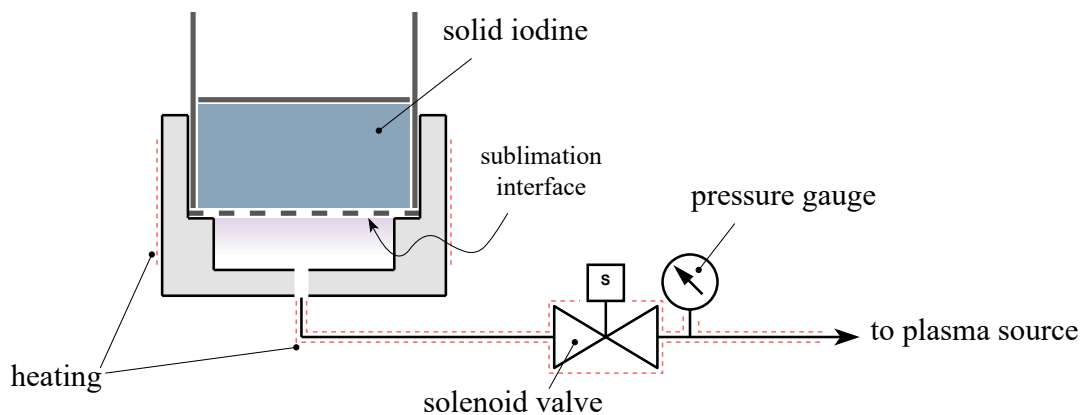


Figure 6.1: Iodine feeding line schematics.

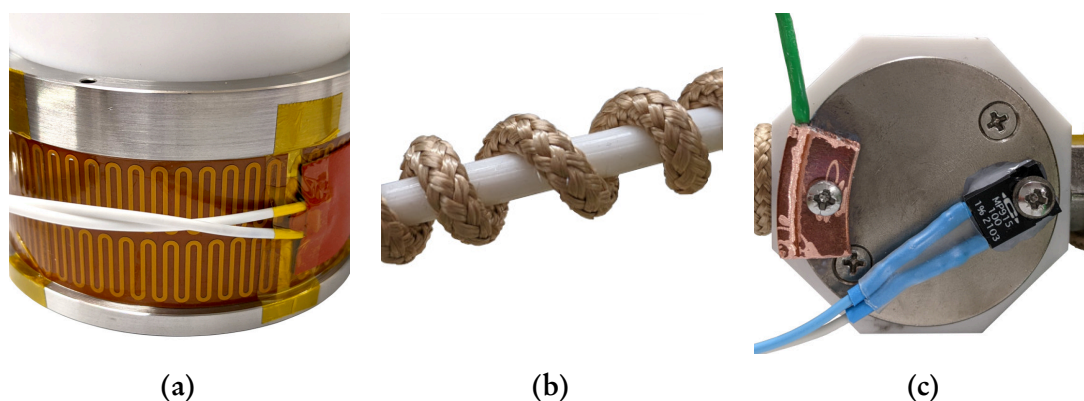


Figure 6.2: Iodine feeding system heaters used on (a) sublimation cup, (b) pipes and (c) solenoid valve.

vides damping to the flow. The rest of the feeding line comprises heated pipes, a heated solenoid valve (on/off) and a heated pressure gauge. Monitoring the vapor pressure is of interest since it can provide information about the mass flow rate fluctuations and spot the possible occurrence of clogging.

Since the amount of sublimated iodine scales with the exposed surface, see Equation 6.5, this architecture theoretically allows to correlate a value of temperature measured on the sublimation cup to a vapor mass flow rate. Such a strategy retains great convenience in practical terms throughout the development and later testing phases. In fact, it dispenses with the need of sophisticated hardware components (such as proportional valves) as well as more complex software control based on combined pressure-temperature sensing.

The design of each system component has to deal with materials selection and sizing process. Materials constituting the feeding systems components must be selected accounting for iodine reactivity, which can depend on temperature. Previous studies reported in [162–164] show that best candidates are: steel alloys with low carbon and high nickel content; superalloys (e.g. Inconel); polymers such as PTFE; glass. Other common material such as copper and aluminum instead show evident reactivity. Two reservoirs have been designed and assembled in this study. The materials that have been chosen for each of their components are detailed in Sections 6.3 and 6.4. The two prototypes share the same piping system (entirely made in PTFE), the solenoid valve (NResearch DT011IC) whose wet surfaces are made of PTFE, and the pressure gauge (Omega PX409) whose wet parts are made in SS316.

Heating power is supplied using three different approaches as shown in Figure 6.2: *i*) polyimide insulated flexible heaters (Omega KHLVA series) for the sublimation cup; *ii*) fiberglass insulated heating cords (Omega HTC series) for the pipes; *iii*) planar film cermet resistors (Kool-Pak MP900 series) for the valve. K-type thermocouples (T/C) are placed along the feeding line to continuously probe the temperature of each component. Heaters and thermocouples are interconnected into a closed-loop control system based on Arduino. Figure 6.3 shows the electronic circuit developed for this study. A custom algorithm based on proportional feedback control is implemented on an Arduino Mega board. It receives in input the temperature readings along the feeding line provided by T/C modules (MAX6675 chip). Then, a signal is sent to a series of relays which are activated or deactivated according to the set-point temperature. Each relay essentially is an electrical switch interposed between a resistor and its power supply. The control

6. PRELIMINARY IODINE FEEDING SYSTEM DEVELOPMENT

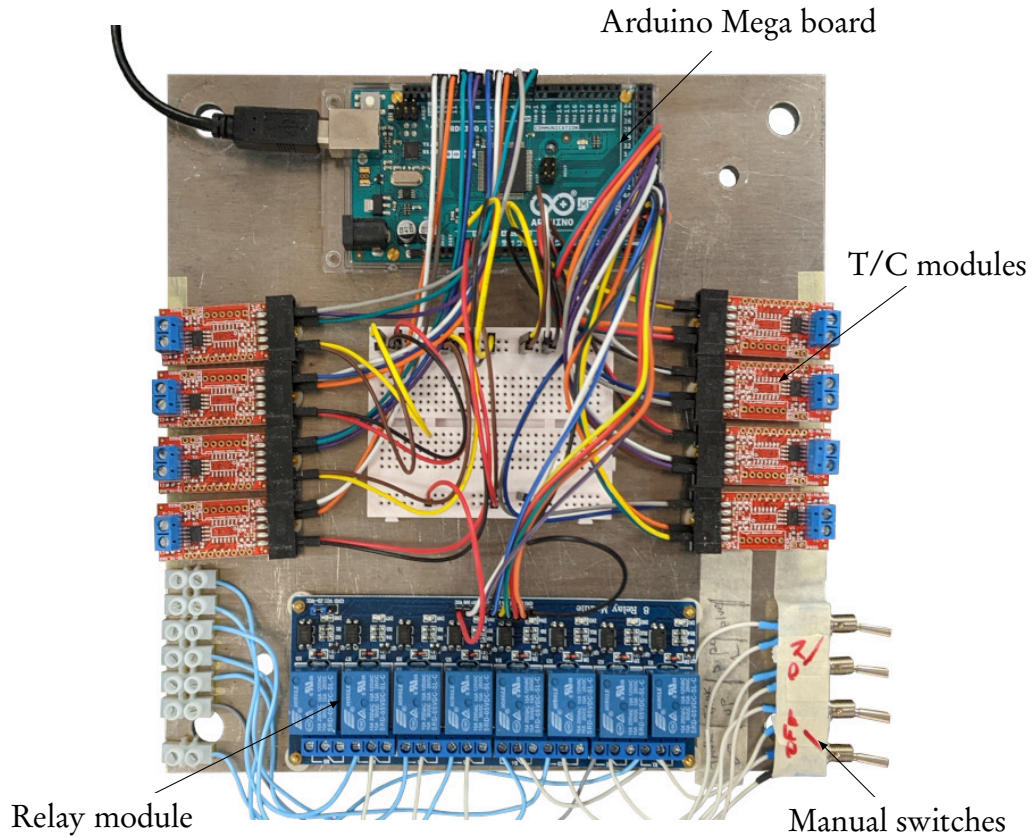


Figure 6.3: Photograph of the temperature control system circuit.

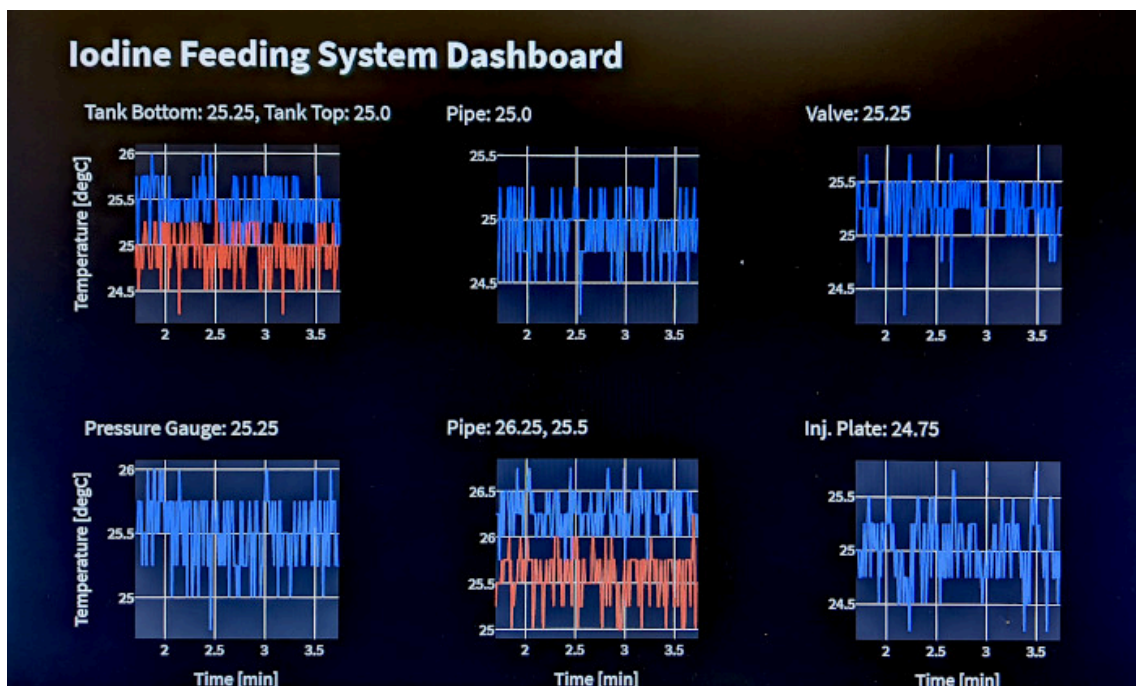


Figure 6.4: Screenshot of the web app dashboard developed to monitor the temperature of each component along the iodine feeding line. Interface based on open-source Python libraries Streamlit and Plotly.

6.2. ARCHITECTURE AND DESIGN CAVEATS

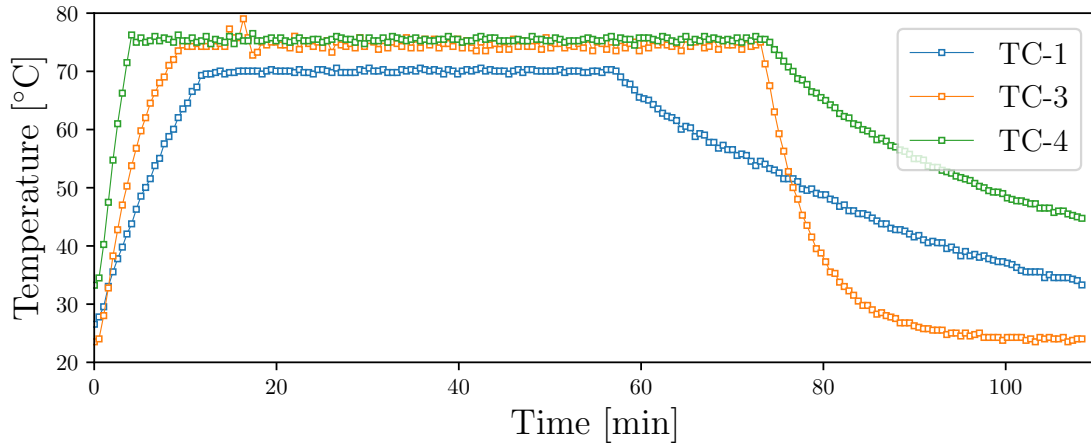


Figure 6.5: Instance of iodine feeding line thermal characterization. The test has been performed on the prototype described in Section 6.3 while no iodine was loaded in the tank. TC-1 is placed on the sublimation cup; TC-3 is placed on the pipe connecting the tank to the valve; TC-4 is placed on the valve.



Figure 6.6: Iodine immobilization strategies.

loop runs with a frequency of about 1 Hz. The stream of temperature data reaching the Arduino board is also sent to an ordinary computer running a Python program for storage and live plotting. Visual monitoring of either heating or cooling process is crucial during experimental phases. This task is accomplished by live-plotting the temperature reading from each thermocouple. Streamlit and Plotly open-source Python libraries are used to create the interface shown in Figure 6.4. It essentially is a web app accessible from multiple devices connected on the same network. An instance of controlled temperature profile is shown in Figure 6.5. These preliminary tests show that the control strategy enables good thermal behavior of the system given that the set-point temperature values are steadily maintained with an accuracy of approximately

± 1 °C.

Beyond vapor generation and control, one must address trapping and disposal of iodine as the last phase of testing. There exist different immobilization approaches, as discussed in Appendix B. In this context, chemical and cryogenic are the most suitable ones. Activated charcoal, see Figure 6.6a, efficiently acts as a solid adsorbent at room temperatures. It is characterized by the so called iodine number defined as the mass of iodine that is consumed per unit mass of charcoal. For typical commercially available charcoal, the iodine number is 500 – 1200 mg g⁻¹. Activated charcoal can also be used to characterize the mass flow rate generated by the system. This approach has been followed in [161, 162], where a glass phial containing the activated charcoal has been exposed to the iodine flow. An integral measurement of flow rate is then quantified from the phial weight before and after exposure. Cryogenic trapping, instead, relies on liquid-nitrogen cooled chevrons, see Figure 6.6b, which require to be manually cleaned to prevent saturation using an adequate solvent, e.g. acetone.

6.3 First prototype setup

Figure 6.7 shows the first tank prototype that has been designed, built and operated. The main cylinder is made of borosilicate glass with 55 mm in internal diameter and 70 mm in height. The advantage of using such a material is that it does not react with iodine and it easily allows to inspect the system without disassembling it. The sublimation cup and the filter are made of nickel-coated aluminum. The nickel layer is a few tens of millimeters thick and it has been achieved through galvanic deposition. The tank includes a lid and a weight to press over the iodine grains both made in PTFE.



Figure 6.7: First prototype iodine tank (a) at first assembly and (b) after iodine loading.

6.3. FIRST PROTOTYPE SETUP

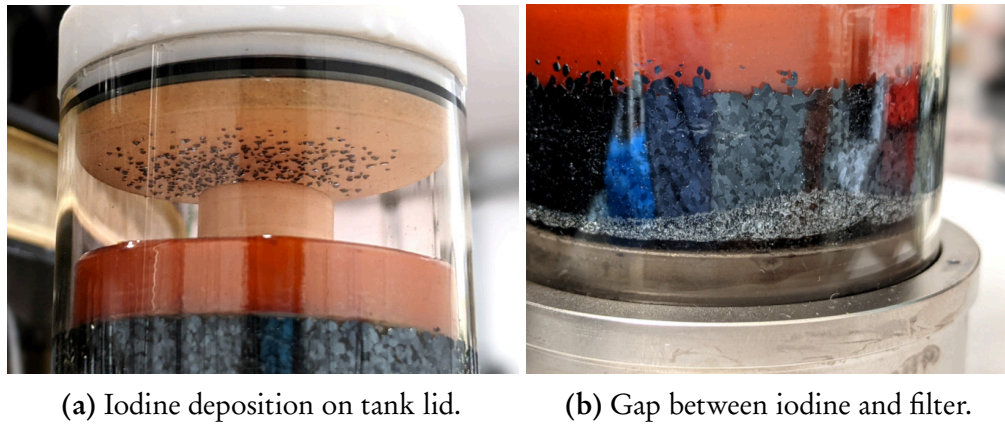


Figure 6.8: Issues relative to the first iodine tank prototype.

This prototype has been implemented in accordance to the schematics shown in Figure 6.1. Preliminary tests without iodine allowed verifying the integrity of each component, ensuring proper sealing and robust thermal control. Afterwards, the tank was loaded with 168 g of iodine grains with 99.8 % purity, see Figure 6.7b, under a chemical fumes hood. Since iodine is supplied and handled in the form of grains at room temperature, during the loading phase it has been possible to compute the packing factor. Using the value of density at room conditions, i.e 4.9 g cm^{-3} , and the volume occupied by the loaded mass, it results that the packing factor for this ordinary grain size approximately equals 0.4. Loading in liquid phase could represent a preferred option for an optimized system aiming at either intensive laboratory tests or in-flight demonstration.

Subsequent tests have proven that the feeding system was effectively able to generate a mass flow rate of iodine vapor. However, a few issues occurred after a few minutes of operation. Figure 6.8 addresses the observed unwanted phenomena. A portion of the sublimated iodine is found to deposit on the lid bottom surface, see Figure 6.8a. This effect occurs because the PTFE weight does not feature any radial sealing since it is required to slide down while remaining in contact with the solid iodine block. The second issue, as depicted in Figure 6.8b, concerns the occurrence of a significant gap between the filter and the iodine block. This major issue greatly affects the conduction of heat which directly translates into a reduction of mass flow rate with time. The source of this phenomenon is the PTFE weight which clearly does not exert a sufficient force on the upper surface of the iodine block to overcome the friction on the walls.

In order to proceed with a major design iteration, the system has been disassembled for inspection and storing of the unused iodine. It is observed that virtually all components did not experience any substantial corrosion. Parts made of PTFE, glass, SS316 (used in pipe fittings), were found in perfect conditions. Likewise, the nickel coating does not show evident signs of corrosion, see Figure 6.9. On the sublimation cup, however, the nickel coating was considerably damaged due to friction with the main glass tube. As a result, a portion of aluminum stood exposed to a mild iodine atmosphere, see Figure 6.10. Right after disassembly and cleaning, this aluminum surface exhibited very good conditions. On the contrary, a few days of shelf storage were sufficient to start showing oxidation signs visible as a white powder which most probably consists in aluminum oxide.

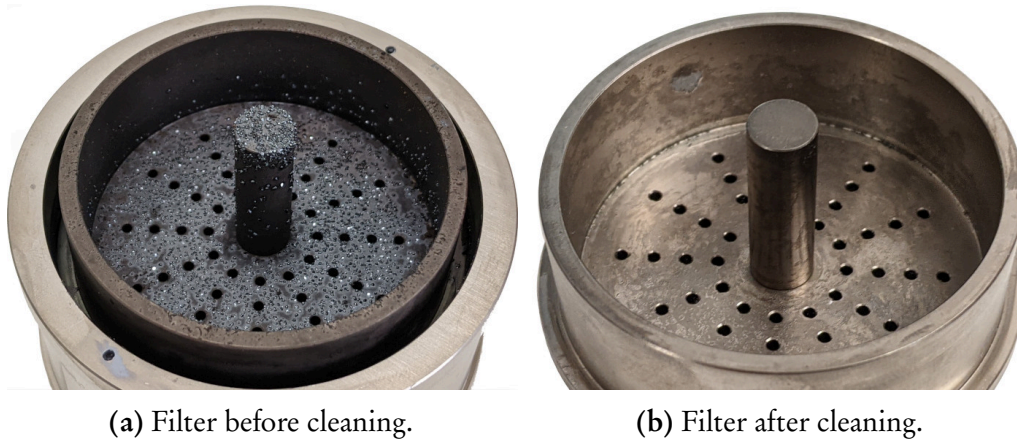


Figure 6.9: Filter condition after system disassembly. The nickel coating does not show evident corrosion signs.



(a) Sublimation cup right after disassembly (b) Sublimation cup after a few days at room conditions.

Figure 6.10: Sublimation cup with damaged nickel coating after disassembly. Iodine exposure effects on the aluminum surface become visible after a few days at room conditions in the form of white powder (aluminum oxide).

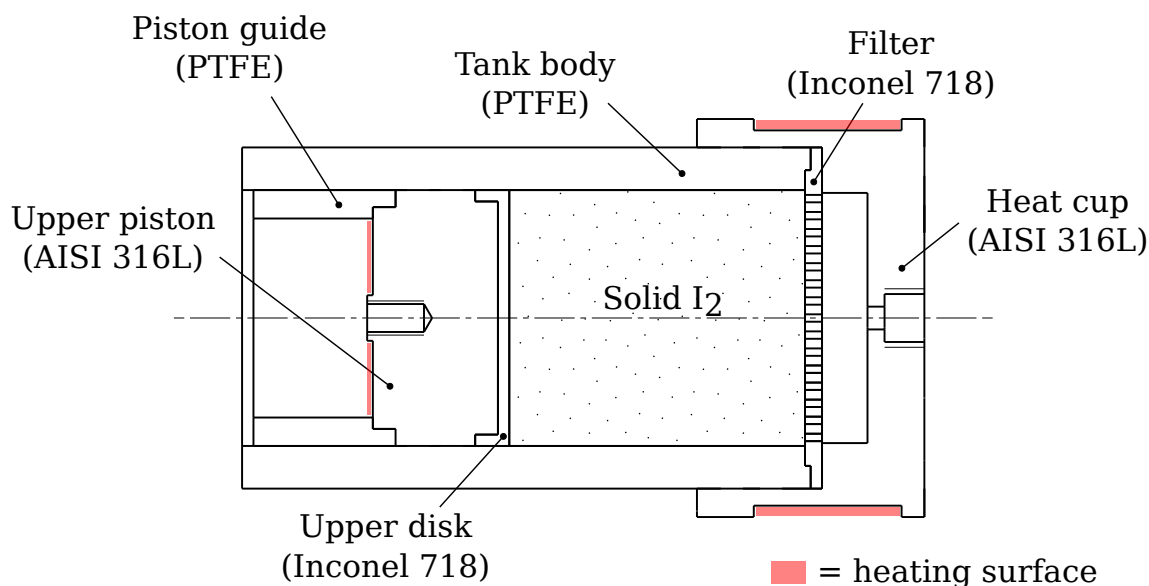


Figure 6.11: Second prototype iodine tank schematics.

6.4 Second prototype setup

The observations reported in Section 6.3 lead to the need for design iteration in order to overcome the issues discussed beforehand. For this reason, a second tank prototype has been designed and manufactured. It is schematically represented in Figure 6.11 whereas a photograph of its first assembly is shown in Figure 6.12.

The major change with respect to the previous design lies in the addition of an upper piston which has both the function of pushing down the iodine to ensure proper contact with the filter and to seal the tank from the external environment. The first task is simply addressed by exploiting the ambient pressure that is about 100 times larger than the iodine vapor pressure at moderate temperatures, see Figure B.2. In a vacuum environment, a spring can be used [162]. Sealing, instead, is achieved by a pair of FKM o-rings. The core of the upper piston is made of SS316L on which a disk made of Inconel 718 is mounted to improve chemical compatibility. The upper disk is manufactured using laser metal fusion technique. The piston also features a guide made of PTFE to prevent seizure. A blind thread has been included on the top surface of the piston to facilitate disassembling of the system. It in fact allows to screw a hook on it to simplify the extraction of the piston. Other changes involve material selection for the remaining components. The main body of the tank has been made of PTFE to reduce friction between the walls and the iodine block. Given the issues experienced regarding the nickel coating, the sublimation cup and the filter have been manufactured using a single material. SS316L is chosen for the sublimation cup, as a trade-off between chemical compatibility and cost. The filter instead, since it is in continuous contact with solid and gaseous iodine, is manufactured in Inconel 718 via laser metal fusion. In this prototype, the filter is a simple plate with multiple holes as depicted in Figure 6.13, in the sense that it does not include a central rod as in the previous prototype.

Dimensions have been slightly update to comply with constraints set by the new materials and their associated manufacturing techniques. The internal diameter of the main body is 45 mm, whereas the length of the full assembly reads 120 mm. The heating



Figure 6.12: Photograph of the second prototype iodine tank, (left) main body and (right) upper piston.



Figure 6.13: Photograph of the filter relative to the second prototype iodine tank.

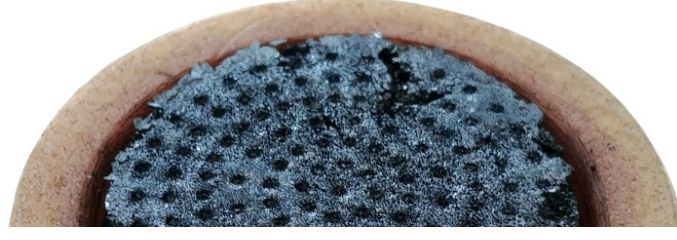


Figure 6.14: Photograph of iodine sublimation surface. A pattern of cone-like wells is evident. These structures are clearly aligned with the filter holes. Courtesy by the authors of [162].

strategy for the sublimation cup involves the use of flexible heaters, as described in Section 6.2. A parallel of three planar cerment resistor are located atop the piston, so that it can be slightly heated (to a much lower temperature than the sublimation cup) to ease its sliding.

At the time of writing of this manuscript, the system is undergoing implementation procedures including preliminary tests to verify the integrity and functionality of every component.

6.5 Heuristic sublimation model

In general, the mass flow rate (i.e. the rate of sublimation) resulting from an ideally flat surface with absolute temperature T_{sub} and saturated vapor pressure p_{sat} facing a vacuum environment is given by the Hertz-Knudsen equation

$$\dot{m} = \frac{p_{sat}}{\sqrt{2\pi RT_{sub}}} A, \quad (6.5)$$

where $R = \mathcal{R}/M$ is the specific gas constant and A is the exposed area. In practice, the pressure in the vapor space is not zero, meaning that molecules have a chance of returning to the solid interface. Equation 6.5 can be modified so as to account for the environment vapor pressure p_{vap} [165]

$$\dot{m} = \frac{(p_{sat} - p_{vap})}{\sqrt{2\pi RT_{sub}}} A. \quad (6.6)$$

Measurements [164] and modeling [161, 166] based on compressible viscous fluid theory have observed that p_{vap} is fairly close to p_{sat} . Given the results discussed in [161, 166], a value of $p_{vap} = 0.9999p_{sat}$ is used in the following. Alternatively, \dot{m} can in principle be estimated from the sublimation heat power \dot{Q}_s and the heat of sublimation Δh_s (typically assumed constant) as

$$\dot{m} = \frac{\dot{Q}_s}{\Delta h_s}. \quad (6.7)$$

However, accurate determination of \dot{Q}_s is challenging. In fact, it represents a fraction of the total input power which is also spent for conduction (through the walls and

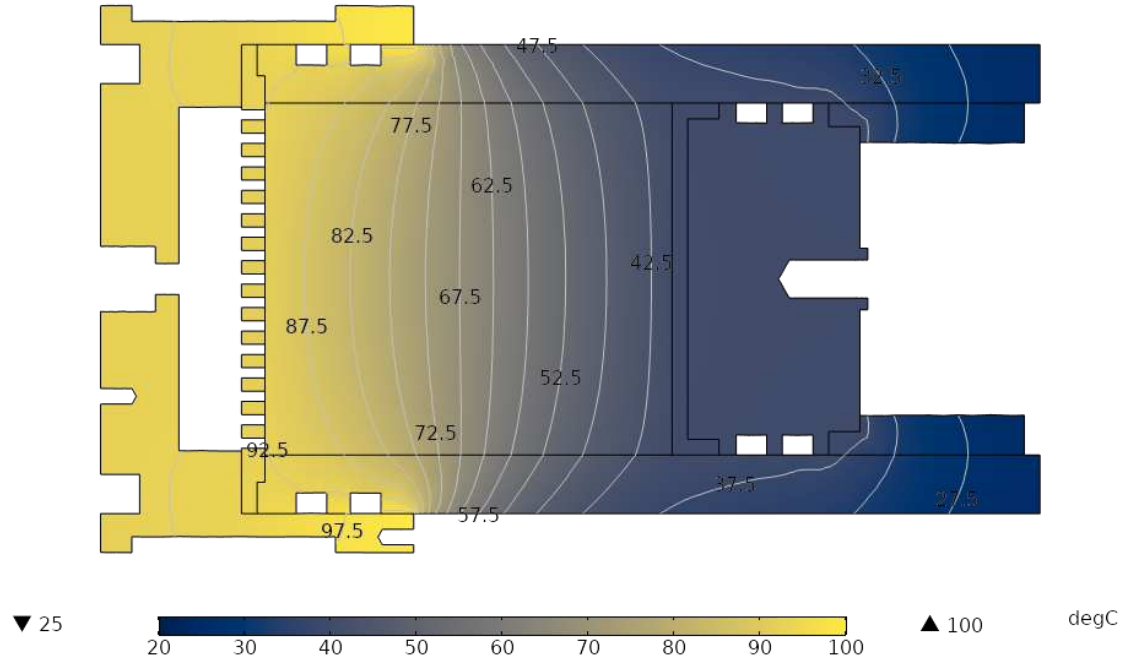


Figure 6.15: Results of steady thermal FEM simulation of the iodine tank. Input values on sublimation cup edge and upper piston are 100 °C and 40 °C, respectively. Small temperature inhomogeneities close to the filter can be seen in Figure 6.17.

the iodine block), radiation and convection losses. The latter are present only during ground testing if the tank is exposed to atmospheric pressure.

Previous experiments performed by the research team at University of Pisa [161, 162, 166] have observed a relatively complex structure of the iodine surface that faces the heated filter, as visible in Figure 6.14. In short, the sublimation does not appear to be perfectly homogeneous in space, instead the exposed surface develops wells in correspondence of the filter holes, suggesting that iodine vapor is more easily evacuated there. A posteriori, this phenomenon does seem reasonable: when heat is supplied to a unit surface that faces a hole, equilibrium is largely unbalanced in favor of sublimation. On the contrary, a heated unit surface that is located in between two holes obviously sees a physical obstacle that shifts the equilibrium in favor of deposition. As a result, the sublimation process should follow a certain dynamics, which is qualitatively proposed in Figure 6.16. Most of the vapor initially comes from the region that faces a filter hole. With time, lateral regions becomes more exposed, hence sublimation is promoted also farther from the holes. The sublimation area keeps increasing up to a point in which the small portions remained in contact with the filter between adjacent holes cannot withstand the pressure exerted by the back-pushing piston. Eventually, after an initial transient, the system essentially oscillates between two macroscopic subsequent states: *i*) the sublimation surface enlarges; *ii*) the piston moves forward (i.e. an iodine layer is depleted). Qualitatively speaking, past the initial transient, the sublimation surface alternates between those two profiles exemplified in Figure 6.16 and marked with $t = t_1$ and $t = t_2$. Here it is assumed that the iodine volume of interest is in thermal equilibrium. Small gradients of temperature can be present in principle, yet steady state thermal simulations show that temperature is nearly constant within a few millimeters, see Figure 6.15. To account for this phenomenon, the Hertz-Knudsen equation can be

6.5. HEURISTIC SUBLIMATION MODEL

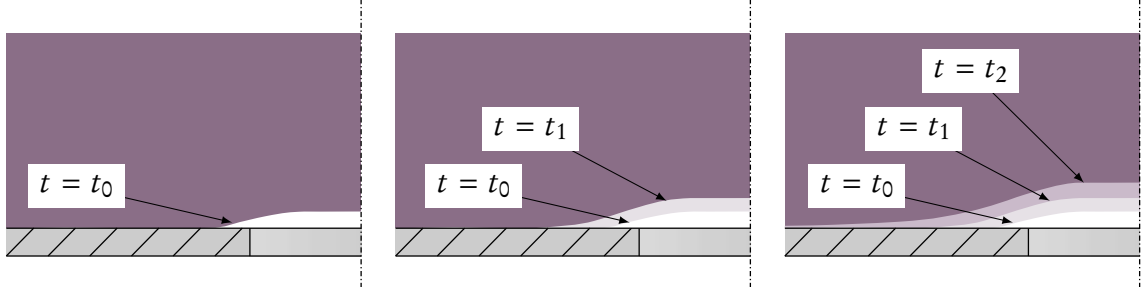


Figure 6.16: Qualitative dynamics of local iodine sublimation. The violet area represents solid iodine, the shaded regions represent the edge of iodine that evolves with t . The gray rectangle is a cross section of the filter with a hole centered on the right-hand side of each sub-figure.

modified by including a factor α ,

$$\dot{m} = \alpha \frac{(p_{sat} - p_{vap})}{\sqrt{2\pi R T_{sub}}} A. \quad (6.8)$$

Typically, $\alpha = 1$ is assumed in many previous works, e.g. [167]. Instead, the main task of the model presented in this section is to provide a formulation of α as a function of the system geometry. The sublimation interface is mapped using Cartesian coordinates (x, y) , so that each hole is centered in a certain point (x_h, y_h) . Time dependency is included to deal with the dynamics, therefore $\alpha = \alpha(x, y, t)$ and $\dot{m} = \dot{m}(t)$. The variable t must be interpreted as a unitless step variable rather than actual time measured in seconds, since the interest here is exclusively on the steady state value of \dot{m} . The mass flow rate at each time step $\dot{m}(t)$ results from Equation 6.8 discretized and integrated in space

$$\dot{m}(t) = \int \int_{x,y} \alpha(x, y, t) \left[\frac{p_{sat}(x, y) - p_{vap}}{\sqrt{2\pi R T_{sub}(x, y)}} \right] dx dy. \quad (6.9)$$

where $T_{sub}(x, y)$ results from steady thermal FEM simulations, $p_{sat}(x, y)$ is derived from Equation B.1 and $\alpha(x, y, t)$ is modeled as follows. An example of $T_{sub}(x, y)$ is shown in Figure 6.17.

Figure 6.18 graphically represents the definition of $\alpha(x, y, t)$. In essence, at $t = t_0$, $\alpha = 1$ is valid only in correspondence of each hole, whereas it is assumed to decay exponentially elsewhere. This decay is defined by the parameters δ and ξ as shown in Figure 6.18. At the following time step $t = t_1$, the portion where $\alpha = 1$ holds extends up to a distance δ from the hole center and then a similar exponential decay is assumed. These profiles are locally applied in correspondence of each hole in the (x, y) domain defined by the filter geometry. The global $\alpha(x, y, t)$ simply results from summing up all the local profiles. Given the full set of holes coordinates (x_h, y_h) , the analytical form of $\alpha(x, y, t)$ reads

$$\alpha(x, y, t) = \begin{cases} 1 & \text{in correspondence of each hole} \\ \exp \left[-\frac{\sqrt{(x - x_h)^2 + (y - y_h)^2} + \beta(t)}{\tau} \right] & \text{elsewhere} \end{cases} \quad (6.10)$$

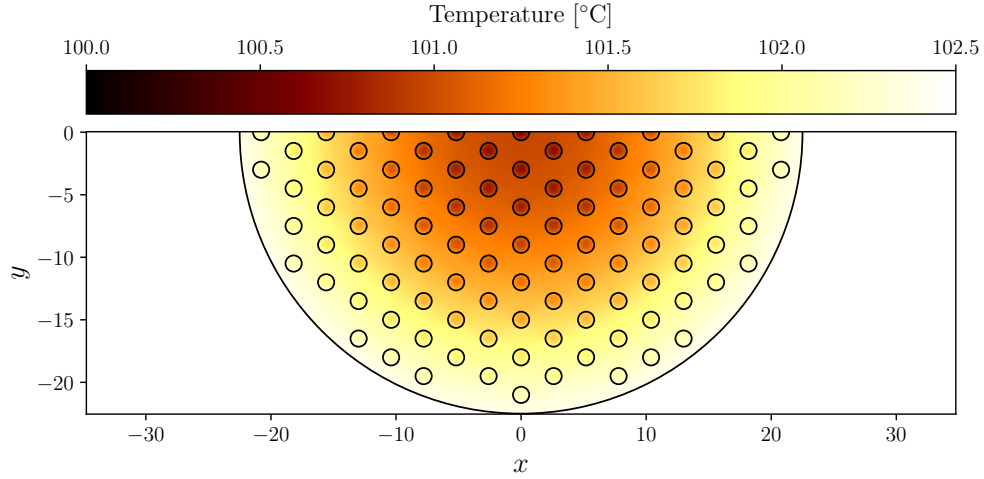


Figure 6.17: Instance of $T_{sub}(x, y)$ obtained via FEM thermal simulation relative to the prototype detailed in Section 6.4.

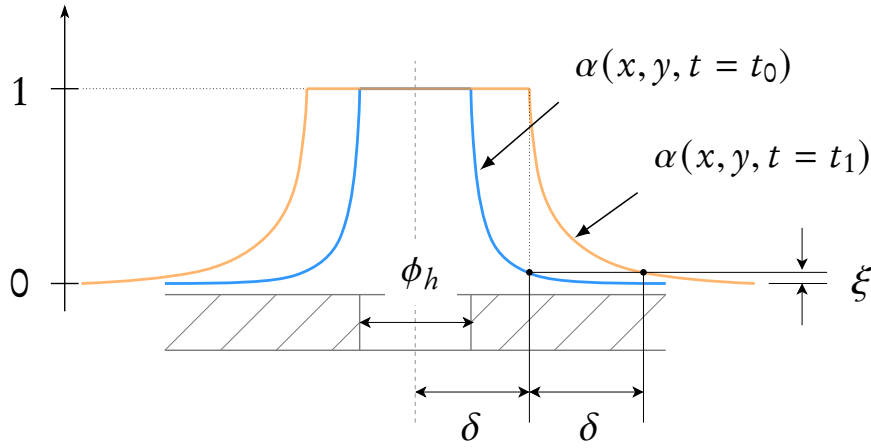


Figure 6.18: Definition of the α profile in space and time.

where the parameters $\beta(t)$ and τ allow shaping the exponential portion and are set by the boundary conditions discussed beforehand as function of δ and ξ

$$\text{at } \begin{cases} x - x_h = \frac{\phi_h}{2} + t\delta \\ y - y_h = 0 \\ \alpha(t) = 1 \end{cases} \Rightarrow \beta(t) = -\frac{\phi_h}{2} - t\delta \quad (6.11)$$

$$\text{at } \begin{cases} x - x_h = \frac{\phi_h}{2} + (t+1)\delta \\ y - y_h = 0 \\ \alpha(t) = \xi \end{cases} \Rightarrow \tau = -\frac{\delta}{\log \xi} \quad (6.12)$$

On the basis of what is experimentally observed and shown in Figure 6.14, it is expected that $\delta < \phi_h$ and $\xi \ll 1$. The α profile keeps enlarging along x and y as shown in Figure 6.18 until $t = t_n$ when two profiles related to adjacent holes cross in the mid-point, meaning that the whole iodine surface contributes to sublimation. The ensemble

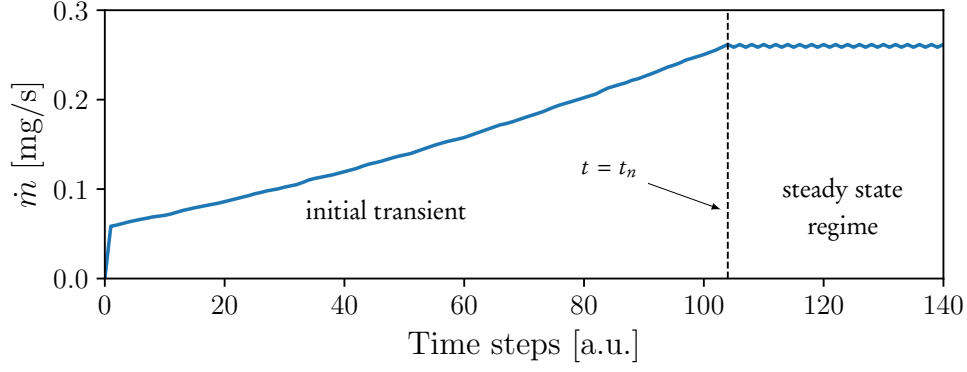


Figure 6.19: Instance of initial transient and steady state regime observed when computing \dot{m} .

of steps between t_0 and t_n represents the initial transient. At $t > t_n$, basically α oscillates between $\alpha(x, y, t = t_{n-1})$ and $\alpha(x, y, t = t_n)$. The latter is defined as the steady state regime. As a result, the stationary mass flow rate equals the mean value between $\dot{m}(t = t_{n-1})$ and $\dot{m}(t = t_n)$. To sum up, the estimation of \dot{m} is performed as follows:

1. the filter geometry is mapped in a (x, y) domain where each hole is identified by a set of coordinates (x_h, y_h) ;
2. $T_{sub}(x, y)$ is retrieved from a FEM simulation;
3. the parameters δ and ξ are set in accordance with a benchmark case using experimental data;
4. $\alpha(x, y, t)$ is computed at each time step from Equation 6.10;
5. the transient mass flow rate is computed at each time step from Equation 6.9;
6. once steady state regime is reached at a generic t_n , the mass flow rate equals $\dot{m} = \text{mean} \{ \dot{m}(t = t_{n-1}), \dot{m}(t = t_n) \}$.

Figure 6.19 shows an example of the dynamics of \dot{m} throughout its estimation as described above, illustrating the initial transient and steady-state oscillations.

In order to verify the accuracy of this model, it is benchmarked against the results reported in [162], where a feeding system prototype using the same architecture as discussed in Section 6.2 is developed. Geometry and operation envelope are provided in references [161, 162, 166]. Raw temperature data obtained from FEM thermal simulations are interpolated using a mesh-free radial basis function method to retrieve the map of $T_{sub}(x, y)$. Figure 6.20 provides the modeled mass flow rate profile compared to the experimental findings. Data are in very good agreement with the model discussed beforehand. Free parameters δ and ξ are found to lead to a poor match with experiments whenever $\delta > \phi_h/10$ and $\xi > 10^{-3}$. The results in Figure 6.20 are obtained setting these parameters to $\delta = \phi_h/20$ and $\xi = 10^{-4}$. A further decrease in both δ and ξ does not imply any substantial change in the mass flow rate profile, while instead it increases the computational time.

Eventually, the same procedure is applied to the geometry described in Section 6.4 so as to estimate the mass flow rate that the prototype in analysis here is able to sustain. In this case, convective losses has to be taken into account because the system is

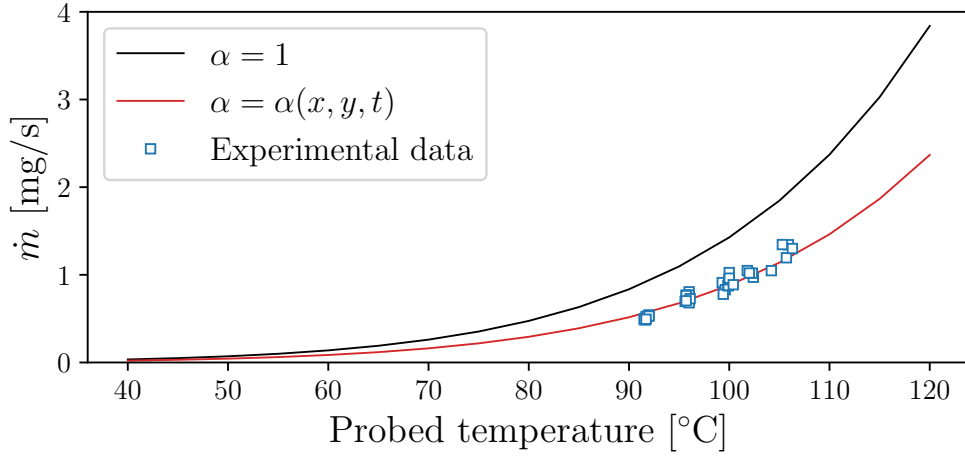


Figure 6.20: Sublimation model benchmark case: mass flow rate versus probed temperature relative to the feeding system prototype developed by University of Pisa [162]. The black solid line represents the sublimation rate computed using Equation 6.6, whereas the red solid line comes from modeling of α in accordance with Equation 6.10. Results obtained with $\delta = \phi_h/20$ and $\xi = 10^{-4}$. Experimental data from [162].

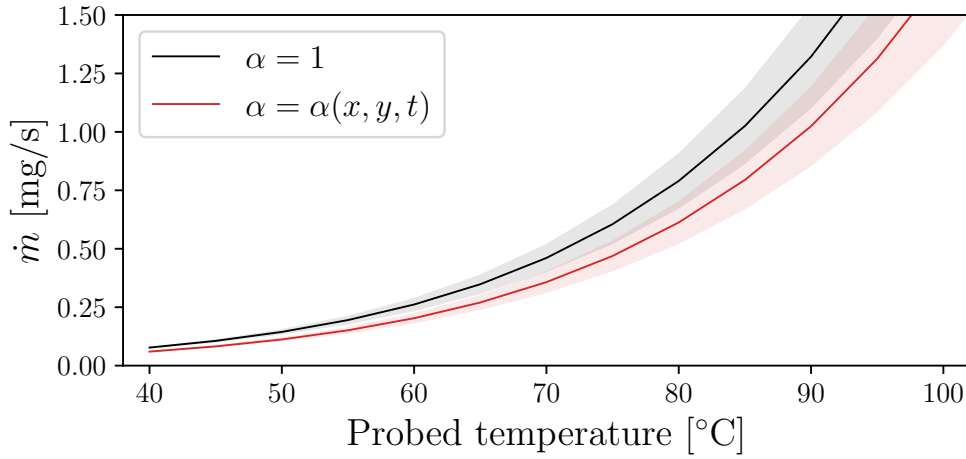


Figure 6.21: Mass flow rate versus probed temperature relative to the feeding system prototype detailed in Section 6.4. The black solid line represents the sublimation rate computed using Equation 6.6, whereas the red solid line comes from modeling of α in accordance with Equation 6.10. Results obtained with $\delta = \phi_h/20$ and $\xi = 10^{-4}$. Shaded areas outline the uncertainty due to convective losses: lower and upper boundaries are relative to $h_c = 7.5 \text{ W m}^{-2} \text{ K}^{-1}$ and $h_c = 2.5 \text{ W m}^{-2} \text{ K}^{-1}$, respectively.

meant to operate outside the vacuum chamber. During experiments, aluminum foil is wrapped around the heated surfaces working as a thermal shield that reduce these losses, therefore the convective heat flux in input to the FEM thermal simulation is modeled using a lower heat transfer coefficient h_c with respect to natural convection. It is estimated that using such an insulation allows reaching $h_c = 2.5 - 7.5 \text{ W m}^{-2} \text{ K}^{-1}$, whereas $h_c > 10 \text{ W m}^{-2} \text{ K}^{-1}$ is typical in natural free convection regime. Figure 6.21 shows the modeling results accounting for the uncertainty in h_c that directly translates into uncertainty in \dot{m} . It is noted that the discrepancy between the simple $\alpha = 1$ case and the more complex $\alpha = \alpha(x, y, t)$ case is less pronounced here than what previously shown in Figure 6.20. This effect is due to the system geometry as the prototype developed in the framework of this thesis features a larger diameter of the iodine block as well as a denser array of holes on the filter.

The characteristic curve \dot{m} vs. T_{probed} is not known for the prototype described in Section 6.4, therefore the red curve shown in Figure 6.21 shall be used for future testing. In the case of a system developed specifically for implementation with a thruster, knowing \dot{m} is not of extreme importance. It is rather more pragmatic to correlate the temperature measured at the tank with the generated thrust.

PART IV
CONCLUSION

Chapter 7

Conclusion

The work contained in this thesis presents a number of experimental findings aiming at expanding and enriching the physical understating of helicon plasma sources and magnetic nozzles. The ensemble of results is grouped into three main parts, whose major points are summarized below and, at last, the perspectives for future lines of research are addressed.

7.1 Summary

The first part of this thesis provides a comprehensive description of all the diagnostics used during the research activities and also describes and discusses the experimental campaigns aimed at studying the plasma generated with a helicon source. The latter has been operated under different conditions to analyze the effects of the principal external parameters. Measurements obtained in comparing xenon and krypton propellants exhibit relevant qualitative and quantitative differences suggesting that the discharge is sustained in distinct modes as an effect of ionization and collision phenomena. In this instance, it is shown that plasma properties in the magnetic nozzle peak off-axis which is a result repeatedly observed within the thesis. This effect possibly arises from anisotropic power deposition inside the source given by the various modes in which the antenna can couple to the plasma. In a separate campaign, plasma properties are inferred as a function of the axial location of the magnetic throat. It is observed that a low-current high-divergence plume is extracted from the plasma source when the magnetic throat is located upstream or in correspondence to the antenna center. In those cases, most of the plasma is lost at the radial and back boundaries. Improved plume characteristics are attained when the magnetic throat is located downstream the antenna at a distance that equals or exceeds two times the antenna length. In studying the effects linked to the magnetic nozzle divergence, the electron thermodynamics has been characterized in 2-D along the magnetic streamlines. This experiment has shown that the electron cooling rate is inhomogeneous in space as a result of phenomena such as ionization within the plume and reduced cross-field electron mobility. The source has also been operated in a promising non-conventional topology of the external magnetic field so as to meet the electron-cyclotron resonance condition near the antenna. This strategy led to the observation of noticeably improved electron properties, foremost among all the effective temperature which is recorded to increase even by 40 % with respect to the

conventional magnetic field topology. The combination of all these parametric analyses represents a repository of experimental evidence that can contribute to improving the efficiency of rf electrodeless propulsion systems. The last portion of the first part is dedicated to plasma oscillations and instabilities. Measurements of the ion current time series show the presence of a drift wave at about 10 kHz whose amplitude correlates with the radial gradient of the plasma density. Probing the azimuthal structure has been also attempted but without any disclosing result given the topological complexity of the instability itself and the setup limitations. Fixed-probe pairs allowed inferring the instability wavenumber in a few locations of the plasma domain, demonstrating the technique feasibility and highlighting the complex evolution in space of the wave.

The second part of this thesis reports on the results obtained during intense experimental campaigns performed in collaboration with the electric propulsion team at Universidad Carlos III de Madrid. The objective of these activities was to assess the poorly documented dynamics of ions and atoms in a magnetic nozzle via laser-induced fluorescence spectroscopy. Such type of datasets largely serves to iterate on prototype design as well as develop and validate numerical models. Experimental data about particles velocity just upstream the thruster exit plane are also of valuable interest whereas it is unfeasible to probe that region using intrusive diagnostics. Measurements have been performed using a HPT and an ECRT as plasma sources. These thrusters require a relatively strong magnetic field, respectively around 70 mT and 200 mT in this case. In these conditions, optical transitions experience a visible splitting due to Zeeman and/or Paschen-Back effect thus leading to a complex fluorescence lineshape. Accurate inference of ions and atoms velocity through Doppler shift required extensive modeling of the spectra by accounting for isotopic shift, hyperfine structure, kinetic and magnetic effects. The dynamics of atoms has been measured in the HPT, finding that they are accelerated up to supersonic speeds downstream the thruster exit plane. This phenomenon occurs as a result of flow expansion, ions recombination at the walls, ion-neutral elastic collisions and ionization collisions. The acceleration region of ions extends several centimeters downstream the exit plane and higher velocities have been recorded at low mass flow rates and high levels of input power. In addition, LIF and RPA techniques have been compared in the far-field plume while the HPT operates with xenon and krypton gases. The results have shown very good agreement. Qualitatively similar results with regard to the ion dynamics have been found also when characterizing the ECRT. In this source, the shape of the magnetic nozzle could be varied by means of an additional coil. Measurements have shown that, when the MN divergence is reduced, the acceleration profile stretches out along the axis but altogether the ultimate ion velocity does not exhibit a visible dependence on the nozzle shape. This results is in accordance with the simple theories describing the MN dynamics in the collisionless regime. Modeling of the fluorescence spectra allowed deducing that the ion kinetic temperature in the axial direction is in the order of a few thousands of K. This relative high dispersion in ion axial velocity likely results from a broad ionization region which overlaps with the acceleration region.

The third and final part of this thesis deals with the use of iodine as propellant. It has been shown that iodine is possibly the best candidate among many possible alternatives to xenon because of several characteristics. However, its chemically reactive nature places certain limits in its implementation on classical technologies, while only some design forethought relative to material selection is necessary in the case of electrodeless thrusters. As a preliminary work in the investigation of iodine as propellant

for helicon sources, a thermally-controlled feeding system has been conceived, designed and tested. It relies on storage of solid iodine at low pressure and room temperature. The sublimation process occurs due to thermal contact with a heated multi-perforated surface. Because of the system design, thermal control of the sublimation surface alone is sufficient for mass flow rate control. Because temperature is a crucial parameter to define sublimation and avoid deposition, a closed-loop system has been implemented from scratch to perform its active monitoring and control along several points of the iodine feeding line. Two prototypes have been designed and manufactured. Tests performed on the first one allowed highlighting certain phenomena about iodine sublimation and interaction with materials that suggested a number of measures to be taken into account for design iteration. These observations led to the second prototype which shows promising characteristics for reliable operation. At last, a sublimation model has been proposed whose formulation relies on experimental evidence previously published by the research group from the University of Pisa. The model has covered the effects linked to dynamic equilibrium that occur in correspondence of the sublimation interface, leading to a very good agreement between measured and predicted mass flow rate profiles.

7.2 Perspectives

This work has analyzed several aspects of helicon plasmas and magnetic nozzles, yet there are certainly many additional matters worth investigating. In the first place, the next logical step is to combine all observations and findings reported in this manuscript to design and test a thruster prototype. Although this task requires a number of efforts especially from the engineering side, it would allow to further progress towards competitive propulsive performance of this technology. Furthermore, such a plasma source would represent an excellent starting point to pursue research activities even more.

It is worth considering the use of advanced diagnostics, first and foremost Thomson scattering, in order to accurately characterize the electron flow in the magnetic nozzle. This type of measurements might allow studying complex phenomena which often are poorly documented in the literature. Perhaps the most fundamental piece of information regards the spatial evolution of the electron energy distribution function in the magnetic nozzle from the close-field to the far-field plume. To name a few, this analysis would provide insights into the evolution of electron cooling and electron demagnetization.

It is deemed of significant interest to further investigate plasma instabilities that occur in the magnetic nozzle region. This is especially true if their characterization goes along with performance measurement so that a quantitative correlation between the two can be sought. A loss of performance can in fact originate from non-ideal transport of species along the magnetic lines which involves an enhanced cross-field diffusion. These results could be achieved either by looking at the electrons via Thomson scattering in the coherent regime or by resolving in time the ion velocity via LIF spectroscopy.

It is clearly of paramount importance to further characterize the ion dynamics. In this regard, another logical step would be to carefully investigate the ion detachment phenomenon via 2-D LIF spectroscopy so to validate and/or improve the theories on which the most advanced numerical tools are currently based. LIF data could also be

7.2. PERSPECTIVES

coupled with probe measurements for a dedicated experiment aiming at the characterization of the ion flux lost at the walls.

Last but not least, it is necessary to support the exploration of new thruster architectures. Starting from the current physical understating, one should invest into testing of different configurations, e.g. in terms of discharge chamber geometry, magnetic field topology and gas injection strategy, with the purpose of enhancing the electron temperature and minimizing wall and collision losses. These activities should preferably proceed in parallel with theoretical modeling aiming at continuous validation and refinement of advanced tools.

PART V
APPENDIX

Appendix A

List of Publications and Conferences

A.1 Peer-reviewed journal papers

A. E. Vinci, M. R. Inchingolo, S. Mazouffre, J. Navarro-Cavallé, "*Ion dynamics in the magnetic nozzle of a waveguide ECR thruster via laser-induced fluorescence spectroscopy*", J. Phys. D: Appl. Phys. **56**, 025204 (2022), doi:10.1088/1361-6463/aca105

A. E. Vinci, S. Mazouffre, *Enhanced electron heating in the magnetic nozzle of a radio-frequency plasma via electron cyclotron resonance*, submitted to EPL (Europhysics Letters).

E. Michaux, A. E. Vinci, S. Mazouffre, *Fractal dimension of cathode spots in a high-current Vacuum Arc Thruster*, submitted to Vacuum.

A. E. Vinci, S. Mazouffre, V. Gómez, P. Fajardo, J. Navarro-Cavallé, "*Laser-induced fluorescence spectroscopy on xenon atoms and ions in the magnetic nozzle of a Helicon plasma thruster*", Plasma Sources Sci. and Technol. **31**, 095007 (2022), doi:10.1088/1361-6595/ac8db8.

A. E. Vinci, Q. Delavière-Delion and S. Mazouffre, "*Electron thermodynamics along magnetic nozzle lines in a helicon plasma*", Journal of Electric Propulsion **1**, 4 (2022), doi:10.1007/s44205-022-00003-0.

A. E. Vinci and S. Mazouffre, "*Plasma properties conditioned by the magnetic throat location in a helicon plasma device*", Journal of Applied Physics **130**, 183301 (2021), doi:10.1063/5.006998.

A. E. Vinci and S. Mazouffre, "*Direct experimental comparison of krypton and xenon discharge properties in the magnetic nozzle of a helicon plasma source*", Physics of Plasmas **28**, 033504 (2021), doi:10.1063/5.0037117.

A.2 Conference contributions

A. E. Vinci, S. Mazouffre, "*Effect of magnetic nozzle geometry on ion and electron properties*", 73rd International Astronautical Congress, Paris (France), September 18-22 (2022).

S. Mazouffre, A. E. Vinci, M. R. Inchingolo, J. Navarro-Cavallé, P. Fajardo, "*Ion transport in the magnetic nozzle of electrodeless plasma thrusters for spacecraft*", 32nd International Symposium on Rarefied Gas Dynamics, Seoul, South Korea – June 4-8 (2022).

C. Royer, A. E. Vinci, S. Mazouffre, T. Hallouin, A. Gurciullo, "*A LIF study on the plasma plume of a cluster of two 100 W Hall thrusters*", 37th International Electric Propulsion Conference, Massachusetts Institute of Technology, Cambridge, MA, USA – June 19-23 (2022).

A. E. Vinci, S. Mazouffre, M. R. Inchingolo, V. Gómez, P. Fajardo and J. Navarro-Cavallé, "*Probing xenon atoms and ions velocity in the magnetic nozzle of a helicon plasma thruster*", 37th International Electric Propulsion Conference, Massachusetts Institute of Technology, Cambridge, MA, USA – June 19-23 (2022).

M. Ruiz and A. Velasco, V. Gómez and J. Navarro-Cavallé, G. Dickeli, A. E. Vinci and S. Mazouffre, "*Results of the first Helicon Plasma Thruster (HPT) coupling test campaign within the HIPATIA project*", 37th International Electric Propulsion Conference, Massachusetts Institute of Technology, Cambridge, MA, USA – June 19-23 (2022).

T. Perrotin, A. E. Vinci, S. Mazouffre, J. Navarro-Cavallé, P. Fajardo, E. Ahedo, "*Characterization of a low-power Cylindrical Hall Thruster*", 37th International Electric Propulsion Conference, Massachusetts Institute of Technology, Cambridge, MA, USA – June 19-23 (2022).

A. E. Vinci, "*Experimental Results on Electron Cooling*", Session 6: Magnetic Nozzles and Plasma Plumes, $E \times B$ Plasma Workshop, Madrid online event (2022). *Invited talk*.

A. E. Vinci, Q. Delavière-Delion and S. Mazouffre, "*Ion energy and electron cooling in a magnetic nozzle with different expansion ratios*", 5th Workshop on MicroPropulsion and CubeSats, Virtual Event (2021).

A. E. Vinci and S. Mazouffre, "*Measurement and comparison of plasma properties depending on the magnetic throat location in a helicon device*", IEPC Student Summer Competition, Virtual Event (2021). *Regional Finalist Presentation Award*.

A. E. Vinci and S. Mazouffre, "*Electron and Ion Properties in the Beam and Discharge of a Helicon Plasma Source for Application in Spacecraft Propulsion*", Space Propulsion 2020+1 Virtual Conference (2021), hal-03576133.

M. Ruiz, V. Gómez, P. Fajardo, J. Navarro, R. Albertoni, G. Dickeli, A. Vinci, S. Mazouffre, N. Hildebrand, "*HIPATIA: A project for the development of the Helicon Plasma Thruster and its associated technologies to intermediate-high TRLs*", 71st International Astronautical Congress (IAC) The CyberSpace Edition, hal-02995461.

Appendix B

Iodine Physical and Chemical Properties

The purpose of this appendix chapter is to gather iodine physical and chemical properties in its different forms: atomic, diatomic molecule, plasma. In addition, solubility properties and immobilization strategies are provided.

B.1 Atomic iodine

Iodine (I) is a non-metallic element of the halogen family (fluorine, chlorine, bromine, iodine, and astatine). Its name comes after the Greek *ιώδης* meaning violet-colored. It is the heaviest of the stable halogens. It appears in group 17th of the periodic table. Because of its high electronegativity and oxidation state -1 , it forms iodides with several elements. Iodine is known in compounds with formal oxidation states ranging from -1 , $+1$, $+3$, $+5$, and $+7$. Iodine also reacts with other halogens, fluorine, chlorine, and bromine, and forms inter-halogens. The basic properties of the atomic iodine are reported in Table B.1.



(a) Solid phase iodine.



(b) Vapor phase iodine [166].

Figure B.1: Molecular iodine in solid and vapor phases.

Table B.1: Atomic iodine properties.

Element category	Halogen
Group, Period, Block	17 (halogens), 5, p
Standard atomic weight	126.90447
Atomic number	53
Electronic configuration	[Kr] 4d ¹⁰ 5s ² 5p ⁵
Electrons per shell	2, 8, 18, 18, 7
Atomic radius	140 pm
Covalent radius	139 ± 3 pm
Ionic radius	220 pm
Electronegativity	2.66 (Pauling scale)
Electron affinity	301 kJ mol ⁻¹

Table B.2: Molecular iodine solid phase properties.

Density	4.933 g cm ⁻³ @298 K 4.866 g cm ⁻³ @333 K
Refractive index	n _{D20} 3.34
Molar heat capacity	53.3 J mol ⁻¹ K ⁻¹
Standard entropy S^0_{solid}	116.14 J mol ⁻¹ K ⁻¹
Vapor pressure	0.031 kPa @298.15 K 9.17 kPa @386.65 K
Van der Waals radius	198 pm
Thermal conductivity	0.45 W m ⁻¹ K ⁻¹
Electrical resistivity	1.3·10 ⁷ Ω m @273.15 K 5.85·10 ⁶ Ω m @298.15 K 1.3·10 ⁵ Ω m @383.15 K

Table B.3: Molecular iodine liquid phase properties.

Boiling point @1 atm	475 K
Heat of vaporization	41.75 kJ mol ⁻¹ @boiling point
Critical point	819 K, 11.7 MPa
Critical compressibility factor	0.268
Density	3.96 g cm ⁻³ @393 K 3.736 g cm ⁻³ @453 K
Dynamic viscosity	2.268·10 ⁻³ Pa s @389 K 1.414·10 ⁻³ Pa s @457 K
Dielectric Constant	11.08 @391 K
Specific heat	316.3 J kg ⁻¹ K ⁻¹ @113.6–184 °C
Standard enthalpy $\Delta_f H_{liquid}^0$	13.52 kJ mol ⁻¹
Standard entropy S_{liquid}^0	150.36 J mol ⁻¹ K ⁻¹

Table B.4: Molecular iodine gaseous phase properties.

Gas constant	32.759 J kg ⁻¹ K ⁻¹
Specific heat at constant pressure	146.4 J kg ⁻¹ K ⁻¹
Adiabatic coefficient	1.2883
Vapor density @101.3 MPa, 458 K	6.75 g L ⁻¹
Standard enthalpy $\Delta_f H_{gas}^0$	62.42 kJ mol ⁻¹
Standard entropy S_{gas}^0	260.69 J mol ⁻¹ K ⁻¹
Fick's diffusion coefficient @101 kPa, 293 K	7·10 ⁻⁶ m ² s ⁻¹

Table B.5: Antoine parameters for I₂.

T [K]	311.9 - 456
A	3.36429
B	1039.159
C	-146.589

Data from nist.gov.

Table B.6: Conditions at triple, boiling and critical point for I₂.

	Temperature [K]	Pressure [Pa]
Triple point	386.65	12100 (10853 from Antoine)
Melting point	386.95	1.01325·10 ⁵
Critical point	819	11.7·10 ⁶

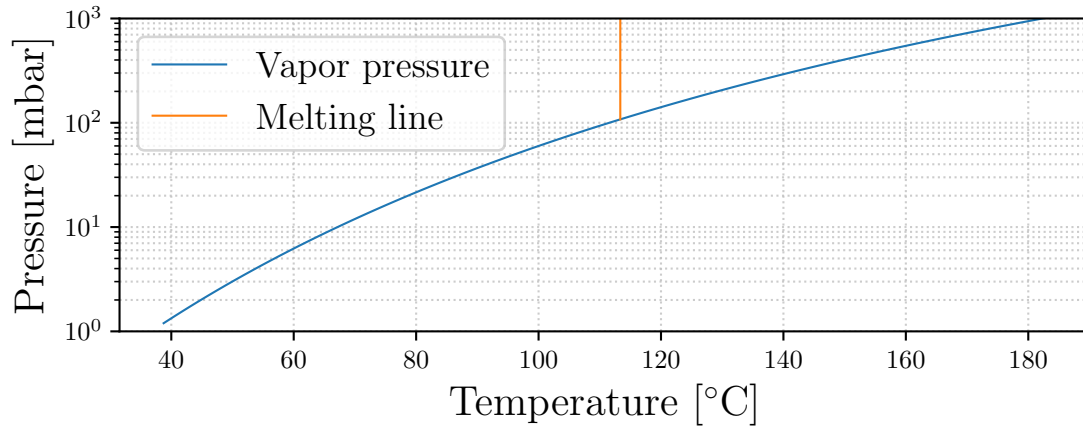


Figure B.2: Iodine phase diagram.

B.2 Molecular iodine

Under standard conditions, iodine is found in the form of diatomic molecule I_2 with a molecular weight of $253.80894 \text{ g mol}^{-1}$. It appears as a purplish-black solid with metallic like surface, see Figure B.1a. It has a moderate vapor pressure at room temperature and in an open vessel slowly sublimates to a deep violet vapor, see Figure B.1b. Under proper heating conditions, iodine melts at 113.7°C and boils at 184°C . Properties are reported in Table B.2, B.3 and B.4 for the solid, liquid and gaseous phase, respectively.

B.2.1 Phase Diagram

The iodine phase diagram is represented in Figure B.2. In obtaining the vapor equilibrium $p - T$ curve, Antoine equation has been used

$$\log_{10}(p[\text{bar}]) = A - \left(\frac{B}{T[\text{K}] + C} \right) \quad (\text{B.1})$$

where A , B and C are the Antoine parameters reported in Table B.5. Triple, boiling and critical points are reported in Table B.6.

B.2.2 Iodine Viscosity

Proper modeling of the iodine vapor viscosity is of relevance for any feeding system design based on fluid dynamics simulation. Often, the Sutherland's law is employed, as proposed by [168], according to which the viscosity equation reads

$$\mu = 2.26 \cdot 10^{-6} \frac{\sqrt{T}}{1 + 590/T} \quad (\text{B.2})$$

This may represents a main cause of the disagreement between theory and experiments, as shown in [166]. Indeed, in accordance with [169], Equation B.2 loses its reliability below the critical pressure and temperature, which is the case of interest since the feeding system works below the triple point.

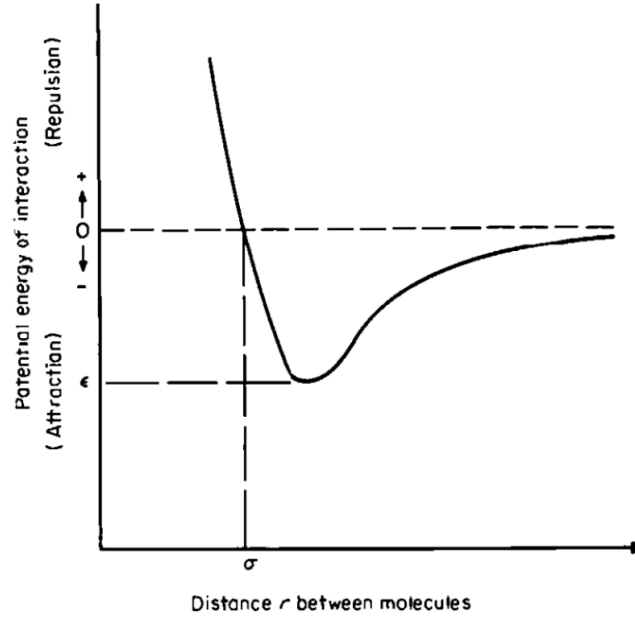


Figure B.3: Intermolecular potential function, [172].

Chung *et al.* [170] [171] proposed a method to estimate the viscosity of low-pressure gases, which is also described in [172]. It relies on the Chapman-Enskog gas kinetic treatment, whose assumptions convey validity to it only for low-pressure, high-temperature gases. Chung's method includes a correction for molecular shapes and polarities. Chapman-Enskog theory considers the interactions between colliding particles by way of a potential energy $\psi(r)$. In general terms, the potential energy solution for viscosity of Chapman-Enskog theory is given by

$$\mu = \frac{26.69 (\mathcal{M}T)^{1/2}}{\sigma^2 \Omega_v} \cdot 10^{-7} \quad [\text{Pa} \cdot \text{s}] \quad (\text{B.3})$$

where

$$\begin{aligned} \mathcal{M} &= \text{molecular weight, g mol}^{-1} \\ T &= \text{temperature, K} \\ \sigma &= \text{hard-sphere diameter, \AA} \\ \Omega_v &= \text{collision integral} \end{aligned} \quad (\text{B.4})$$

To use Equation B.3, the collision diameter σ and collision integral Ω_v need to be made explicit. In the derivation of Equation B.3, Ω_v is obtained as a function of a dimensionless temperature T^* . The functionality depends on the intermolecular potential $\psi(r)$ chosen. For a general potential energy of interaction $\psi(r)$ between two molecules separated by distance r , see Figure B.3, the minimum in the $\psi(r)$ versus r curve is termed characteristic energy ϵ , while the separation distance $\psi(r) = 0$ is defined to be the collision diameter σ . For any potential curve, the dimensionless temperature T^* is related to ϵ by

$$T^* = \frac{k_B T}{\epsilon}, \quad (\text{B.5})$$

where k_B is the Boltzmann constant. A simple and extensively used two-parameter relation for the intermolecular potential function is the Lennard-Jones formulation, which is given by

$$\psi(r) = 4\epsilon \left[\left(\frac{\sigma}{r} \right)^{12} - \left(\frac{\sigma}{r} \right)^6 \right]. \quad (\text{B.6})$$

According to [172], the employed potential function does not affect substantially the Ω_v determination therefore this potential has been used by Neufeld *et al.* [173] who proposed a practical empirical equation for Ω_v , easy to be implemented numerically that is

$$\Omega_v = \left[A (T^*)^{-B} \right] + C \left[\exp(-DT^*) \right] + E \left[\exp(-FT^*) \right], \quad (\text{B.7})$$

where T^* is defined in Equation B.5 and

$$\begin{aligned} A &= 1.16145 \\ B &= 0.14874 \\ C &= 0.52487 \\ D &= 0.77320 \\ E &= 2.16178 \\ F &= 2.43787 \end{aligned}$$

Equation B.7 is valid for $0.3 \leq T^* \leq 100$ with an average deviation of only 0.064%, [172]. Starting from this point, Chung *et al.* have utilized Equation B.3 with a specific set of ϵ/k_B and σ which are

$$\frac{\epsilon}{k_B} = \frac{T_c}{1.2593}, \quad (\text{B.8})$$

$$\sigma = 0.809 V_c^{1/3}, \quad (\text{B.9})$$

where ϵ/k_B is in K, σ is in Å, and

$$\begin{aligned} T_c &= \text{critical temperature [K]}, \\ V_c &= \text{critical volume [cm}^3 \text{ mol}^{-1}]. \end{aligned}$$

Combining Equation B.5 and B.8, it results

$$T^* = 1.2593 T_r, \quad (\text{B.10})$$

with $T_r = T/T_c$ named reduced temperature. An additional factor $F_c(\omega, \eta_r)$ is included in the model to account for molecular shapes and polarities, as previously mentioned. From [170], it is given by

$$F_c(\omega, \eta_r) = 1 - 0.2756 \omega + 0.059035 \eta_r^4, \quad (\text{B.11})$$

where ω is the acentric factor (or nonsphericity of a molecule) from [172] given by

$$\omega = \frac{3}{7} \frac{T_b/T_c}{1 - T_b/T_c} \log_{10} \left(\frac{p_c}{101325} \right) - 1, \quad (\text{B.12})$$

with

$$\begin{aligned} T_b &= \text{boiling temperature, [K]}, \\ p_c &= \text{critical pressure, [Pa]}, \end{aligned}$$

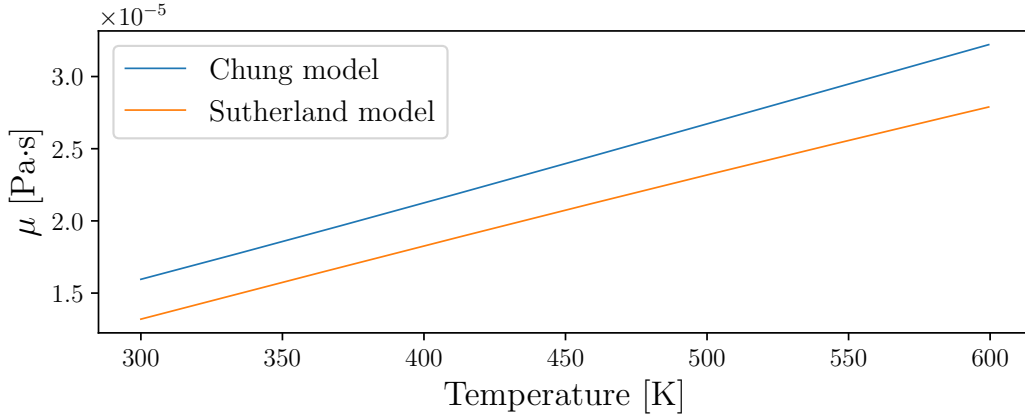


Figure B.4: Chung vs. Sutherland viscosity model.

and η_r is a reduced dipole moment given by

$$\eta_r = 131.3 \frac{\eta}{(V_c T_c)^{1/2}}. \quad (\text{B.13})$$

Hence, the final relation proposed is

$$\mu = \frac{40.785 F_c(\omega, \eta_r) (MT)^{1/2}}{V_c^{2/3} \Omega_v} \cdot 10^{-7} \quad [\text{Pa} \cdot \text{s}] \quad (\text{B.14})$$

where input values for molecular iodine in consistent units are:

$$\begin{aligned} \mathcal{M} &= 253.8 \text{ g mol}^{-1} \\ T_b &= 457.4 \text{ K} \\ T_c &= 819 \text{ K} \\ p_c &= 11.7 \cdot 10^6 \text{ Pa} \\ V_c &= 155 \text{ cm}^3 \text{ mol}^{-1} \\ \eta &= 1.3 \text{ D} \end{aligned}$$

The resulting viscosity profile and the Sutherland's model are compared in Figure B.4. It reveals that the viscosity estimated by the Sutherland's model is more than 15 % smaller than that resulting from the Chung *et al.* model in the temperature range of interest.

B.2.3 Iodine thermal conductivity

Similarly to what has been done for the viscosity, Chung *et al.* proposed a thermal conductivity model in [171] based on the approximation of Mason and Monchick [174] for polyatomic low-pressure gases, in the framework of the kinetic theory. This model aims at providing a better estimates of the thermal conductivity with respect to the Sutherland model according to which

$$\lambda = 3.9 \cdot 10^{-3} \left(\frac{T}{400} \right)^{0.97} \quad [\text{W m}^{-1} \text{ K}^{-1}] \quad (\text{B.15})$$

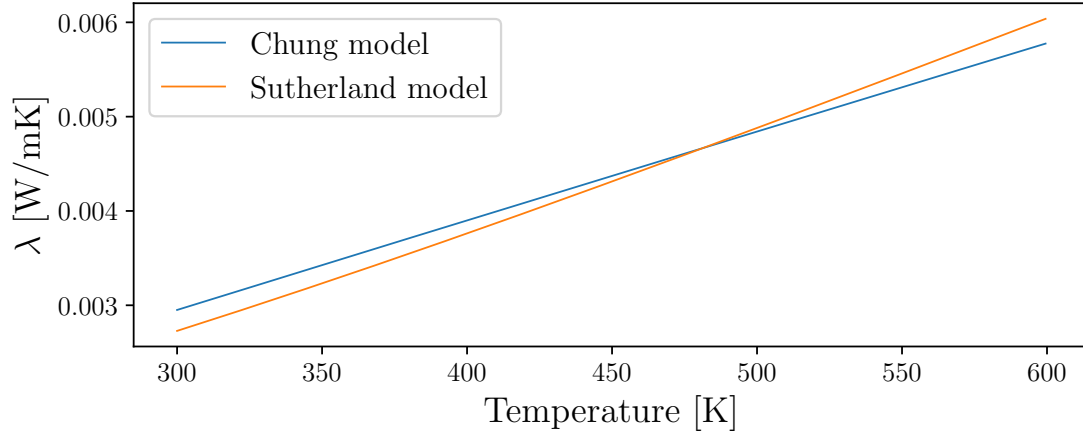


Figure B.5: Chung vs. Sutherland thermal conductivity model.

As almost all the equations for the thermal conductivity λ , Chung *et al.* model starts assuming that $\lambda = \lambda_{tr} + \lambda_{int}$, i.e. it is composed of a translation contribution and an internal one. Using the expressions of Mason and Monchick for both contributions, the proposed equation is given by

$$\lambda = 3.75\Psi R\mu \quad [\text{W m}^{-1} \text{K}^{-1}] \quad (\text{B.16})$$

where

$$\Psi = 1 + \alpha \{ [0.215 + 0.28288\alpha - 1.061\beta + 0.26665Z] / [0.6366 + \beta Z + 1.061\alpha\beta] \},$$

$$\alpha = \frac{c_v}{R} - \frac{3}{2},$$

$$c_v = \text{heat capacity at constant volume, } [\text{J kg}^{-1} \text{K}^{-1}],$$

$$R = \text{specific gas constant, } [\text{J kg}^{-1} \text{K}^{-1}],$$

$$Z = 2.0 + 10.5T_r^2,$$

$$\beta = 0.7862 - 0.7109\omega + 1.3168\omega^2,$$

$$\omega = \text{acentric factor, from Equation B.12,}$$

$$\mu = \text{low-pressure gas viscosity, } [\text{Pa s}], \text{ from Equation B.14.}$$

The resulting thermal conductivity profile and the Sutherland's model are compared in Figure B.5. It is worth noticing that no substantial differences lie between Chung *et al.* model and the Sutherland's one described by Equation B.15.

B.2.4 Iodine Solubility

Iodine solubility properties are particularly of interest for cleaning and disposal processes throughout any test campaign. Iodine solubility for various solvents is reported in Table B.7. According to [175], iodine dissolves easily in most organic solvents such as hexane, benzene, carbon tetrachloride, and chloroform owing to its lack of polarity. The solubility of elemental iodine in water can be improved by the generating the triiodide anion addition of sodium or potassium iodide. Molecular iodine reacts reversibly with the negative ion, in equilibrium, which is soluble in water. Iodine solutions appear brown in solvents such as unsaturated hydrocarbons, liquid SO_2 , water, alcohols, and ketones, pinkish brown in benzene, and violet in chlorinated solvents.

Table B.7: Iodine Solubility, [166].

Solvent	Solubility [g/kg]	Color
Acetone	High	Brown
Benzene	164	Red
Butan-2-ol	97	Brown
Carbon disulfide	197	Red
Carbon tetrachloride	19.2	Violet
Chloroform	49.7	Violet
Dichloromethane	46.3	Violet
Ether	337.3	Brown
Ethanol	271.7	Brown
Ethyl acetate	157	Brown
Hexane	13.2	Violet
Toluene	182.5	Red
Water	0.33	Brown

B.2.5 Iodine Immobilization

A number of methods are available for the immobilization of iodine vapors that are categorized as wet scrubbing methods, solid adsorbent methods and cryogenic trapping. Obviously, for use in high vacuum applications only solid adsorbents and cryogenic trapping are suitable. Activated carbon is an efficient immobilizer for molecular iodine, widely used for removing radioiodine from gaseous streams at nuclear power plants [176]. Activated charcoal generally performs well in iodine retention, but it exhibits poor iodine retention at high temperatures so, probably, the efficiency decreases in high vacuum conditions. In alternative to solid adsorbents, a realistic solution in iodine immobilization is to use liquid nitrogen-cooled chevrons inside the vacuum facility [177].

B.3 Iodine Plasma

Iodine as a plasma is introduced in the following. The presence of diatomic molecules leads to different phenomena observed in the plasma phase in comparison with typical discharges based on argon or xenon.

B.3.1 Ionization Cross Section

Neutrals flowing in the channel of a generic low-pressure plasma source can usually be modeled as a cold population with respect to the hot electrons ($T_e/T_n \sim 10^2 - 10^3$). This implies that plasma internal kinetics and dynamics are mainly dominated by the electrons motion and collisions with the different species, given their higher temperature and mobility. Collision interactions are fundamentally characterized by the collision

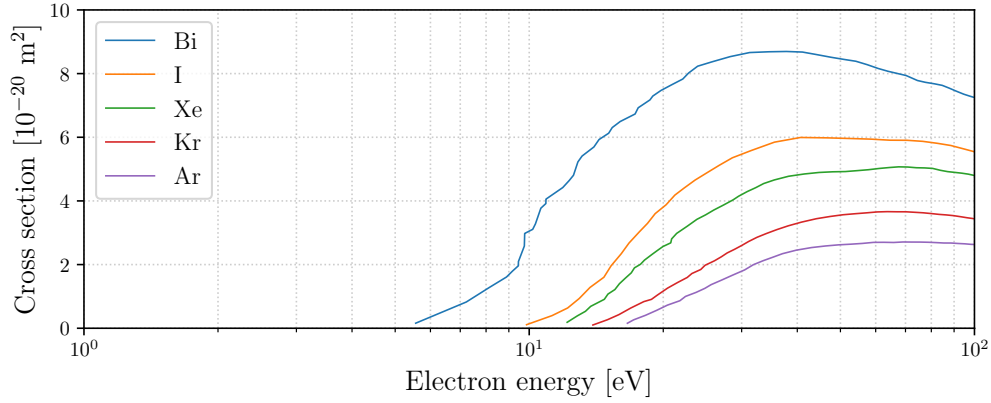


Figure B.6: First ionization cross-section for different propellants. Reproduced from [178].

cross section. Atomic iodine ionization is foremost related to the first ionization cross section. It is worth to be analyzed as it has an impact on the ionization cost, i.e. the ratio between propellant ionization power and total input power. As the cross section increases, more likely the ionization events occur in the plasma thus to increase the efficiency of the process.

Figure B.6 presents the value of the cross section for different propellants, including atomic iodine. It shows that iodine should behave better than both xenon and krypton. However, iodine is injected as a diatomic molecule, hence assuming a lower ionization cost with respect to Xe or Kr may overestimate the related advantages. Indeed, dissociation cost, as well as other reactions present in the discharge, must be included. Additional data on cross sections for other collisions can be found in [161, 179].

B.3.2 Plasma Chemistry

The set of reactions used in [157] to model the main chemical phenomena occurring in an electric plasma thruster are reported in Table B.8. In addition to them, other reactions linked to chemical interaction with the thruster materials should be considered as well. The electron mediated reaction rate factors are computed assuming a Maxwellian electrons,

$$K(T) = \langle \sigma(v)v \rangle_v = \left(\frac{m_e}{2\pi k_B T_e} \right)^{3/2} \int_0^\infty \sigma(v)v \exp\left(-\frac{m_e v^2}{2k_B T_e}\right) 4\pi v^2 dv, \quad (\text{B.17})$$

where m_e and T_e are the electron mass and temperature respectively. The results are reported in Figure B.7 [157]. This dataset includes reaction rates calculated up to $T_e = 10$ eV, which is enough for typical rf discharges. In analyzing ECRTs or Hall thrusters instead, values up to $T_e = 100$ eV are clearly necessary.

Ionization energy of atomic and diatomic iodine is 10.5 eV and 9.3 eV, respectively. Although I_2 dissociation energy is merely 1.567 eV [157], much lower than the electron temperature in a typical discharge, the presence of I_2^+ in the thruster plume has been reported by [163], suggesting an incomplete dissociation. The high electronegativity the iodine possesses entails the presence of negatives ions I^- in the discharge by way of dissociative attachment. Attachment of an electron to I_2 leads to the formation of very unstable I_2^- ions for which the electron is rapidly lost by auto-detachment.

Table B.8: Chemical reactions in iodine plasma, [157].

Excitation of I	$e^{-*} + \text{I} \rightarrow e^{-} + \text{I}^{*}$	K_{exc1}
Elastic collision of I_2	$e^{-} + \text{I}_2 \rightarrow e^{-} + \text{I}_2$	$K_{el\text{I}_2}$
Elastic collision of I	$e^{-} + \text{I} \rightarrow e^{-} + \text{I}$	K_{el1}
Dissociative attachment	$e^{-} + \text{I}_2 \rightarrow \text{I}^{-} + \text{I}$	$K_{dissatt}$
Dissociative ionization	$e^{-} + \text{I}_2 \rightarrow \text{I}^{+} + \text{I} + 2e^{-}$	K_{dissiz}
Ionization of I	$e^{-} + \text{I} \rightarrow \text{I}^{+} + 2e^{-}$	K_{iz1}
Ionization of I_2	$e^{-} + \text{I}_2 \rightarrow \text{I}_2^{+} + 2e^{-}$	$K_{iz\text{I}_2}$
Charge exchange	$\text{I}^{-} + \text{I}_2^{+} \rightarrow \text{I} + \text{I}_2$	K_{cex}
Ion recombination	$\text{I}^{-} + \text{I}^{+} \rightarrow 2\text{I}$	K_{ionrec}
Surface recombination	$\text{I} \rightarrow \frac{1}{2}\text{I}_2$	γ
Dissociation	$e^{-} + \text{I}_2 \rightarrow 2\text{I} + e^{-}$	K_{diss}

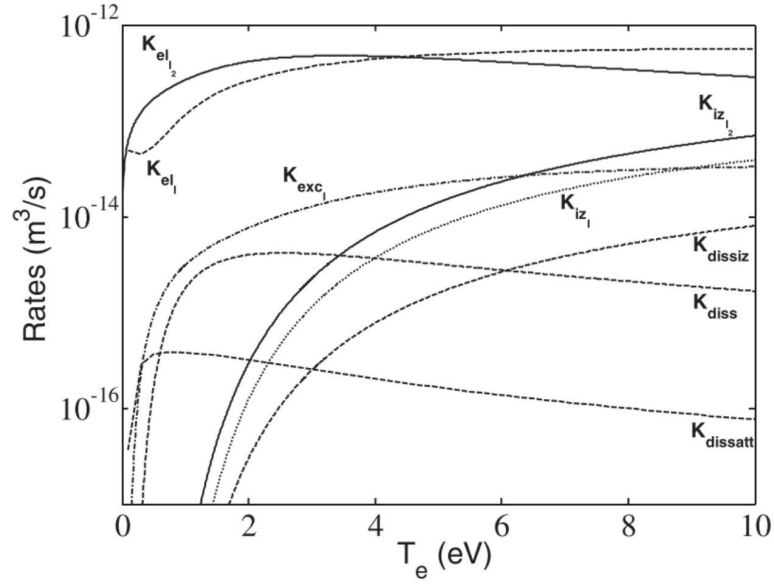


Figure B.7: Iodine plasma reaction rates, [157].

Appendix C

Version française

Ce chapitre annexe rassemble brièvement les points les plus importants qui ont été discutés dans le corps de la thèse. Ci-dessous, chaque section principale est traitée indépendamment.

C.0.1 Chapitre 1: Introduction

La propulsion électrique (PE) est actuellement utilisée dans les plateformes spatiales pour la mise en orbite, le maintien de l'orbite, la désorbitation et finalement l'exploration de l'espace lointain. Aujourd'hui, les objectifs des missions vont de la construction de constellations de satellites en orbite basse à la colonisation de Mars en passant par les stations spatiales lunaires. La nécessité de réduire la consommation de propergol, parallèlement à la disponibilité accrue d'énergie, a fait des systèmes de propulsion électrique une option intéressante. Ces dernières années, d'intenses activités de recherche se sont concentrées sur les décharges sans électrodes afin d'étendre la portée des missions généralement couvertes par les technologies matures, par exemple les propulseurs ioniques à grille et les propulseurs Hall. Ces derniers restent les concepts les plus populaires et les plus durables, car ils offrent de bonnes performances en termes de niveau de poussée et de impulsion spécifique, même à des niveaux de puissance faibles ou modérés. En général, chaque mission apporte avec elle des exigences uniques en termes de impulsion spécifique et de durée de vie. Les propulseurs à plasma actuels ne bénéficient souvent pas de durées de vie exceptionnelles, principalement en raison de la forte érosion des électrodes exposées et des parois des canaux de décharge par les flux d'ions et d'électrons. Un autre élément à prendre en compte est que la grande majorité des systèmes PE actuellement dans l'espace fonctionnent avec des gaz nobles, principalement du xénon mais aussi, plus récemment, du krypton. L'exclusivité de ces propergols, bien qu'offrant des avantages pratiques inégalés à certains égards, notamment lors des essais en laboratoire, constitue une énorme limitation.

En définitive, des durées de vie plus longues et la compatibilité avec les propergols non conventionnels sont considérées comme des caractéristiques précieuses pour un système de PE. Ces qualités soutiennent largement l'intérêt pour les propulseurs sans électrodes. Des caractéristiques telles que l'absence de courant net, l'élimination de l'interaction plasma-électrodes, la simplicité de conception, sont les atouts de ces dispositifs qui peuvent fonctionner nominalement sans neutralisation et avec pratiquement n'importe quel propergol. Les concepts sans électrodes qui sont actuellement étudiés par les équipes de recherche comprennent essentiellement les propulseurs à plasma hélicon

(HPT), les propulseurs à Résonance Cyclotron Électronique (ECRT) et le Propulsion Magnéto-plasmique à Impulsion Spécifique Variable (VASIMR). Tous les systèmes sans électrodes fonctionnent en courant alternatif, mais la façon dont le rayonnement électromagnétique se couple avec la décharge gazeuse dépend fortement de la fréquence de travail et de la géométrie du champ.

Cette thèse se concentre spécifiquement sur les décharges de plasma hélicon et les tuyères magnétiques, qui sont les deux constituants fondamentaux d'un HPT ordinaire. Les dispositifs à plasma hélicon sont des sources de plasma froid qui reposent sur des mécanismes de chauffage par ondes pour entretenir une décharge gazeuse. Une source hélicoïdale classique comprend trois composants principaux : *i*) un tube diélectrique qui délimite physiquement le domaine du plasma, *ii*) une antenne alimentée par radiofréquence (rf) pour l'ionisation du gaz, et *iii*) un champ magnétique axial constant pour la propagation des ondes hélicon et pour réduire les interactions plasma-paroi. Les modes hélicon sont des 'whistler waves' qui se propagent dans une colonne de plasma magnétisée axialement avec une géométrie cylindrique limitée radialement. Les champs électriques et magnétiques des ondes présentent des modes radiaux, axiaux et souvent azimutaux qui varient en fonction des conditions aux limites. La puissance électromagnétique associée aux modes excités est convertie en énergie thermique des électrons qui régit une série de phénomènes de transport dans le domaine du plasma. À l'intérieur du tube source, la conservation du moment cinétique axial implique que l'énergie stockée sous forme de pression statique des électrons est convertie en accélération des ions. Dans tous les HPTs, le champ magnétique externe forme également une géométrie divergente en aval du tube de décharge pour accélérer le plasma, ce qu'on appelle la tuyère magnétique (TM). Une tuyère magnétique conventionnelle est essentiellement un champ magnétique permanent ayant une géométrie convergente-divergente dont le but est d'accélérer et de diriger un faisceau de plasma dans le vide. Les premières expériences ont permis d'observer une grande similitude entre les tuyères magnétiques et les tuyères de Laval en dynamique des gaz classique, avec un flux de plasma subissant une transition subsonique à supersonique en correspondance avec la gorge magnétique. Cependant, la physique de la TM conserve une nature plus compliquée, où les forces électromagnétiques volumétriques s'ajoutent à l'expansion classique induite par la pression.

Dans ce cadre, la maturité des propulseurs à plasma sans électrodes est encore relativement faible et divers aspects méritent d'être étudiés. Cette thèse vise à approfondir la recherche sur les mécanismes physiques à l'œuvre dans de tels propulseurs. L'objectif principal est de rassembler des résultats expérimentaux qui peuvent servir de point de départ pour améliorer la compétitivité des propulseurs sans électrodes. La disponibilité de données expérimentales est également d'un intérêt particulier pour le développement et la validation de modèles numériques prédictifs.

C.1 Partie I: Recherche sur une source de plasma hélicon et développement des diagnostics

C.1.1 Chapitre 2: Dispositifs expérimentaux

La source de plasma hélicon (HP) utilisée à ICARE comprend un tube de quartz orienté verticalement avec 9 cm de diamètre intérieur et 58 cm de longueur. L'ouverture supérieure est équipée d'un injecteur de gaz, alors que la partie inférieure est reliée à une chambre d'expansion de 30 cm de diamètre intérieur et de 50 cm de longueur. Un côté latéral de la chambre est relié à un système de pompage turbomoléculaire/primaire fournissant une pression de base ultime de l'ordre de 10^{-5} mbar. Les valeurs typiques de la pression pendant le fonctionnement sont de l'ordre de 10^{-3} mbar. La puissance RF est générée par une alimentation de classe 1 kW à 13.56 MHz et alimente une antenne double-selle en cuivre à travers un réseau d'adaptation de type π . La source HP comprend neuf électroaimants entourant à la fois le tube de décharge et la chambre d'expansion. La présence de plusieurs électroaimants permet d'étudier des topologies de champ magnétique profondément différentes. À ce propos, la plupart des campagnes expérimentales réalisées dans le cadre de ce doctorat se concentrent sur une géométrie spécifique du champ magnétique.

Plusieurs diagnostics ont été utilisés. Certains d'entre eux ont été développés spécifiquement pour les expériences détaillées dans ce qui suit. Il s'agit notamment de :

- une sonde *B-dot*; elle permet de mesurer la composante magnétique du champ électromagnétique qui se propage dans le plasma.
- une sonde capacitive; elle fonctionne essentiellement comme un condensateur et sert à mesurer les fluctuations du potentiel flottant.
- une sonde de Langmuir compensée par radiofréquence; elle permet de mesurer les propriétés des ions et des électrons tout en garantissant que l'effet des oscillations du plasma ne perturbe pas les courbes caractéristiques tension-courant déduites.
- une sonde plane avec un anneau de garde; elle permet de mesurer la densité de courant ionique.
- un analyseur de potentiel de retardement; il permet de déduire la fonction de distribution de l'énergie ionique et, surtout, l'énergie ionique la plus probable.
- spectroscopie de fluorescence induite par laser; une technique optique avancée qui permet de mesurer avec précision la vitesse des ions et des atomes.

Tous les détails techniques relatifs à cette liste de diagnostics se trouvent dans le corps du document.

C.1.2 Chapitre 3: Campagnes expérimentales et résultats

La source de plasma hélicon a été exploitée dans différentes conditions afin d'analyser les effets des principaux paramètres externes. Les mesures obtenues en comparant les propergols xénon et krypton présentent des différences qualitatives et quantitatives suggérant que la décharge est entretenue dans des modes distincts sous l'effet de phénomènes

d'ionisation et de collision. Dans ce cas, il est démontré que les propriétés du plasma dans la tuyère magnétique présentent un pic hors axe, ce qui est un résultat observé à plusieurs reprises lors de la thèse. Cet effet provient probablement d'un dépôt d'énergie anisotrope à l'intérieur de la source donné par les différents modes de couplage antenne-plasma. Dans une autre campagne, les propriétés du plasma sont déterminées en fonction de la position axiale de la gorge magnétique. On observe qu'une plume à faible courant et haute divergence est éjectée de la source de plasma lorsque la gorge magnétique est située en amont ou en correspondance avec le centre de l'antenne. Dans ces cas, la majeure partie du plasma est perdue aux limites radiales et arrière. Les caractéristiques de la plume sont améliorées lorsque la gorge magnétique est située en aval de l'antenne à une distance égale ou supérieure à deux fois la longueur de l'antenne. En étudiant les effets liés à la divergence de la tuyère magnétique, la thermodynamique des électrons a été caractérisée en 2-D le long des lignes magnétiques. Cette expérience a montré que le taux de refroidissement des électrons n'est pas homogène dans l'espace en raison de phénomènes tels que l'ionisation dans la plume et la réduction de la mobilité des électrons à travers le champ. La source de plasma a également été opérée dans une topologie de champ magnétique externe non conventionnelle mais prometteuse afin de satisfaire la condition de résonance électron-cyclotron près de l'antenne. Cette stratégie a permis d'observer une amélioration notable des propriétés des électrons, en particulier de la température effective, qui a augmenté de 40 % par rapport à la topologie conventionnelle du champ magnétique. La combinaison de toutes ces analyses paramétriques représente un référentiel de preuves expérimentales qui peut contribuer à améliorer l'efficacité des systèmes de propulsion RF sans électrodes. La dernière portion de la première partie est consacrée aux oscillations et instabilités du plasma. Les mesures de la série temporelle du courant ionique montrent la présence d'une onde de dérive à environ 10 kHz dont l'amplitude est corrélée avec le gradient radial de la densité du plasma. La structure azimutale a également été sondée, mais sans résultat probant étant donné la complexité topologique de l'instabilité elle-même et les limites de l'installation. Des paires de sondes fixes ont permis de déduire le nombre d'onde de l'instabilité en quelques endroits du domaine du plasma, démontrant la faisabilité de la technique et mettant en évidence l'évolution complexe dans l'espace de l'onde.

C.2 Partie II: Recherche sur la dynamique des tuyères magnétiques à UC3M

C.2.1 Chapitre 4: Dynamique des atomes et des ions dans la tuyère magnétique d'un propulseur à plasma hélicon

Cette partie de la thèse rend compte des résultats obtenus lors de campagnes expérimentales intensives réalisées en collaboration avec l'équipe de propulsion électrique de l'Université Carlos III de Madrid. L'objectif de ces activités était d'évaluer la dynamique peu documentée des ions et des atomes dans une tuyère magnétique via la spectroscopie de fluorescence induite par laser (LIF). Ce type d'ensemble de données sert principalement à itérer sur la conception du prototype ainsi qu'à développer et valider les modèles numériques. Les données expérimentales sur la vitesse des particules juste en amont du plan de sortie du propulseur sont également d'un grand intérêt, car il est impossible de

sonder cette région à l'aide de diagnostics intrusifs. La vitesse des ions a été résolue en différents points de l'espace à l'aide de la spectroscopie LIF et d'un RPA dans la tuyère magnétique d'un HPT fonctionnant dans plusieurs conditions. La vitesse axiale des ions la plus probable obtenue avec les deux instruments est comparée et un bon accord est trouvé.

La dynamique des atomes et des ions de xénon est étudiée à l'intérieur et à l'extérieur de la chambre de décharge par LIF. Dans la plume de proximité, le champ magnétique intense induit l'effet Zeeman, conduisant à une forme relativement complexe des spectres de fluorescence. Par conséquent, il est impossible de déduire avec précision la vitesse des atomes et des ions dans la région du champ magnétique intense sans modélisation préalable de la forme des lignes atomiques. Cette tâche est donc abordée en tenant compte des mécanismes d'élargissement, à savoir le décalage isotopique, la structure hyperfine et l'effet Zeeman. L'ajustement des profils modélisés et mesurés a permis de déduire l'évolution de la vitesse la plus probable pour les atomes et les ions de xénon. On constate que la vitesse axiale des neutres augmente jusqu'à des valeurs supersoniques en aval du plan de sortie du propulseur. Ce phénomène est associé à l'apparition parallèle de plusieurs processus. L'aile des atomes rapides de la fonction de distribution est peuplée en raison de l'expansion de l'écoulement, de la recombinaison des ions aux parois et des collisions de transfert de moment ion-neutre, tandis que l'aile des atomes lents est sélectivement dépeuplée en raison de l'ionisation. L'évolution axiale de la vitesse des ions met en évidence l'effet des paramètres de fonctionnement du propulseur. Des ions plus rapides sont obtenus pour des débits massiques plus faibles et des niveaux de puissance d'entrée plus élevés. Les profils de vitesse montrent également que la région d'accélération s'étend sur plusieurs centimètres en aval du plan de sortie.

C.2.2 Chapitre 5: Dynamique des ions dans la tuyère magnétique d'un propulseur ECR à guide d'ondes

Comme il a été présenté dans la section précédente, ce chapitre présente également des résultats obtenus lors d'une intense campagne expérimentale réalisée en collaboration avec l'équipe de propulsion électrique de l'Université Carlos III de Madrid. L'intérêt de cette analyse est d'évaluer par spectroscopie laser la dynamique des ions dans la plume et dans la chambre de décharge d'un ECRT à guide d'ondes. Bien que la physique des TM soit commune à d'autres dispositifs, ces mesures sont les premières jamais rapportées pour un propulseur à guide d'ondes, et sont donc d'une importance essentielle pour valider les futurs modèles de TM et les simulations de plasma.

Le ECRT est d'un intérêt central dans la catégorie des propulseurs sans électrodes, car il présente des performances intéressantes. Le principe de fonctionnement d'un ECRT repose sur la résonance cyclotronique des électrons pour transférer efficacement la puissance d'une onde électromagnétique (généralement dans la gamme des micro-ondes) aux électrons, en augmentant leur température perpendiculaire. La conversion de l'énergie thermique des électrons en énergie cinétique des ions est ensuite véhiculée par l'expansion du plasma dans la tuyère magnétique. Les mécanismes de décharge et d'accélération nécessitent donc l'existence d'un champ magnétique appliqué. Des résultats qualitativement similaires à ceux de la campagne précédente concernant le HPT ont été également trouvés lors de la caractérisation de l'ECRT. Dans cette source, la forme de la tuyère magnétique pouvait être modifiée au moyen d'une bobine supplémentaire. Les mesures ont montré que lorsque la divergence de la TM est réduite, le

profil d'accélération s'étire le long de l'axe mais que, dans l'ensemble, la vitesse finale des ions ne présente pas de dépendance visible avec la forme de la tuyère. Ce résultat est en accord avec les théories simples décrivant la dynamique de la TM dans le régime sans collisions. La modélisation des spectres de fluorescence a permis de déduire que la température cinétique des ions dans la direction axiale est de l'ordre de quelques milliers de K. Cette dispersion relativement élevée de la vitesse axiale des ions résulte probablement d'une large région d'ionisation qui chevauche la région d'accélération.

C.3 Partie III: Recherche sur l'iode comme propergol pour les plasmas hélicon

C.3.1 Chapitre 6: Développement préliminaire d'un système de distribution de l'iode

La troisième et dernière partie de cette thèse traite de l'utilisation de l'iode comme propergol. Il est démontré que l'iode est probablement le meilleur candidat parmi les nombreuses alternatives possibles au xénon en raison de plusieurs caractéristiques. Cependant, sa nature chimiquement réactive impose certaines limites à son utilisation dans les technologies classiques, alors que seules quelques précautions relatives à la sélection des matériaux sont nécessaires dans le cas des propulseurs sans électrodes. Comme travail préliminaire dans l'étude de l'iode comme propergol pour les sources hélicon, un système d'alimentation thermiquement contrôlé a été conçu, dessiné et testé. Il se base sur le stockage d'iode solide à basse pression et à température ambiante. Le processus de sublimation se produit par contact thermique avec une surface chauffée multi-perforée. En raison de la conception du système, le contrôle thermique de la surface de sublimation suffit à lui seul à réguler le débit massique. Étant donné que la température est un paramètre crucial pour atteindre la sublimation et éviter le dépôt, un système en boucle fermée a été mis en œuvre à partir de zéro afin d'effectuer sa supervision et son contrôle actif en plusieurs points de la ligne d'alimentation. Deux prototypes ont été conçus et fabriqués. Les tests effectués sur le premier ont permis de mettre en évidence certains phénomènes concernant la sublimation de l'iode et l'interaction avec les matériaux. Ces tests ont suggéré un certain nombre de mesures à prendre en compte pour l'itération du design. Ces observations ont conduit au deuxième prototype qui présente des caractéristiques prometteuses pour un fonctionnement fiable. Enfin, un modèle de sublimation a été proposé dont la formulation s'appuie sur des preuves expérimentales précédemment publiées par le groupe de recherche de l'Université de Pise. Le modèle a couvert les effets liés à l'équilibre dynamique qui se produisent en correspondance de l'interface de sublimation, conduisant à un très bon accord entre les profils de débit massique mesurés et prédits.

C.4 Chapitre 7: Conclusion

Cette thèse a analysé plusieurs aspects des plasmas hélicon et des tuyères magnétiques, mais il y a certainement beaucoup d'autres sujets qui méritent d'être étudiés. En premier lieu, la prochaine étape logique consiste à combiner toutes les observations et les résultats

rapportés dans ce manuscrit pour concevoir et tester un prototype de propulseur. Bien que cette tâche nécessite un certain nombre d'efforts, en particulier en ce qui concerne l'ingénierie, elle permettrait de poursuivre les progrès vers des performances propulsives compétitives de cette technologie. En outre, une telle source de plasma représenterait un excellent point sur lequel poursuivre les activités de recherche.

Il est intéressant d'envisager l'utilisation de diagnostics avancés, en premier lieu la diffusion Thomson, afin de caractériser avec précision le flux d'électrons dans la tuyère magnétique. Ce type de mesures pourrait permettre d'étudier des phénomènes complexes qui sont généralement peu documentés dans la littérature. L'information la plus fondamentale concerne peut-être l'évolution spatiale de la fonction de distribution de l'énergie des électrons dans la tuyère magnétique. Pour ne mentionner que quelques exemples, cette analyse permettrait de comprendre l'évolution du refroidissement des électrons et de leur démagnétisation.

Il est également intéressant de poursuivre l'étude des instabilités plasma qui se produisent dans la région de la tuyère magnétique. Cela est particulièrement important si leur caractérisation s'accompagne d'une mesure des performances, afin de rechercher une corrélation quantitative entre les deux. Une perte de performance peut en effet provenir d'un transport non idéal des espèces le long des lignes magnétiques, ce qui implique une diffusion transversale au champ magnétique. Ces résultats pourraient être obtenus soit en observant les électrons par diffusion Thomson dans le régime cohérent, soit en résolvant dans le temps la vitesse des ions par spectroscopie LIF.

Il est clairement de la plus haute importance de caractériser plus profondément la dynamique des ions. À cet égard, une autre étape logique serait d'étudier soigneusement le phénomène de détachement des ions par spectroscopie LIF 2-D afin de valider et/ou d'améliorer les théories sur lesquelles les outils numériques les plus avancés sont actuellement basés. Les données LIF pourraient également être couplées aux mesures de la sonde pour une expérience dédiée visant à caractériser le flux d'ions perdus aux parois.

Enfin et surtout, il est nécessaire de soutenir l'exploration de nouvelles architectures de propulseurs. En partant de la compréhension physique actuelle, il faut investir dans l'essai de différentes configurations, par exemple en termes de géométrie de la chambre de décharge, de topologie du champ magnétique et de stratégie d'injection de gaz, dans le but d'augmenter la température des électrons et de minimiser les pertes au niveau des parois et des collisions. Ces activités devraient de préférence se dérouler en parallèle avec la modélisation théorique visant à valider et à affiner en permanence les outils avancés.

Bibliography

- [1] M. Keidar, T. Zhuang, A. Shashurin, G. Teel, D. Chiu, J. Lukas, S. Haque, and L. Brieda, “Electric propulsion for small satellites,” *Plasma Physics and Controlled Fusion*, vol. 57, no. 1, p. 014005, nov 2014. [Online]. Available: <https://doi.org/10.1088/0741-3335/57/1/014005>
- [2] I. Levchenko, S. Xu, S. Mazouffre, D. Lev, D. Pedrini, D. Goebel, L. Garrigues, F. Taccogna, and K. Bazaka, “Perspectives, frontiers, and new horizons for plasma-based space electric propulsion,” *Physics of Plasmas*, vol. 27, no. 2, 2020. [Online]. Available: <https://doi.org/10.1063/1.5109141>
- [3] D. O'Reilly, G. Herdrich, and D. F. Kavanagh, “Electric propulsion methods for small satellites: A review,” *Aerospace*, vol. 8, no. 1, 2021. [Online]. Available: <https://www.mdpi.com/2226-4310/8/1/22>
- [4] E. Dale, B. Jorns, and A. Gallimore, “Future directions for electric propulsion research,” *Aerospace*, vol. 7, no. 9, 2020. [Online]. Available: <https://www.mdpi.com/2226-4310/7/9/120>
- [5] S. Mazouffre, “Electric propulsion for satellites and spacecraft: established technologies and novel approaches,” *Plasma Sources Science and Technology*, vol. 25, no. 3, p. 033002, apr 2016. [Online]. Available: <https://doi.org/10.1088/0963-0252/25/3/033002>
- [6] I. Levchenko, S. Xu, S. Mazouffre, M. Keidar, and K. Bazaka, “Mars colonization: Beyond getting there,” *Global Challenges*, vol. 3, no. 1, p. 1800062, 2019. [Online]. Available: <https://onlinelibrary.wiley.com/doi/abs/10.1002/gch2.201800062>
- [7] E. Musk, “Making humans a multi-planetary species,” *New Space*, vol. 5, no. 2, pp. 46–61, 2017. [Online]. Available: <https://doi.org/10.1089/space.2017.29009.emu>
- [8] D. A. Herman, T. Gray, I. Johnson, S. Hussein, and T. Winkelmann, “Development and qualification status of the electric propulsion systems for the NASA PPE mission and gateway program,” in *37th International Electric Propulsion Conference, Massachusetts Institute of Technology, Cambridge, MA USA*, 2022.
- [9] D. Krejci and A. Reissner, “The first 100 FEEP propulsion systems in space: A statistical view and lessons learnt of 4 years of ENPULSION,” in *37th International Electric Propulsion Conference, Massachusetts Institute of Technology, Cambridge, MA USA*, 2022.

- [10] National Aeronautics and Space Administration, *NSSDCA Master Catalog Search*, 2019. [Online]. Available: <https://nssdc.gsfc.nasa.gov/nmc/spacecraft/display.action?id=2019-074A>
- [11] I. Kaminska, “Analysis | Noble gases are suffering from Putin’s war in Ukraine,” *The Washington Post*, 2022. [Online]. Available: https://www.washingtonpost.com/business/energy/noble-gases-are-suffering-from-putins-war-in-ukraine/2022/05/19/594109ec-d731-11ec-be17-286164974c54_story.html
- [12] Reuters, “Ukraine halts half of worlds neon output for chips, clouding outlook,” *CNN*, 2022. [Online]. Available: <https://edition.cnn.com/2022/03/11/tech/ukraine-neon-chips/index.html>
- [13] D. Rafalskyi, J. M. Martínez, L. Habl, E. Z. Rossi, P. P. A. Boré, T. Baret, A. Poyet, T. Lafleur, S. Dudin, and A. Aanesland, “In-orbit demonstration of an iodine electric propulsion system,” *Nature*, vol. 599, p. 411415, 2021. [Online]. Available: <https://doi.org/10.1038/s41586-021-04015-y>
- [14] N. Bellomo, M. Magarotto, M. Manente, F. Trezzolani, R. Mantellato, L. Cappellini, D. Paulon, A. Selmo, D. Scalzi, M. Minute, M. Duzzi, A. Barbato, A. Schiavon, S. Di Fedè, N. Souhair, P. De Carlo, F. Barato, F. Milza, E. Toson, and D. Pavarin, “Design and In-orbit Demonstration of REGULUS, an Iodine electric propulsion system,” *CEAS Space Journal*, no. 0123456789, 2021. [Online]. Available: <https://doi.org/10.1007/s12567-021-00374-4>
- [15] S. N. Bathgate, M. M. M. Bilek, and D. R. McKenzie, “Electrodeless plasma thrusters for spacecraft: a review,” *Plasma Science and Technology*, vol. 19, no. 8, p. 083001, jun 2017. [Online]. Available: <https://doi.org/10.1088/2058-6272/aa71fe>
- [16] R. Moloney, B. Karadag, A. L. Fabris, D. Staab, A. Frey, A. Garbayo, L. Shadbolt, E. R. Azevedo, D. Faircloth, S. Lawrie, and O. Tarvainen, “Experimental validation and performance measurements of an ecr thruster operating on multiple propellants,” in *36th International Electric Propulsion Conference, University of Vienna (Austria), September 15-20, 2019*, 2019.
- [17] M. A. Lieberman and A. J. Lichtenberg, *Principles of Plasma Discharges and Materials Processing*, 2nd ed. John Wiley & Sons, Inc., Hoboken, New Jersey, 2005.
- [18] R. G. Jahn, *Physics of Electric Propulsion*. McGraw-Hill, 1968.
- [19] R. W. Boswell, “Very efficient plasma generation by whistler waves near the lower hybrid frequency,” *Plasma Physics and Controlled Fusion*, vol. 26, no. 10, pp. 1147–1162, 1984. [Online]. Available: <https://doi.org/10.1088/0741-3335/26/10/001>
- [20] F. F. Chen, “Plasma ionization by helicon waves,” *Plasma Physics and Controlled Fusion*, vol. 33, no. 4, pp. 339–364, 1991. [Online]. Available: <https://doi.org/10.1088/0741-3335/33/4/006>
- [21] —, “Experiments on helicon plasma sources,” *Journal of Vacuum Science & Technology A: Vacuum, Surfaces, and Films*, vol. 10, no. 4, pp. 1389–1401, 1992. [Online]. Available: <https://doi.org/10.1116/1.578256>

- [22] F. F. Chen, M. J. Hsieh, and M. Light, "Helicon waves in a non-uniform plasma," *Plasma Sources Science and Technology*, vol. 3, no. 1, pp. 49–57, feb 1994. [Online]. Available: <https://doi.org/10.1088/0963-0252/3/1/006>
- [23] R. W. Boswell and F. F. Chen, "Helicons-the early years," *IEEE Transactions on Plasma Science*, vol. 25, no. 6, pp. 1229–1244, 1997. [Online]. Available: <https://doi.org/10.1109/27.650898>
- [24] F. F. Chen, "Physics of helicon discharges," *Physics of Plasmas*, vol. 3, no. 5, pp. 1783–1793, 1996. [Online]. Available: <https://doi.org/10.1063/1.871697>
- [25] F. F. Chen and D. Arnush, "Generalized theory of helicon waves. I. Normal modes," *Physics of Plasmas*, vol. 4, no. 9, pp. 3411–3421, 1997. [Online]. Available: <https://doi.org/10.1063/1.872483>
- [26] D. Arnush and F. F. Chen, "Generalized theory of helicon waves. II. Excitation and absorption," *Physics of Plasmas*, vol. 5, no. 5, pp. 1239–1254, 1998. [Online]. Available: <https://doi.org/10.1063/1.872782>
- [27] I. D. Sudit and F. F. Chen, "Discharge equilibrium of a helicon plasma," *Plasma Sources Science and Technology*, vol. 5, no. 1, pp. 43–53, 1996. [Online]. Available: <https://doi.org/10.1088/0963-0252/5/1/006>
- [28] D. D. Blackwell and F. F. Chen, "Two-dimensional imaging of a helicon discharge," *Plasma Sources Science and Technology*, vol. 6, no. 4, pp. 569–576, 1997. [Online]. Available: <https://doi.org/10.1088/0963-0252/6/4/015>
- [29] M. M. Balkey, R. Boivin, J. L. Kline, and E. E. Scime, "Ion heating and density production in helicon sources near the lower hybrid frequency," *Plasma Sources Science and Technology*, vol. 10, no. 2, pp. 284–294, 2001. [Online]. Available: <https://doi.org/10.1088/0963-0252/10/2/318>
- [30] A. Degeling, N. Mikhelson, R. Boswell, and N. Sadeghi, "Characterization of helicon waves in a magnetized inductive discharge," *Physics of Plasmas*, vol. 5, no. 3, pp. 572–579, 1998. [Online]. Available: <https://doi.org/10.1063/1.872749>
- [31] A. R. Ellingboe and R. W. Boswell, "Capacitive, inductive and helicon-wave modes of operation of a helicon plasma source," *Physics of Plasmas*, vol. 3, no. 7, pp. 2797–2804, 1996. [Online]. Available: <https://doi.org/10.1063/1.871713>
- [32] A. E. Vinci and S. Mazouffre, "Direct experimental comparison of krypton and xenon discharge properties in the magnetic nozzle of a helicon plasma source," *Physics of Plasmas*, vol. 28, no. 3, p. 033504, 2021. [Online]. Available: <https://doi.org/10.1063/5.0037117>
- [33] —, "Plasma properties conditioned by the magnetic throat location in a helicon plasma device," *Journal of Applied Physics*, vol. 130, no. 183301, 2021. [Online]. Available: <https://doi.org/10.1063/5.0069983>
- [34] A. W. Degeling, C. O. Jung, R. W. Boswell, and A. R. Ellingboe, "Plasma production from helicon waves," *Physics of Plasmas*, vol. 3, no. 7, pp. 2788–2796, 1996. [Online]. Available: <https://doi.org/10.1063/1.871712>

- [35] J. Navarro-Cavallé, M. Wijnen, P. Fajardo, and E. Ahedo, "Experimental characterization of a 1 kW Helicon Plasma Thruster," *Vacuum*, vol. 149, pp. 69–73, 2018. [Online]. Available: <https://doi.org/10.1016/j.vacuum.2017.11.036>
- [36] J. Navarro-Cavallé, M. Wijnen, P. Fajardo, E. Ahedo, V. Gomez, A. Giménez, and M. Ruiz, "Development and Characterization of the Helicon Plasma Thruster Prototype HPT05M," in *36th International Electric Propulsion Conference*, no. September, 2019.
- [37] S. Shinohara, Y. Miyauchi, and Y. Kawai, "Dynamic plasma behaviour excited by $m = +$ or -1 helicon wave," *Plasma Phys. Contrml. Fusion*, vol. 37, 1995. [Online]. Available: <https://doi.org/10.1088/0741-3335/37/9/007>
- [38] K. Takahashi, "Magnetic nozzle radiofrequency plasma thruster approaching twenty percent thruster efficiency," *Scientific Reports*, vol. 11, no. 1, pp. 1–12, 2021. [Online]. Available: <https://doi.org/10.1038/s41598-021-82471-2>
- [39] K. Takahashi, C. Charles, R. Boswell, and A. Ando, "Performance improvement of a permanent magnet helicon plasma thruster," *Journal of Physics D: Applied Physics*, vol. 46, no. 35, p. 352001, aug 2013. [Online]. Available: <https://doi.org/10.1088/0022-3727/46/35/352001>
- [40] K. Takahashi and A. Ando, "Enhancement of axial momentum lost to the radial wall by the upstream magnetic field in a helicon source," *Plasma Physics and Controlled Fusion*, vol. 59, no. 5, 2017. [Online]. Available: <https://doi.org/10.1088/1361-6587/aa626f>
- [41] P. Guittienne, E. Chevalier, and C. Hollenstein, "Towards an optimal antenna for helicon waves excitation," *Journal of Applied Physics*, vol. 98, no. 8, 2005. [Online]. Available: <https://doi.org/10.1063/1.2081107>
- [42] P. Guittienne, A. A. Howling, and C. Hollenstein, "Analysis of resonant planar dissipative network antennas for rf inductively coupled plasma sources," *Plasma Sources Science and Technology*, vol. 23, no. 015006, 2014. [Online]. Available: <https://doi.org/10.1088/0963-0252/23/1/015006>
- [43] P. Guittienne, R. Jacquier, B. Pouradier Duteil, A. A. Howling, R. Agnello, and I. Furno, "Helicon wave plasma generated by a resonant birdcage antenna: Magnetic field measurements and analysis in the RAID linear device," *Plasma Sources Science and Technology*, vol. 30, no. 075023, 2021. [Online]. Available: <https://doi.org/10.1088/1361-6595/ac0da3>
- [44] F. Romano, Y.-A. Chan, G. Herdrich, C. Traub, S. Fasoulas, P. Roberts, K. Smith, S. Edmondson, S. Haigh, N. Crisp, V. Oiko, S. Worrall, S. Livadiotti, C. Huyton, L. Sinpetru, A. Straker, J. Becedas, R. Domínguez, D. González, V. Cañas, V. Sullioti-Linner, V. Hanessian, A. Mølgaard, J. Nielsen, M. Bisgaard, D. Garcia-Almiñana, S. Rodriguez-Donaire, M. Sureda, D. Kataria, R. Outlaw, R. Villain, J. Perez, A. Conte, B. Belkouchi, A. Schwalber, and B. HeiSSerer, "RF Helicon-based Inductive Plasma Thruster (IPT) Design for an Atmosphere-Breathing Electric Propulsion system (ABEP)," *Acta Astronautica*, vol. 176, pp. 476–483, 2020. [Online]. Available: <https://doi.org/10.1016/j.actaastro.2020.07.008>

- [45] F. Romano, Y. A. Chan, G. Herdrich, C. Traub, S. Fasoulas, P. C. Roberts, K. Smith, S. Edmondson, S. Haigh, N. H. Crisp, V. T. Oiko, S. D. Worrall, S. Livadiotti, C. Huyton, L. A. Sinpetru, A. Straker, J. Becedas, R. M. Domínguez, D. González, V. Cañas, V. Sullioti-Linner, V. Hanessian, A. Mølgaard, J. Nielsen, M. Bisgaard, D. Garcia-Almiñana, S. Rodriguez-Donaire, M. Sureda, D. Kataria, R. Outlaw, R. Villain, J. S. Perez, A. Conte, B. Belkouchi, A. Schwalber, and B. Heißerer, “RF Helicon-based Inductive Plasma Thruster (IPT) Design for an Atmosphere-Breathing Electric Propulsion system (ABEP),” *Acta Astronautica*, vol. 176, no. June, pp. 476–483, 2020. [Online]. Available: <https://doi.org/10.1016/j.actaastro.2020.07.008>
- [46] T. Lafleur, “Helicon plasma thruster discharge model,” *Physics of Plasmas*, vol. 21, no. 4, p. 043507, 2014. [Online]. Available: <https://doi.org/10.1063/1.4871727>
- [47] E. Ahedo and M. Merino, “Two-dimensional supersonic plasma acceleration in a magnetic nozzle,” *Physics of Plasmas*, vol. 17, no. 7, p. 073501, 2010. [Online]. Available: <https://doi.org/10.1063/1.3442736>
- [48] M. M. Martínez, “Analysis of Magnetic Nozzles For Space Plasma Thrusters,” Ph.D. dissertation, Universidad Politécnica de Madrid, 2013. [Online]. Available: http://oa.upm.es/21887/1/MARIO_MERINO_MARTINEZ.pdf
- [49] S. Correyero, J. Jarrige, D. Packan, and E. Ahedo, “Plasma beam characterization along the magnetic nozzle of an ECR thruster,” *Plasma Sources Science and Technology*, vol. 28, no. 9, p. 095004, sep 2019. [Online]. Available: <https://doi.org/10.1088/1361-6595/ab38e1>
- [50] M. R. Inchingolo, M. Merino, and J. Navarro-Cavallé, “Direct thrust measurements of a circular waveguide electron cyclotron resonance thruster,” *37th International Electric Propulsion Conference, Massachusetts Institute of Technology, Cambridge, MA, USA, June 19-23, 2022*, 2022.
- [51] S. A. Andersen, V. O. Jensen, P. Nielsen, and N. D’Angelo, “Continuous supersonic plasma wind tunnel,” *Physics of Fluids*, vol. 12, no. 3, pp. 557–560, 1969. [Online]. Available: <https://doi.org/10.1063/1.1692519>
- [52] J. Bittencourt, *Fundamentals of plasma physics*. Springer, Berlin, Germany, 2004.
- [53] K. Takahashi, T. Lafleur, C. Charles, P. Alexander, and R. W. Boswell, “Axial force imparted by a current-free magnetically expanding plasma,” *Physics of Plasmas*, vol. 19, no. 8, pp. 1–9, 2012. [Online]. Available: <https://doi.org/10.1063/1.4747701>
- [54] K. Takahashi, A. Chiba, A. Komuro, and A. Ando, “Experimental identification of an azimuthal current in a magnetic nozzle of a radiofrequency plasma thruster,” *Plasma Sources Science and Technology*, vol. 25, no. 5, p. 055011, aug 2016. [Online]. Available: <https://doi.org/10.1088/0963-0252/25/5/055011>
- [55] M. Merino, J. Nuez, and E. Ahedo, “Fluid-kinetic model of a propulsive magnetic nozzle,” *Plasma Sources Sci. Technol.*, 2021. [Online]. Available: <https://doi.org/10.1088/1361-6595/ac2a0b>

- [56] C. M. Franck, O. Grulke, and T. Klinger, "Magnetic fluctuation probe design and capacitive pickup rejection," *Review of Scientific Instruments*, vol. 73, no. 11, p. 3768, 2002. [Online]. Available: <https://doi.org/10.1063/1.1512341>
- [57] M. P. Reilly, W. Lewis, and G. H. Miley, "Magnetic field probes for use in radio frequency plasma," *Review of Scientific Instruments*, vol. 80, no. 5, 2009. [Online]. Available: <https://doi.org/10.1063/1.3136907>
- [58] D. Gerst, M. Cirisan, S. Mazouffre, and A. Aanesland, "Investigation of Ion-Ion Plasmas for Application in electric thrusters," in *IEPC*, 2011, pp. 1–7. [Online]. Available: <http://electricrocket.org/IEPC/IEPC-2011-127.pdf>
- [59] I. D. Sudit and F. F. Chen, "RF Compensated Probes for High-density Discharges," *Plasma Sources Science and Technology*, vol. 3, no. 2, pp. 162–168, 1994. [Online]. Available: <https://doi.org/10.1088/0963-0252/3/2/006>
- [60] F. F. Chen, "Lectures Notes on Langmuir Probe Diagnostics," in *Mini-Course on Plasma Diagnostics, IEEE-ICOPS meeting, Jeju, Korea*, 2003.
- [61] —, "Langmuir probes in RF plasma: Surprising validity of OML theory," *Plasma Sources Science and Technology*, vol. 18, no. 3, 2009. [Online]. Available: <https://doi.org/10.1088/0963-0252/18/3/035012>
- [62] —, "Langmuir probe analysis for high density plasmas," *Physics of Plasmas*, vol. 8, no. 6, pp. 3029–3041, 2001. [Online]. Available: <https://doi.org/10.1063/1.1368874>
- [63] J. Vaudolon, "Electric field determination and magnetic topology optimization in Hall thrusters," Ph.D. dissertation, Université d'Orléans, 2015. [Online]. Available: <https://tel.archives-ouvertes.fr/tel-01320637>
- [64] S. Mazouffre, G. Largeau, L. Garrigues, C. Boniface, and K. Dannenmayer, "Evaluation of various probe designs for measuring the ion current density in a Hall thruster plume," *35th International Electric Propulsion Conference*, no. 8-12 October, pp. IEPC-2017-336, 2017. [Online]. Available: <https://hal.archives-ouvertes.fr/hal-03573874>
- [65] S. Mazouffre, "Mesure de la densité de courant ionique dans le jet plasma d'un propulseur de Hall. Théorie et instrumentation." Tech. Rep., 2016.
- [66] I. H. Hutchinson, *Principles of Plasma Diagnostics: Second Edition*. IOP Publishing, nov 2002, vol. 44, no. 12. [Online]. Available: <https://doi.org/10.1088/0741-3335/44/12/701>
- [67] S. Mazouffre, "Laser-induced fluorescence diagnostics of the cross-field discharge of hall thrusters," *Plasma Sources Science and Technology*, vol. 22, no. 1, p. 013001, nov 2012. [Online]. Available: <https://doi.org/10.1088/0963-0252/22/1/013001>
- [68] A. Lejeune, G. Bourgeois, and S. Mazouffre, "Kr II and Xe II axial velocity distribution functions in a cross-field ion source," *Physics of Plasmas*, vol. 19, no. 7, p. 073501, 2012. [Online]. Available: <https://doi.org/10.1063/1.4731688>

- [69] A. Kramida, Y. Ralchenko, J. Reader, and N. A. Team, "NIST Atomic Spectra Database (ver. 5.8), [Online]. Available: <https://physics.nist.gov/asd> [2021, September 16]. National Institute of Standards and Technology, Gaithersburg, MD." 2020.
- [70] V. Kaufman, "Wavelengths and Energy Levels of Neutral Kr⁸⁴ and Level Shifts in All Kr Even Isotopes," *J. Res. Natl. Inst. Stand. Technol.*, vol. 98, 1993. [Online]. Available: <https://doi.org/10.6028/jres.098.047>
- [71] C. J. Humphreys and E. P. Jr., "Interferometric Observations in the Spectra of ⁸⁶Kr," *J. Opt. Soc. Am.*, vol. 60, pp. 200–205, 1970. [Online]. Available: <https://doi.org/10.1364/JOSA.60.000200>
- [72] C. Niu, G. Zhao, Y. Wang, Z. Liu, and Q. Chen, "Correlation of wave propagation modes in helicon plasma with source tube lengths," *Physics of Plasmas*, vol. 24, no. 013518, 2017. [Online]. Available: <https://doi.org/10.1063/1.4975008>
- [73] P. Chabert and N. Braithwaite, *Physics of Radio-Frequency Plasmas*. Cambridge University Press, 2011.
- [74] M. Light, I. D. Sudit, F. F. Chen, and D. Arnush, "Axial propagation of helicon waves," *Physics of Plasmas*, vol. 2, no. 11, pp. 4094–4103, 1995. [Online]. Available: <https://doi.org/10.1063/1.871032>
- [75] C. Charles, "High density conics in a magnetically expanding helicon plasma," *Applied Physics Letters*, vol. 96, no. 5, pp. 13–16, 2010. [Online]. Available: <https://doi.org/10.1063/1.3309668>
- [76] K. Takahashi, C. Charles, R. Boswell, W. Cox, and R. Hatakeyama, "Transport of energetic electrons in a magnetically expanding helicon double layer plasma," *Applied Physics Letters*, vol. 94, no. 19, pp. 2007–2010, 2009. [Online]. Available: <https://doi.org/10.1063/1.3136721>
- [77] K. Takahashi, S. Takayama, A. Komuro, and A. Ando, "Standing Helicon Wave Induced by a Rapidly Bent Magnetic Field in Plasmas," *Physical Review Letters*, vol. 116, no. 13, pp. 1–5, 2016. [Online]. Available: <https://doi.org/10.1103/PhysRevLett.116.135001>
- [78] H. W. Coleman and W. G. Steele, *Experimentation, Validation, and Uncertainty Analysis for Engineers*. Wiley, 2009.
- [79] D. Bose, T. R. Govidan, and M. Meyyappan, "Modeling of a helicon plasma source," *IEEE Transactions on Plasma Science*, vol. 31, no. 4, 2003. [Online]. Available: <https://doi.org/10.1109/PPPS.2001.01002007>
- [80] . Biagi-v7.1 database, www.lxcat.net, retrieved on November 8, "Biagi-v7.1 database, www.lxcat.net, retrieved on November 8, 2020." [Online]. Available: www.lxcat.net
- [81] C. Charles and R. W. Boswell, "Laboratory evidence of supersonic ion beam generated by a current-free "helicon" double-layer," *Physics of Plasmas*, vol. 11,

- no. 4, pp. 1706–1714, 2004. [Online]. Available: <https://doi.org/10.1063/1.1652058>
- [82] —, “Effect of exhaust magnetic field in a helicon double-layer thruster operating in Xenon,” *IEEE Transactions on Plasma Science*, vol. 36, no. 5 PART 1, pp. 2141–2146, 2008. [Online]. Available: <https://doi.org/10.1109/TPS.2008.2004233>
 - [83] O. V. Batishchev, “Minihelicon plasma thruster,” *IEEE Transactions on Plasma Science*, vol. 37, no. 8 PART 2, pp. 1563–1571, 2009. [Online]. Available: <https://doi.org/10.1109/TPS.2009.2023990>
 - [84] T. Lafleur, C. Charles, and R. W. Boswell, “Characterization of the ion beam formed in a low magnetic field helicon mode,” *Journal of Physics D: Applied Physics*, vol. 44, no. 14, 2011. [Online]. Available: <https://doi.org/10.1088/0022-3727/44/14/145204>
 - [85] N. Gulbrandsen and Å. Fredriksen, “RFEA measurements of high-energy electrons in a helicon plasma device with expanding magnetic field,” *Frontiers in Physics*, vol. 5, no. JAN, pp. 1–8, 2017.
 - [86] E. Ahedo and J. Navarro-Cavallé, “Helicon thruster plasma modeling: Two-dimensional fluid-dynamics and propulsive performances,” *Physics of Plasmas*, vol. 20, no. 4, 2013. [Online]. Available: <https://doi.org/10.1063/1.4798409>
 - [87] M. Magarotto, D. Melazzi, and D. Pavarin, “Study on the influence of the magnetic field geometry on the power deposition in a helicon plasma source,” *Journal of Plasma Physics*, vol. 85, no. 4, pp. 1–19, 2019. [Online]. Available: <https://doi.org/10.1017/S0022377819000473>
 - [88] K. Takahashi, Y. Takao, and A. Ando, “Increased Thrust-to-Power Ratio of a Stepped-Diameter Helicon Plasma Thruster with Krypton Propellant,” *Journal of Propulsion and Power*, vol. 36, no. 6, 2020. [Online]. Available: <https://doi.org/10.2514/1.J054179>
 - [89] J. M. Little and E. Y. Choueiri, “Electron Cooling in a Magnetically Expanding Plasma,” *Physical Review Letters*, vol. 117, no. 22, pp. 1–5, 2016. [Online]. Available: <https://doi.org/10.1103/PhysRevLett.117.225003>
 - [90] T. Lafleur, C. Charles, and R. W. Boswell, “Characterization of a helicon plasma source in low diverging magnetic fields,” *Journal of Physics D: Applied Physics*, vol. 44, no. 5, 2011. [Online]. Available: <https://doi.org/10.1088/0022-3727/44/5/055202>
 - [91] A. Bennet, C. Charles, and R. Boswell, “Non-local plasma generation in a magnetic nozzle,” *Physics of Plasmas*, vol. 26, no. 7, 2019. [Online]. Available: <https://doi.org/10.1063/1.5098484>
 - [92] M. Martinez-Sanchez, J. Navarro-Cavallé, and E. Ahedo, “Electron cooling and finite potential drop in a magnetized plasma expansion,” *Physics of Plasmas*, vol. 22, no. 5, p. 053501, 2015. [Online]. Available: <https://aip.scitation.org/doi/abs/10.1063/1.4919627>

- [93] Y. Tanida, D. Kuwahara, and S. Shinohara, "Spatial Profile of Ion Velocity Distribution Function in Helicon High-Density Plasma by Laser Induced Fluorescence Method," *Transactions of the Japan Society for Aeronautical and Space Sciences, Aerospace Technology Japan*, vol. 14, no. ists30, pp. Pb7–Pb12, 2016. [Online]. Available: https://doi.org/10.2322/tastj.14.Pb_7
- [94] M. Merino and E. Ahedo, "Plasma detachment in a propulsive magnetic nozzle via ion demagnetization," *Plasma Sources Science and Technology*, vol. 23, no. 3, 2014. [Online]. Available: <https://doi.org/10.1088/0963-0252/23/3/032001>
- [95] E. Ahedo, S. Correyero, J. Navarro, and M. Merino, "Macroscopic and parametric study of a kinetic plasma expansion in a paraxial magnetic nozzle," *Plasma Sources Science and Technology*, vol. 29, no. 045017, pp. 0–20, 2020.
- [96] S. Correyero, J. Jarrige, D. Packan, and E. Ahedo, "Ion acceleration in the magnetic nozzle of an ECR thruster: Comparison of experimental measurements with a quasi 1D kinetic model," *Space Propulsion 2018, May 2018, SEVILLE, Spain*, no. May, pp. 1–8, 2018. [Online]. Available: <https://hal.archives-ouvertes.fr/hal-01961064>
- [97] T. A. Collard and B. A. Jorns, "Magnetic nozzle efficiency in a low power inductive plasma source," *Plasma Sources Science and Technology*, vol. 28, no. 10, p. 105019, oct 2019. [Online]. Available: <https://doi.org/10.1088/1361-6595/ab2d7d>
- [98] K. Takahashi, T. Sugawara, and A. Ando, "Spatial measurement of axial and radial momentum fluxes of a plasma expanding in a magnetic nozzle," *New Journal of Physics*, vol. 22, no. 7, pp. 0–9, 2020. [Online]. Available: <https://doi.org/10.1088/1367-2630/ab98d5>
- [99] K. Takahashi, H. Akahoshi, C. Charles, R. W. Boswell, and A. Ando, "High temperature electrons exhausted from rf plasma sources along a magnetic nozzle," *Physics of Plasmas*, vol. 24, no. 8, pp. 0–4, 2017. [Online]. Available: <https://doi.org/10.1063/1.4990110>
- [100] R. B. Lobbia and B. E. Beal, "Recommended practice for use of langmuir probes in electric propulsion testing," *Journal of Propulsion and Power*, vol. 33, no. 3, pp. 566–581, 2017. [Online]. Available: <https://doi.org/10.2514/1.B35531>
- [101] M. Merino and E. Ahedo, "Influence of electron and ion thermodynamics on the magnetic nozzle plasma expansion," *IEEE Transactions on Plasma Science*, vol. 43, no. 1, pp. 244–251, 2015. [Online]. Available: <https://doi.org/10.1109/TPS.2014.2316020>
- [102] Y. Zhang, C. Charles, and R. Boswell, "Thermodynamic Study on Plasma Expansion along a Divergent Magnetic Field," *Physical Review Letters*, vol. 116, no. 2, pp. 1–5, 2016. [Online]. Available: <https://doi.org/10.1103/PhysRevLett.116.025001>
- [103] F. F. Chen, *Introduction to Plasma Physics and Controlled Fusion*, 3rd ed. Springer Cham, 2016. [Online]. Available: <https://doi.org/10.1007/978-3-319-22309-4>

- [104] K. T. Burm, W. J. Goedheer, and D. C. Schram, "The isentropic exponent in plasmas," *Physics of Plasmas*, vol. 6, no. 6, pp. 2622–2627, 1999. [Online]. Available: <https://doi.org/10.1063/1.873535>
- [105] K. Dannenmayer and S. Mazouffre, "Electron flow properties in the far-field plume of a Electron flow properties in the far-field plume of a Hall thruster," *Plasma Sources Sci. Technol.*, vol. 22, no. 035004, 2013. [Online]. Available: <https://doi.org/10.1088/0963-0252/22/3/035004>
- [106] K. Takahashi, C. Charles, R. W. Boswell, and A. Ando, "Thermodynamic Analogy for Electrons Interacting with a Magnetic Nozzle," *Physical Review Letters*, vol. 125, no. 16, p. 165001, 2020. [Online]. Available: <https://doi.org/10.1103/PhysRevLett.125.165001>
- [107] J. Y. Kim, G. Go, Y. S. Hwang, and K. J. Chung, "Dependence of the polytropic index of plasma on magnetic field," *New Journal of Physics*, vol. 23, no. 5, 2021. [Online]. Available: <https://doi.org/10.1088/1367-2630/abfab1>
- [108] P. M. Bellan, *Fundamentals of plasma physics*. Cambridge University Press, 2006. [Online]. Available: <https://doi.org/10.1017/CBO9780511807183>
- [109] B. Wachs and B. Jorns, "Background pressure effects on ion dynamics in a low-power magnetic nozzle thruster," *Plasma Sources Science and Technology*, vol. 29, no. 4, p. 045002, mar 2020. [Online]. Available: <https://doi.org/10.1088/1361-6595/ab74b6>
- [110] F. Cannat, T. Lafleur, J. Jarrige, P. Chabert, P. Elias, and D. Packan, "Optimization of a coaxial electron cyclotron resonance plasma thruster with an analytical model," *Physics of Plasmas*, vol. 22, p. 053503, 2015. [Online]. Available: <https://hal.archives-ouvertes.fr/hal-01229071>
- [111] K. Nishiyama, S. Hosoda, K. Ueno, and H. Kunina, "The Ion Engine System for Hayabusa2," *32nd International Electric Propulsion Conference, Wiesbaden, Germany, September 11-15, 2011*, 2011. [Online]. Available: <http://electricrocket.org/IEPC/IEPC-2011-309.pdf>
- [112] H. Koizumi, K. Komurasaki, J. Aoyama, and K. Yamaguchi, "Engineering model of the miniature ion propulsion system for the nano-satellite: Hodoyoshi-4," *Transactions of the Japan Society for Aeronautical and Space Sciences, Aerospace Technology Japan*, vol. 12, no. ists29, pp. Tb_19–Tb_24, 2014. [Online]. Available: https://doi.org/10.2322/tastj.12.Tb_19
- [113] H. Koizumi, H. Kawahara, K. Yaginuma, J. Asakawa, Y. Nakagawa, Y. Nakamura, S. Kojima, T. Matsuguma, R. Funase, J. Nakatsuka, and K. Komurasaki, "Initial flight operations of the miniature propulsion system installed on small space probe: Procyon," *Transactions of the Japan Society for Aeronautical and Space Sciences, Aerospace Technology Japan*, vol. 14, no. ists30, pp. Pb_13–Pb_22, 2016. [Online]. Available: https://doi.org/10.2322/tastj.14.Pb_13

- [114] K. Nishiyama, S. Hosoda, K. Ueno, R. Tsukizaki, and H. Kuninaka, “Development and Testing of the Hayabusa2 Ion Engine System,” *Transactions of the Japan Society for Aeronautical and Space Sciences, Aerospace Technology Japan*, vol. 14, no. ists30, pp. Pb_131–Pb_140, 2016. [Online]. Available: https://doi.org/10.2322/tastj.14.Pb_131
- [115] Y. Nakagawa, H. Koizumi, H. Kawahara, and K. Komurasaki, “Performance characterization of a miniature microwave discharge ion thruster operated with water,” *Acta Astronautica*, vol. 157, pp. 294–299, 2019. [Online]. Available: <https://doi.org/10.1016/j.actaastro.2018.12.031>
- [116] Y. Tani, R. Tsukizaki, D. Koda, K. Nishiyama, and H. Kuninaka, “Performance improvement of the 10 microwave discharge ion thruster by expansion of the plasma production volume,” *Acta Astronautica*, vol. 157, pp. 425–434, 2019. [Online]. Available: <https://doi.org/10.1016/j.actaastro.2018.12.023>
- [117] D. Packan, P. Elias, J. Jarrige, T. Vialis, S. Correyero, S. Peterschmitt, J.-C. Porto-Hernandez, M. Merino, A. Sánchez-Villar, E. Ahedo, G. Peyresoubes, A. Thorinius, S. Denis, K. Holste, P. Klar, S. Scharmann, J. Zorn, M. Beke-mans, T. Scalais, E. Bourguignon, S. Zurbach, P. Azais, I. Habbassi, M. Mares, and A. Hoque, “H2020 MINOTOR : Magnetic Nozzle Electron Cyclotron Resonance Thruster,” *36th International Electric Propulsion Conference*, 2019.
- [118] C. Chung, S. S. Kim, and H. Y. Chang, “Electron cyclotron resonance in a weakly magnetized radio-frequency inductive discharge,” *Phys. Rev. Lett.*, vol. 88, p. 095002, Feb 2002. [Online]. Available: <https://link.aps.org/doi/10.1103/PhysRevLett.88.095002>
- [119] —, “Experimental measurement of the electron energy distribution function in the radio frequency electron cyclotron resonance inductive discharge,” *Phys. Rev. E*, vol. 69, p. 016406, Jan 2004. [Online]. Available: <https://link.aps.org/doi/10.1103/PhysRevE.69.016406>
- [120] A. E. Vinci and S. Mazouffre, “Electron and Ion Properties in the Beam and Discharge of a Helicon Plasma Source,” in *Space Propulsion 2020+1*, 2021.
- [121] V. A. Godyak and V. I. Demidov, “Probe measurements of electron-energy distributions in plasmas: what can we measure and how can we achieve reliable results?” *Journal of Physics D: Applied Physics*, vol. 44, no. 23, p. 233001, may 2011. [Online]. Available: <https://doi.org/10.1088/0022-3727/44/23/233001>
- [122] V. Godyak, “Rf discharge diagnostics: Some problems and their resolution,” *Journal of Applied Physics*, vol. 129, no. 4, p. 041101, 2021. [Online]. Available: <https://doi.org/10.1063/5.0024258>
- [123] C. Schröder, O. Grulke, T. Klinger, and V. Naulin, “Spatial mode structures of electrostatic drift waves in a collisional cylindrical helicon plasma,” *Physics of Plasmas*, vol. 11, no. 9, pp. 4249–4253, 2004. [Online]. Available: <https://doi.org/10.1063/1.1779225>

- [124] —, “Drift waves in a high-density cylindrical helicon discharge,” *Physics of Plasmas*, vol. 12, no. 4, pp. 1–6, 2005. [Online]. Available: <https://doi.org/10.1063/1.1864076>
- [125] M. J. Burin, G. R. Tynan, G. Y. Antar, N. A. Crocker, and C. Holland, “On the transition to drift turbulence in a magnetized plasma column,” *Physics of Plasmas*, vol. 12, no. 5, pp. 1–14, 2005. [Online]. Available: <https://doi.org/10.1063/1.1889443>
- [126] O. Grulke, S. Ullrich, T. Windisch, and T. Klinger, “Spatiotemporal dynamics of drift wave turbulence in a helicon discharge,” in *AIP Conference Proceedings*, vol. 993, 2008, pp. 87–92. [Online]. Available: <https://doi.org/10.1063/1.2909181>
- [127] S. C. Thakur, C. Brandt, L. Cui, J. J. Gosselin, A. D. Light, and G. R. Tynan, “Multi-instability plasma dynamics during the route to fully developed turbulence in a helicon plasma,” *Plasma Sources Science and Technology*, vol. 23, no. 4, 2014. [Online]. Available: <https://doi.org/10.1088/0963-0252/23/4/044006>
- [128] S. J. Doyle, A. Bennet, D. Tsifakis, J. P. Dedrick, R. W. Boswell, and C. Charles, “Characterization and Control of an Ion-Acoustic Plasma Instability Downstream of a Diverging Magnetic Nozzle,” *Frontiers in Physics*, vol. 8, no. February, pp. 1–11, 2020. [Online]. Available: <https://doi.org/10.3389/fphy.2020.00024>
- [129] S. C. Thakur, C. Brandt, L. Cui, J. J. Gosselin, and G. R. Tynan, “Formation of the Blue Core in Argon Helicon Plasma,” *IEEE Transactions on Plasma Science*, vol. 43, no. 8, pp. 2754–2759, 2015. [Online]. Available: <https://doi.org/10.1109/TPS.2015.2446537>
- [130] S. Hepner, B. Wachs, and B. Jorns, “Wave-driven non-classical electron transport in a low temperature magnetically expanding plasma,” *Applied Physics Letters*, vol. 116, no. 26, 2020. [Online]. Available: <https://doi.org/10.1063/5.0012668>
- [131] J. M. Beall, Y. C. Kim, and E. J. Powers, “Estimation of wavenumber and frequency spectra using fixed probe pairs,” *Journal of Applied Physics*, vol. 53, no. 6, pp. 3933–3940, 1982. [Online]. Available: <https://doi.org/10.1063/1.331279>
- [132] V. Gomez, A. Giménez, M. Ruiz, J. Navarro-Cavallé, P. Fajardo, M. Wijnen, and E. Ahedo, “RF Power - Plasma Coupling Experimental Results in a Helicon Plasma Thruster Prototype,” in *36th International Electric Propulsion Conference*, no. University of Vienna, Austria, September 15-20, 2019, 2019.
- [133] A. E. Vinci, S. Mazouffre, M. R. Inchingolo, V. Gómez, P. Fajardo, and J. Navarro-Cavallé, “Probing xenon atoms and ions velocity in the magnetic nozzle of a helicon plasma thruster,” in *37th International Electric Propulsion Conference, Massachusetts Institute of Technology, Cambridge, MA USA*, 2022. [Online]. Available: https://www.researchgate.net/publication/361591971_Probing_xenon_atoms_and_ions_velocity_in_the_magnetic_nozzle_of_a_helicon_plasma_thruster

- [134] S. Mazouffre, G. Bourgeois, L. Garrigues, and E. Pawelec, “A comprehensive study on the atom flow in the cross-field discharge of a hall thruster,” *Journal of Physics D: Applied Physics*, vol. 44, no. 10, p. 105203, feb 2011. [Online]. Available: <https://doi.org/10.1088/0022-3727/44/10/105203>
- [135] J. E. Sansonetti and W. C. Martin, “Handbook of basic atomic spectroscopic data,” *Journal of Physical and Chemical Reference Data*, vol. 34, no. 4, pp. 1559–2259, 2005. [Online]. Available: <https://doi.org/10.1063/1.1800011>
- [136] G. K. Woodgate, *Elementary Atomic Structure*. Oxford University Press, 1980.
- [137] E. Pawelec, S. Mazouffre, and N. Sadeghi, “Hyperfine structure of some near-infrared Xe I and Xe II lines,” *Spectrochimica Acta Part B: Atomic Spectroscopy*, vol. 66, no. 6, pp. 470–475, 2011. [Online]. Available: <https://doi.org/10.1016/j.sab.2011.05.009>
- [138] M. Suzuki, K. Katoh, and N. Nishimiya, “Saturated absorption spectroscopy of xe using a gaas semiconductor laser,” *Spectrochimica Acta Part A: Molecular and Biomolecular Spectroscopy*, vol. 58, no. 11, pp. 2519–2531, 2002. [Online]. Available: [https://doi.org/10.1016/S1386-1425\(02\)00069-0](https://doi.org/10.1016/S1386-1425(02)00069-0)
- [139] T. Smith, B. Ngom, J. Linnell, and A. Gallimore, *Diode Laser-Induced Fluorescence of Xenon Ion Velocity Distributions*, 2005. [Online]. Available: <https://arc.aiaa.org/doi/abs/10.2514/6.2005-4406>
- [140] A. Sargsyan, A. Tonoyan, G. Hakhumyan, C. Leroy, Y. Pashayan-Leroy, and D. Sarkisyan, “Atomic transitions of rb, d2 line in strong magnetic fields: Hyperfine paschenback regime,” *Optics Communications*, vol. 334, pp. 208–213, 2015. [Online]. Available: <https://doi.org/10.1016/j.optcom.2014.08.022>
- [141] L. Broström, A. Kastberg, J. Lidberg, and S. Mannervik, “Hyperfine-structure measurements in xe ii,” *Phys. Rev. A*, vol. 53, pp. 109–112, Jan 1996. [Online]. Available: <https://link.aps.org/doi/10.1103/PhysRevA.53.109>
- [142] G. H. Fuller, “Nuclear spins and moments,” *Journal of Physical and Chemical Reference Data*, vol. 5, no. 4, pp. 835–1092, 1976. [Online]. Available: <https://doi.org/10.1063/1.555544>
- [143] H. Kopfermann, *Nuclear Moments*, ser. Pure and Applied Physics, H. Kopfermann, Ed. Elsevier, 1958, vol. 2. [Online]. Available: <https://doi.org/10.1016/B978-1-4832-3061-0.50001-5>
- [144] Phelps, “database, www.lxcat.net, retrieved on September 27, 2021.”
- [145] S. Pullins, Y.-H. Chiu, D. Levandier, and R. Dressler, *Ion dynamics in Hall effect and ion thrusters - Xe(+) + Xe symmetric charge transfer*, 2000. [Online]. Available: <https://arc.aiaa.org/doi/abs/10.2514/6.2000-603>
- [146] T. H. Stix, *Waves in plasmas*. American Institute of Physics, 1992.
- [147] J. Jarrige, P. Elias, F. Cannat, and D. Packan, “Characterization of a coaxial ecr plasma thruster,” in *44th AIAA Plasmadynamics and Lasers Conference, San Diego*, 2013. [Online]. Available: <https://doi.org/10.2514/6.2013-2628>

- [148] S. Peterschmitt and D. Packan, "Impact of the microwave coupling structure on an electron-cyclotron resonance thruster," *Journal of Propulsion and Power*, vol. 37, no. 6, pp. 806–815, 2021. [Online]. Available: <https://doi.org/10.2514/1.B38156>
- [149] D. B. Miller and E. F. Gibbons, "Experiments with an electron cyclotron resonance plasma accelerator," *AIAA Journal*, vol. 2, no. 1, pp. 35–41, 1964. [Online]. Available: <https://doi.org/10.2514/3.2210>
- [150] H. Kosmahl, D. Miller, and G. Bethke, "Plasma acceleration with microwaves near cyclotron resonance," *Journal of Applied Physics*, vol. 38, no. 12, pp. 4576–4582, 1967. [Online]. Available: <https://doi.org/10.1063/1.1709188>
- [151] G. Crimi, A. Eckert, and D. Miller, "Microwave driven magnetic plasma accelerator studies (cyclops)," General Electric Company, Space Sciences Laboratory, Missile and Space Division, Tech. Rep., 1967.
- [152] J. Sercel, "An experimental and theoretical study of the ECR plasma engine," Ph.D. dissertation, California Institute of Technology, 1993.
- [153] Marco Inchingolo and Jaume Navarro-Cavallé and Mario Merino, "Design, ignition and plume characterization of a waveguide ecr thruster," *Submitted to Plasma Sources Science and Technology*, 2022.
- [154] A. E. Vinci, S. Mazouffre, V. Gómez, P. Fajardo, and J. Navarro-Cavallé, "Laser-induced fluorescence spectroscopy on xenon atoms and ions in the magnetic nozzle of a helicon plasma thruster," *Plasma Sources Science and Technology*, vol. 31, no. 9, p. 095007, 2022. [Online]. Available: <https://doi.org/10.1088/1361-6595/ac8db8>
- [155] J. J. Szabo, "Fully kinetic numerical modeling of a plasma thruster," Ph.D. dissertation, Massachusetts Institute of Technology, Dept. of Aeronautics and Astronautics, 2001. [Online]. Available: <http://hdl.handle.net/1721.1/8889>
- [156] S. Mazouffre, V. Kulaev, and J. P. Luna, "Ion diagnostics of a discharge in crossed electric and magnetic fields for electric propulsion," *Plasma Sources Science and Technology*, vol. 18, no. 3, p. 034022, jul 2009. [Online]. Available: <https://doi.org/10.1088/0963-0252/18/3/034022>
- [157] P. Grondein, T. Lafleur, P. Chabert, and A. Aanesland, "Global model of an iodine gridded plasma thruster," *Physics of Plasmas*, vol. 23, no. 3, 2016. [Online]. Available: <https://doi.org/10.1063/1.4944882>
- [158] J. Szabo and M. Robin, "Plasma species measurements in the plume of an iodine fueled hall thruster," *Journal of Propulsion and Power*, vol. 30, no. 5, pp. 1357–1367, 2014. [Online]. Available: <https://doi.org/10.2514/1.B35075>
- [159] Z. R. Taillefer, J. J. Blandino, and J. Szabo, "Characterization of a Barium Oxide Cathode Operating on Xenon and Iodine Propellants," *Journal of Propulsion and Power*, vol. 36, no. 4, pp. 575–585, 2020. [Online]. Available: <https://doi.org/10.2514/1.b37315>

- [160] S. J. Thompson, F. Collins, C. C. Farnell, S. C. Farnell, P. Controls, F. Collins, D. D. Williams, J. P. Chandler, F. Collins, J. D. Williams, and F. Collins, "Evaluation of Iodine Compatible Cathode Configurations," *36th International Electric Propulsion Conference*, pp. 1–21, 2019.
- [161] M. M. Saravia, "Alternative propellants for Hall Thrusters," Ph.D. dissertation, University of Pisa, 2018. [Online]. Available: <https://etd.adm.unipi.it/t/etd-05032019-204758/>
- [162] M. M. Saravia, L. Bernazzani, A. Ceccarini, A. E. Vinci, and F. Paganucci, "Modeling and characterization of a thermally controlled iodine feeding system for electric propulsion applications," *Aerospace*, vol. 7, no. 2, pp. 1–18, 2020. [Online]. Available: <https://doi.org/10.3390/aerospace7020010>
- [163] J. Szabo, M. Robin, S. Paintal, B. Pote, V. Hruby, and C. Freeman, "Iodine plasma propulsion test results at 110 kw," *IEEE Transactions on Plasma Science*, vol. 43, pp. 141 – 148, 2014. [Online]. Available: <https://doi.org/10.1109/TPS.2014.2367417>
- [164] J. Martínez Martínez and D. Rafalskyi, "Design and development of iodine flow control systems for miniaturized propulsion systems," *CEAS Space Journal*, no. 0123456789, 2021. [Online]. Available: <https://doi.org/10.1007/s12567-021-00384-2>
- [165] H. Kramers and S. Stemmerding, "The sublimation of ice in vacuum," *Applied Scientific Research, Section A*, vol. 3, pp. 73–82, 1951. [Online]. Available: <https://doi.org/10.1007/BF03184673>
- [166] A. E. Vinci, "Modeling and testing of an iodine feeding system for hall-effect thrusters," Università di Pisa, Tech. Rep., 2019. [Online]. Available: <https://etd.adm.unipi.it/t/etd-06272019-160553/>
- [167] K. A. Polzin, S. R. Peeples, A. Martinez, J. F. Seixal, S. Mauro, A. O. Burt, and J. L. Myers, "Engineering Model Propellant Feed System Development for an Iodine Hall Thruster Demonstration Mission," in *52nd AIAA/SAE/ASEE Joint Propulsion Conference AIAA*, 2016, pp. 1–12. [Online]. Available: <https://doi.org/10.2514/6.2016-4730>
- [168] A. O. Rankine, "On the Viscosity of the Vapour of Iodine," 1915. [Online]. Available: <https://doi.org/10.1098/rspa.1915.0010>
- [169] W. Sutherland, "The viscosity of gases and molecular force," *Philosophical Magazine*, vol. 5, no. 36:223, pp. 507–531, 1893. [Online]. Available: <https://doi.org/10.1080/14786449308620508>
- [170] T.-H. Chung, L. L. Lee, and K. E. Starling, "Application of Kinetic Gas Theories and Multiparameter Correlation for Prediction of Dilute Gas Viscosity and Thermal Conductivity," *Industrial and Engineering Chemistry Research*, vol. 23, no. 1, pp. 8–13, 1984. [Online]. Available: <https://doi.org/10.1021/i100013a002>
- [171] T.-H. Chung, A. Mohammad, L. L. Lee, K. E. Starling, and M. Ajlan, "Generalized Multiparameter Correlation for Nonpolar and Polar Fluid Transport Properties," *Industrial and Engineering Chemistry Research*, vol. 27,

- no. 4, pp. 671–679, 1988. [Online]. Available: <https://doi.org/10.1021/ie00076a024>
- [172] Robert C. Reid, J. M. Prausnitz, and B. E. Poling, *The Properties of Gases & Liquids*, 1987. [Online]. Available: <https://www.osti.gov/biblio/6504847>
- [173] P. D. Neufeld, A. R. Janzen, and R. A. Aziz, “Empirical equations to calculate 16 of the transport collision integrals $\Omega(l,s)^*$ for the lennard-jones (12-6) potential,” *The Journal of Chemical Physics*, vol. 57, no. 3, pp. 1100–1102, 1972. [Online]. Available: <https://doi.org/10.1063/1.1678363>
- [174] E. A. Mason and L. Monchick, “Transport properties of polar-gas mixtures,” *The Journal of Chemical Physics*, vol. 36, no. 10, pp. 2746–2757, 1962. [Online]. Available: <https://doi.org/10.1063/1.1732363>
- [175] T. Kaiho, *Iodine Chemistry and Applications*. Wiley, 2015.
- [176] R. T. Jubin, “Airborne Waste Management Technology Applicable for Use in Reprocessing Plants for Control of Iodine and Other Off-Gas Constituents,” Tech. Rep., 1988. [Online]. Available: <https://doi.org/10.2172/5169490>
- [177] K. A. Polzin, S. R. Peeples, J. F. Seixal, S. L. Mauro, B. L. Lewis, G. A. Jerman, D. H. Calvert, J. Dankanich, H. Kamhawi, T. A. Hickman, J. Szabo, B. Pote, and L. Lee, “Propulsion System Development for the Iodine Satellite (iSAT) Demonstration Mission,” *Joint Conference of 30th International Symposium on Space Technology and Science, 34th International Electric Propulsion Conference and 6th Nano-satellite Symposium*, pp. 1–14, 2015.
- [178] R. S. Freund, R. C. Wetzal, R. J. Shul, and T. R. Hayes, “Cross-section measurements for electron-impact ionization of atoms,” *Phys. Rev. A*, vol. 41, pp. 3575–3595, Apr 1990. [Online]. Available: <https://link.aps.org/doi/10.1103/PhysRevA.41.3575>
- [179] T. R. Hayes, R. C. Wetzal, and R. S. Freund, “Absolute electron-impact-ionization cross-section measurements of the halogen atoms,” vol. 35, no. 2, pp. 578–584, 1987. [Online]. Available: <https://doi.org/10.1103/PhysRevA.35.578>

Physique des tuyères magnétiques et des décharges à plasma helicon

Résumé:

Les propulseurs à plasma sans électrodes représentent une nouvelle classe de propulseurs spatiaux électriques possédant un certain nombre de caractéristiques intéressantes. Leur absence de courant net et l'absence d'électrodes exposées au plasma sont des avantages précieux pour répondre aux exigences de longue durée de vie et de fonctionnement avec des propergols alternatifs. Cependant, étant donné la complexité de la physique de ces dispositifs, les indicateurs de performance ne sont généralement pas assez compétitives par rapport aux autres technologies établies. La recherche fondamentale est donc nécessaire pour fournir un aperçu des phénomènes pertinents afin de suggérer des stratégies d'amélioration.

Dans ce cadre, cette thèse présente et discute les résultats de plusieurs campagnes expérimentales visant spécifiquement à mieux comprendre la physique à la base des décharges plasma helicon et des tuyères magnétiques. Des mesures ont été effectuées sur trois dispositifs plasma différents en utilisant une multitude de techniques de diagnostic. Les analyses paramétriques ont impliqué l'utilisation de différents propergols, de gammes spécifiques de puissance, de diverses topologies du champ magnétique appliqué. En fonction de ces paramètres externes, les propriétés des ions et des électrons ont été caractérisées de manière approfondie afin de recueillir des observations et des résultats susceptibles d'étayer la conception de futurs propulseurs à tuyères magnétiques.

Mots clés: propulsion électrique, tuyère magnétique, plasma, helicon

Physics of magnetic nozzles and helicon plasma discharges

Abstract:

Electrodeless plasma thrusters represent a new class of electric space propulsion possessing a number of interesting features. Their current-free nature and lack of plasma-exposed electrodes are valuable characteristics for meeting long lifetime requirements and operation with alternative propellants. However, given the complex physics involved in these devices, performance metrics are typically not competitive enough with other established technologies. Fundamental research is therefore needed to provide an insight on the relevant phenomena so as to suggest strategies for improvement.

In this framework, this thesis presents and discusses the results of several experimental campaigns specifically aimed at better understanding the physics underlying helicon plasma discharges and magnetic nozzles. Measurements have been performed on three different plasma devices using a multitude of diagnostic techniques. Parametric analyses have involved the use of different propellants, specific ranges of input power, diverse topologies of the applied magnetic field. As a function of these external parameters, ions and electrons properties have been extensively characterized to collect observations and findings that can support future designs of magnetic-nozzle-based thrusters.

Keywords: electric propulsion, magnetic nozzle, plasma, helicon